



HAL
open science

Development and characterization of microscopy-based approaches to monitor autophagy and mitochondrial functions in living cells

Elif Begüm Gökerküçük

► **To cite this version:**

Elif Begüm Gökerküçük. Development and characterization of microscopy-based approaches to monitor autophagy and mitochondrial functions in living cells. Cellular Biology. Université de Rennes, 2022. English. NNT: 2022REN1B041 . tel-04725069

HAL Id: tel-04725069

<https://theses.hal.science/tel-04725069v1>

Submitted on 8 Oct 2024

HAL is a multi-disciplinary open access archive for the deposit and dissemination of scientific research documents, whether they are published or not. The documents may come from teaching and research institutions in France or abroad, or from public or private research centers.

L'archive ouverte pluridisciplinaire **HAL**, est destinée au dépôt et à la diffusion de documents scientifiques de niveau recherche, publiés ou non, émanant des établissements d'enseignement et de recherche français ou étrangers, des laboratoires publics ou privés.

THESE DE DOCTORAT DE

L'UNIVERSITE DE RENNES 1

ECOLE DOCTORALE N° 605

Biologie Santé

Spécialité : Biologie Cellulaire, Biologie du Développement

Par

Elif Begüm GÖKERKÜÇÜK

**Development and characterization of microscopy-based approaches
to monitor autophagy and mitochondrial functions in living cells**

Thèse présentée et soutenue à Rennes, le 28 Septembre 2022

Unité de recherche : Institut de Génétique et de Développement de Rennes UMR6290

Rapporteurs avant soutenance :

Olivier DESTAING Institute for Advanced Biosciences, Grenoble
Robin KETTELER University College London, London

Composition du Jury :

Président :	Anne CORLU	Institut NuMeCan, Rennes
Examineurs :	Anne CORLU	Institut NuMeCan, Rennes
	Kristine SCHAUER	Institut Gustave Roussy, Villejuif
	Olivier DESTAING	Institute for Advanced Biosciences, Grenoble
	Robin KETTELER	University College London, London
Dir. de thèse :	Marc TRAMIER	Institut de Génétique et de Développement de Rennes, Rennes
Co-dir. de thèse :	Giulia BERTOLIN	Institut de Génétique et de Développement de Rennes, Rennes

ACKNOWLEDGEMENTS

Even though it is my name on the cover, this work would not be possible without a long list of people who supported me throughout this tough journey.

First and foremost, I would like to thank my thesis supervisors Giulia Bertolin and Marc Tramier for giving me the opportunity to join the team of Microscopy for Cell Biosensing. I would like to thank them for their guidance, support, and advice whenever I needed. Thank you for helping me in my way to develop into an independent and rigorous scientist.

I also would like to thank past and current members of the MCB team. I especially would like to thank Gilles Le Marchand for being my punching bag whenever fastFLIM was not working. Our past member Angélique Cheron also deserves a special thank you for providing me with every means of guidance and support during experiments. I also would like to thank Florian, Rakesh, Julia and Shruti for their help and support.

One of the biggest thank you goes to Seyta Ley-Ngardigal for being there for me personally, professionally, and mentally. I don't think that I can forget all the good and bad moments that we shared together, but more importantly the pure joy that we had together. I also would like to thank beautiful ladies of Labo340, Siham, Rebecca and Catherine. In addition to providing me with every means of technical support, they filled my life in and out of the lab with so much joy and laughter. Of course, this was also possible with the great helps of Nicolas, Nina, Audrey and Eva whom I am incredibly thankful for.

I also would like to thank Sébastien Huet, Jacques Pécréaux and their team members for all the helpful discussions and support. A special thank you goes to MRic microscopy facility for helping me with all sorts of imaging problems and more. I also would like to thank team "Gestion" and more specifically Géraldine Le Provost for helping me with all my administration problems.

I don't know if a "thank you" is enough but here is a big shoutout thank you to my partner in crime Çağlayan Tuna for sharing the hardest four years of our lives. Finally, I thank my parents who have always been there for me and given me the best support and opportunities they could give in life.

TABLE OF CONTENTS

ACKNOWLEDGEMENTS	ii
LIST OF TABLES	vi
LIST OF FIGURES	vii
LIST OF ABBREVIATIONS	ix
RÉSUMÉ	xii
SUMMARY	xvii
1. INTRODUCTION	1
1.1 Autophagy mechanisms	1
1.1.1 Types of autophagy in mammalian cells	2
1.1.2 The autophagy machinery	5
1.1.3 Structural details and conformational changes of the ATG8 family proteins	15
1.2 Selective autophagy pathways	18
1.2.1 Ubiquitin and cargo recognition	18
1.2.2 Distinct mechanisms of selective autophagy	19
1.3 Methods for monitoring autophagy	22
1.3.1 Biochemical detection of the levels of LC3 and other autophagic proteins	22
1.3.2 Electron microscopy	23
1.3.3 Fluorescence microscopy	24
1.4 FRET-based methods to monitor autophagy	32
1.4.1 Principles of FRET phenomenon	32
1.4.2 Measuring FRET by FLIM	35
1.4.3 FRET-based autophagy and mitophagy sensors	38
2. AIMS OF THIS THESIS	40
3. MATERIALS AND METHODS	41
3.1 Molecular and cellular biology	41
3.1.1 Expression vectors and molecular cloning	41
3.1.2 Cell culture and transfections	46
3.1.3 Chemical compounds	46
3.1.4 Western blotting	47
3.1.5 Immunocytochemistry	48
3.2 Microscopy	48
3.2.1 Confocal microscopy	48
3.2.2 FLIM	49
3.3 Data analysis	50
3.3.1 Western blotting analysis	50
3.3.2 Image analysis	50
3.3.3 Statistical analysis	51

4. RESULTS AND DISCUSSION	53
4.1 The LC3B biosensor based on the conformational change hypothesis	53
4.1.1 Preliminary data on the LC3B biosensor supporting the conformational change hypothesis	54
4.1.2 Current data on the LC3B biosensor challenging the conformational change hypothesis	59
4.1.3 Analyzing the LC3B biosensor sequence and revalidation of the preliminary findings	64
4.1.4 Discussion	71
4.2 The LC3B biosensor to follow the modes of action of ATG4B	75
4.3 Mitochondrial changes in BRAFi sensitive and resistant melanoma cells	138
4.3.1 Introduction	138
4.3.2 Changes in the mitochondrial dynamics of BRAFi sensitive and resistant melanoma cells	146
4.3.3 Changes in the OXPHOS chain protein levels in BRAFi sensitive and resistant melanoma cells	150
4.3.4 Discussion	151
5. CONCLUSIONS AND PERSPECTIVES	154
6. REFERENCES	157
Appendix A	190

LIST OF TABLES

Table 1	List of plasmids used in this study.	42
---------	--------------------------------------	----

LIST OF FIGURES

Figure 1	Three major types of mammalian autophagy.	2
Figure 2	Microautophagy differences in yeast and mammalian cells.	4
Figure 3	Stages of autophagy.	7
Figure 4	The subunit composition of PtdIns3K complex I and PtdIns3K complex II.	9
Figure 5	UBL conjugation systems.	11
Figure 6	The structure of LC3 shown as a ribbon model.	16
Figure 7	Conformations of GABARAP.	17
Figure 8	Receptor-mediated autophagy.	19
Figure 9	Two distinct mechanisms of mitophagy.	21
Figure 10	An immunoblotting of LC3-I conversion into LC3-II.	23
Figure 11	Jablonski diagram displaying the energy states of a molecule.	26
Figure 12	Detection of autophagic vesicles.	28
Figure 13	Monitoring autophagy progression by tandem or triple FP-tagged LC3 biosensors.	30
Figure 14	Principles of FRET.	34
Figure 15	Principle of TCSPC-based FLIM.	37
Figure 16	Principle of time-gated FLIM.	38
Figure 17	Schematic representation of the LC3B biosensor and its working mechanism based on conformational change hypothesis.	55
Figure 18	The LC3B biosensor is activated upon early- or late-stage autophagy inhibition.	57
Figure 19	The LC3B biosensor activity is dependent on the presence of ATG5.	58
Figure 20	The LC3B biosensor activity does not change upon starvation.	60

Figure 21	Mutant LC3B biosensors as compared to the WT LC3B biosensor.	62
Figure 22	The LC3B biosensor cannot detect mitophagy.	64
Figure 23	Revealing the LC3B biosensor sequence.	65
Figure 24	The WT and mutant LC3B biosensors are cleaved except the LC3B ^{G120A} biosensor.	66
Figure 25	Reproducing the preliminary findings.	68
Figure 26	The choice of cell on the Δ Lifetime values of the LC3B biosensor.	70
Figure 27	The opposing events of mitochondrial fusion and mission.	143
Figure 28	Spectrum of mitochondrial morphologies.	145
Figure 29	Scheme representing the principles of using mitoDendra2 to evaluate the mitochondrial interconnectivity.	147
Figure 30	Mitochondrial network connectivity in melanoma cells of 501Mel and SKMel28 is not altered due to BRAFi resistance.	149
Figure 31	Abundance of OXPPOS chain proteins in BRAFi sensitive or resistant 501Mel and SKMel28 melanoma cells.	151

LIST OF ABBREVIATIONS

^{18}F	Fluorine 18
3-MA	3-methyladenine
ATG	Autophagy-related
ATP	Adenosine triphosphate
BafA ₁	Bafilomycin A ₁
CCCP	Carbonyl cyanide m-chlorophenylhydrazone
CCD	Charged-couple device
CMA	Chaperone-mediated autophagy
DNM2	Dynamin 2
DRP1	Dynamin-related protein 1
EGFR	Epidermal factor receptor
EM	Electron microscopy
ER	Endoplasmic reticulum
FDG PET/CT	Positron emission tomography-computed tomography with ^{18}F fluorodeoxyglucose
FLIM	Fluorescence lifetime imaging microscopy
FP	Fluorescent protein
FRAP	Fluorescence recovery after photobleaching
FRET	Förster's resonance energy transfer
FRRG motif	Phenylalanine-arginine-arginine-glycine motif
GABARAP	Gamma-aminobutyric acid (GABA) type A receptor-associated protein
GFP	Green fluorescence protein
HBSS	Hank's Balanced Salt Solution

HSPA8/HSC70	Heat shock 70 kDa protein 8
HyD	Hydrophobic domain
IGFR1	Insulin like growth factor 1 receptor
IMM	Inner mitochondrial membrane
KO	Knock out
LAMP2A	Lysosomal-associated membrane protein 2A
LIR	LC3-interacting region
MAP1LC3	Microtubule-associated protein 1 light chain 3
MAPK	Mitogen-activated protein kinase
MC1R	Melanocortin1 receptor
MFF	Mitochondrial fission factor
MFN1	Mitofusin 1
MFN2	Mitofusin 2
Mito-QC	Mito-Quality Control
MSH	Melanocyte stimulating hormone
mtDNA	Mitochondrial DNA
MTORC1	Mammalian target of rapamycin complex 1
MVBs	Multivesicular bodies
MW	Molecular weight
NRBF2	Nuclear receptor binding factor 2
OE	Overexpression
OMM	Outer mitochondrial membrane
OPA1	Mitochondrial dynamin like GTPase optic atrophy 1
OXPPOS	Oxidative phosphorylation
PARK2	Parkin RBR E3 ubiquitin protein ligase

PBS	Phosphate Buffer Saline
PDGFR β	Platelet derived growth factor receptor β
PE	Phosphatidylethanolamine
PHB2	Prohibitin 2
PINK1	PTEN-induced putative kinase 1
PIS	Phosphatidylinositol synthetase
PMPCB	Mitochondrial processing peptidase
PtdIns3K	Phosphatidylinositol 3-kinase
PtdIns3P	Phosphatidylinositol 3-phosphate
PTEN	Phosphatase and tension homologue
RB1CC1/FIP200	RB1-inducible coiled-coil 1
RFP	Red fluorescence protein
RGB	Red green blue
ROI	Region of interest
ROS	Reactive oxygen species
RTK	Receptor tyrosine kinase
TCSPC	Time-correlated single photon counting
TOLLES	Tolerance of lysosomal environment
Ub	Ubiquitin
UBL	Ubiquitin-like
ULK1/2	Unc-51-like 1/2
V-ATPase	Vacuolar-type ATPase
WT	Wild type
YFP	Yellow fluorescence protein

RÉSUMÉ

Cette thèse de doctorat vise à développer et caractériser des approches basées sur la microscopie pour surveiller les fonctions d'autophagie et mitochondriales dans les cellules vivantes. L'étude principale présentée dans ce travail de thèse porte sur le développement et la caractérisation d'un rapporteur d'autophagie que nous avons appelé le biocapteur LC3B. De surcroît, une étude secondaire, portant sur l'étude des changements mitochondriaux dans les cellules de mélanome sensibles et résistantes à la chimiothérapie (reposant sur l'inhibition de BRAF) en utilisant la microscopie de photoconversion et des techniques biochimiques conventionnelles, est également présentée dans cette thèse de doctorat. Lorsqu'elles sont combinées, ces études ouvrent la voie à l'utilisation d'associations de biocapteurs, dit biocapteurs multiplex, y compris le biocapteur LC3B, pour suivre l'autophagie/mitophagie et plusieurs fonctions mitochondriales simultanément dans les cellules vivantes.

L'introduction de la thèse commence par un focus sur l'autophagie qui est la capacité inhérente des cellules à « s'auto-alimenter ». En effet, l'autophagie est la voie de dégradation majeure conservée chez tous les eucaryotes, de la levure à l'homme, et elle est essentielle au maintien de l'homéostasie cellulaire. L'autophagie nécessite la génération d'un organe à double membrane appelé autophagosome qui fusionne avec les lysosomes pour dégrader les composants cytoplasmiques, y compris les protéines à longue durée de vie et les organites tels que les mitochondries. Bien que plusieurs mécanismes de l'autophagie aient été décrits au cours de la dernière décennie, explorer cette voie en temps réel reste difficile. À cette fin, mon premier et principal objectif était de développer et de caractériser un biocapteur basé sur la technologie FRET (Förster's Resonance Energy Transfer) afin de suivre l'autophagie dans les cellules vivantes. L'utilisation de ce biocapteur FRET est à double lecture puisqu'il permet de suivre l'initiation mais également la progression de l'autophagie. À cet égard, l'introduction de la thèse débute par une brève description de l'autophagie et se poursuit par la description des différents types d'autophagie, notamment par des détails sur la machinerie de l'autophagie et par les voies sélectives de l'autophagie. Puis, les méthodes et les sondes

actuellement disponibles pour suivre l'autophagie sont décrites en mettant l'accent sur les techniques et les outils de microscopie à fluorescence. Dans la dernière partie de l'introduction, les méthodes et outils FRET, y compris les différentes façons de mesurer le phénomène de FRET ainsi que la description des capteurs d'autophagie basés sur le FRET.

Suivant l'introduction, les résultats sont présentés en trois sections principales. Dans la première section, notre première hypothèse sur le mécanisme de fonctionnement du biocapteur LC3B est présentée ainsi que les expériences d'optimisation que j'ai effectuées pour caractériser le capteur. Dans la deuxième partie, notre compréhension actuelle du mécanisme de fonctionnement du capteur est brièvement décrite et présentée sous la forme du manuscrit de mon premier article de recherche d'auteur qui a été soumis à *Autophagy* et qui est actuellement en cours de révision. Brièvement, notre manuscrit décrit le mécanisme de fonctionnement du biocapteur LC3B, qui a été construit à partir de la protéine clef de l'autophagie LC3B. LC3B appartient à la famille de protéines AuTophagy-related 8 (ATG8) et est considérée comme une protéine marqueur des autophagosomes puisqu'elle se trouve sur les membranes autophagosomales à toutes les étapes de la voie de l'autophagie. Chez les mammifères, les protéines ATG8 appartiennent à deux sous-familles, les MAP1LC3/LC3 (microtubule-associated protein 1 light chain 3) et GABARAP (gamma-aminobutyric acid [GABA] type A receptor-associated protein). Au total sept gènes - *LC3A*, *LC3B*, *LC3B2*, *LC3C*, *GABARAP*, *GABARAPL1* et *GABARAPL2* - codent pour les sous-familles LC3 et GABARAP chez l'homme. Les LC3/GABARAP se trouvent sous forme dites « pro-forme » inactive suite à la traduction et sont activés par des protéases à cystéine de la famille ATG4. Chez l'homme, quatre membres de la famille ATG4 (ATG4A, B, C et D) sont responsables de cette étape d'activation qui consiste à cliver protéolytiquement l'extrémité C-terminale des protéines pro-LC3/GABARAP et à les convertir en la forme dite « forme-I ». Ce clivage crucial est connu sous le nom de « d'initiation pro-LC3/GABARAP », et il est essentiel car il permet d'exposer un résidu de glycine spécifique nécessaire à la lipidation des protéines cytosoliques LC3/GABARAP-I aux groupes de tête phosphatidyléthanolamine (PE) des phagophores en formation. Les protéines LC3/GABARAP conjuguées à la PE sont alors appelées LC3/GABARAP-II et

interviennent dans l'attachement membranaire, l'hémifusion, la formation d'autophagosomes et le recrutement de cargaisons. Une fois que le phagophore est complètement fermé, les protéines LC3/GABARAP-II sont retirées (déconjuguées) de la surface externe de la membrane du phagophore par les ATG4 via l'hydrolyse du lien entre PE et LC3/GABARAP.

Du fait que les ATG4 sont impliqués dans les premiers stades d'activation de l'autophagie, le ciblage de ces protéines pour inhiber l'autophagie a un potentiel important pour bloquer la voie de l'autophagie. Cependant, les composés actuellement disponibles ciblant l'activité ATG4 présentent une faible spécificité et/ou efficacité. De plus, il y a un manque de sondes qui peuvent être utilisées dans les cellules vivantes pour suivre l'activité d'ATG4 au cours de la progression de l'autophagie. Dans l'ensemble, cela crée un obstacle pour l'identification des inhibiteurs d'ATG4 aux propriétés améliorées. Pour ces raisons, nous avons développé le biocapteur LC3B pour surveiller simultanément : 1) l'amorçage de LC3B par ATG4 et 2) l'accumulation de LC3B sur les membranes autophagiques. Le biocapteur repose sur le phénomène FRET qui est un transfert d'énergie non radiatif entre un donneur et un accepteur d'une paire de fluorophores. Ce phénomène peut se produire lorsque le spectre d'émission du fluorophore donneur recouvre partiellement le spectre d'excitation du fluorophore accepteur, et ce uniquement lorsque les deux fragments fluorescents sont très proches (moins de 10 nm l'un de l'autre). Dans cette étude, le biocapteur a été conçu en greffant les extrémités N- et C-terminales de proLC3B avec une paire donneur-accepteur FRET appelé Aquamarine (donneur, cyan) et tdLanYFP (accepteur, jaune). En l'absence d'activité ATG4, le biocapteur LC3B devrait rester tel quel dans les cellules, permettant à Aquamarine et tdLanYFP d'effectuer le FRET. Si l'ATG4 est actif, le biocapteur devrait subir un clivage protéolytique dépendant d'ATG4 à son extrémité C-terminal, perdant ainsi le fragment tdLanYFP et le phénomène FRET avec lui. Cela permet de suivre l'activité initiale d'amorçage d'ATG4 en C-terminal, en tant que cadre de lecture précoce basé sur le FRET. De plus, l'amorçage de LC3B conduit à sa conversion en la forme I, qui sera toujours étiquetée par Aquamarine (Aquamarine-LC3B-I) en N-terminal. Lorsque la protéine Aquamarine-LC3B-I résultante est intégrée dans les groupes PE des phagophores, le biocapteur

devrait fonctionner comme une sonde fluorescente canonique pour quantifier les structures ponctiformes LC3B-positives.

Suite à cette stratégie de conception, nous montrons que le biocapteur reproduit les principales caractéristiques de la protéine LC3B endogène en termes de formation de structures ponctiformes, de clivage dépendant d'ATG4B et de sa colocalisation avec des protéines lysosomales lors de l'induction de l'autophagie et/ou de l'inhibition lysosomale. Nous montrons également que le biocapteur peut relater les changements d'amorçage de proLC3B, de manière dépendante à ATG4B. En utilisant des cellules dont l'activité ATG4 est abolie (*knock-out ATG4*), nous démontrons que l'absence d'ATG4B maximise la réponse FRET du biocapteur en raison de l'absence totale d'amorçage proLC3B. Nous montrons ensuite que l'amorçage proLC3B peut être reconstituée avec l'expression ectopique de d'ATG4B de type sauvage. Fait intéressant, nous démontrons que le mutant ATG4B^{W142A}, dont il a été démontré que l'activité catalytique est considérablement réduite, est capable de rétablir l'amorçage proLC3B de la même manière que la protéine de type sauvage. En utilisant le biocapteur LC3B et en effectuant plusieurs approches pour analyser FRET/FLIM, nous rapportons les mécanismes d'action des inhibiteurs ATG4 disponibles. Ce faisant, nous fournissons un cadre d'utilisation du biocapteur LC3B et analysons les données acquises pour identifier de nouveaux inhibiteurs d'ATG4 avec une meilleure spécificité et efficacité.

Après la présentation du biocapteur LC3B, dans la troisième et dernière partie des résultats, un angle différent de mon étude de thèse concernant l'investigation des changements mitochondriaux dans les cellules de mélanome sensibles et résistantes à la chimiothérapie est présenté. Cette étude fait partie d'un projet qui vise à utiliser des biocapteurs FRET multiplexés, dont le biocapteur LC3B, pour suivre l'autophagie/mitophagie ainsi que plusieurs autres fonctions mitochondriales simultanément dans des cellules vivantes afin de déchiffrer les mécanismes conduisant à la chimiorésistance. Sur ce sujet, j'ai également écrit un article de synthèse (cf. Annexe A), qui a été publié dans *Genes* en 2020 et décrit les outils allant des sondes fluorescents aux capteurs génétiquement codés pour imager et surveiller les fonctions mitochondriales.

Enfin, la thèse se termine par les conclusions et perspectives sur le biocapteur LC3B et sur les résultats préliminaires concernant les modifications mitochondriales observées dans les cellules de mélanome sensibles et résistantes à la chimiothérapie. Au total, ces études ont posées les bases de l'utilisation de biocapteurs multiplex - y compris le biocapteur LC3B - pour suivre l'autophagie/mitophagie et plusieurs fonctions mitochondriales simultanément dans des cellules vivantes.

SUMMARY

Autophagy is the major degradation pathway conserved in all eukaryotes. It requires the generation of a double membrane organelle termed autophagosome which fuses with lysosomes to degrade the cytoplasmic components including long-lived proteins and organelles such as mitochondria. Autophagy plays a crucial role for cellular homeostasis and is involved in response to many physiological and pathological conditions. Although several mechanisms of autophagy have been dissected in the last decade, following this pathway in real time remains challenging. To this end, within the scope of my thesis project, my first and main aim was to develop and characterize a FRET-based biosensor to monitor autophagy in living cells and with a dual readout on autophagy initiation and progression, respectively. In this regard, the introduction of this thesis starts with the brief description of autophagy and followed with the description of different types of autophagy, details of the autophagy machinery, and selective autophagy pathways. Following this, currently available methods for monitoring autophagy is described with an emphasis on fluorescence microscopy techniques and tools. In the final part of the introduction, FRET methods and tools including different ways to measure FRET and FRET-based autophagy sensors are described.

The results are presented in three main sections. In the first section, our early hypothesis on the working mechanism of the autophagy sensor is presented along with the optimization experiments that I performed to characterize the sensor. In the second part, our current understanding on the working mechanism of the sensor is briefly described and presented in the form of my first author research paper manuscript which was submitted to *Autophagy* and currently under revision. In the third and last part of the results, a different angle of my thesis study regarding the investigation of mitochondrial changes in chemotherapy sensitive and resistant melanoma cells are presented. Though it may seem diverse from my main PhD studies (therefore the related introduction presented in *section 4.3.1*), this study is part of a project that aims to use multiplexed FRET biosensors, including the autophagy biosensor, to monitor autophagy/mitophagy together with several other mitochondrial functions simultaneously in melanoma cells to

decipher mechanisms leading to chemoresistance. Along the process of this project, I also wrote a review article (*cf. Appendix A*), which was published in *Genes* in 2020 and describes the tools ranging from fluorescent dyes to genetically-encoded sensors to image and monitor mitochondrial functions.

Finally, the conclusions and perspectives on our autophagy biosensor and preliminary results regarding mitochondrial changes observed in chemotherapy sensitive and resistant melanoma cells are discussed.

1. INTRODUCTION

1.1 Autophagy mechanisms

Degradation and recycling of damaged or redundant cellular components is critical to maintain homeostasis [1]. Over the course of evolution, organisms with the ability to optimally use, conserve and recycle cellular resources and cytoplasmic components have gained substantial advantage to survive in extreme conditions which includes nutrient deprivation, limited oxygen supply and high toxicity [2]. Conserved from yeast to humans, this inherent ability is a form of cellular “self-eating” known as autophagy [3–6].

Derived from the Greek “*auto*” meaning “self”, and “*phagein*” meaning “to eat”, autophagy is the major cellular pathway to degrade intracellular components including long-lived proteins and organelles via lysosomal systems [7]. The initial finding that led to the recognition of autophagy dates back to the study of Christian de Duve in 1955, where he discovered lysosomes in his attempts to understand how cells manage to compartmentalize highly lytic enzymes to avoid widespread proteolysis [3]. The lysosome is an organelle that contains an acidic environment with an acid phosphatase and a variety of hydrolytic enzymes including proteases, nucleases, glycosidases, lipases and phospholipases [2]. Soon after de Duve’s discovery, and with the advances in electron microscopy, it became clear that the lysosomes are found in various cells and tissues, and moreover they contain variety of cytoplasmic components such as mitochondria, the endoplasmic reticulum (ER) and ribosomes [8–12]. Based on these subsequent observations, the term “autophagy” was coined by de Duve in 1963 and defined as the mechanism of delivering cytoplasmic components to the lysosomes for degradation [1]. Since then, autophagy has been reported from yeast to plants and in varying tissues and organs of animals. Today, autophagy is considered as the fundamental pathway of degradation in all eukaryotes, and has been reported to be involved in response to many physiological and pathological conditions such as fasting and feeding [13], amino acid availability and deprivation [14], levels of circulating hormones [12], pathogen infection [15], DNA damage [16] and cancer [17]. Furthermore,

it has been revealed that autophagy has important roles in cellular differentiation [18], immunity [19], aging [20] and cell death [21]. While the basal levels of autophagy in these varying biological processes is key for cell survival and maintenance, altered levels of autophagy may have harmful effects leading to pathologies. To this end, deciphering the molecular mechanisms of autophagy is not only crucial to understand the balance between the beneficial and detrimental effects of this pathway, but also to develop new treatments targeting dysfunctional autophagy.

1.1.1 Types of autophagy in mammalian cells

Mammalian cells have three major types of autophagy: microautophagy, chaperone-mediated autophagy (CMA) and macroautophagy [22]. Though these different types of autophagy processes have mechanistically distinct features whereby different molecular players are involved, all three serve to deliver cytoplasmic cargo to the lysosomes for degradation (Fig. 1).

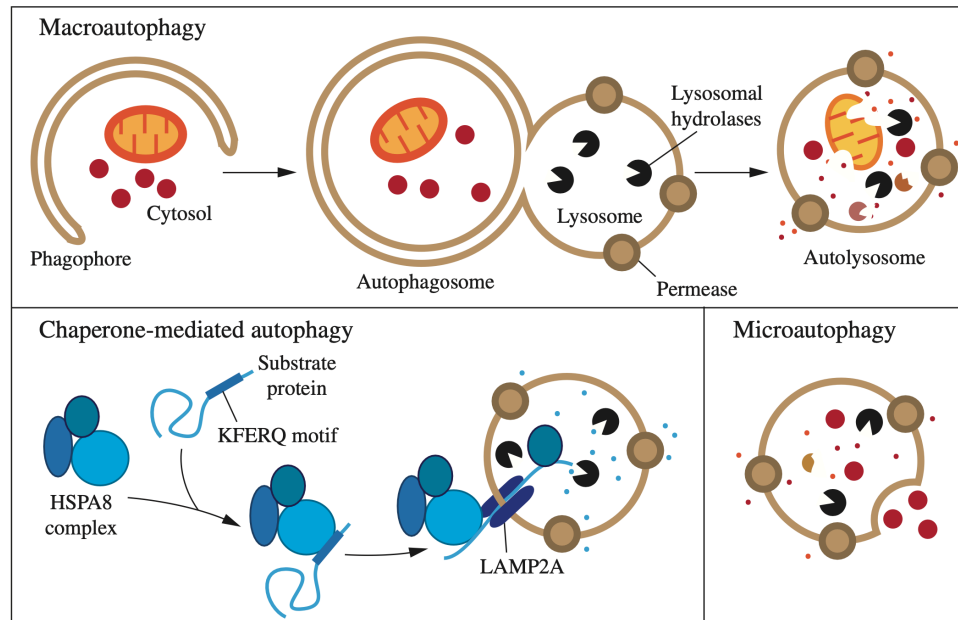


Figure 1: Three major types of mammalian autophagy. Diagram adapted from [22].

Microautophagy refers to the direct uptake of the cytoplasmic cargo into lysosomes [23]. Since the microautophagy pathway has been discovered and studied primarily in yeast [24], its definition is rather based on the mechanism observed in this organism where the cargo proteins directly enter the vacuoles (lysosomes in yeast) through cup-like invaginations or deformations on the membrane causing protrusions (Fig. 2A) [25,26]. In mammalian cells, on the other hand, it is rather referred as “endosomal microautophagy” in which the cargo proteins are first recognized by heat shock 70 kDa protein 8 (HSPA8/HSC70) and later delivered into late endosomes where they form multivesicular bodies (MVBs) (Fig. 2B) [27,28]. Subsequent fusion of MVBs with lysosomes then lead to the degradation of Hsc70-bound cargo proteins. Due to the lack of robust tools and methods to study the microautophagy processes in mammalian cells, its relevance in human health and diseases remained to be further understood.

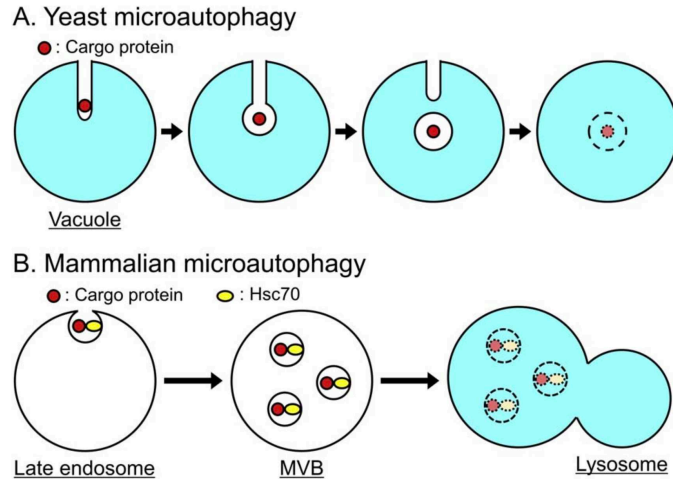


Figure 2: Microautophagy differences in yeast (A) and mammalian cells (B). Diagram adapted from [26].

In contrast to microautophagy, CMA has only been described in mammalian cells and it requires chaperons to recognize cargo proteins [22]. However, mammalian microautophagy and CMA also have a common in their dependency to the protein HSPA8/HSC70. In CMA, HSPA8/HSC70 acts as a chaperon and recognizes proteins carrying the amino acid sequence of Lys–Phe–Glu–Arg–Gln known as “KFERQ” motif (Fig. 1) [29,30]. HSPA8/HSC70 then delivers the substrate protein into the lysosome with the assistance of lysosomal-associated membrane protein 2A (LAMP2A) in the lysosomal membrane [31]. CMA is suggested to be highly specific as it only targets the proteins with KFERQ motif and therefore cannot degrade organelles or nonspecific bulk proteins [32]. Although it is known that basal CMA levels can be observed in many cell types and tissues [33,34], and CMA is triggered upon starvation [33,35,36], oxidative stress [37,38], DNA damage [39,40] and hypoxia [41,42] similar to other types of mammalian autophagy, our current understanding on how CMA is specifically regulated is limited and requires further investigations [32]. In this light, recent findings show that CMA contributes to the rhythmic removal of circadian clock proteins, thereby suggesting an interplay between circadian clock and CMA regulation [43,44]

Unlike microautophagy or CMA, macroautophagy requires the formation of autophagosome, a double-membrane vesicular structure (Fig. 1). The autophagosome is *de novo* synthesized by forming a membrane cisterna termed phagophore (previously

referred as the “isolation membrane”) [45]. As the phagophore elongates into a crescent-shaped structure, it sequesters bulk or selective cargoes and finally seals itself to generate an autophagosome. The subsequent fusion of autophagosome with the lysosome generates an autolysosome and results in the degradation of the sequestered cargo by the resident acid hydrolases [46]. The degraded products are exported back into the cytoplasm via specific lysosomal permeases/exporters to be used by the cell for biosynthesis and generating energy [47–49].

Among the three types of autophagy, macroautophagy is the heavily studied and therefore the best characterized pathway. That is why, macroautophagy is simply referred as “autophagy” in the field. Thanks to numerous studies, macroautophagy regulation under basal and induced conditions, and the involvement of key macroautophagy-related protein players are well described. However, dysfunctional macroautophagy and its relevance in human pathologies, and the molecular mechanisms leading to altered macroautophagy are remained to be deciphered and require robust tools and methods to study them. By being also the focus of this study, macroautophagy will be referred as “autophagy” hereafter.

1.1.2 The autophagy machinery

1.1.2.1 Origin of the phagophore membrane

The formation of autophagosomes starts at the phagophore assembly site (PAS). Though there is a single PAS in yeast, mammalian cells can have multiple PASs, where numerous autophagy-related (ATG) proteins are recruited to facilitate the expansion of the phagophore membrane in an orchestrated manner [50]. The initial requirement to *de novo* generate a phagosome is to provide a source of membrane. Based on electron microscopy and electron tomography studies, there can be varying sources of membranes originating from the ER, plasma membrane, mitochondria, recycling and late endosomes and lipid droplets, of which the ER and its subdomains in contact with other organelles being the primary origin of phagophore formation [51]. The PASs associated with the ER subdomains are known as omegasomes, which are dynamic and punctate structures enriched in phosphatidylinositol 3-phosphate (PtdIns3P) [52,53]. Recent studies showed

that PASs on the ER subdomains are also enriched in phosphatidylinositol synthetase (PIS) and that PIS is localized in the close vicinity of the forming phagophore, suggesting *de novo* phospholipid synthesis occurring at the contact sites to further facilitate phagophore expansion [54].

1.1.2.2 Initiation of autophagosome biogenesis by the ULK1/2 kinase complex

As mentioned above, ATG proteins are recruited to the PAS in an orchestrated manner. In this regard, the Unc-51-like 1/2 (ULK1/2) serine/threonine kinase complex is considered as the first complex to cluster at the PAS. The ULK1/2 complex consists of either ULK1 or ULK2, ATG13, RB1-inducible coiled-coil 1 (RB1CC1/FIP200), and ATG101 [55]. The ULK1/2 complex components – that are localized in the cytoplasm under basal conditions – assemble, associate with membranes and are recruited to PIS-enriched ER subdomains upon autophagy induction (Fig. 3) [54,56–58].

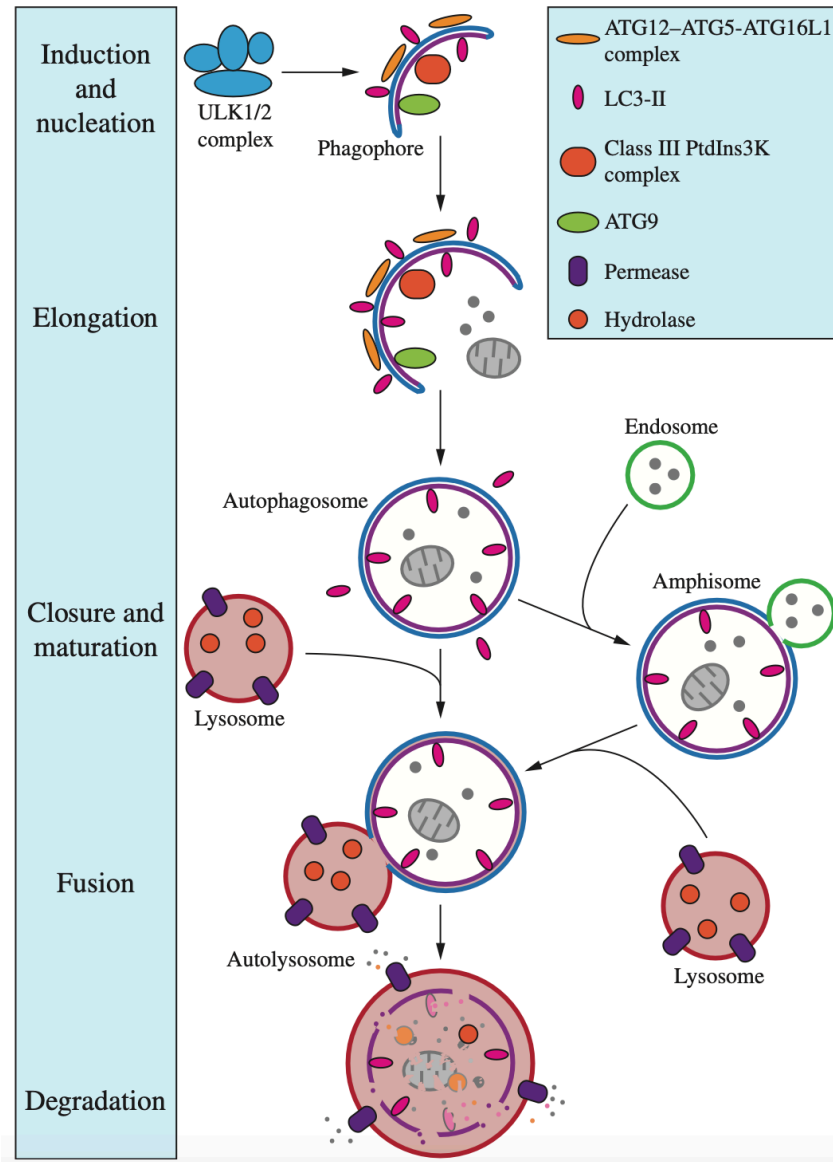


Figure 3: Stages of autophagy. Diagram adapted from [22].

Since the recruitment of ULK1/2 complex is considered as the first step initiating autophagosome formation, an active area of research focuses on the upstream signals involved in the recruitment of this complex. One of the upstream signals includes the inhibition of the mammalian target of rapamycin complex 1 (MTORC1) upon nutrient deprivation [59]. Under nutrient-rich conditions, MTORC1 associates with the ULK1/2 complex to inactivate ULK1/2 and ATG13 through phosphorylation. On the contrary, MTORC1 dissociates with the complex upon nutrient starvation, resulting in the dephosphorylation of ULK1/2 and ATG13, and autophagy induction thereafter [59,60].

1.1.2.3 PtdIns3K complex activation and PtdIns3P production at the phagophore assembly site

After the recruitment of ULK1/2 kinase complex, the next complex recruited to the autophagosome formation site is constituted by the components of the VPS34 class III phosphatidylinositol 3-kinase (PtdIns3K) complex [61]. The PtdIns3K complex is phosphorylated and activated by the ULK1 kinase, and generates PtdIns3P which localizes to the PAS. Further, it recruits PtdIns3P-binding ATG18/WIPI family proteins that are essential for autophagosome formation [62]. The PtdIns3K complex consists of VPS34, VPS15/p15 and BECN1 (Fig. 4) [55,63]. Based on its function, PtdIns3K complex can either be in complex I or complex II status (Fig. 4A vs 4B). If the PtdIns3K complex is associated with ATG14, it is considered as PtdIns3K complex I and functions in early autophagosome formation (Fig. 4A). Additionally, a fifth member for complex I – nuclear receptor binding factor 2 (NRBF2) – has recently been identified [64,65]. On the other hand, if the PtdIns3K complex is associated with UVRAG, it is considered as PtdIns3K complex II and functions in endocytic sorting (Fig. 4B). In addition to its function in endocytic trafficking, complex II may also participate in the later stages of autophagosome maturation by inducing membrane curvature [66].

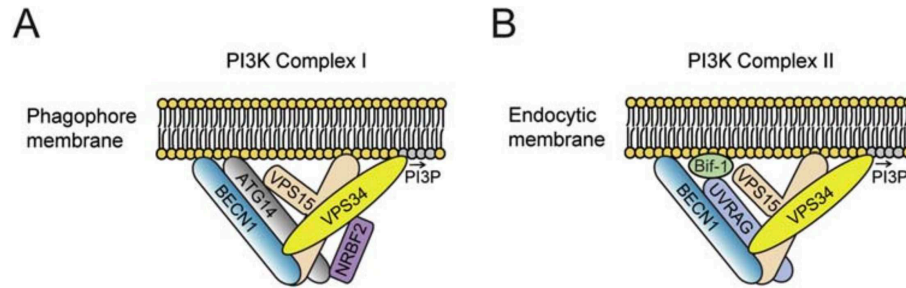


Figure 4: The subunit composition of PtdIns3K complex I (A) and PtdIns3K complex II (B). Diagram adapted from [55].

Autophagy regulation through the PtdIns3K complex mostly occurs via the interactions of proteins with BECN1 [67,68]. The antiapoptotic protein BCL2 is a binding partner of BECN1 [69]. BCL2-BECN1 interaction blocks the interaction between BECN1 and VPS34, and inhibits autophagy [69–71]. However, BCL2-BECN1 interaction weakens when multiple residues of BCL2 are phosphorylated upon autophagy induction by nutrient deprivation [72]. Another BECN-1 binding protein is AMBRA1. In nutrient-rich conditions, AMBRA1 negatively regulates autophagy by tethering the PtdIns3K complex at the cytoskeleton. However, this inhibition is lost upon starvation, when AMBRA1 is phosphorylated by ULK1 kinase [73]. Today, the upstream events regulating the PtdIns3K complexes are subject to intense research due to their link between autophagy and other cellular processes such as the cell cycle.

1.1.2.4 Recruitment of PtdIns3P-binding proteins to the PAS

PtdIns3P-binding proteins, in other words PtdIns3P effectors, bridge the gap between PtdIns3K complex and downstream autophagy machinery. In mammalian cells, the primary PtdIns3P-binding proteins belong to the WIPI family of proteins [74–76]. WIPI family has four members: WIPI1–4. WIPIs are recruited to the omegasome at the PAS and associated with the phosphorylated lipid head group in PtdIns3P by a conserved phenylalanine-arginine-arginine-glycine (FRRG) motif [75,77–79]. WIPIs function in facilitating MAP1LC3 lipidation to the autophagosome membranes by binding and recruiting the E3-like ATG12–ATG5–ATG16L1 complex. MAP1LC3 is a key protein of

autophagosomal membrane, and its function and lipidation pathway will be further detailed in the upcoming section.

1.1.2.5 Phagophore expansion facilitated by ubiquitin-like conjugation systems

Both in yeast and in mammals, there are two ubiquitin-like (UBL) conjugation systems that facilitates the phagophore membrane expansion [80]. These systems are known as the LC3 system and the ATG12 system (Fig. 5). Both systems involve proteins resembling ubiquitin which are lipidated into the phagophore membrane via ubiquitin-like conjugation mechanisms. At the final step of these conjugation systems, the key autophagy protein LC3 is lipidated into the phosphatidylethanolamine (PE) lipid head groups of the forming phagophore with a covalent bond. LC3 is a protein belonging to the ATG8 family of proteins and it is used as a marker of autophagosomes to measure autophagy activity. The activation mechanism of these conjugation systems represented the key findings of the Nobel Prize in Physiology or Medicine in 2016 that was awarded to Dr. Yoshinori Ohsumi, whose laboratory made key mechanistic discoveries to reveal mechanisms of autophagy by using mass spectrometry and biochemical methods.

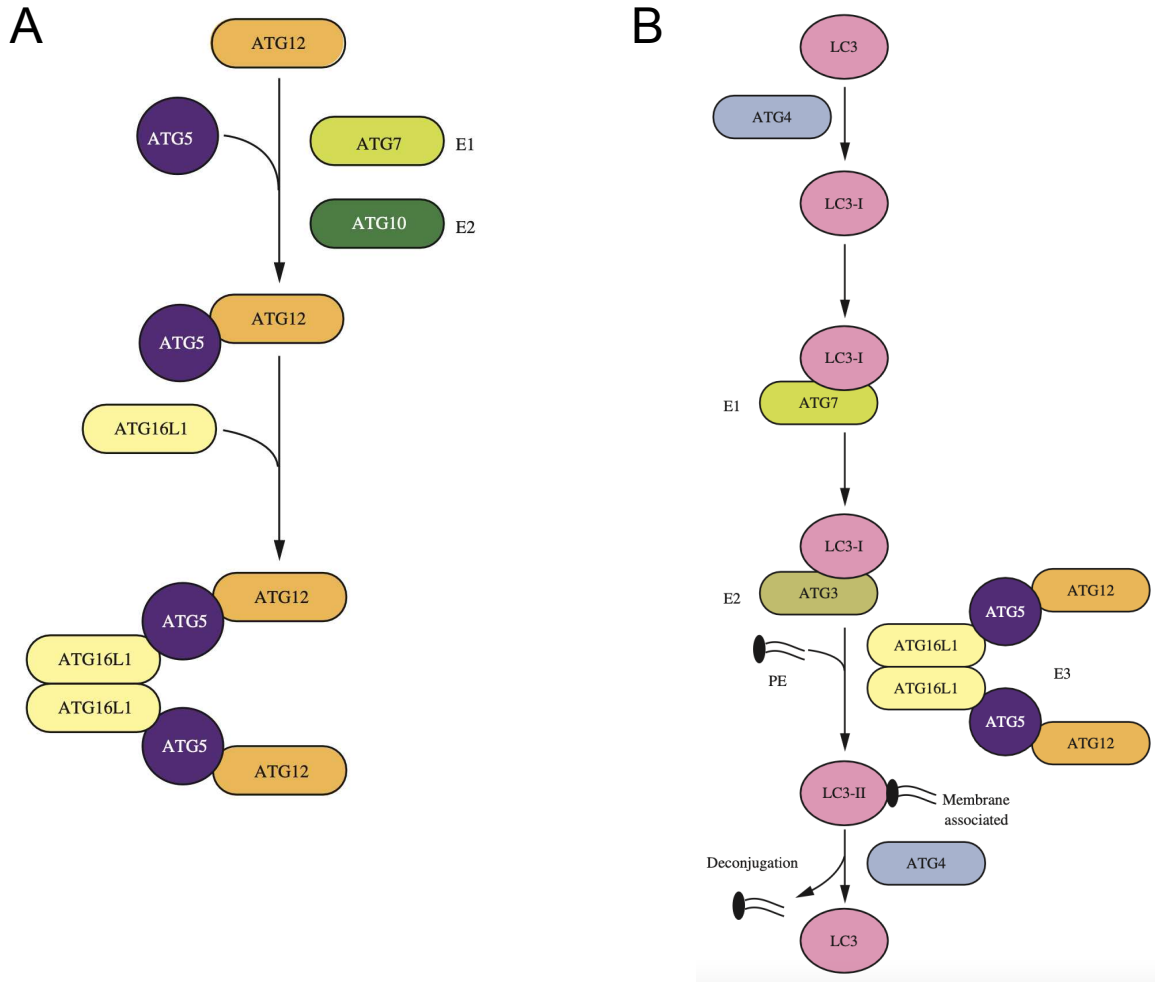


Figure 5: UBL conjugation systems. (A) ATG12–ATG5–ATG16L1 conjugation complex. (B) LC3 conjugation system. Diagram adapted from [22].

The ATG12 conjugation system involves the formation of ATG12–ATG5–ATG16L1 complex (Fig. 5A). To this end, the UBL protein ATG12 is activated by an E1-like enzyme ATG7 and conjugated to ATG7 via a thioester linkage in an ATP-dependent manner [81]. Activated ATG12 is transferred to an E2-like enzyme ATG10 and irreversibly conjugated to ATG5 [82,83]. This reaction differs from ubiquitination by being irreversible and not requiring a specific E3 ligase enzyme [84]. Two ATG12–ATG5 conjugates then form a complex with an ATG16L1 dimer to form the larger complex of ATG12–ATG5–ATG16L1 [82,85]. Though the ATG12–ATG5–ATG16L1

complex associates with the phagophore membrane, it dissociates upon autophagosome closure [85].

The other UBL conjugation system that facilitates the phagophore expansion is the LC3 system (Fig. 5B). As mentioned above, LC3 is a ubiquitin-like protein and the key regulator of autophagy. LC3 belongs to the ATG8 family of proteins. While yeast has only one Atg8 protein, in mammals, ATG8 family divides into two subfamilies, the MAP1LC3 or LC3 in short (microtubule-associated protein 1 light chain 3) and the GABARAP (gamma-aminobutyric acid [GABA] type A receptor-associated protein) subfamilies [86,87]. A total of seven genes – *LC3A*, *LC3B*, *LC3B2*, *LC3C*, *GABARAP*, *GABARAPL1* and *GABARAPL2* – code for the LC3 and GABARAP subfamilies [88]. All the members of the ATG8 family have been demonstrated to be involved in autophagosome formation and biogenesis [89]. However, the functional and the tissue-specific expression differences between LC3 and GABARAP subfamilies are not well defined. The ATG8 family is usually represented by LC3, since the LC3 subfamily and more specifically LC3B is the foremost studied isoform in mammalian systems [90]. Upon translation, LC3 is in an inactive pro- form and activated by the ATG4 family of cysteine proteases [91,92]. In humans, four members of the ATG4 family (ATG4A, B, C and D) are responsible for this activation step, which is to proteolytically cleave the C-terminus of pro-LC3 protein and convert it into the so-called form-I. This crucial cleavage is known as “pro-LC3 priming”, and it is essential to expose a specific glycine residue – G120 – required for the lipidation of the cytosolic LC3-I protein to the PE head groups of the forming phagophores. The processed LC3-I is then activated by the E1-like enzyme ATG7 and transferred to the E2-like enzyme ATG3 [93]. At the final step of LC3 lipidation, the ATG12–ATG5 conjugate acts as an E3-like ligase and facilitates the covalent conjugation of the C-terminal glycine of LC3 to the lipid PE [93–95]. The PE conjugated LC3 is then called LC3-II. In contrast to the ATG12 conjugation system, LC3-PE conjugation is reversible. Once the phagophore is fully closed, LC3-II proteins are removed from the outer surface of the autophagosome membrane by ATG4s, through the hydrolysis of the link between PE and LC3 [91]. A regulation mechanism on ATG4 activity has been demonstrated to be achieved by ULK1 kinase, where the phosphorylation by ULK1 negatively regulates ATG4 activity to avoid immature LC3

cleavage by ATG4 itself (referred as deconjugation hereafter) [96,97]. Although the importance of this second round of deconjugation by ATG4 was shown to be important for the normal progression of autophagy in yeast [98–100], recent studies in human cells suggest the existence of autophagy-independent roles for the deconjugation activity of ATG4s [101,102]. Therefore, the relevance of ATG4-mediated deconjugation for the progression and completion of autophagy in models other than yeast still requires further investigation [98–103].

Even though the LC3 conjugation system has been heavily studied for decades and in turn well understood in terms of its mechanism, the precise function of LC3 on autophagic membranes is still unclear. Studies in mice lacking the components of the LC3 conjugation machinery revealed that the LC3 lipidation and in general autophagy is crucial for neonatal survival [104,105]. Moreover, the tissue-specific knockout of the conjugation machinery components in adult mice reported to cause diseases such as cancer and neurodegeneration, the latter being caused by the accumulation of the protein aggregates in the brain [104,105]. Since LC3 acts as a coat protein for autophagosomes, an important function is related to the recruitment and scaffolding of proteins containing the LC3-interacting region (LIR) motif. The LIR is a consensus motif and a common feature of autophagic cargo receptors such as p62/SQSTM1 and facilitates the binding of the cargo receptors with LC3 and the phagophore. This way, a specific cargo to be degraded is recruited to the autophagic machinery to mediate selective autophagy [106]. Alternatively, cargo receptors with the LIR motif can also promote the formation of autophagosomes around the cargoes [55]. While both the LC3 and GABARAP subfamilies function to recruit cargo, there is also a subfamily-specific role in different stages of the autophagosome biogenesis. Indeed, while LC3s are suggested to be involved in the early stages of the phagophore membrane elongation, GABARAPs are suggested to function in the later stages of autophagosome maturation and completion [107]. In addition to this, recent studies also suggest that both LC3 and GABARAP proteins, and the components of the conjugation machinery are involved in other membrane trafficking and signaling pathways [102,108].

Another protein suggested to participate in phagophore expansion is the transmembrane protein ATG9. ATG9 is a six-pass-transmembrane protein that can form highly mobile single-membrane vesicles [109,110]. ATG9-containing vesicles are transported to shift their localization within the cells in a nutrient-regulated manner to function in membrane recruitment for the phagophore [111]. Under nutrient-rich conditions, ATG9 localizes to the non-PAS peripheral sites such as trans-Golgi network and late endosomes [111]. Upon starvation however, ATG9 is transported to PAS and then shuttles from the PAS back to the peripheral sites. Although the exact function of ATG9 trafficking is not fully understood, it has been shown to be dependent on both ULK1 kinase complex and PtdIns3K activity [111]. Moreover, in a recent study, ATG4s and their proximity partners LRBA and ARFIP2 have been suggested to regulate ATG9 vesicle trafficking to mitochondria to mediate selective mitochondrial degradation (mitophagy) [102].

1.1.2.6 Autophagosome completion and fusion with lysosomes

Once the expanding phagophore matures to fully surround its cargo, it closes to form a completed double-membrane autophagosome. Although the size of an autophagosome varies based on organism and cargo type, its diameter typically ranges from 0.5 to 1.5 μm in mammals [112–114]. Once the autophagosome is formed, it is trafficked via the microtubule network to ultimately fuse with lysosome, which then generates a structure known as autolysosome (Fig. 3) [115,116]. In mammals, it is possible that the autophagy pathway converges with the endocytic pathway before the fusion of the autophagosome with the lysosome. If it is the case, autophagosome may first fuse with early or late endosomes to form amphisomes, that are intermediate/hybrid organelles formed prior to generating autolysosomes (Fig. 3) [117,118]. While the fusion of the autophagosome with the lysosome is ongoing, the outer autophagosome membrane fuses with the lysosome membrane. The inner autophagosome membrane and the autophagic cargo are exposed to acidic lumen of the lysosome, where they are degraded and finally exported back to cytoplasm through lysosomal permeases to be used in cellular biosynthesis pathways [46]. The autophagosome-endosome/lysosome membrane fusion requires the components of the soluble N-ethylmaleimide-sensitive factor

attachment protein receptor (SNARE) machinery which localizes on the two target membranes and mediate membrane tethering and fusion [119]. To prevent premature fusion, autophagosomal membrane SNARE protein STX17 localizes on the outer membrane of the completed autophagosomes, and then interacts with the cytosolic tethering factor SNAP29 to finally mediate the assembly of STX17 and SNAP29 with the lysosomal SNARE proteins VAMP7 or VAMP8 [119]. Several ATG proteins such as ATG14 and the components of the phagophore assembly pathway such as the class III PtdIns3K complex are also suggested to promote in autophagosome-lysosome fusion, as they are found to localize on the mature autophagosomes [120].

1.1.3 Structural details and conformational changes of the ATG8 family proteins

The structural studies on ATG8 family proteins were fundamental to understand not only the structural similarities of ATG8 proteins with ubiquitin but also to enlighten their unique features that facilitates the autophagosome biogenesis.

Based on the structure of rat LC3-I (the primed LC3) published by Sugawara *et al.* in 2004, LC3 protein was shown to contain a ubiquitin core with five-stranded central β -sheets (β 1- β 5) flanked by two pairs of α -helices (α 1 and α 2, α 3 and α 5) (Fig. 6) [121]. Even though LC3 and GABARAP subfamilies were suggested to be structurally similar to each other, some differences were also reported such as the amino acid insertions observed in the loops between β 1- β 2 and β 3- β 4 strands of LC3 as compared to GABARAP [121–126]. On the other hand, a key characteristic feature of the ATG8 family proteins is the presence of α 1 and α 2 helices at the N-terminus that are attached to the ubiquitin core by a number of hydrophilic and hydrophobic interactions [121]. The majority of the residues mediating these interactions are found to be strictly conserved in the ATG8 family, thus highlighting the functional importance of the α 1 and α 2 helices, and their interaction with the ubiquitin core [121].

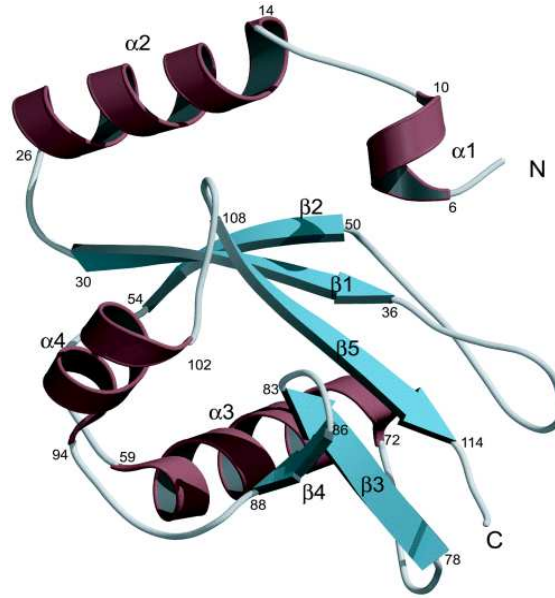


Figure 6: The structure of LC3 shown as a ribbon model. Diagram adapted from [121].

Even though Sugawara *et al.* only reported a closed conformation of LC3 in their crystals, another study published by Coyle *et al.* reported two conformations – open and closed – depending on the position of the $\alpha 1$ helix of GABARAP, and therefore raising the possibility that ATG8 family proteins may adopt different conformations depending on their function during autophagy (Fig. 7) [124]. According to this study, the $\alpha 1$ helix, which corresponds to the first 10 amino acids of the N-terminus (referred as NH[10]), was found to be almost 180° projected away from the ubiquitin core in the open conformation. The authors termed this open conformation as “the oligomeric form”, as GABARAP was found to be binding a neighboring molecule in the crystal lattice. Conversely, the closed form was referred as “the monomeric form” due to GABARAP being in a relatively compact conformation where the NH(10) residues were projected down toward the surface of the ubiquitin core and subsequently not accessible for any interaction. Based on further structure-based mutational analyses, authors suggested that the open conformation being responsible for association with membranes, other proteins, and tubulin binding [124]. Supported by other studies performed with yeast Atg8, it was demonstrated that the NH(10) has the structural flexibility to form intermolecular

interactions with another Atg8 protein or tubulin when it is extended away from the ubiquitin core (open conformation) [127,128].

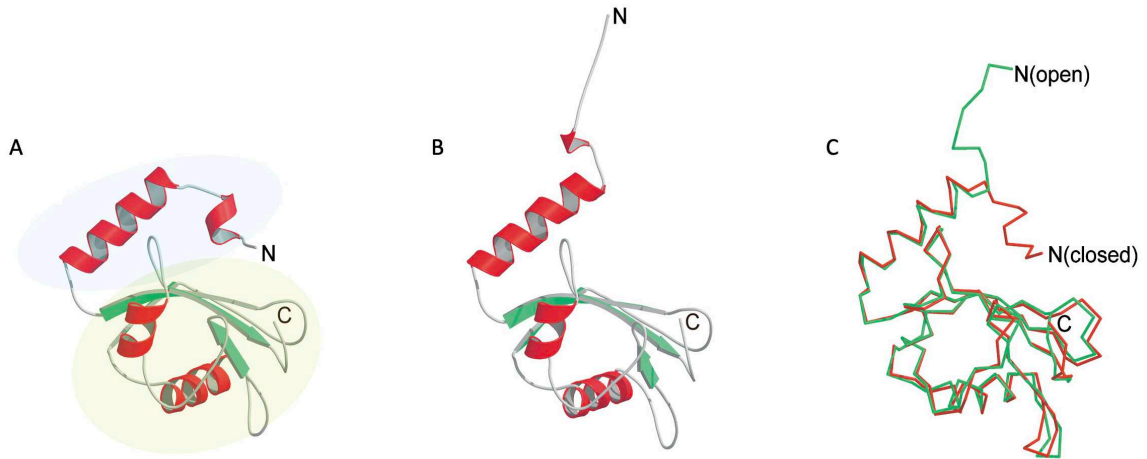


Figure 7: Conformations of GABARAP. (A) Closed monomeric form. (B) Open oligomeric form. (C) Superimposition of monomeric and oligomeric form. Diagram adapted from [124].

In a more recent study performed with *C. elegans*, it has been suggested that LC3 and GABARAP subfamilies may function in different stages of phagophore biogenesis and completion depending on their conformations [129]. While LC3 mediates phagophore tethering, GABARAP was suggested to act downstream, possibly at the sealing of the phagophore membrane. In this regard, the study suggests that LC3 may have an open conformation at the N-terminus when it is conjugated to PE to control autophagosome size, while the downstream acting GABARAP may be in a closed conformation when sealing the phagophore membrane [129]. Considering the highly specific interactions stabilizing the N-terminus in both open and closed conformations, it is very likely that these conformations are not the results of a flexible N-terminus, but rather a switch system with a functional relevance that is induced upon interactions with other ATG proteins and tubulin, and conjugation with phagophore membrane [124,129]. However, the isoform-specific conformational changes of mammalian ATG8 proteins are still unclear and require further investigations.

1.2 Selective autophagy pathways

The bulk or nonselective autophagy is the degradation and recycling of cytoplasmic components to compensate for the lack of building blocks upon nutrient or energy deprivation. In bulk autophagy, there is no selectivity towards the cargo to be degraded when autophagy is induced [130,131]. On the other hand, under nutrient-rich and non-autophagy induced conditions, a basal level of autophagy is facilitated by the cells to remove specific cargos such as aggregated proteins, damaged organelles, excess peroxisomes and invading pathogens for cellular maintenance purposes [132–134]. Such removal of a specific cargo is referred as selective autophagy and serves a house-keeping function to maintain cellular homeostasis by selectively degrading cargo. Selective autophagy pathways require autophagy receptors that can recognize the cargo and bind to ATG8 family proteins via the LIR motif [135]. Depending on the autophagic cargo to be degraded, the selective autophagy pathway is classified, *e.g.*, the selective degradation of mitochondria is called mitophagy. Currently, more than twenty selective autophagy pathways have been identified, together with their respective receptor(s) recognizing the specific cargo [136].

1.2.1 Ubiquitin and cargo recognition

A mechanism used by the autophagy receptors to recognize cargo is to identify them by their tags such as ubiquitin [134]. Ubiquitin (Ub) is a highly conserved small (8.6 kDa) protein used by the eukaryotic cells to modify proteins in a process called ubiquitylation [137]. Ubiquitylation regulates many cellular processes including protein degradation, autophagy, signal transduction and DNA repair [137]. Ubiquitins can form chains with varying topology while attaching to their target protein (Fig. 8). A ubiquitylated cargo can also be degraded by the proteasome [138]. The degradation pathway of which the ubiquitylated cargo will go through is decided based on the type and number of ubiquitin linkages. When the ubiquitylation cue leads to the autophagic degradation, autophagy receptors such as p62/SQSTM1 serve as adaptor proteins that associate both with the ubiquitin and LC3-II on the phagophore membrane to facilitate the cargo internalization within the autophagosome (Fig. 8) [136,139–141].

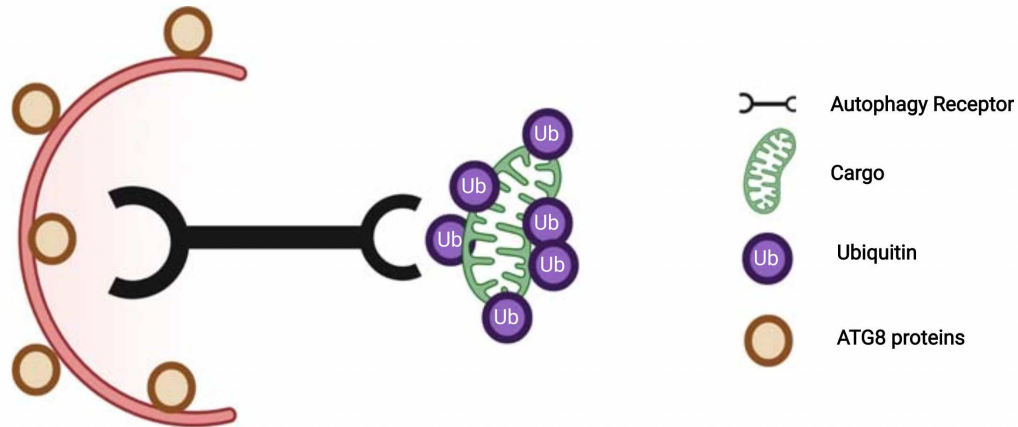


Figure 8: Receptor-mediated autophagy. The autophagic cargo mitochondrion is ubiquitylated at multiples sites and recognized by the receptor for cargo internalization within the autophagosome. Diagram adapted from [136].

1.2.2 Distinct mechanisms of selective autophagy

In addition to ubiquitin-dependent selective autophagy pathway, there are also distinct pathways to degrade specific cargo. Mitophagy is an example of such a selective autophagy pathway that is mediated by two distinct mechanisms.

Mitophagy is an organelle-specific autophagy pathway in which the mitochondria are selectively degraded to mediate a steady-state turnover of these organelles as well as the clearance of damaged ones [142,143]. Mitochondria are double membrane bound multifunctional organelles that are essentially known for their role in adenosine triphosphate (ATP) synthesis and contribution to cellular metabolism. Yet these organelles regulate a varying cellular functions including calcium buffering, cellular signaling, phospholipid biosynthesis/transport, iron homeostasis, and apoptotic cell death [144–146]. The electron transport chain of mitochondria generates reactive oxygen species (ROS) that can be harmful for the organelle integrity and function [147]. Increased levels of mitochondrial ROS can promote excessive calcium uptake, leading to a loss in membrane potential and subsequently causing the release of apoptotic factors that can initiate cell death signaling [148–150]. In this context, mitochondrial quality

control, and thus the maintenance of a healthy and functional mitochondrial population, is an important determinant of cell fate [151]. To this end, mitophagy serves as a protective mechanism to selectively sequester and degrade damaged mitochondrial units before they activate cell death pathways [152,153].

The most well studied molecular pathway of mitophagy is mediated by the phosphatase and tension homologue (PTEN)-induced putative kinase 1 (PINK1) and the E3 ligase PARK2 (Parkin) (Fig. 9) [154]. Under basal conditions, PINK1 is imported into the inner mitochondrial membrane (IMM) and cleaved by several intramitochondrial proteases such as the mitochondrial processing peptidase (PMPCB) [155–158]. Truncated PINK1 is then released into the cytoplasm and degraded by the ubiquitin-proteasome system [159,160]. Upon membrane potential loss, PINK1 can no longer be imported into the IMM, but it is rather stabilized on the outer mitochondrial membrane (OMM) [161–163] where it recruits Parkin [161]. The E3 ligase activity of Parkin is activated when PINK1 phosphorylates ubiquitin at Ser 65 [164]. Parkin then ubiquitinates OMM proteins for their recognition and engulfment by the autophagosomes or degradation by proteasomal machinery [165–170]. In the case of autophagosomal engulfment, autophagy receptor proteins such as p62/SQSTM1 bind to the ubiquitinated mitochondrial units to link them with LC3 [171]. Subsequent fusion of the autophagosomes with the lysosomes results in the complete degradation of mitochondrial remnants. This mechanism was shown to be impaired in inherited forms of Parkinson disease, in which the accumulation of dysfunctional mitochondria contributes to the death of dopaminergic neurons [172].

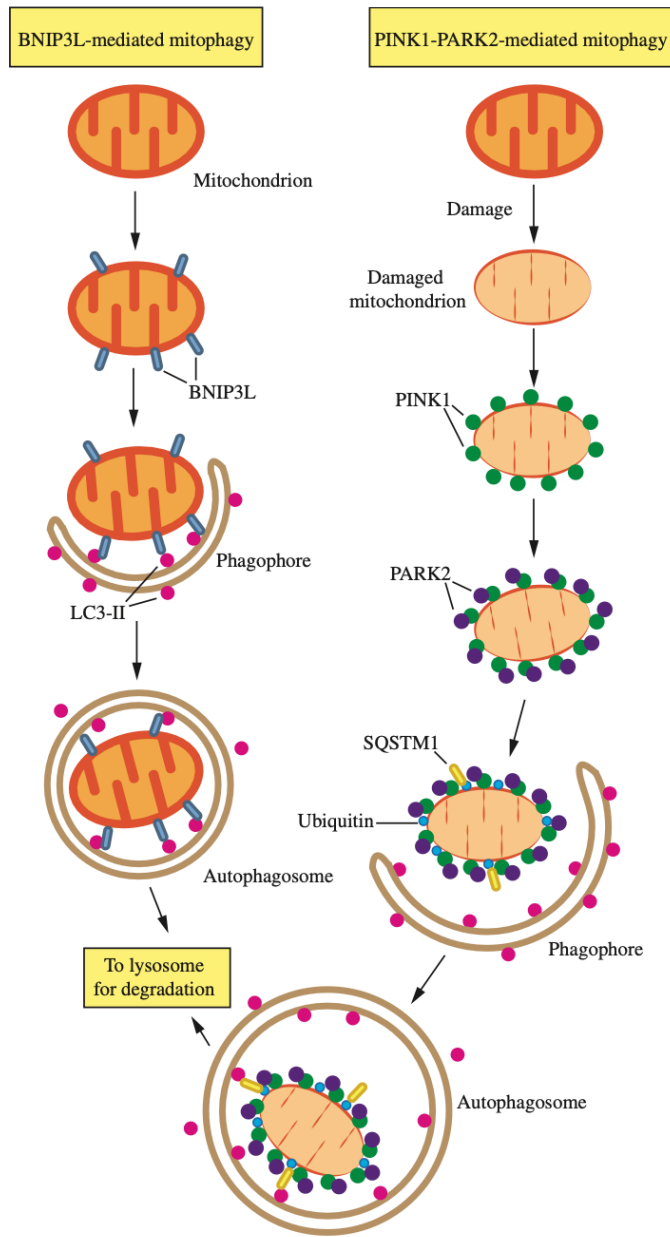


Figure 9: Two distinct mechanisms of mitophagy. BNIP3L-mediated mitophagy and PINK-PARK2 mediated mitophagy. Diagram adapted from [22].

Aside from PINK1/Parkin-mediated mitophagy, mitochondrial membrane proteins

such as BNIP3L may serve as a mitophagy receptor to mediate mitophagy as well (Fig. 9). In this case, mitophagy receptor BNIP3L directly interacts with LC3 through its LIR motif and allows for cargo recognition [173]. Interestingly, recent studies demonstrated that BNIP3L and another mitophagy receptor Prohibitin 2 (PHB2) may also act in PINK1/Parkin-mediated mitophagy to promote mitochondrial clearance [174–177].

1.3 Methods for monitoring autophagy

Autophagy has been implicated in many pathological conditions such as neurodegenerative diseases, cancer, inflammation, muscular and heart disorders [178]. Consequently, the need for developing better tools and robust methods to accurately detect, monitor and measure autophagic activity has been the focus of interest in the field.

The dynamic nature of autophagy is defined by the term “autophagic flux” which is used to describe the series of events that include the autophagosome biogenesis and completion, delivery of autophagic cargo, and the degradation by the lysosomes. Therefore, a static measurement that focuses on only one aspect of this dynamic process can be misleading. To this end, flux assays designed to induce or block autophagic activity at different steps are necessary to accurately measure the rate of autophagy [179]. Today, the principal methods that are used to measure autophagy in mammalian systems include i) the biochemical detection of the membrane-conjugated form of LC3, ii) electron microscopy, and iii) fluorescence microscopy detection of the subcellular LC3 localization [179].

1.3.1 Biochemical detection of the levels of LC3 and other autophagic proteins

A commonly used biochemical method to assess autophagic activity is the western blotting to measure the changes in the protein levels of the autophagy proteins. LC3, p62/SQSTM1, ULK1, ATG12–ATG5 complex and ATG16L1 are the most frequently used reference proteins for autophagic activity. Among them, LC3 is particularly useful to assess autophagosome numbers due to its conversion from cytosolic LC3-I to lipidated LC3-II. Even though the lipidated LC3-II has a molecular weight (MW) bigger than LC3-I, it migrates faster in an SDS-PAGE gel because of extreme

hydrophobicity and appears as a smaller molecular weight protein (Fig. 10) [90,180,181]. The amount of LC3-II is then used to estimate the number of autophagosomes [182]. However, it is important to note that not all lipidated LC3-II is associated with autophagic membranes, and that some portion of the LC3 pool can be lipidated into non-autophagic membranes in an autophagy-independent manner [183]. In such cases, it would not be possible to discriminate autophagic-membrane lipidated LC3-II from that of non-autophagic membrane ones in western blotting, therefore complementary approaches are required to validate the results.

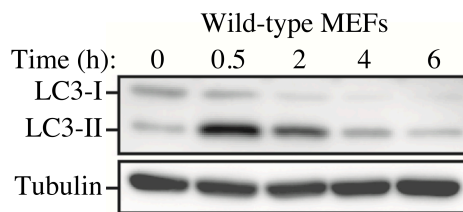


Figure 10: An immunoblotting of LC3-I conversion into LC3-II. Expression levels of LC3-I and LC3-II have been observed in a 6h time-course starvation of wild type MEF cells. Tubulin used as a loading control. Micrograph adapted from [90].

1.3.2 Electron microscopy

Electron microscopy (EM) is the method that led to the discovery of mammalian autophagy in the late 1950s. Therefore, it is the most traditional method utilized in the field and considered as a gold standard until the 1970s with the introduction of biochemical assays [184]. The ultrastructure of an autophagosome is defined as the double membrane organelle that is containing undigested cytoplasmic components such as mitochondria and protein aggregates [179]. Since this definition is rather straightforward, detecting the autophagosomes on EM images is considered relatively easy. However, unlike the autophagosome, an autolysosome is a hybrid organelle with a single membrane and contains cytoplasmic components that are digested fully or partially [179]. That is why, it can be harder to identify autolysosomes from endocytic compartments. In addition to this, EM has a limitation regarding the quantitative assessment of autophagy as the chosen images may be misleading if the sampling size is

not large enough [181]. Thus, even though EM is a powerful technique, it should be coupled with other methods to support the conclusion based on an EM image.

1.3.3 *Fluorescence microscopy*

With the remarkable growth in the use of fluorescence in the biological sciences over the last 30 years, fluorescence microscopy has been the major source of discoveries in the field of autophagy. Fluorescence microscopy offers numerous techniques and tools that are rapidly and constantly advancing not only to visualize but also to accurately quantify biological processes. Together with the increased accessibility, fluorescence microscopy became an invaluable tool to study autophagy and many other cellular processes. By being also the central instrument of this study, the basic principles and autophagy-related applications of this methodology will be presented in the following sections.

1.3.3.1 Principles of fluorescence

Excitation and emission

In fluorescence microscopy, the aim is to reveal the object of interest that can fluoresce in a black background. Fluorescence is a physical phenomenon described by the absorption of light of a particular wavelength and after a brief period of time – termed as the fluorescence lifetime (τ) – emission of light at longer wavelengths [185]. The phenomenon of fluorescence is first described by George G. Stokes in 1852. Stokes observed that the fluorescence emission always occurred at a longer wavelength than that of the excitation light, which is later termed as the “Stokes shift” to describe the difference between the exciting and emitted wavelengths. This critical property of fluorescence is utilized in fluorescence microscopy by using fluorescence filter combinations that allows to filter out the exciting light without blocking the emitted fluorescence thereby making it possible to reveal only the objects that are fluorescent [185].

Fluorophores

Fluorophores are the molecules with fluorescent properties. The efficiency and the wavelengths of absorption and emission of a fluorophore is determined by its outermost electron orbitals. Upon absorption of light energy – in other words photons – fluorophore molecules that are normally in their “ground state” exhibit alterations in their electronic, vibrational, and rotational states. When this absorbed energy triggers an electron to move into a different orbital that is farther away from the nucleus, the fluorophore molecule reaches an “excited state” due to this rapidly occurring transition. Excitation also causes molecular vibrations in which the internuclear distances vary over time. Eventually, fluorophore returns to its low-energy ground state during which the vibrational relaxation and fluorescence emission occurs. In fluorescence microscopy, synthesized compounds that usually have ring structures (aromatic molecules) with pi bonds are used since they can easily distribute outer orbital electrons over a wide area. These compounds are easily excited with relatively low energy photons since they exhibit rather a small energy difference between their excited state and ground state orbitals.

Jablonski diagram

Described by the scientist Alexander Jablonski in 1930s, a Jablonski diagram is the depiction of different energy levels involved in the absorption and emission of light (Fig. 11) [185]. On the left side, the diagram shows the singlet states of ground (S_0), first (S_1), and second (S_2) which are the electronic energy states. Within each of these energy states, fluorophores can exist in distinct vibrational energy levels, described by 0, 1, 2, 3, and so on. The ground state S_0 depicts the energy of a fluorophore that is not being excited by the light. The singlet states of S_1 and S_2 , on the other hand, depicts the excited states upon which an electron moves into a different orbital. While the excited state of S_2 contains more energy than S_1 , S_1 contains more energy than the ground state S_0 . Upon light absorption, a fluorophore is usually excited to some higher vibrational level of either S_1 or S_2 . This is followed by the internal conversion which is the rapid relax to the lowest vibrational level of S_1 . Typically, return to the ground state occurs to a higher excited vibrational ground state level, and then quickly reaches a thermal equilibrium.

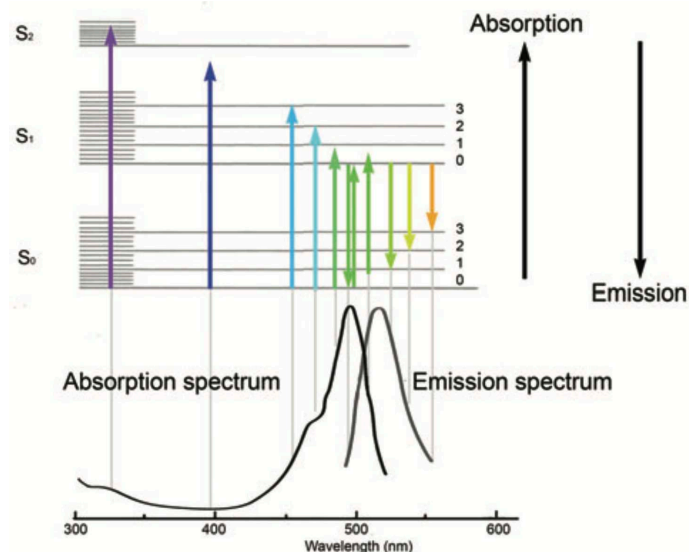


Figure 11: Jablonski diagram displaying the energy states of a molecule. The absorption and emission spectra of a common fluorophore FITC are shown below the Jablonski diagram. The vertical gray lines are aligned with the spectra of the absorbed (arrows pointing up) and emitted (arrows pointing down) photons. The colors of the arrows depict the wavelength of the photons. Diagram adapted from [185].

1.3.3.2 Fluorescent proteins and their applications in monitoring autophagy

Since the discovery of green fluorescence protein (GFP) in the early 1960s when studying the bioluminescent properties of the jellyfish *Aequorea victoria* [186], a broad range of fluorescent proteins (FPs) with varying colors have been developed to be used as fluorescent tags for bioimaging. Today, FPs with different physicochemical properties based on excitation/emission spectra, Stokes shift, maturation rate, stability, photo-reactivity, and pH-sensitivity are used as tools to “sense” varying cellular and molecular events in living cells with high spatiotemporal resolution [187–192].

Fluorescent proteins (FPs) are members of a structurally homologous class of proteins that can self-generate an intrinsic chromophore from a sequence of three amino acids within their own polypeptide sequence and without requiring any cofactors or enzymatic components [193]. FPs have a rigid β -barrel shell which contains the protein matrix surrounding the vital chromophore [194,195]. The formation of a chromophore is

achieved by correctly orienting the crucial residues to catalyze and direct chromophore synthesis pathway [196]. By experimentally altering the processes of chromophore formation and maturation, new FPs with new features and sensing capabilities can be generated [196].

FPs are genetically encodable and can be expressed in cells using transient or stable transfections, or integrated into the genome with gene editing techniques. Thus, a protein of interest can easily be fused with a dedicated FP which is suitable for the strategy of the desired molecular sensing. As such, FP-tagged proteins are called biosensors and are used to perform real-time monitoring in space and time when coupled with live cell imaging techniques.

To monitor autophagy, FP-based biosensors are available, though majority of them are targeted to follow autophagy progression. These biosensors were generated with different FPs, which have different properties such as pH sensitivity, stability, brightness, spectral profiles and Förster's resonance energy transfer (FRET) [197], and will be described in the following sub-sections.

GFP-LC3

GFP-tagged LC3 is a widely used construct to visualize both the cytosolic (GFP-LC3-I) and the membrane lipidated (GFP-LC3-II) pools of LC3 (Fig. 12A) [182,197]. Upon expressing this construct in the cells, GFP-LC3-I form of the biosensor is observed to be dispersed in the cytosol, while GFP-LC3-II form is observed to be present in the form of puncta-shaped structures representing the autophagic vesicles. By quantifying the number of punctate GFP, one can determine the number of autophagosomes or autolysosomes. Therefore, an increase or decrease in the number of these structures can be indicative of autophagy induction or inhibition, respectively. In addition to GFP, FPs with different colors such as YFP, CFP, RFP, mCherry and HcRed have been used to fuse LC3 and monitor autophagy [198–203].

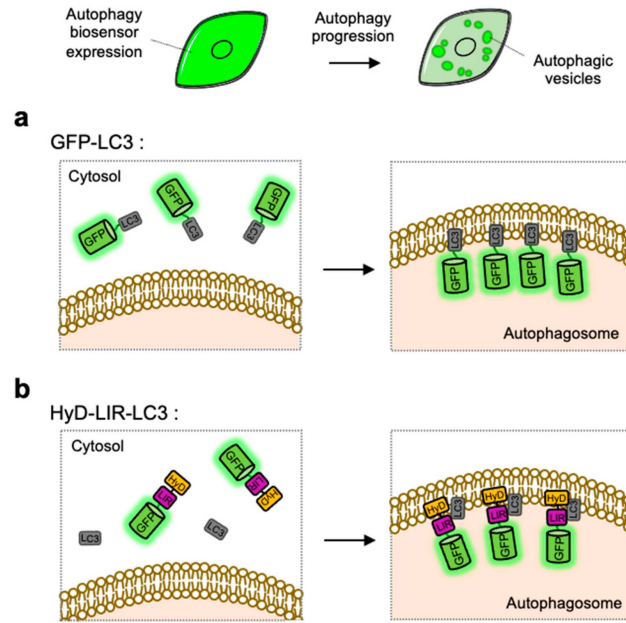


Figure 12: Detection of autophagic vesicles. The working principle of GFP-LC3 (A) and HyD-LIR-LC3 (B) to detect autophagy. Diagram adapted from [197].

Due to the easily aggregated nature of LC3, a caution must be exercised when detecting GFP-LC3 punctate structures. Indeed, exogenously expressed LC3, and even endogenous LC3, are prone to form aggregates in an autophagy-independent manner [179,204]. Aggregated LC3s form puncta-shaped structures thus making it impossible to distinguish them from true autophagic vesicles. To limit the artificial LC3 aggregate formation, plasmid dosing experiments when transiently expressing the FP-tagged LC3 constructs can be performed. Alternatively, stable clones that are expressing the construct in relatively low amounts can be generated [179]. Another good strategy is to benefit from control constructs that cannot be incorporated into the autophagic vesicles such as the mutated GFP-LC3^{G120A}. LC3^{G120A} has a mutation on its critical C-terminal glycine residue (G120) which is necessary for LC3 lipidation into PE head groups of phagophores. By using GFP-LC3^{G120A} as a negative control, one can determine the number of autophagic vesicles in experimental settings where only the WT GFP-LC3 forms puncta-shaped structures, but not GFP-LC3^{G120A} [203].

Another limitation of GFP-LC3 is related with GFP and its sensitivity to low pH values. The chromophore of GFP can exist in both protonated and deprotonated states [205]. The deprotonated state has a maximum absorbance around 488 nm and it emits light that peaks at 508 nm. In contrast, the protonated state does not absorb light at 488 nm. The ratio between two states is described by pKa, which is around 6.0 for GFP, indicating that only 50% of the available GFPs can emit light at pH 6. That is why, GFP is rapidly quenched in the acidic environment of lysosomes where pH values can drop down to 4.5-5 [206]. Thus, a different strategy is required if the experimental aim is to follow completion of autophagic degradation.

HyD-LIR-GFP

Instead of exogenously expressing LC3, HyD-LIR-GFP was developed to visualize endogenous LC3 [207]. HyD-LIR-GFP consists of a short hydrophobic domain (HyD), a LIR motif and a GFP (Fig. 12B) [208]. In this biosensor, the HyD domain is required for the membrane tethering upon autophagy induction and the LIR motif allows for the detection of endogenous LC3-positive autophagic vesicles. While the HyD-LIR-GFP sensor is an alternative to avoid exogenously expressing LC3, it may cause a competition between its own LIR motif and the endogenous LIR-containing proteins. Moreover, as in the case of GFP-LC3, the GFP tag of HyD-LIR-GFP is not suitable for autolysosome detection.

RFP-GFP-LC3

To be able to follow different stages of autophagy, a tandem FP-tagged LC3 probe named RFP-GFP-LC3 was developed (Fig. 13A) [209]. The additional RFP (red fluorescence protein) of RFP-GFP-LC3 biosensor has a pKa of 4.5, which makes it suitable for acidic environments. With this probe, the idea is to detect autophagosomes by the presence of both GFP and RFP signals, whereas autolysosomes are expected to only contain RFP signal due to the GFP quenching upon lysosomal entry. However, the GFP moiety of this biosensor has been reported to show a weak signal even in acidic autolysosomes, therefore requiring further optimization to replace GFP with another FP.

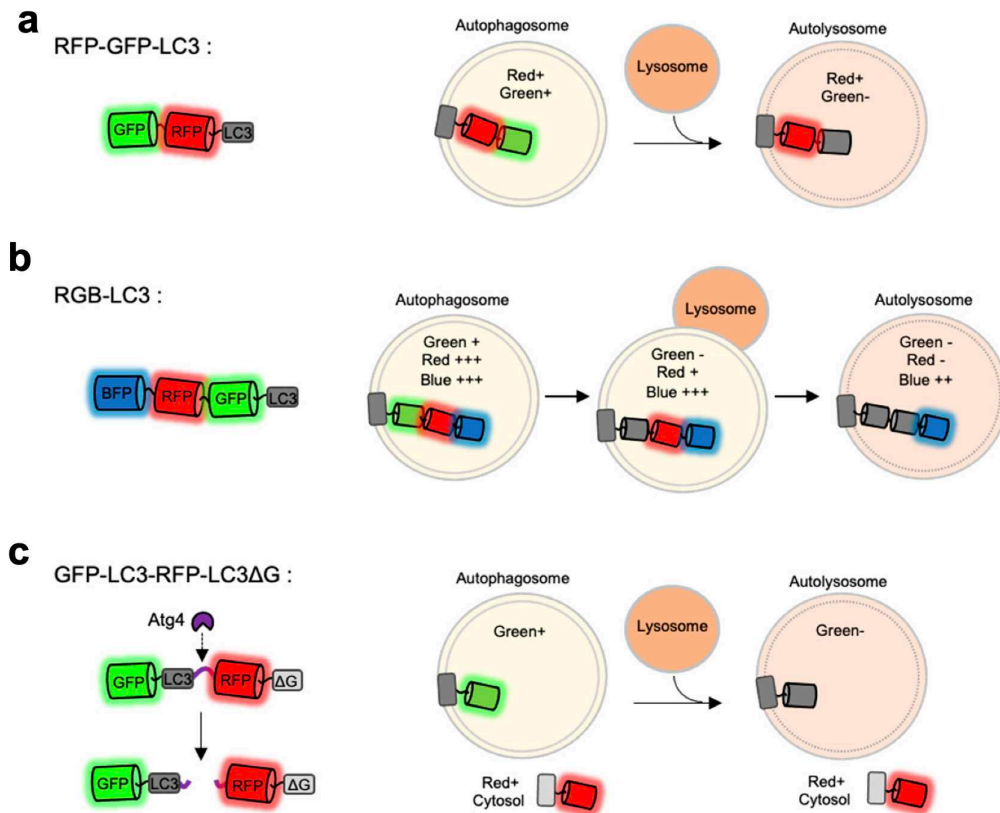


Figure 13: Monitoring autophagy progression by tandem or triple FP-tagged LC3 biosensors. The working principle of RFP-GFP-LC3 (A), GFP-LC3-RFP-LC3 Δ G (B), and RGB-LC3 (C). Diagram adapted from [197].

RGB-LC3

Red, green and blue (RGB)-LC3 has been developed to overcome challenges faced with the tandem FP-tagged LC3. RGB-LC3 has three different colors of FPs which are highly pH-sensitive green FP SEP (pKa 7.2), moderately pH-sensitive red FP mApple (pKa 6.5), and pH-resistant blue FP mTagBFP2 (pKa 2.7) [210] (Fig. 13B). RGB-LC3 is suggested to be an autophagy flux biosensor that can help to identify phagophores (with the presence of all three of the FPs), lysosomal fusion stage of autophagosomes (with the loss of green FP but remaining positive with red and blue FP signal), and mature autolysosomes (with the additional loss of red FP and remaining only with blue FP

signal). This relatively new biosensor is remained to be tested by other research groups to validate its capabilities in different cell lines and experimental settings.

GFP-LC3-RFP-LC3ΔG

GFP-LC3-RFP-LC3ΔG is a biosensor to measure a rather early event in the process of autophagy induction. This probe contains a classical GFP-LC3 fused C-terminally with RFP-LC3ΔG [211] (Fig. 13C). Upon autophagy induction, the protease ATG4 cleaves the C-terminus of GFP-LC3 to prime the protein during which the fused RFP-LC3ΔG is cleaved. While the primed GFP-LC3 can be conjugated into PE and used to visualize autophagosomes, the released RFP-LC3ΔG remains cytosolic due to the lack of glycine (G120) necessary for phagophore lipidation. The status of autophagy progression is then estimated by calculating the GFP/RFP signal ratio. This probe has been shown to be used in cultured cells as well as whole organisms.

Biosensors to monitor mitophagy

In addition to the bulk autophagy sensors, there are genetically-encoded mitophagy sensors that can provide spatiotemporal information on the selective degradation of mitochondria.

A tandem RFP-GFP fusion protein targeted to mitochondria is an example of a simple mitophagy sensor. With a similar idea to that of RFP-GFP-LC3, this probe is designed to distinguish key steps in the mitophagy flux such as the autophagosome formation and lysosomal fusion [209]. There are different versions of this biosensor where the tandem RFP-GFP is either targeted to OMM or IMM [212,213]. By following a similar design strategy, a pH-sensitive mitochondrial fluorescent probe was developed [214]. This construct was named mito-Quality Control (mito-QC), and it is constituted of a mCherry-GFP tandem protein targeted to the OMM via the mitochondrial targeting sequence of the mitochondrial fission protein FIS1 [214]. By following the mCherry-only punctate structures, McWilliams *et al.* used mito-QC to monitor mitochondria targeted at lysosomes upon mitophagy activation.

Mt-Keima is another genetically-encoded fluorescent reporter used to follow mitophagy events in cells and *in vivo* [215,216]. Mt-Keima is a probe targeted to the mitochondrial matrix that can change its spectral properties depending on the surrounding pH [216]. When mt-Keima is in an environment with elevated or physiological pH, as in mitochondria (pH ~8.0), it has a green fluorescence. On the contrary, when pH drops as in lysosomes (pH ~4.5), mt-Keima becomes ionized and it shows a red fluorescence [216]. Mt-Keima has been used to follow the delivery of mitochondria to lysosomes upon mitophagy activation, and it was reported to be stable in lysosomes [216,217]. It should also be acknowledged that mt-Keima was shown to have limitations in terms of spectral separation between the green and the red forms [207], which therefore questions whether its use is pertinent for mitophagy [214].

1.4 FRET-based methods to monitor autophagy

Förster's resonance energy transfer (FRET) applications have been dramatically increasing over the past twenty years due to the rapid advancement of FPs and growing diversity of available FRET methods [218]. Today, FRET is a widespread method that offers simple and accessible forms of quantitative fluorescence microscopy while providing information about intra- and intermolecular distances on the nanometer length scale in living systems [219]. Indeed, there are other optical techniques such as super resolution microscopy or non-optical techniques such as X-ray crystallography that offer higher resolution. However, these techniques are more complex, less accessible and restrictive in terms of samples preparation and measurement conditions [218]. On the contrary, FRET is a simple yet powerful technique that has minimal restrictions when preparing samples, therefore easily applied in living cells. In this thesis study, FRET has been used as the main method to monitor autophagy, and paved the way in developing and characterizing an LC3B FRET biosensor that can monitor the modes of action of ATG4B during autophagy processes in living cells.

1.4.1 Principles of FRET phenomenon

FRET is a distance-dependent photophysical process where non-radiative energy transfer occurs between an excited state donor (D) fluorophore and a ground state

acceptor (A) fluorophore within close proximity [220]. The term “resonance energy transfer” is used to describe the fact that energy transfer is by the dipole-dipole interaction that does not involve emission and reabsorption of photons [221]. FRET efficacy depends on three parameters that are listed below (Fig. 14) [222,223].

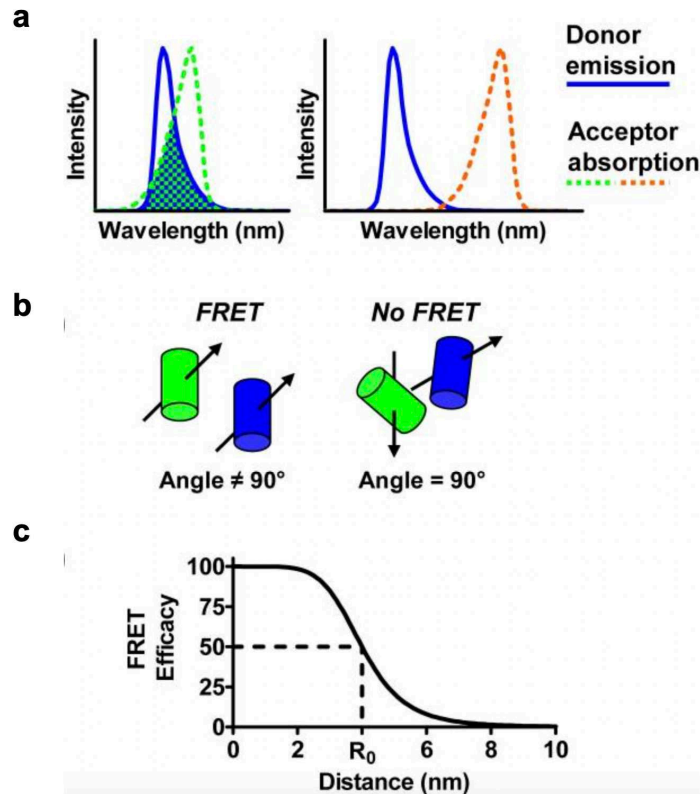


Figure 14: Principles of FRET. Three conditions that are necessary for FRET phenomenon: (a) energy compatibility, (b) alignment of fluorophores' dipoles (c) distance between the fluorophores. Förster distance (R_0) depicts the characteristic feature of each donor and acceptor FRET pair. It is generally in the range of 4-8 nm. Diagram adapted from [223].

- (i) The donor-acceptor pair has to exhibit energy compatibility. Typically donor absorbs energy at shorter wavelengths while acceptor has energy absorption at longer wavelengths [224,225]. For the energetic resonance that is necessary for FRET, the emission spectrum of the donor must overlap with the absorption spectrum of the acceptor (Fig. 14A).
- (ii) The dipole moments of the donor-acceptor pair have to be correctly in favorable directions (Fig. 14B). FRET efficiency is the highest when the two vectors are parallel to each other. In contrast, FRET becomes null when the two vectors are perpendicular.

- (iii) The donor-acceptor pair has to be in close proximity less than 10 nm and within the range of 1-10 nm [219,226]. (Fig. 14C). When the pair is away from each other more than 10 nm, photon emission by the donor molecule would be dominant. On the other hand, when the donor-acceptor pair is closer than 1 nm, a collision between the molecules would occur. Due to this feature, FRET can be used to accurately measure molecular proximity at a nanometric distance scale of 1-10 nm.

Because the working distance of FRET matches with the scale of many biological molecules including proteins, lipids, nucleotides and the distance between the interacting macromolecules, FRET is described as the “molecular ruler” of biological studies [227]. Indeed, FRET-based biosensors and measurement techniques can be used to monitor many different cellular events including protein-protein interactions, conformational changes of proteins, and up- or down-regulation of signaling pathways [228,229].

1.4.2 Measuring FRET by FLIM

To be able measure FRET, there are different imaging-based techniques which can be divided into methods of following the changes in donor-acceptor fluorescence intensity, donor-acceptor fluorescence polarization/anisotropy, and the lifetime of the donor fluorescence [230]. While the intensity-based (steady state) FRET methods are susceptible to variations in expression levels and molecule diffusion rates of the probes in the sample, fluorescence lifetime imaging microscopy (FLIM) allows to determine FRET independent of these disturbances [231].

1.4.2.1 Fluorescence lifetime

The fluorescence lifetime (τ) is an intrinsic property of a fluorophore and defined by the average amount of time that the molecule spends in the excited state upon absorption of a photon of light and before returning to the ground state [232]. Fluorescence lifetime is considered as a state function since it does not depend on the method of measurement, initial perturbation conditions such as wavelength of excitation,

duration of light exposure or the use of one- or multiphoton excitation [233]. Moreover, fluorescence lifetime is a parameter that is independent of the fluorescence intensity and fluorophore concentration [234]. On the other hand, fluorescence lifetime is sensitive to excited state reactions such as FRET, therefore being a suitable readout to be measured independent of other factors [235]. The presence of FRET shortens the excited state donor fluorescence lifetime. Thus, by using FLIM to follow the changes in the donor lifetime, one can measure the FRET status of the donor molecule.

1.4.2.2 TCSPC-based FLIM

Time-correlated single photon counting (TCSPC) is a technique of measuring the fluorescence decay to be able to extract the fluorescence lifetime parameter [236]. The basic principle behind this technique depends on repeatedly exciting the sample and then time the arrival of fluorescence photons to be able to build a histogram that represents the fluorescence decay (Fig. 15) [237]. Here the photon timing means the arrival time of a photon at the dedicated detector after the excitation laser pulse. The photons are then assigned a “time bin” and the measurement is repeated until sufficient number of photons for fluorescence decay analysis is collected to extract fluorescence lifetime [238–241]. In order to extract fluorescence lifetime information, it is essential to apply a fitting procedure as a post-acquisition analysis. To be able to accurately fit a model and get statistically reasonable fluorescence lifetime values, high number of photons are needed, which in turn, causes extended periods of time to acquire data [231]. Long acquisition times (usually in the order of minutes) not only cause photodamages on the sample but also makes it highly likely to miss a biological event with a fast kinetic.

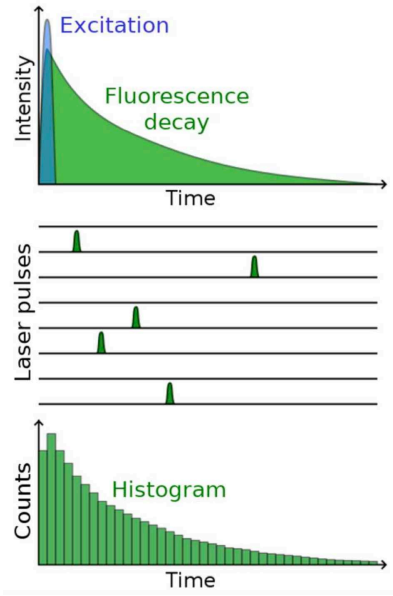


Figure 15: Principle of TCSPC-based FLIM. The sample is excited repeatedly during which the arrival of photons is timed to generate a histogram of fluorescence decay. Diagram adapted from [237].

1.4.2.3 Time-gated FLIM

Time-gated FLIM is based on the principle of measuring fluorescence decay at several temporal positions using a time-gated detector (Fig. 16) [242]. Similar to TCSPC-based FLIM, time-gated FLIM requires a pulsed laser to excite the sample. The generation of temporal gates is achieved by using a light intensifier coupled to a charged-couple device (CCD) camera [243–245]. Together with a programmable delay generator, the electronic signal coming from the pulsed laser triggers the gate of the intensifier, that is adjusted to 1 or 2 ns depending on the experiment to acquire a stack of time-correlated images each of which corresponds to a particular time delay of the fluorescence decay [231].

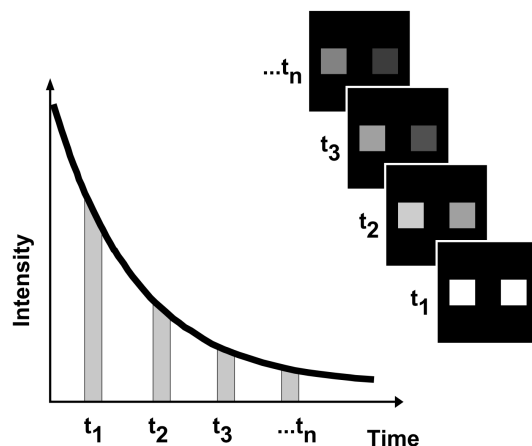


Figure 16: Principle of time-gated FLIM. Time-gated images are collected at consecutive delays generated after excitation. The intensity is then plotted against time to be able to determine fluorescence lifetime after fitting the data to an exponential curve. Diagram adapted from [242].

Compared to TCSPC-based FLIM, time-gated FLIM offers fast acquisition of fluorescence lifetime images (in the order of few seconds). Though time-gated FLIM has a higher speed than conventional techniques, it has a compromised spatial resolution due to relatively big pixel size of the intensifier. Within the team, a time-gated FLIM microscope called fastFLIM, has been developed [246,247] and demonstrated to be a powerful tool to discover various biological processes when coupled with the FRET biosensors of PKA and ERK1&2 kinase [248] and aurora kinase A [249,250]. FastFLIM system was also shown to be suitable for the automated screening purposes in living cells and in a 96-well plate format, thereby paving the way to the screening of novel pharmaceutical compound libraries [251]. The LC3B FRET biosensor that was developed within the scope of this thesis study was also characterized by using our fastFLIM which has proven to be an invaluable system to study the fast dynamics of autophagic processes.

1.4.3 FRET-based autophagy and mitophagy sensors

One of the available FRET-based biosensors that can monitor autophagy is pHlameleon [252]. pHlameleon is a pH sensor with a pH-sensitive yellow EYFP (pKa 6.9) as an acceptor and a pH-stable cyan ECFP (pKa 4.8) as a donor [253–256].

pHlameleon reports decreased FRET values in acidic conditions due to the decreased emission of pH sensitive EYFP. pHlameleon has recently been improved by replacing ECFP with a more stable cyan FP mTurquoise2 (pKa 3.1) and yellow FP pH-Lemon. This improved version was fused with LC3 to follow acidification of LC3-positive autophagic vesicles [257].

Another recently developed FRET-based biosensor is mito-SRAI which has been generated to follow specifically mitophagy [258]. Mito-SRAI has a mitochondrial targeting sequence and consists of a pH resistant cyan FP TOLLES (tolerance of lysosomal environment) and a yellow FP YPet as the donor-acceptor FRET pair. While the mito-SRAI labelled healthy mitochondria can give a FRET signal, the autophagosome engulfed mitochondria loses its YPet moiety upon lysosome fusion which results in loss of FRET. Thus by following the loss of FRET, one can monitor mitochondrial units that are undergoing lysosomal degradation [259].

2. AIMS OF THIS THESIS

This thesis aims to develop and characterize microscopy-based approaches to monitor autophagy and mitochondrial functions in living cells.

As previously introduced, autophagy is the major cellular pathway to degrade intracellular components including long-lived proteins and organelles via lysosomal systems. Although several mechanisms of autophagy have been dissected in the last decade, following this pathway in real time remains challenging. Among the early events leading to autophagy activation, the ATG4B protease primes the key autophagy player LC3B. Given the lack of probes to follow this event in living cells, the first and main aim of this thesis is to develop and characterize a FRET biosensor that can report autophagy activation and progression based on LC3B regulation by ATG4B, in real time and with high spatial resolution. To this end, the LC3B biosensor was aimed to report: i) the priming of LC3B by ATG4B based on a FRET readout quantified by FLIM and ii) LC3B accumulation on autophagic vesicles based on quantifying puncta-shaped structures.

The second aim of this study is to investigate the mitochondrial changes in chemotherapy (BRAF inhibition) sensitive and resistant melanoma cells by using photoconversion microscopy and conventional biochemical techniques. This study is part of a larger project that aims to use multiplexed FRET biosensors, including the LC3B biosensor, to monitor autophagy/mitophagy together with several other mitochondrial functions simultaneously in melanoma cells to decipher mechanisms leading to chemoresistance.

3. MATERIALS AND METHODS

3.1 Molecular and cellular biology

3.1.1 Expression vectors and molecular cloning

All the plasmids used in this study are listed in Table 1. The cloning reactions were performed using the Gibson Assembly Master Mix (New England Biolabs). Site-directed mutagenesis was performed with the Quik-Change kit (Agilent). All the constructs from cloning and mutagenesis reactions were verified using a 3130 XL sequencer (Applied Biosystems) and a BigDye Terminator V3.1 sequencing kit (Applied Biosystems).

Table 1: List of plasmids used in this study. Table listing the source of each plasmid with the cloning sites and the primers for mutagenesis, if applicable.

Plasmid	Cloning sites	Remarks	Primers for mutagenesis (5' to 3'): sense	Primers for mutagenesis (5' to 3'): anti-sense
pcDNA 3.1		Purchased from Thermo Fisher Scientific.		
pCMV Aquamarine C1		Kind gift from F. Merola, Université Paris-Saclay, France.		
pE tdLanYFP N1		Kind gift from F. Merola, Université Paris-Saclay, France.		
pCMV Aquamarine-tdLanYFP tandem		Kind gift from F. Merola, Université Paris-Saclay, France.		
pcDNA 3.1 mCherry-hLC3B		Addgene plasmid #40827.		
pCMV-proLC3B-tdLanYFP	BglII/NotI	pE tdLanYFP N1 was used as a backbone vector. Insert proLC3B was subcloned from pcDNA 3.1 mCherry-hLC3B.		

pCMV Aquamarine-proLC3B	BglII/EcoRI	pCMV Aquamarine C1 was used as a backbone vector. Insert proLC3B was subcloned from pcDNA 3.1 mCherry-hLC3B.		
pCMV Aquamarine-proLC3B-tdLanYFP	BglII/EcoRI	pCMV Aquamarine-tdLanYFP tandem was used as a backbone vector. proLC3B was inserted by subcloning it from pcDNA 3.1 mCherry-hLC3B.		
pCMV Aquamarine-proLC3B G120A		Obtained from pCMV Aquamarine-proLC3B.	cactgacaatttcacgcgaacgtctcctggga	tcccaggagacgttcgcgatgaaattgtcagtg
pCMV Aquamarine-proLC3B G120A-tdLanYFP		Obtained from pCMV Aquamarine-proLC3B-tdLanYFP.	Cactgacaatttcacgcgaacgtctcctggga	tcccaggagacgttcgcgatgaaattgtcagtg
pCMV Aquamarine-proLC3B F52A		Obtained from pCMV Aquamarine-proLC3B.	ttgacatggtcaggtacaagggcctttgtttatccagaacagg	cctgttctggataaaacaaggccctgtacctgacctgtcaa
pCMV Aquamarine-proLC3B F52A-tdLanYFP		Obtained from pCMV Aquamarine-proLC3B-tdLanYFP.	Ttgacatggtcaggtacaagggcctttgtttatccagaacagg	cctgttctggataaaacaaggccctgtacctgacctgtcaa

pCMV Aquamarine-proLC3B Δ10	BglII/EcoRI	pCMV Aquamarine C1 was used as a backbone vector. proLC3B Δ10 was inserted by subcloning it from pCMV Aquamarine-proLC3B while also deleting the sequence corresponding to the first 10 amino acids.	gctgtacaagtccggactcagatctatgcgcaccttgaacaaagag	cgcggtaccgtcactgcagaattcttactgacaatttcatccc
pCMV Aquamarine-proLC3B Δ10-tdLanYFP	BglII/EcoRI	pCMV Aquamarine-tdLanYFP tandem was used as a backbone vector. proLC3B Δ10 was inserted by subcloning it from pCMV Aquamarine-proLC3B while also deleting the sequence corresponding to the first 10 amino acids.	gctgtacaagtccggactcagatctatgcgcaccttgaacaaagag	ccctccttggagaccatgaattccactgacaatttcatcccg
pGEX GST-ATG4B		Kind gift from R. Ketteler, LMCB, UCL, United Kingdom.		
pCMV WT ATG4B	NheI/EcoRI	pcDNA 3.1 was used as a backbone vector. Insert WT ATG4B was subcloned from pGEX GST-ATG4B.		

pCMV ATG4B C74S		Obtained from pCMV WT ATG4B.	ccgcagcatgctgccccagcctg	caggctggggcagcatgctgagg
pCMV ATG4B W142A		Obtained from pCMV WT ATG4B.	gtgtgggccgtacgcctggcctatggactt	aagtccataggccaggcgtacgggccaacac
pCMV WT Parkin		Kind gift from O. Corti, Paris Brain Institute, France.		
pCMV mitoDendra2		Addgene plasmid #157757.		

3.1.2 Cell culture and transfections

U2OS cells (HTB-96) were purchased from American Type Culture Collection. Control and ATG4 KO HeLa cells were kind gifts of Dr. Robin Ketteler (UCL, LMCB, United Kingdom). 501Mel and SKMel28 melanoma cells sensitive or resistant to Vemurafenib (BRAFi) were kind gifts of Marie-Dominique Galibert (IGDR, Univ Rennes 1, France). U2OS and HeLa cells were cultured in DMEM (Thermo Fisher Scientific) supplemented with 10% FBS (Eurobio Scientific) and penicillin-streptomycin (100 U/mL, Thermo Fisher Scientific). Mel501 and SKMel28 cells were cultured in RPMI (Thermo Fisher Scientific) supplemented with 10% FBS (Eurobio Scientific) and penicillin-streptomycin (100 U/mL, Thermo Fisher Scientific). All cells were maintained at 37°C with 5% CO₂. All cell lines were routinely checked for the absence of mycoplasma. Before imaging, growth medium was replaced with phenol red-free Leibovitz's L-15 medium (Thermo Fisher Scientific) supplemented with 20% FBS and penicillin-streptomycin (100 U/mL). Cells were seeded at 70% confluence in Nunc Lab-Tek II Chamber slides (Thermo Fisher Scientific) or Cellview cell culture slides (Greiner bio-one, 543979) for live cell imaging, 24-well plates for immunocytochemistry, or 6-well plates for total cell lysates. Plasmid DNA transfection, or plasmid DNA and siRNA co-transfection experiments were performed using Lipofectamine 2000 (Invitrogen) according to the manufacturer's instructions. Cells were analyzed 48h after transfection. AllStars negative control siRNA (SI03650318), *ATG5*-specific siRNA (SI02655310) and *ATG4B*-specific siRNA (SI03156314) were purchased from QIAGEN.

3.1.3 Chemical compounds

The chemical compounds used in this study were as follows: 3-methyladenine (Selleckchem, S2767), Bafilomycin A1 (Sigma-Aldrich, B1793), carbonyl cyanide *m*-chlorophenylhydrazone (Sigma-Aldrich, C2759), FMK 9a (MedChemExpress, HY-100522), LV-320 (MedChemExpress, HY-112711), MG-132 (Selleckchem, S2619), NSC 185058 (Selleckchem, S6716), Tioconazole (Sigma-Aldrich, 03907), Torin1 (Sigma-Aldrich, 475991), *Z-L*-Phe chloromethyl ketone (Sigma-Aldrich, 860794). All chemical compounds were dissolved in dimethyl sulfoxide (Sigma-Aldrich, D2438) and

stored at -80°C . For starvation assay, a home-made Hank's Balanced Salt Solution (HBSS) containing 8 mg/ml NaCl, 0.4 mg/ml KCl, 0.06 mg/ml KH_2PO_4 , 0.048 mg/ml Na_2HPO_4 anhydrous, 1 mg/ml glucose, 0.348 mg/ml NaHCO_3 and penicillin-streptomycin (100 U/mL) was used. Concentrations and durations of each treatment are indicated in the figure legends of the thesis manuscript and the BioRxiv preprint manuscript (*cf. section 4.2*).

3.1.4 Western blotting

To collect total cell lysates, cells were rinsed with ice-cold Phosphate Buffer Saline (PBS) 1X (Euromedex, ET330-A) and lysed on ice in a buffer containing 50 mM Tris-HCL (pH 7.4), 150 mM NaCl, 1% Triton X-100 (Euromedex, 2000-A), 1.5 mM MgCl_2 , supplemented with 0.2 mM Na_3VO_4 (Sigma-Aldrich, S6508), 0.5 mM DTT (Thermo Fisher Scientific, R0861), 4 mg/ml NaF (Sigma-Aldrich, S-7920), 5.4 mg/ml β -glycerolphosphate (Sigma-Aldrich, G5422) and a protease inhibitor cocktail (Roche, 11873580001) immediately prior to lysis. Lysates were centrifuged at 13000 g for 20 minutes at 4°C . Protein levels were quantified by using the Bradford protein assay dye reagent (BioRad, 5000006). Lysates were then heated in Laemmli sample buffer at 95°C for 5 minutes, resolved in home-made Acrylamide/Bis 37.5:1 SDS-PAGE mini gels and transferred onto nitrocellulose membrane (AmershamTM Protran[®], 10600004). Membranes were blocked in a solution containing 5% skimmed milk in TBS-T (1X TBS [Euromedex, ET220] containing 0.1% Tween [Euromedex, 2001-B]) and incubated overnight at 4°C with primary antibodies diluted in the blocking solution. The next day, membrane was washed in TBS-T, incubated with the secondary antibody diluted in the blocking solution for 1h at room temperature, and washed again in TBS-T prior to detection. The primary antibodies and dilutions were as follows: rabbit anti-Actin (Sigma-Aldrich, A5060; 1:1000), ATG4B (Cell Signaling, 5299; 1:1000), LC3B (Cell Signaling, 3868; 1:1000), OXPHOS Rodent western blot antibody cocktail (Mitosciences, ab110413; 1:1000), Tubulin (Millipore, MAB1864; 1:5000). The secondary antibodies used were horseradish-peroxidase-conjugated rabbit anti-mouse, donkey anti-rat or goat anti-rabbit antibodies (Jackson ImmunoResearch; 1:6000-1:10000). After incubating the membrane in an ECL western blotting substrate (Thermo

Fisher Scientific, 32209), chemiluminescence signals were captured on a film (Thermo Fisher Scientific, 34091) and developed with a CURIX 60 developer (Agfa Healthcare).

3.1.5 Immunocytochemistry

For immunocytochemistry, cells were seeded on 15 mm round coverslips placed onto 24-well plates. Cells were washed with 1X PBS and fixed in 1X PBS containing a mixture of 4% paraformaldehyde (Electron Microscopy Sciences, 15710) and 0.2% Glutaraldehyde (Euromedex, EM-16221) at room temperature for 20 minutes. After washing in 1X PBS, cells were permeabilized with 0.2% Triton in PBS for 10 minutes, washed again in 1X PBS and blocked for 1h in 5% BSA (Euromedex, 04-100-812-C) in 1X PBS at room temperature. Cells were incubated overnight at 4°C with primary antibodies diluted in the blocking buffer, and then washed with 1X PBS. Cells were then incubated with the secondary antibody diluted in the blocking buffer for 45 minutes at room temperature. Primary monoclonal anti-LAMP2 (Abcam, ab25631; 1:200) was used as a primary antibody and a goat anti-mouse IgG (H+L) cross-adsorbed antibody Alexa Fluor™ 647 (Thermo Fisher Scientific, A-21235; 1:500) was used as a secondary antibody. After washing in 1X PBS, coverslips were mounted in ProLong Gold Antifade reagent (Invitrogen, P36930).

3.2 Microscopy

3.2.1 Confocal microscopy

Confocal imaging experiments were performed with a Leica SP8 inverted confocal microscope equipped with a 63x oil immersion objective (NA 1.4) and driven by the LAS software. For live cell imaging of perinuclear aggregates, U2OS cells expressing the LC3B-tdLanYFP construct were imaged to acquire the fluorescence of tdLanYFP by using a 514 nm argon laser. The emission wavelengths were 525-565 nm. For Aqu-LC3B-II puncta counting and LAMP2 colocalization experiments, U2OS cells were fixed after transfection, and imaged to acquire Aquamarine fluorescence with a 440 nm pulsed laser, and an emission wavelength of 467-499 nm. The fluorescence of tdLanYFP and of LAMP2/Alexa 647 were captured by using a 514 nm and a 633 nm argon laser,

respectively. The emission wavelengths were 525-565 nm for tdLanYFP, and 650-720 nm for LAMP2/Alexa 647. For mitoDendra2 experiments, 501Mel and SKMel28 cells sensitive or resistant to BRAFi were imaged to perform photoconversion on a region of interest (ROI) by using the fluorescence recovery after photobleaching (FRAP) module of the LAS software, with a 405 nm laser at 0.25% power for 5 msec. The excitation and emission wavelengths were 490 and 507 nm for green mitoDendra2 species, and 553 and 573 nm for red mitoDendra2 species, respectively. Both green and red mitoDendra2 species were acquired for 80s after the photoconversion by taking one image on every five seconds.

3.2.2 FLIM

FLIM images were acquired with a custom-made microscopy setup that allows for a rapid FLIM acquisition (the fastFLIM microscope) [246,247]. The fastFLIM system is composed of a Leica DMI6000 microscope (Leica) with a CSU-X1 spinning disk module (Yokogawa), a 63x oil immersion objective (NA 1.4), a supercontinuum picosecond pulsed white laser at 40 MHz frequency (Fianium), and a High-Rate Intensifier (Picostar LaVision integrating an HRI Kentech Instrument). The fastFLIM system is controlled by the Inscoper Suite solution (Inscoper, France) which consists of an electronic hardware unit (Inscoper box) and a software (Inscoper software). While the Inscoper box runs the communication between the computer and the other devices, the Inscoper software calculates and displays the lifetime values in real-time and during acquisition. Briefly, the pulsed laser sends a trigger to the intensifier for each pulse. The intensifier generates a gate of 2.2 ns during acquisition when capturing the fluorescence emission. A delay generator driven by the Inscoper box is then used to shift the gate at the desired timing during the fluorescence decay. Finally, a CCD camera (Coolsnap HQ Photometrics) captures a stack of five time-gated images, which is then sent to the computer to be processed by the Inscoper software. The sequential acquisition of these five time-gated images allows to cover the whole fluorescence decay. The mean fluorescence lifetime is then calculated from the intensity of the time-gated images and by using the following equation: $\tau = \sum \Delta t_i \cdot I_i / \sum I_i$, where Δt_i is the delay time after a laser pulse of the i th image and I is the pixel-by-pixel fluorescence intensity in each

image [246,247]. In all FLIM experiments, Aquamarine was used as a FRET donor, and excited at 440 ± 10 nm with the pulsed laser source and filtered by a home-made wavelength selector. Emission was selected using a band pass filter of 483/35 nm.

3.3 Data analysis

3.3.1 Western blotting analysis

The density of the bands was quantified by using the *Gel Analyzer* function in Fiji (NIH) software. The relative abundance of each band was calculated by normalizing the density of the band to that of the respective loading control. Loading controls are indicated in each western blot panel and in the corresponding figure legends of the thesis manuscript and the BioRxiv preprint manuscript (*cf. section 4.2*).

3.3.2 Image analysis

All the image analyses were performed in Fiji software. 3D puncta counting and fluorescence colocalization analyses were performed by using the macro developed by Cordelières and Zhang [260] in batch processing mode, and available in a GitHub repository at <https://github.com/NEUBIAS/neubias-springer-book-2020>. The minimum size of the objects for Aquamarine-LC3B and LAMP2/Alexa 647 was set to 10 voxels. The threshold to separate the objects from the background was set manually for both channels. The total number of objects in Aquamarine-LC3B channel was used to determine the number of Aqua-LC3B-II puncta-shaped structures. The objects in the Aquamarine-LC3B channel superposing with the LAMP2/Alexa 647 objects were used for colocalization analyses, and only the Aquamarine-LC3B objects superposing with the LAMP2/Alexa 647 objects with a ratio of 0.5 or more were quantified for analyses. The colocalizing objects were then normalized to the total number of Aquamarine-LC3B objects.

For mitochondrial connectivity analysis, *JaCoP* plugin [261] was used to determine the total number of red objects present at 5s (the first image acquired after the photoconversion of the ROI) and 80s after the photoconversion. To calculate the mitochondrial connectivity, the number of red objects present 80s after the

photoconversion was normalized to the number of red objects present 5s after the photoconversion.

For FLIM analysis, Aquamarine lifetime was calculated by the Inscoper software only when the pixel-by-pixel fluorescence intensity in the first gate was above 1000 grey levels. In all experiments, the raw lifetime values of the donor-only expressing cells were averaged to determine the average lifetime value of Aquamarine. Then the net difference between the raw lifetime value of a desired cell (expressing biosensor or donor-only) and the average lifetime value of Aquamarine was calculated to determine the mean Δ Lifetime value. The number of Aqua-LC3B-II puncta structures in the fluorescence images acquired during FLIM experiments were quantified using the *Find Maxima* function in the Fiji imaging software, and by setting the prominence value as 1500. To analyze the high- Δ Lifetime pixels, the *Histogram* tool in Fiji was used to measure the number of pixels with a lifetime value between 2000 and 4000 psec. Each histogram was then converted to a Δ Lifetime format by using the average lifetime values of the donor-only construct as a normalizer. To determine the number of pixels with high Δ Lifetime, the mean Δ Lifetime value of the G120A biosensor or the mean Δ Lifetime value of the WT biosensor expressed in *ATG4B* SKO cells were used as a threshold. The number of pixels showing G120A biosensor-like Δ Lifetime or higher were then quantified and normalized to the total number of pixels, and this to determine the high- Δ Lifetime pixel ratio per cell. For line analysis, a 17.8 μm linear region of interest (ROI) that contains both the high- and low- Δ Lifetime pixels was manually drawn near or on the puncta-like structures. The *Plot profile* function in Fiji was then used to obtain Δ Lifetime values on the line, which were then plotted. For histogram analyses, the average number of pixels per Δ Lifetime was quantified for each condition.

3.3.3 Statistical analysis

All statistical tests were performed by using GraphPad Prism 9. Statistical significance was calculated using two-way ANOVA with Tukey method for multiple comparisons or Student's t test for comparison between two sets of data as specified in the figure legends. Two-way ANOVA with two-stage step-up method of Benjamini,

Krieger and Yekutieli was applied to make multiple comparisons in western blotting analyses. Correlation analysis between the Δ Lifetime values and the puncta numbers were performed to compute R^2 and P.

4. RESULTS AND DISCUSSION

The results and discussion section is divided into three subsections. In the first and the second subsections, the FRET biosensor (the LC3B biosensor hereafter), in which we aimed to follow autophagy based on FRET/FLIM is described. The first subsection describes our early hypothesis on the LC3B biosensor to follow the conformational changes of LC3B upon phagophore attachment. This is followed after with the second subsection where our current understanding on the biosensor is described and presented in the form of my first author research paper manuscript which was submitted to *Autophagy* and currently under revision. In the third and last part of the results and discussion, a different angle of my thesis study regarding the investigation of mitochondrial changes in chemotherapy sensitive and resistant melanoma cells are presented.

4.1 The LC3B biosensor based on the conformational change hypothesis

Based on our current findings (*cf. section 4.2*), the LC3B FRET biosensor follows the ATG4B-mediated priming and deconjugation activities. The biosensor provides (i) a FRET readout specific to the priming activity of ATG4B, and (ii) a conventional fluorescent readout allowing to follow LC3B protein throughout the autophagy pathway. This was achieved by flanking the N- and C-termini of proLC3B with a donor-acceptor FRET pair. However, in the initial phases of the study, the biosensor was sought to be developed by using the sequence of LC3B-I instead of proLC3B to follow the conformational changes of the primed LC3B protein during autophagy. Following this, the preliminary results reported by a former student were in line with the idea of monitoring the conformational changes of LC3B, therefore never raising a doubt on the sequence of the biosensor. Later in the study and after the start of my PhD, assays performed to further challenge the LC3B biosensor to test its ability to follow conformational changes resulted in conflicting findings as compared to the preliminary results. Finally, the attempts to reproduce the initial findings failed and led us to inspect the sequence of the construct. Re-sequencing the biosensor revealed the sequence of proLC3B instead of LC3B-I being used to construct the sensor. These results provided

strong evidence on the questionability of the preliminary findings and directed towards a paradigm shift within the framework of my PhD project. To acknowledge these challenges, this section is dedicated to present the early work that has helped us to reach our final understanding on the LC3B biosensor.

4.1.1 Preliminary data on the LC3B biosensor supporting the conformational change hypothesis

In the initial phases of the study, the LC3B biosensor was envisioned to follow the conformational changes of LC3B upon phagophore attachment [124,127–129]. For this purpose, LC3B-I, which is the C-terminally primed form of the protein, was intended to be used while constructing the biosensor. The reason behind targeting LC3B-I instead of proLC3B was due to the C-terminal cleavage of proLC3B by ATG4B as one would expect to lose any C-terminally tagged fluorescent protein after this proteolytic event. Therefore, the biosensor was designed to flank the N- and C-termini of LC3B-I with a donor-acceptor FRET pair (Fig. 17). The FRET pair composed of Aquamarine (donor, cyan) and tdLanYFP (acceptor, yellow) was selected on the resistance of both fluorophores to acidic pH [262,263]. The aim was to follow the conformational changes of LC3B that it may adopt when it is lipidated into the PE head groups of the autophagic membranes. In the case of membrane attachment causing LC3B to adopt a closed conformation, the donor-acceptor pair was expected to be in close proximity due to the N-terminal $\alpha 1$ loop projecting down towards the ubiquitin-like C-terminal domain. This conformational change in turn was expected to allow for the FRET phenomenon, which can then be measured by FLIM and by following the lifetime changes of the N-terminal donor molecule (Aquamarine) (Fig. 17).

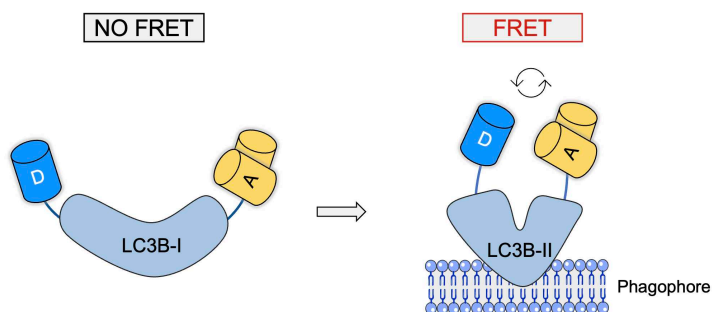


Figure 17: Schematic representation of the LC3B biosensor and its working mechanism based on conformational change hypothesis.

In the following sub-sections, the data obtained by a former student before the start of my PhD project is presented to demonstrate the findings that supports the conformational change hypothesis of the LC3B biosensor.

4.1.1.1 Pharmacological manipulations to inhibit early- or late-stages of autophagy results in the activation of the LC3B biosensor

As an initial attempt to follow the activity of the LC3B biosensor, U2OS cells were transiently transfected to express the donor-only (Aquamarine-LC3B-I) or the biosensor (Aquamarine-LC3B-I-tdLanYFP) constructs and treated with Bafilomycin A₁ (BafA₁) or 3-methyladenine (3-MA). BafA₁ is a late-stage autophagy inhibitor which inhibits the vacuolar-type ATPase (V-ATPase) enzyme that acidifies the intracellular organelles such as lysosomes [264]. Inhibiting V-ATPases causes an increase in the lysosomal pH and prevents the fusion of autophagosomes with lysosomes, which ultimately causes accumulation of completed autophagosomes in cells. 3-MA, on the other hand, is an early-stage autophagy inhibitor that inhibits the class III PtdIns3K and thereby suppresses the maturation of autophagosomes [265]. Treatment with these compounds is a standard practice in the field of autophagy to study the accumulation of autophagosomes or immature phagophores. From the perspective of measuring the activity of the LC3B biosensor, these compounds were expected to increase the number of lipidated LC3B biosensor on the autophagic membranes, thus allowing to measure FRET/FLIM response of the sensor in maximized conditions.

To detect FRET events, which are highlighted when the donor lifetime decreases, donor (Aquamarine) lifetime differences between the donor-only and the biosensor expressing cells were compared. Here the donor-only is a separate construct than the biosensor and used as a normalizer in all experiments. The donor-only lacks the acceptor moiety, and therefore cannot perform FRET by default and displays the lifetime value of Aquamarine-only fused with LC3B. On the other hand, biosensor has the donor-acceptor pair that would allow for a FRET event depending on the conformation of LC3B, which in turn manifests itself as reduced Aquamarine lifetime values. By calculating the net difference between the lifetime of the donor-only construct (Aquamarine-LC3B-I) and that of a biosensor (Aquamarine-LC3B-I-tdLanYFP), we then report the Δ Lifetime values. A positive Δ Lifetime value would be indicative of a FRET event between Aquamarine and tdLanYFP, therefore corresponding to the closed conformation of the biosensor.

When measuring the FRET/FLIM response of U2OS cells, a difference in the LC3B protein labelling was observed in between the donor-only and the biosensor expressing cells. Although puncta-shaped structures resembling the conventional autophagosome labelling were observed with both constructs, perinuclear aggregates were observable only in cells expressing the biosensor (Fig. 18A, donor-only vs. biosensor panels). As expected, the Δ Lifetime values collected from the puncta-shaped structures of the donor-only expressing cells were fluctuating around zero due to the lack of acceptor moiety (Fig. 18A-B). On the other hand, the Δ Lifetime values measured on the perinuclear aggregates of the biosensor expressing cells were approximately ~100 picoseconds higher than the Δ Lifetime values of the donor-only expressing cells. In addition to this, treatment with BafA₁ or 3-MA caused a further increase in the Δ Lifetime values of the biosensor expressing cells as compared to the control condition (DMSO treatment). Conversely, no difference in the Δ Lifetime values were observed in the donor-only expressing cells upon treatment with BafA₁ or 3-MA. These initial results highlighted the first clue on the activity of the LC3B biosensor. Due to the observation of a basal FRET response only in the perinuclear aggregates of the biosensor expressing cells, it was deemed necessary to focus on these regions when measuring the Δ Lifetime response of the biosensor. Moreover, these aggregates were suggested to be the regions

where the biosensor was active due to its possible conformational change upon lipidation since a further increase in the Δ Lifetime values were observed when cells treated with BafA₁ or 3-MA.

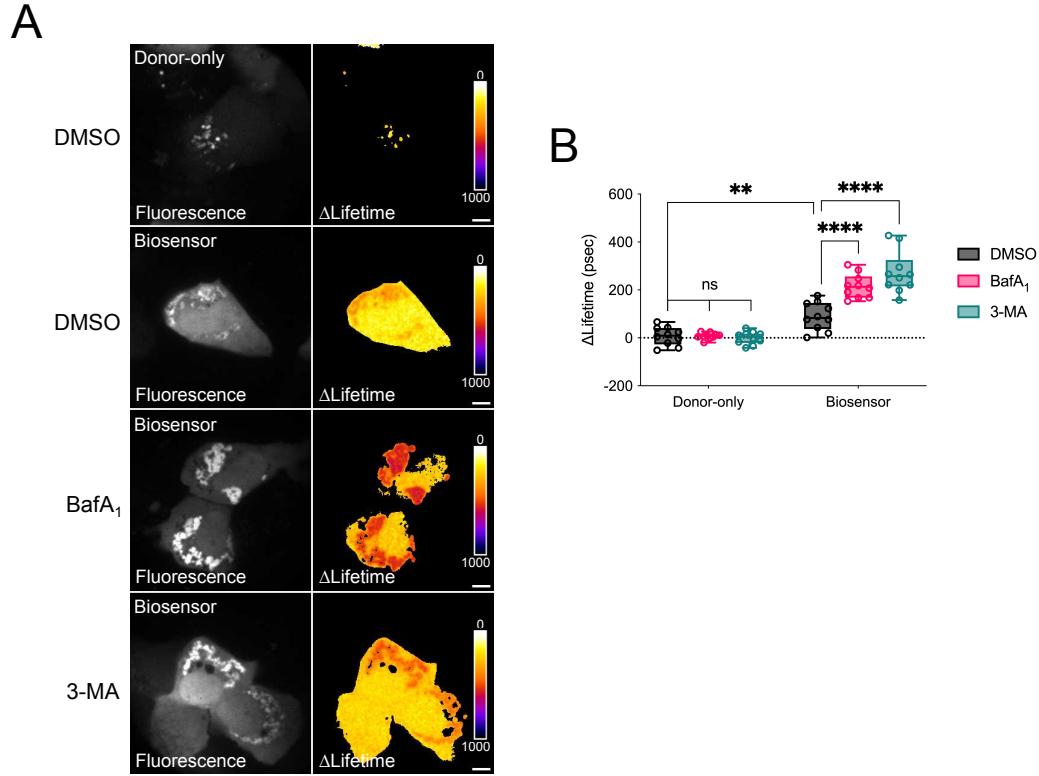


Figure 18: The LC3B biosensor is activated upon early- or late-stage autophagy inhibition. Representative fluorescence and Δ Lifetime images (A) and quantification of Aquamarine Δ Lifetime values (B) of U2OS cells expressing the LC3B biosensor or LC3B donor-only and treated with DMSO, BafA₁ (100 nM for 24h) or 3-MA (5 mM for 24h). Pseudocolor scale: pixel-by-pixel Δ Lifetime. Scale bars: 30 μ m. $n = 10$ cells per condition from one representative experiment (of three). ** $P < 0.01$, **** $P < 0.0001$, ns (not significant) as determined by two-way ANOVA with Tukey's multiple comparison test. The data presented in this figure adapted from former Master 2 student's report.

4.1.1.2 The LC3B biosensor activity is ATG5-dependent

After demonstrating that the Δ Lifetime values displayed by the biosensor was increased when LC3B lipidation levels were induced upon pharmacological

manipulations, the biosensor activity was sought to be assessed upon diminishing the autophagic membrane lipidation. To this end, *ATG5* – a key protein component of E3-like *ATG12-ATG5-ATG16L1* complex which facilitates the lipidation of *LC3B* – was downregulated by using siRNA-mediated gene silencing. Upon downregulation of *ATG5*, the Δ lifetime values calculated on the perinuclear aggregate regions of the biosensor expressing cells were significantly lowered, almost to the level of donor-only expressing cells (Fig. 19A-B). This shows that the FRET event is heavily dependent on the presence of *ATG5*. On the other hand, when *ATG5* is downregulated, the *LC3B* biosensor is still capable of conjugating to the autophagic membranes since the localization of biosensor is similar to that of the control siRNA condition, *i.e.* the perinuclear aggregates in both conditions. However, even the biosensor is lipidated into the autophagic membranes, the probe is not reaching its closed conformation, as it displayed a significantly lowered Δ lifetime values upon *ATG5* downregulation.

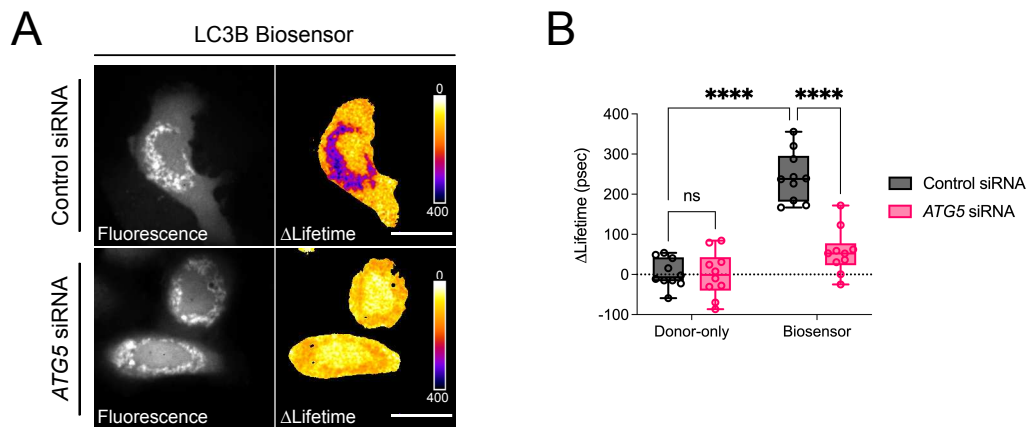


Figure 19: The *LC3B* biosensor activity is dependent on the presence of *ATG5*. Representative fluorescence and Δ Lifetime images (A) and quantification of Aquamarine Δ Lifetime values (B) of U2OS cells co-expressing the *LC3B* biosensor or *LC3B* donor-only with control or *ATG5*-specific siRNA, and analyzed by FRET/FLIM. Pseudocolor scale: pixel-by-pixel Δ Lifetime. Scale bars: 10 μ m. $n = 10$ cells per condition from one representative experiment (of three). **** $P < 0.0001$, ns (not significant) as determined by two-way ANOVA with Tukey's multiple comparison test. The data presented in this figure adapted from former Master 2 student's report.

4.1.2 *Current data on the LC3B biosensor challenging the conformational change hypothesis*

Based on the preliminary findings of the LC3B biosensor activity upon pharmacological and genetic manipulations, it was interpreted that the FRET/FLIM readout measured by the changes in Δ Lifetime values were highlighted when the LC3B biosensor was lipidated to the autophagic membranes and changed its conformation to a closed form in the presence of ATG5. Therefore, the FRET phenomenon detected by the LC3B biosensor was attributed to the activation of the autophagy pathway.

After establishing this preliminary notion on the mechanism of action of the LC3B biosensor, my PhD project which involves the characterization of the LC3B biosensor to follow autophagy in living cells was initiated. The results presented hereafter demonstrates the findings generated by me throughout my PhD studies and the following chapter describes my early results challenging the conformational change hypothesis of the LC3B biosensor upon autophagy activation.

4.1.2.1 Challenging the LC3B biosensor with starvation assay

To test the activity of the biosensor with physiological means of inducing autophagy, U2OS cells transiently expressing the donor-only or the biosensor constructs were treated with the starvation medium (HBSS). Based on previous findings, it was expected that the biosensor would be activated upon induced autophagy by starvation. However, there was not a significant difference between the untreated and starved conditions (Fig. 20A-B). Although the biosensor was present on the perinuclear aggregates, we could not detect any significant level of activation. Though the results were different than expected, we attributed this to the survival mechanisms that may be activated by the cells under the short-term starvation [266,267].

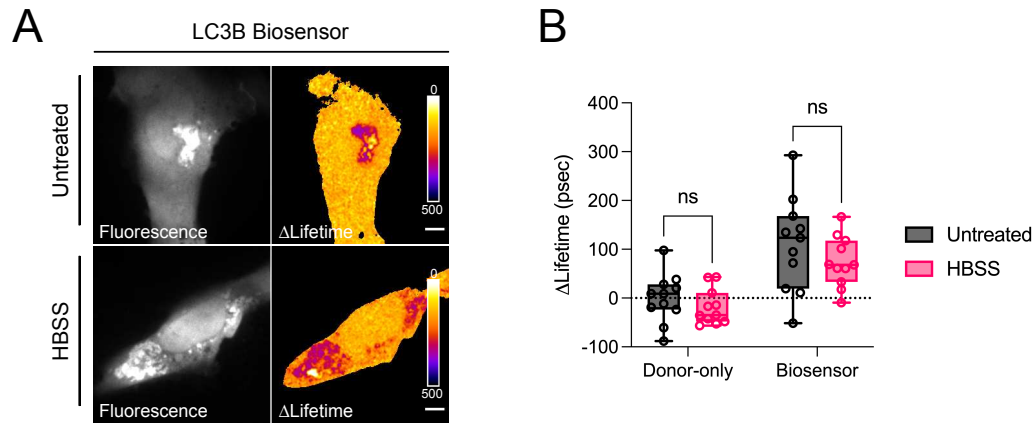


Figure 20: The LC3B biosensor activity does not change upon starvation. Representative fluorescence and Δ Lifetime images (A) and quantification of Aquamarine Δ Lifetime values (B) of U2OS cells expressing the LC3B biosensor or LC3B donor-only and treated or not with HBSS for 1h. Pseudocolor scale: pixel-by-pixel Δ Lifetime. Scale bars: 30 μ m. $n = 10$ cells per condition from one representative experiment (of three). ns (not significant) as determined by two-way ANOVA with Tukey's multiple comparison test.

4.1.2.2 The mutant LC3B biosensors to investigate the mode of action

To understand the link between the FRET response of the biosensor in relation to LC3B protein function, we aimed to mutate several residues of the LC3B biosensor that are known to be associated with the key functions of LC3B during autophagy. We targeted three residues/regions of LC3B which are known to be important for its autophagic membrane lipidation, autophagic cargo receptor binding, and oligomerization and tubulin binding. Overall, three different mutant biosensors were generated: LC3B^{G120A}, LC3B^{F52A} and LC3B ^{Δ 10}. LC3B^{G120A} contains an alanine instead of the specific glycine residue (G120) required for the lipidation of the cytosolic LC3B-I protein to the PE head groups of the forming phagophores [93]. Thus, replacement of G120 blocks the LC3B-I conjugation to the autophagic membranes. Of note, when G120A mutation is present on proLC3B, it also causes the abolishment of proLC3B cleavage (priming) by ATG4B [268]. The LC3B^{F52A} mutant, on the other hand, has a mutation on the phenylalanine at the 52nd residue (F52) to convert it into alanine. The F52 residue is known to interact with the autophagic cargo receptor 1 p62/SQSTM1, which is the key autophagy receptor binding to ubiquitin [139,269]. Alanine in place of the phenylalanine

at the 52nd residue abolishes LC3B-p62/SQSTM1 interaction [269]. Last, LC3B^{Δ10} lacks the N-terminal first 10 amino acids which correspond to the α1 loop that is important for oligomerization (with the membrane or other LC3B proteins) and tubulin binding via changing its conformation away from the ubiquitin core of the protein [124].

After generating the LC3B mutant biosensors, we tested the impact of mutations on the capacity of mutant LC3B biosensors to report FRET events as comparison to the wild-type biosensor (WT biosensor). Our first mutant LC3B^{G120A} biosensor displayed significantly increased ΔLifetime values as compared to the WT biosensor (Fig. 21A-B). This was to our surprise as it was expected for the LC3B^{G120A} mutant to lose its ability to display FRET events as compared to the WT biosensor. The LC3B^{G120A} mutant biosensor, that was expected lipidation-deficient, did not only show significantly higher Δlifetime values, but also observed in the perinuclear areas similar to the WT biosensor. This surprising result has led us to think that there may be a pool of mutant LC3B^{G120A} molecules that can overcome the lipid conjugation pathway and participate in non-canonical autophagy pathway. However, no further investigation was made on this.

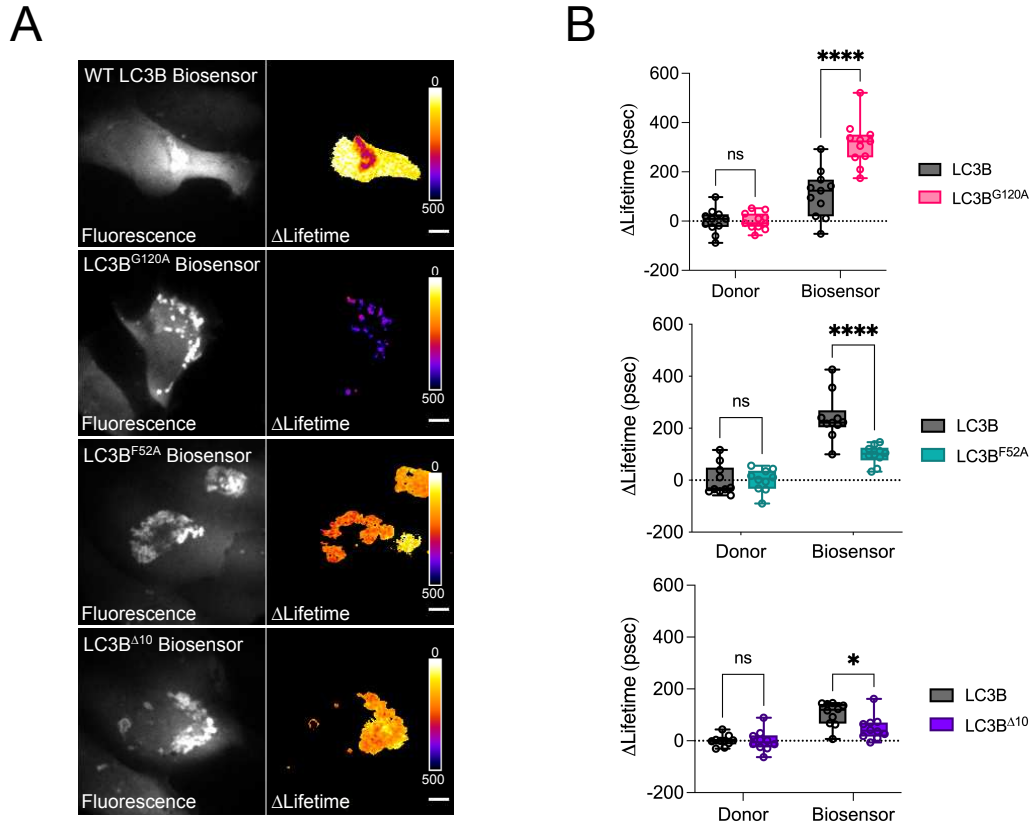


Figure 21: Mutant LC3B biosensors as compared to the WT LC3B biosensor. Representative fluorescence and Δ Lifetime images (A) and quantification of Aquamarine Δ Lifetime values (B) of U2OS cells expressing the WT, G120A, F52A or Δ 10 LC3B biosensors or their donor-only counterparts. Pseudocolor scale: pixel-by-pixel Δ Lifetime. Scale bars: 30 μ m. $n = 10$ cells per condition from one representative experiment (of three). * $P < 0.05$, **** $P < 0.0001$, ns (not significant) as determined by two-way ANOVA with Tukey's multiple comparison test.

The LC3B^{F52A} mutant, on the other hand, has shown a significant loss in Δ lifetime values as compared to the WT biosensor (Fig. 21A-B). This abolishment of FRET with the LC3B^{F52A} mutant indicates the necessity of LC3B-p62/SQSTM1 interaction for the activation of the biosensor, suggesting that our biosensor undergoes the same activation mechanism as of the endogenous LC3B protein. The LC3B^{Δ10} mutant has also shown a significant loss in Δ lifetime values as compared to the WT biosensor (Fig. 21A-B). This suggests that the N-terminal α 1 loop is important for the FRET events and its loss causes

a decrease in Δ lifetime values, further highlighting the FRET events being with linked with the possible oligomerization and tubulin binding events during autophagy.

4.1.2.3 The LC3B biosensor on the mitophagy paradigm

In addition to the mechanisms related to bulk autophagy, we also investigated if the LC3B biosensor can detect mitophagy. To this end, we co-expressed the biosensor with the E3 ligase Parkin in U2OS cells and treated with the mitochondrial uncoupler carbonyl cyanide m-chlorophenylhydrazone (CCCP). Treatment with CCCP depolarizes mitochondria while overexpressed Parkin is recruited on the OMM. When activated by PINK1, Parkin ubiquitinates OMM proteins for their recognition and engulfment by the autophagosomes or degradation by proteasomal machinery [164–170]. Globally, this is considered as the gold-standard paradigm of inducing mitophagy. When mitophagy was induced, we expected that the LC3B biosensor would be activated more than the basal conditions. However, we could not detect any difference in Δ lifetime values when Parkin over-expressing U2OS cells were treated with CCCP, as compared to the control conditions (Fig. 22). Neither Parkin over-expression alone, nor the CCCP treatment only, or the combination of both showed an effect on the activity of the LC3B biosensor. In the light of these results, we concluded that the LC3B biosensor is likely to be more specific for bulk autophagy rather than detecting mitophagy.

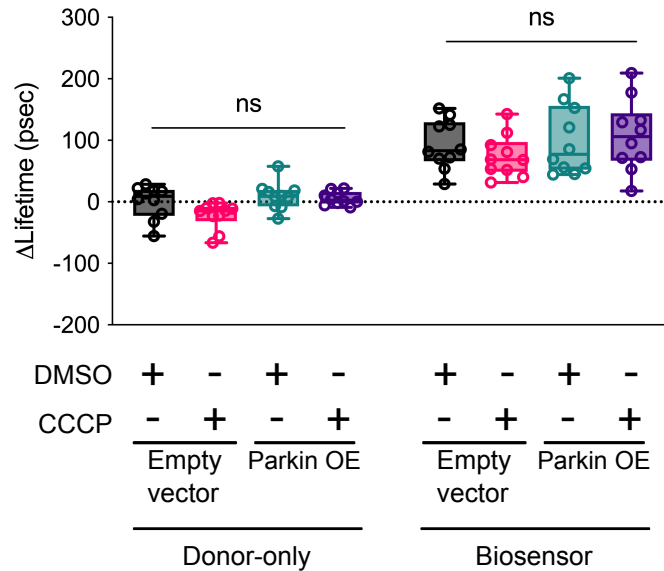


Figure 22: The LC3B biosensor cannot detect mitophagy. Quantification of Aquamarine Δ Lifetime values of U2OS cells co-expressing the LC3B biosensor or LC3B donor-only construct with empty vector or Parkin overexpression (OE) vector. The cells were treated with DMSO or CCCP (10 μ m) for 4h. $n = 10$ cells per condition from one representative experiment (of three). ns (not significant) as determined by two-way ANOVA with Tukey's multiple comparison test.

4.1.3 Analyzing the LC3B biosensor sequence and revalidation of the preliminary findings

As demonstrated in *section 4.1.1*, when the autophagic pathway was stalled in the early- or late-phases with autophagy inhibitors to accumulate LC3B on the autophagic membrane, the biosensor showed a significant increase in Δ lifetime values. Under these conditions, the LC3B biosensor was thought to be reaching its closed conformation upon membrane conjugation. In this light, the initial results with these respective drugs were promising to correlate this significant increase in Δ lifetime values with the activation of the LC3B biosensor. Moreover, the loss in Δ lifetime values almost to the level of donor-only construct in *ATG5* downregulated cells further strengthened the idea that the activation of autophagy is associated with the FRET events.

On the other hand, the LC3B biosensor did not display any difference in Δ lifetime values in other conditions where cells were starved to induce autophagy or treated with CCCP when Parkin was overexpressed to induce mitophagy. Moreover, the Δ lifetime difference peaked when the LC3B^{G120A} mutant was expressed in cells. These puzzling data in which we expected to see the opposite effect, tempted us to inspect the basics of the biosensor. To this end, we first checked the sequence of the biosensor and donor-only constructs. Indeed, we realized that the sequence of LC3B used to build the biosensor and the donor-only constructs corresponded to proLC3B instead of LC3B-I (Fig. 23A-B). In other words, proLC3B was flanked by the donor-acceptor FRET pair: Aquamarine at the N-terminus, and tdLanYFP at the C-terminus (Fig. 23B). When expressed in cells, the proLC3B biosensor is expected to be cleaved C-terminally by ATG4B to reveal G120 residue [270]. The resulting Aquamarine-LC3B-I would then lack the C-terminal tdLanYFP. Therefore, when proLC3B biosensor is expressed in the cells, it is not expected to detect FRET when autophagy is induced.

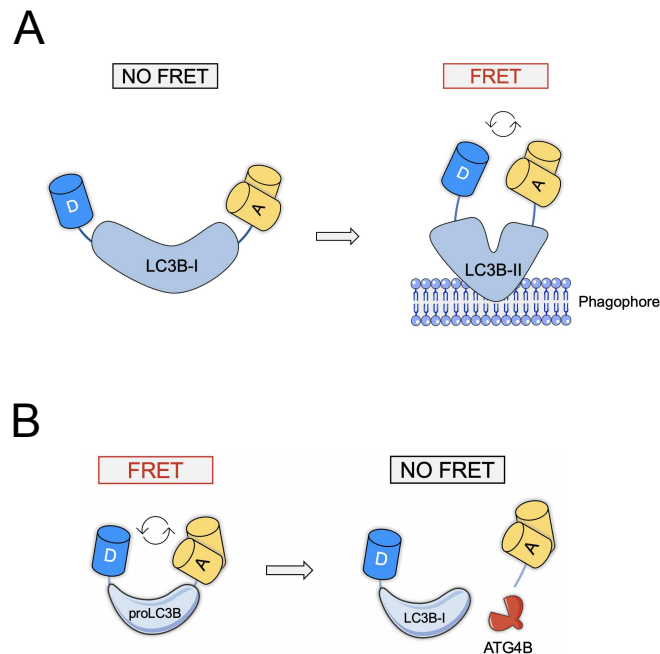


Figure 23: Revealing the LC3B biosensor sequence. (A) Schematic representation of the LC3B biosensor before discovering the real sequence. (B) Schematic representation of the current LC3B biosensor. When expressed in the cells, LC3B biosensor is expected to

be cleaved C-terminally by ATG4B to reveal G120 residue. The resulting Aquamarine-LC3B-I would then lack the C-terminal tdLanYFP moiety.

In the light of this finding, it was also possible to understand why the highest Δ lifetime difference was observed with the mutant LC3B^{G120A} biosensor. Since this biosensor is also a mutated version of proLC3B, it is resistant to be cleaved by ATG4B, therefore the C-terminal tdLanYFP remains intact within the biosensor. Uncleaved tdLanYFP can then accept energy from Aquamarine, resulting in FRET phenomenon and displays a maximized Δ lifetime response. To further investigate if tdLanYFP remains intact in the mutant LC3B^{G120A} biosensor, U2OS cells transiently expressing the WT or the mutant biosensors or donor-only constructs were subjected to the western blotting (Fig. 24). Indeed, the full-length biosensor with a molecular weight of ~95 kDa corresponding to – Aquamarine + LC3B + tdLanYFP – can only be observed in cells expressing the mutant LC3B^{G120A} biosensor (Fig. 24, lane 6). On the other hand, both the WT and the other mutant biosensors lose their tdLanYFP moiety and therefore have a molecular weight of ~43 kDa which corresponds to – Aquamarine + LC3B – and similar to donor-only constructs (Fig. 24, 43 kDa bands).

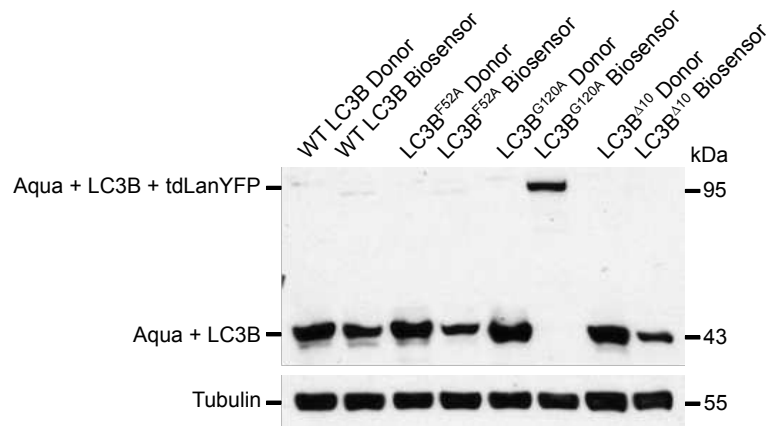


Figure 24: The WT and mutant LC3B biosensors are cleaved except the LC3B^{G120A} biosensor. Representative western blotting images of total lysates from U2OS cells expressing the WT, F52A, G120A, Δ 10 biosensor or donor-only constructs. Loading control: Tubulin.

Although it was possible to understand the FRET response of the mutant LC3B^{G120A} biosensor after our observation on the western blotting, it was still confusing to interpret: 1) why the WT biosensor was showing a significant Δ Lifetime difference when the cells treated with BafA₁ or 3-MA, and 2) why the WT biosensor was displaying significantly reduced Δ Lifetime values upon *ATG5* downregulation? If the biosensor is indeed based on proLC3B, tdLanYFP should be cleaved at the initiation of the autophagy pathway. Hence, the Δ Lifetime values of the resulting Aqua-LC3B-I should not get affected upon increases in lipidation levels with drugs or when lipidation is abolished upon genetic manipulations.

To further investigate on this, we primarily tried to reproduce the experimental results with BafA₁ and 3-MA. Unfortunately, we failed to reproduce the initial results collected by the former student (presented in *section 4.1.1*). Treatment with both drugs did not cause any change in the Δ lifetime values as compared to the control conditions (Fig. 25A). We also could not reproduce the initial experimental results collected upon *ATG5* downregulation. In recent experiments, *ATG5* downregulation did not affect the Δ lifetime values as compared to the control condition (Fig. 25B). These results have confirmed that the manipulation with the drugs to induce lipidated LC3B levels or downregulation of proteins that facilitate the LC3B lipidation do not impact the activity of the LC3B biosensor.

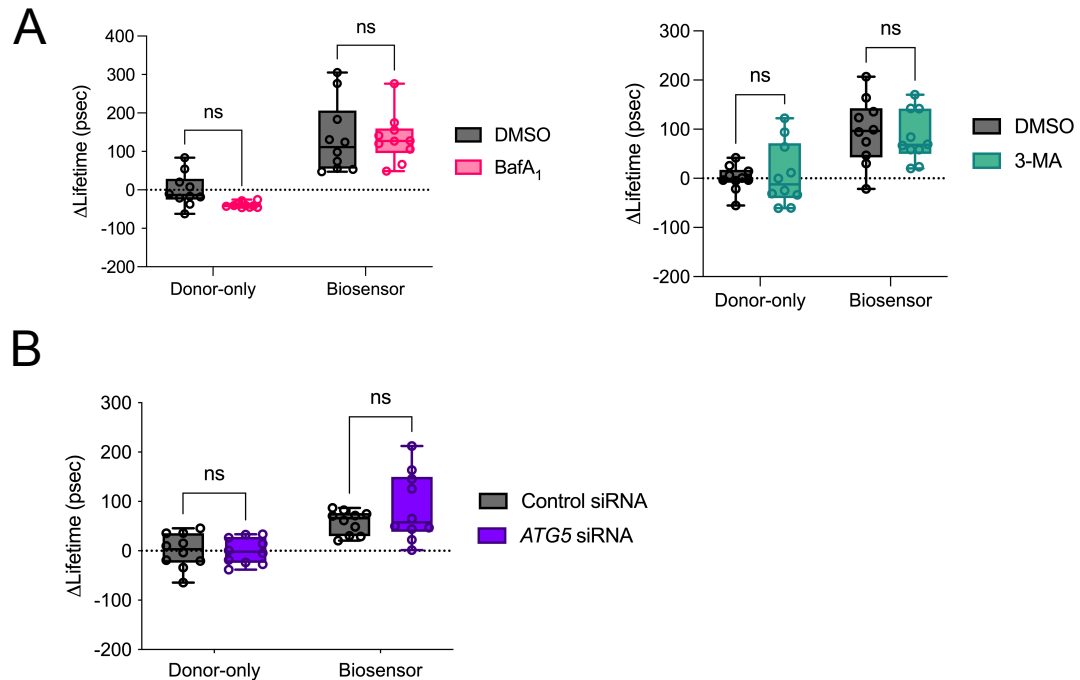


Figure 25: Reproducing the preliminary findings. Quantification of Aquamarine Δ Lifetime values of U2OS cells expressing the LC3B biosensor or LC3B donor-only construct and treated with DMSO, BafA₁ (100 nM for 24h) or 3-MA (5 mM for 24h) (A). (B) Quantification of Aquamarine Δ Lifetime values of U2OS cells co-expressing the LC3B biosensor or LC3B donor-only construct with control or *ATG5*-specific siRNA. $n = 10$ cells per condition from one representative experiment (of three). ns (not significant) as determined by two-way ANOVA with Tukey's multiple comparison test.

In a final attempt to understand why there is a Δ Lifetime difference between the donor-only and the biosensor expressing cells, we investigated the choice of cell when acquiring FRET/FLIM measurements. Up until then, when analyzing the Δ Lifetime values of the cells expressing the biosensor, we focused on the LC3B biosensor presented on the perinuclear aggregate regions. However, this was only applicable for the biosensor expressing cells. The perinuclear aggregates cannot be observed in the donor-only expressing cells, thus the analysis was done on the puncta-shaped structures (Fig. 26A-B, donor panels). Typically, ~ 100 psec of Δ Lifetime difference is observed when the Δ Lifetime values of the puncta-shaped structures of the donor-only expressing cells are compared to the perinuclear aggregates of the biosensor expressing cells (Fig. 26A). On the contrary, when the comparison is performed on the puncta-shaped structures of the

donor-only and biosensor expressing cells, this difference cannot be observed anymore (Fig. 26B). This striking difference based on the choice of cell prompted us to examine if tdLanYFP remain intact within the perinuclear aggregates. For this purpose, U2OS cells transfected with proLC3B-tdLanYFP (tdLanYFP at the C-terminus-only) construct. When analyzed with confocal microscopy, a low number of cells exhibited perinuclear aggregates similar to the ones observed in the biosensor expressing cells (Fig. 26C). Given that tdLanYFP was still present in these aggregates, we concluded that the perinuclear aggregates are possibly the cleaved tdLanYFP moieties accumulating with the primed Aqua-LC3B-I molecules in these regions. It was most likely possible to detect non-specific FRET events, which corresponded to ~100 psec difference between the donor-only and the biosensor expressing cells. Additionally, these aggregates may also small portions of biosensor that is not fully cleaved and therefore contributing to ~100 psec of Δ Lifetime difference. On the contrary, one should expect to observe a larger Δ Lifetime difference around ~400-500 psec when the full-length biosensor is present (similar to that of LC3^{G120A} biosensor). In the light of these findings and from now on, we decided to avoid the cells with perinuclear aggregates and perform the FRET/FLIM analyses on the puncta-shaped structures and on the cytosolic regions both for the donor-only and biosensor expressing cells.

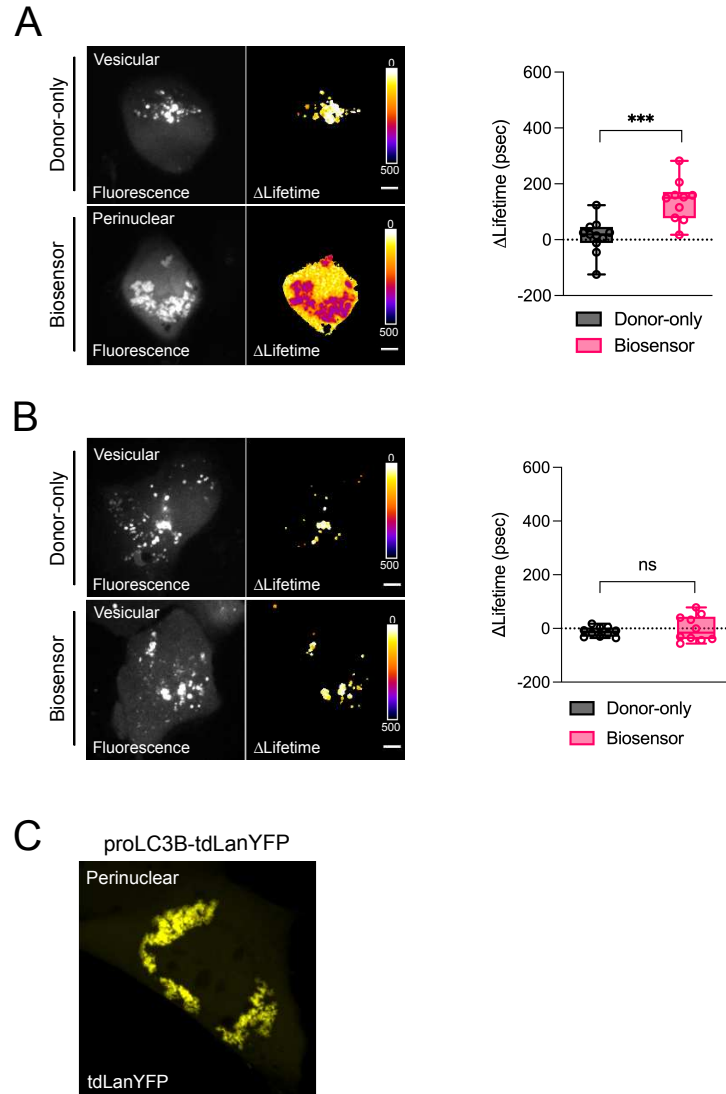


Figure 26: The choice of cell on the Δ Lifetime values of the LC3B biosensor. Representative fluorescence and Δ Lifetime images, and quantification of Aquamarine Δ Lifetime values collected from perinuclear aggregate regions (A) or vesicular structures (B) of U2OS cells expressing the LC3B biosensor or donor-only construct. (C) Representative fluorescence image of U2OS cells transfected with proLC3B-tdLanYFP. Pseudocolor scale: pixel-by-pixel Δ Lifetime. Scale bars: 30 μ m. $n = 10$ cells per condition from one representative experiment (of three). *** $P < 0.001$, ns (not significant) as determined by Student's t-test.

4.1.4 Discussion

Unforeseen challenges were faced in the early stages of developing and characterizing the LC3B biosensor. Embracing these challenges and continuing to perform studies to overcome them eventually led us to repurpose the biosensor to be used in monitoring the ATG4B-LC3B axis.

The foremost challenge was the initial design strategy of the biosensor. As shown in figure 17, the initial idea was to flank the N- and C-termini of the primed LC3B (LC3B-I) with a donor-acceptor FRET pair. This design was based on a study that demonstrated the crystal structure of GABARAP protein which is a member of ATG8 family of proteins [124]. According to this study published by Coyle *et al.*, GABARAP was found in two distinct conformations: 1) a closed monomeric form, and 2) an open oligomeric form. Authors suggested the monomeric form as “the closed conformation” since the first 10 amino acids of the N-terminal region of GABARAP was found to be projecting down toward the surface of the ubiquitin-like C-terminal region of the protein. On the other hand, these first 10 amino acids were found to be projected away from the ubiquitin-like domain in the oligomeric form, therefore leading to its classification as “the open form”. While the monomeric closed form is suggested to be representing the conformation of GABARAP when it is not associated with other proteins or membranes, the oligomeric open form is suggested to be induced upon interaction with other proteins or membranes.

Given the high homology between GABARAP and LC3B, the initial design idea of the LC3B biosensor was to follow a similar conformational change that is likely to be induced on LC3B upon autophagic membrane conjugation. However, this idea had a major pitfall which was the fusion of a C-terminal fluorescent protein blocking the glycine residue (G120) that is crucial for the autophagic membrane conjugation of LC3B. In addition to this, presence of a C-terminal fluorescent protein may likely to prevent the ubiquitylation-like reactions governed by ATG7 and ATG3 to activate LC3B-I prior to the membrane conjugation, thus potentially causing a problem even before the autophagic membrane conjugation of the biosensor. Noticeably, these pitfalls were relevant for a biosensor that was developed with the primed LC3B-I sequence. Since we later realized

that the biosensor was developed by using proLC3B sequence, we also understood that these problems were not relevant for a proLC3B-based biosensor as the C-terminal fluorescent protein was to be cleaved by ATG4 when priming proLC3B and leading to the exposure of G120. Nevertheless, these pitfalls were the main reasons why we did not re-develop a second biosensor with LC3B-I sequence and rather repurposed the proLC3B-based sensor.

Another challenge that we faced in the early phases of the study was the reproducibility issue of the preliminary results collected by a former student. Based on these findings, when the LC3B biosensor was accumulated on autophagosomes or phagosomes upon autophagy inhibition with late- or early-stage inhibitors, the sensor was displaying a significant increase in FRET as compared to the control condition. On the contrary, when the membrane conjugation of the biosensor was diminished by downregulating *ATG5*, the sensor was displaying significantly reduced FRET as compared to the control cells. In the light of these results and under the assumption of biosensor being based on LC3B-I, the initial hypothesis on the mechanism of action of the sensor was formed. According to this hypothesis, the sensor was suggested to reach a closed conformation that brings the N- and C-terminal fluorescent proteins in close vicinity upon autophagic membrane conjugation. Letting aside that this hypothesis does not describe how the C-terminal acceptor moiety does not block LC3B membrane conjugation, it was also not clearly explaining the preliminary results. If the biosensor displays an increased FRET upon membrane conjugation, how it is still observed to be present in the perinuclear aggregates – which are believed to be autophagic membranes back then – upon *ATG5* downregulation while displaying significantly reduced FRET as compared to control cells? Does that imply that the biosensor is able to be conjugated into the autophagic membranes when *ATG5* is downregulated but rather stay in an open conformation which indicates the inactive state? Taking over the project from this point on, those were the questions that I needed to answer by further challenging the biosensor.

While it was troublesome to answer these questions, it was also not easy to implement my results in the light conformational change hypothesis. Though the activation of autophagy by starving the cells expressing the biosensor was expected to

result in the increased levels of FRET, no change was observed between the control and the starved conditions. When we moved forward with the LC3B mutant biosensors later on, the G120A biosensor which was supposed to be not conjugated into the autophagic membranes therefore expected to display diminished levels of FRET, resulted in the highest levels of FRET observed among the wild-type and the other mutant biosensors. This striking difference in the FRET response of the G120A biosensor combined with the western blotting results where the full-length sensor can only be observed in cells expressing the G120A biosensor have given important clues on the cleavage status of the sensor. In addition to this, in our attempts to test the FRET response of the biosensor upon inducing mitophagy, we again detected no difference in between the control and the mitophagy-induced cells. Taken together, these unexpected results were the main reasons why we decided to try reproducing the preliminary findings. After failing to reproduce the preliminary findings and realizing that the sequence of LC3B used to build the biosensor was proLC3B instead of LC3B-I, we finally had a concrete answer on the puzzling findings that we had. Simply put, the proLC3B-based biosensor was getting C-terminally cleaved by ATG4. The primed biosensor which had lost its acceptor moiety after the ATG4-dependent cleavage was in turn not displaying any change in its FRET response upon autophagy inhibition or induction with pharmacological, genetic, or physiological means. The G120A biosensor, on the other hand, was resistant to be C-terminally cleaved by ATG4 since the mutation on G120 residue in proLC3B form of the protein prevents the proteolytic priming activity of ATG4. Therefore, the G120A biosensor that remains intact with its C-terminal tdLanYFP moiety, allows the sensor to perform FRET and was observed as a full-length protein in western blotting.

Another challenge in the early phases of the study was related with the selection of cells to be imaged for FLIM analyses. While collecting the preliminary results, it was decided to focus on the cells displaying the biosensor on the perinuclear aggregates as the analyses performed to calculate Δ Lifetime values on these regions were resulting in significant differences between the control and the treated conditions. However, these aggregates were exclusively present in the biosensor expressing cells and not in the donor-only expressing cells. Moreover, the localization of the biosensor in these aggregates were observable in only very few cells in a well full of cells expressing the

sensor localized in the cytosol or in the puncta-shaped structures. After revealing the proLC3B-based sequence of the construct and in the process of repurposing the biosensor, we tried to understand the differences between the FRET response of the aggregates and the puncta-shaped structures. While the aggregates were typically displaying a basal FRET illustrated by a Δ Lifetime difference of 100-200 psec when compared to the donor-only expressing cells, the puncta-shaped structures were displaying Δ Lifetime differences close to zero. This indicates that the puncta-shaped structures mostly consist of C-terminally cleaved biosensor as expected. On the other hand, perinuclear aggregates are likely to be made of uncleaved (Aqua-proLC3B-tdLanYFP), and cleaved (Aqua-LC3B) biosensor molecules aggregated together. We suggested that these aggregates are likely to be autophagy-independent LC3B incorporation into the protein aggregates such as inclusion bodies. Indeed, this type of LC3B incorporation has previously been reported by others and suggested to be an artifact of overexpression of LC3 constructs by transient transfection [204,271,272]. To this end, we decided to avoid cells with LC3B localization to perinuclear aggregates. In the process of revalidating the biosensor, we also performed plasmid dosing experiments and found an optimal amount of plasmid which was five times less than the amount used in the initial experiments. When low amounts of plasmid were used, we also noticed a substantial decrease in the number of cells with perinuclear aggregates. Overall, these findings highlighted key steps in taking precautions while choosing the cells to be imaged and optimizing the plasmid amount to be used.

In the process of revalidating the biosensor, one of the design ideas to follow the conformational changes of LC3B upon membrane conjugation was to place the C-terminal acceptor moiety before G120 residue. This way, G120 residue would be freely exposed and conjugated into PE while allowing donor and acceptor fluorescent proteins to perform FRET. However, this plan has not been carried on for several reasons. The main reason was due to the knowledge gap in terms of the exact conformation of LC3B upon PE conjugation, which was considered as a risk factor in the early phases of the study as well. To this date, studies performed in mammalian systems and different model organisms to identify the conformational changes of LC3 and GABARAP sub-families suggested that these two sub-families may act differently upon PE conjugation in

autophagosome biogenesis [129,273]. The current model on the conformational changes of ATG8 family proteins suggests that both the open and the closed conformations are co-existing during the autophagic membrane tethering and fusion events, and that these conformational changes are dynamic [274]. Due to these potential multiple changes of conformation over time, it would be difficult to correlate a precise conformational change with a given FRET readout of a second-generation biosensor that has the acceptor moiety before the G120 residue. In addition to this, designing this second-generation biosensor would require us to find an ideal structural placement for the acceptor protein, which overall makes the project assessment very risky to be carried out within the timeframe of my PhD studies.

In conclusion, the reproducibility issues combined with the realization of the actual sequence of the biosensor led us to pursue the project in a new direction. In this new direction, we took the advantage of the current design of the biosensor to follow the C-terminal priming of proLC3B by ATG4B. By learning from our mistakes and combining our expertise in the FRET/FLIM methods, we succeeded on revalidating the biosensor and provided a highly quantitative monitoring of ATG4B activity in living cells and in real time, with unprecedented spatial resolution. The upcoming chapter is describing this new direction and presents our submitted manuscript.

4.2 The LC3B biosensor to follow the modes of action of ATG4B

After discovering the C-terminal cleavage of LC3B biosensor and in the process of rethinking about our design, we observed that there is a lack of reporters to follow ATG4B activity. Following the ATG4B-mediated proLC3B priming activity is particularly challenging in living cells due to the fast kinetics of this event. Indeed, it has been shown by many reports that proLC3B is almost immediately primed after its translation [182,275,276]. This is due to the constitutive proteolytic activity of ATG4B. Thus, the spatiotemporal regulation of this event is poorly understood in living systems and rather studied *in vitro*.

Considering the early results showing the efficient cleavage of LC3B biosensor, we decided to benefit from the current design and repurpose the sensor to monitor ATG4B-

LC3B axis. In this new direction, we included the G120A mutant biosensor as an uncleavable positive control to determine the maximal Δ Lifetime values that can be obtained with this biosensor, when all proLC3B molecules are unprimed. We also modified the way we acquire the FRET/FLIM images to be able to image the whole cellular area. This way, we aimed to include both the cytosol and the puncta-shaped structures, in which the precursor (proLC3B), primed (LC3B-I) and lipidated (LC3B-II) forms of LC3B are expected to be present. In addition to this, we implemented a framework of broad-to-sensitive analyses that combines FRET and the quantification of autophagic puncta. We expanded the methods of analyzing the FRET/FLIM data, by including more sensitive approaches to detect the proLC3B pixels which would otherwise remain undetected in the classical mean Δ Lifetime analyses. To this end, we implemented three sensitive analysis methods: 1) high Δ Lifetime pixel counting, 2) histogram and 3) line analyses.

Finally, our manuscript describing the LC3B FRET biosensor and the modes of action of ATG4B revealed by the sensor has recently been submitted to *Autophagy* and is currently under revision. Given the rising interest on ATG4 family of proteins, we believe that our tool and findings are not only of interest to study LC3B-ATG4B axis but also will be valuable for the identification of more potent and specific compounds inhibiting ATG4B.

The LC3B FRET biosensor monitors the modes of action of ATG4B during autophagy in living cells

Elif Begüm Gökerküçük¹, Angélique Cheron¹, Marc Tramier^{1,*}, Giulia Bertolin^{1,2,*}.

¹ Univ Rennes, CNRS, IGDR (Institute of Genetics and Development of Rennes), UMR 6290, F-35000 Rennes, France

² Lead contact

* Correspondence and requests for materials should be addressed to G.B. (giulia.bertolin@univ-rennes1.fr; Tel: +330223237516) or to M.T. (marc.tramier@univ-rennes1.fr; Tel: +330223235487).

Abstract

Although several mechanisms of autophagy have been dissected in the last decade, following this pathway in real time remains challenging. Among the early events leading to autophagy activation, the ATG4B protease primes the key autophagy player LC3B. Given the lack of reporters to follow this event in living cells, we developed a Förster's Resonance Energy Transfer (FRET) biosensor responding to the priming of LC3B by ATG4B. The biosensor was generated by flanking LC3B within a pH-resistant donor-acceptor FRET pair, Aquamarine/tdLanYFP. We here showed that the biosensor has a dual readout. First, FRET indicates the priming of LC3B by ATG4B and the resolution of the FRET image allows to characterize the spatial heterogeneity of the priming activity. Second, quantifying the number of Aquamarine-LC3B puncta determines the degree of autophagy activation. We then showed that there are small pools of unprimed LC3B upon *ATG4B* downregulation, and that the priming of the biosensor is completely abolished in *ATG4B* knockout cells. The lack of priming can be rescued with the wild-type ATG4B or with the partially active W142A mutant, but not with the catalytically dead C74S mutant. Last, we screened for commercially-available ATG4B inhibitors, and we illustrated their differential mode of action by implementing a spatially-resolved, broad-to-sensitive analysis pipeline combining FRET and the quantification of autophagic puncta. Therefore, the LC3B FRET biosensor paves the way for a highly-

31 quantitative monitoring of the ATG4B activity in living cells and in real time, with
32 unprecedented spatiotemporal resolution.

33

34 Keywords: autophagy, LC3B, ATG4B, FRET/FLIM, biosensor

35 **Introduction**

36 Conserved in all eukaryotic cells, macroautophagy/autophagy is the lysosome-mediated degradation and
37 recycling of the intracellular components [1]. Autophagy is triggered as a survival response in paradigms such
38 as starvation, pathogen infection or DNA damage, and it contributes to cellular differentiation, immunity,
39 aging and cell death [2–4]. In mammals, autophagy starts at sites of endoplasmic reticulum (ER) enriched for
40 phosphatidylinositol 3-phosphate [PI(3)P]. On these subdomains, a double-membrane structure termed
41 phagophore forms [5]. As the phagophore elongates into a crescent-shaped structure, it engulfs bulk or
42 selective cargoes and then closes into a double-membrane vesicle, the autophagosome. The fusion of
43 autophagosomes with lysosomes results in the degradation of the sequestered cargo by the lysosomal acid
44 hydrolases.

45 A series of AuTophagy-related (ATG) proteins regulate the autophagic pathway [6]. Among them, a
46 special attention is given to the ATG8 family, which are the key proteins found on autophagosomal
47 membranes at all stages of the pathway. ATG8 proteins are ubiquitin-like adaptor proteins involved in
48 autophagosome formation, biogenesis and cargo selection [7–9]. In mammals, ATG8 proteins belong to two
49 subfamilies, the MAP1LC3/LC3 (microtubule-associated protein 1 light chain 3) and GABARAP (gamma-
50 aminobutyric acid [GABA] type A receptor-associated protein) [10,11]. A total of seven genes - *LC3A*, *LC3B*,
51 *LC3B2*, *LC3C*, *GABARAP*, *GABARAPL1* and *GABARAPL2* - code for the LC3 and GABARAP subfamilies
52 in humans [10]. LC3/GABARAPs are found as inactive pro- forms upon translation, and are activated by the
53 ATG4 family of cysteine proteases [12,13]. In humans, four members of the ATG4 family (ATG4A, B, C and
54 D) are responsible for this activation step, which is to proteolytically cleave the C-terminus of pro-
55 LC3/GABARAP proteins and convert them into the so-called form-I. This crucial cleavage is known as “pro-

56 LC3/GABARAP priming”, and it is essential to expose a specific glycine residue required for the lipidation
57 of the cytosolic LC3/GABARAP-I proteins to the phosphatidylethanolamine (PE) head groups of the forming
58 phagophores. This is achieved after a series of reactions that involves the E1-like enzyme ATG7, the E2-like
59 enzyme ATG3 and the E3-like complex ATG12–ATG5-ATG16L1 [12,14–16]. The PE-conjugated
60 LC3/GABARAP proteins are then called LC3/GABARAP-II, and function in membrane tethering,
61 hemifusion, autophagosome formation and cargo recruitment [17–20]. Once the phagophore is fully closed,
62 LC3/GABARAP-II proteins are removed from the outer surface of the phagophore membrane by ATG4s,
63 through the hydrolysis of the link between PE and LC3/GABARAP [12]. Although the importance of this
64 second round of cleavage activity (referred as deconjugation hereafter) by ATG4 was shown to be important
65 for the normal progression of autophagy in yeast [21–23], recent studies in human cells suggest the existence
66 of autophagy-independent roles for the deconjugation activity of ATG4s [24,25]. Therefore, the relevance of
67 ATG4-mediated deconjugation for the progression and completion of autophagy in models other than yeast
68 still requires further investigation [21–26].

69 Autophagy plays an essential role to maintain cellular homeostasis, and its dysfunction has been
70 implicated in many pathological conditions such as neurodegenerative diseases, cancer, inflammation,
71 muscular and hearth disorders [27]. As a consequence, therapeutic options to modulate autophagy emerged as
72 promising strategies for the treatment of these complex pathologies [28]. In this light, targeting ATG4s to
73 inhibit autophagy in its early stages has a significant potential to completely block autophagy [29]. However,
74 currently available compounds targeting ATG4 activity show poor specificity and/or efficacy [30]. In addition,
75 there is a lack of dedicated probes that can be used in living cells to monitor ATG4 activity during autophagy
76 progression. Overall, this creates a bottleneck for the identification of ATG4 inhibitors with improved
77 properties. For these reasons, we developed a Förster’s Resonance Energy Transfer (FRET) biosensor, named
78 the LC3B biosensor, to simultaneously monitor: 1) the priming of LC3B by ATG4 and 2) the accumulation
79 of LC3B on the autophagic membranes.

80 The FRET phenomenon is a non-radiative energy transfer between a donor and an acceptor pair of
81 fluorophores. FRET can occur when the emission spectrum of the donor fluorophore partially overlaps with
82 the excitation spectrum of the acceptor, and this only when the two fluorescent moieties are in close proximity
83 (less than 10 nm apart) [31]. This phenomenon can be used to monitor many different cellular events including
84 the exploration of protein-protein interactions, the changes in conformation of proteins, and the up- or
85 downregulation of signaling pathways [32,33]. With the recent advances, FRET quantification by fluorescence
86 lifetime imaging microscopy (FLIM) became a very useful method to study molecular activities in living cells
87 [34].

88 In this study, we present the LC3B biosensor as a superior probe that can be used in living cells to
89 monitor the activation – LC3B priming by ATG4 – and progression – LC3B accumulation on the autophagic
90 membranes – of autophagy, in real time and with high spatial resolution. We show that the biosensor
91 recapitulates the main features of the endogenous LC3B protein in terms of forming puncta-shaped structures,
92 of ATG4B-dependent cleavage, and of its colocalization with lysosomal proteins upon autophagy induction
93 and/or lysosomal inhibition. We also show that the biosensor can report on the changes in proLC3B priming,
94 and this in an ATG4B-dependent manner. Using *ATG4* knockout cells, we demonstrate that the absence of
95 ATG4B maximizes the FRET response of the biosensor as a consequence of the complete lack of proLC3B
96 priming. We then show that proLC3B priming can be rescued with the ectopic expression of the wild-type
97 ATG4B. Interestingly, we demonstrate that the ATG4B^{W142A} mutant, previously shown to possess a
98 significantly reduced catalytic activity [35], is capable of rescuing proLC3B priming similarly to the wild-
99 type protein. By using the LC3B biosensor and performing multiple approaches to analyze FRET/FLIM, we
100 report on the action of mechanisms of available ATG4 inhibitors. By doing so, we provide a framework of
101 how to use the LC3B biosensor and analyze the acquired data to identify new ATG4 inhibitors with better
102 specificity and efficacy.

103 **Results**

104 ***The LC3B biosensor dynamically reports on the activation or the inhibition of the autophagy flux, and it*** 105 ***colocalizes with LAMP2 in an autophagy-dependent manner***

106 To monitor the priming activity of ATG4 in real time and with spatial resolution, we developed a FRET-based
107 biosensor that can be utilized in living cells. We chose LC3B as it is a known target of the ATG4 activity that
108 undergoes an ATG4-mediated cleavage on Gly120, and it is among the best characterized players of the
109 autophagy pathway [36]. The biosensor was designed to flank the N- and C-termini of proLC3B with a donor-
110 acceptor FRET pair (Fig. 1A). The FRET pair composed of Aquamarine (donor, cyan) and tdLanYFP
111 (acceptor, yellow) was selected on the resistance of both fluorophores to acidic pH [37–39]. In the absence of
112 ATG4 activity, the LC3B biosensor is expected to remain unprocessed in cells, allowing Aquamarine and
113 tdLanYFP to perform FRET (Fig. 1A). If ATG4 is active, the biosensor is expected to undergo an ATG4-
114 dependent proteolytic cleavage at its C-terminus, thereby losing the tdLanYFP moiety and the FRET effect
115 with it. This allows to follow the initial C-terminal priming activity of ATG4 as an early, FRET-based readout.
116 In addition, the priming of LC3B leads to its conversion into the I form, which will still be tagged by
117 Aquamarine (Aquamarine-LC3B-I). When the resulting Aquamarine-LC3B-I protein is integrated into the PE
118 head groups of the phagophores, the biosensor is expected to function as a canonical fluorescent probe to
119 quantify LC3B-positive puncta structures. Therefore, our biosensor also provides a quantitative readout on
120 the late stages of the autophagic pathway, and it can be used to estimate the number of autophagosomes in
121 individual cells (Fig. 1A).

122 We first explored whether the LC3B biosensor is capable of localizing to autophagosomes, which
123 normally appear as puncta-shaped structures. In U2OS cells transiently transfected to express the biosensor,
124 Aquamarine was observed to be present both in puncta-shaped structures, which are compatible with LC3B-
125 II, and in the cytosol, which is compatible with Aqua-LC3B-I (Fig. 1B). To confirm that the puncta-shaped
126 structures were autophagosomes, cells were treated with autophagy inducers as Torin1 or HBSS, in the

127 presence or absence of the lysosomal inhibitor Bafilomycin A₁ (BafA₁). Compared to control cells, a
128 significant increase in the number of Aquamarine-positive puncta was observed in cells expressing the wild-
129 type LC3B biosensor (WT biosensor) and treated with BafA₁ or Torin1 alone (Fig. 1B, C). A further increase
130 in the number of Aquamarine-positive puncta was observed when cells were treated simultaneously with
131 BafA₁ and Torin1. This indicates that the puncta-shaped structures observed under these conditions are
132 Aquamarine-LC3B-II (Aqua-LC3B-II)-positive autophagosomes, since they respond to autophagy induction
133 and to lysosomal inhibition alone or in combination. Conversely, autophagy induction by starvation did not
134 cause any increase in the number of puncta-shaped structures when compared to the control (Fig. 1B, C).
135 However, when starvation with HBSS was coupled with BafA₁ treatment, we observed a significant
136 accumulation of puncta-shaped structures (Fig. 1B, C). In all conditions tested, tdLanYFP appeared to be
137 diffused in the cytosol, thereby showing a dramatic difference compared to the distribution of Aquamarine
138 into puncta-shaped structures. This strongly suggests that tdLanYFP is cleaved along with the C-terminal part
139 of proLC3B, and therefore it cannot colocalize with Aquamarine on the puncta-shaped structures. To
140 corroborate this observation, we explored the distribution of an uncleavable variant of the LC3B biosensor,
141 which is mutated on Gly120 (hereby, G120A biosensor) and cannot be primed by ATG4 [36]. In cells
142 expressing the G120A biosensor, both Aquamarine and tdLanYFP were exclusively diffused in the cytosol
143 (Fig. S1), and they exhibited no puncta-shaped structures under any treatment (Fig. 1C and S1). The difference
144 in puncta numbers between the WT and the G120A biosensors supports the notion that the WT construct is
145 cleaved at the C-ter, and that it efficiently forms autophagosome-related puncta structures. In this light, we
146 verified the cleavage profiles of the WT and G120A biosensors by western blotting. While the G120A
147 biosensor had a molecular weight of ~95 kDa – corresponding to Aquamarine + proLC3B^{G120A} + tdLanYFP
148 –, the WT biosensor was cleaved in all conditions tested and appeared as two bands at ~45kDa and ~43kDa.
149 These bands were compatible with the molecular weight of Aquamarine + LC3B-I at ~45 kDa, and of
150 Aquamarine + LC3B-II at ~43 kDa (Fig. 1E). Consistent with the quantifications of puncta numbers in cells
151 expressing the WT biosensor (Fig. 1B, C), the levels of the Aqua-LC3B-II band increased upon BafA₁ or

152 Torin1 treatment, but remained unaltered upon starvation with HBSS (Fig. 1E, F). A further increase in Aqua-
153 LC3B-II abundance was observed upon the co-treatment with BafA₁ and Torin1 when compared to BafA₁ or
154 Torin1 alone (Fig. 1E, F). Similarly, the combination of HBSS and BafA₁ increased the levels of Aqua-LC3B-
155 II when compared to HBSS alone (Fig. 1E, F). These findings suggest a rather rapid degradation of Aqua-
156 LC3B-II via lysosomal turnover in U2OS cells upon starvation with HBSS. This also suggests that the
157 degradation of Aqua-LC3B-II can be slowed down when starvation is coupled with a late-stage lysosomal
158 inhibitor such as BafA₁. This was previously reported to occur in several other cell lines [24,40,41], and it
159 substantiates the importance of measuring the autophagy flux in the absence or presence of lysosomal
160 inhibitors. The differences observed in the levels of Aqua-LC3B-II were also observable at the level of the
161 endogenous LC3B-II, confirming that the lipidation levels of the LC3B biosensor are similar to those of
162 endogenous protein upon autophagy induction and/or lysosomal inhibition (Fig. 1E, G).

163 To provide conclusive evidence that Aqua-LC3B-II puncta structures are autophagosomes and are
164 capable of colocalizing with lysosomes, we analyzed their colocalization with the lysosomal protein
165 Lysosomal Associated Membrane Protein 2 (LAMP2). Compared to control cells, we found that the
166 colocalization of Aqua-LC3B-II puncta structures with LAMP2-positive objects significantly increased when
167 autophagy is induced with Torin1, but not with HBSS (Fig. 1B, D). As expected in cells expressing the WT
168 biosensor, we observed that treatment with BafA₁ significantly reduced the colocalization of Aqua-LC3B-II
169 puncta with LAMP2 compared to untreated, Torin1- or HBSS-treated cells. Conversely, the G120A biosensor
170 did not colocalize with LAMP2 in any condition (Fig. 1D and S1). Overall, these results show that the WT
171 biosensor colocalizes with LAMP2 in an autophagy-dependent manner.

172 Taken together, these results demonstrate that the LC3B biosensor is efficiently cleaved. The biosensor
173 is capable of forming puncta structures that are consistent with the lipidated, Aqua-LC3B-II form, and they
174 colocalize with the lysosomal protein LAMP2. The autophagy-dependent changes in the number of puncta-
175 shaped structures or their degree of colocalization with LAMP2 indicate that the biosensor is capable of
176 successfully reporting on autophagy induction and/or lysosomal inhibition.

The LC3B biosensor responds to the changes in proLC3B priming in an ATG4B-dependent manner

After establishing that the biosensor behaves like endogenous LC3B in cells, we sought to assess its capacity to dynamically report on LC3B processing. To this end, live cells expressing the WT or the uncleavable G120A biosensor were analyzed using FRET/FLIM. We compared the donor (Aquamarine) lifetime differences between the donor-only and the biosensor to detect FRET events, which are highlighted when the donor lifetime decreases. We then used Δ Lifetime as a readout for FRET/FLIM analyses, which was determined by calculating the net difference between the lifetime of the donor-only construct (Aquamarine-proLC3B) and that of a biosensor (either Aquamarine-proLC3B- or proLC3B^{G120A}-tdLanYFP). We hypothesized that a positive Δ Lifetime would be indicative of a FRET event between Aquamarine and tdLanYFP, therefore corresponding to the presence of unprimed proLC3B.

First, we measured the FRET/FLIM readout of the WT biosensor by calculating its mean Δ Lifetime in the total cell area. This includes the cytosol and the puncta structures, in which the precursor, primed and lipidated forms of LC3B are expected to be present. We observed that no FRET was occurring in control cells, as illustrated by a Δ Lifetime difference close to zero (Fig. 2A, B). This indicates that the LC3B biosensor is completely primed under basal conditions, leading to the loss of the tdLanYFP moiety. Conversely, the uncleavable G120A biosensor reported a significant increase of \sim 500 psec in Δ Lifetime compared to the WT biosensor. This led us to conclude that the FRET readout of the LC3B biosensor is directly linked to its cleavage on G120. In addition, the FRET readout is specific to the biosensor constructs, as we observed no difference in Δ Lifetime between the WT and G120A donor-only constructs (Fig. S2A, B).

We then reasoned that the direct correlation between FRET and priming should make the LC3B biosensor responsive to the presence or absence of ATG4. To this end, we used siRNA-mediated gene silencing to downregulate the *ATG4B* isoform, as it exhibits the highest catalytic efficiency towards LC3B compared to the other members of the ATG4 family [42]. First, we verified the efficiency of the siRNA-mediated downregulation strategy by western blotting, in cells expressing the WT or the G120A biosensor (Fig. S2C, D). When comparing the mean Δ Lifetime values, no difference was observed in cells expressing

202 the G120A biosensor under any condition, as expected (Fig. 2A, B). Although no difference in mean Δ Lifetime
203 was observable in control or *ATG4B*-depleted cells expressing the WT biosensor (Fig. 2A, B), we noticed the
204 presence of a significant subset of pixels exhibiting high Δ Lifetime values only in *ATG4B*-depleted cells (Fig
205 2A, enlarged Δ Lifetime image of the WT biosensor with *ATG4B* siRNA). Therefore, we hypothesized that
206 these pixels might correspond to unprimed proLC3B. To verify our hypothesis, we ascertained that these
207 pixels could be retrieved only upon *ATG4B* downregulation, and that they could represent unprimed pools of
208 LC3B by showing a G120A-like FRET. To this end, we performed a pixel-by-pixel FRET/FLIM analysis to
209 quantify the number of pixels showing Δ Lifetime values similar or higher than the mean Δ Lifetime of the
210 G120A biosensor. Indeed, *ATG4B* silencing caused a significant increase in the number of pixels with high
211 Δ Lifetime values compared to the control condition (Fig. 2C). We then used the power of FRET microscopy
212 to visualize these high Δ Lifetime pixels with a line analysis. This analysis allows to observe the local variations
213 in Δ Lifetime occurring in the pixels crossed by a straight line. Δ Lifetime values along the line went from zero
214 to the levels of the G120A biosensor only in cells silenced for *ATG4B* (Fig. 2A, D). This indicates a lack of
215 proLC3B cleavage occurring locally, and it substantiates the role of *ATG4B* in this process. We also noticed
216 that the increase in Δ Lifetime was localized in pixels found on or near the puncta-shaped structures (Fig. 2A).
217 This reveals the spatial heterogeneity of the priming activity in these areas and uncovers a possible spatial
218 regulation of proLC3B priming, which may be taking place in discrete regions in the vicinity of
219 autophagosomes. When we performed the same analysis for donor-only constructs, we could not detect any
220 high Δ Lifetime pixels, ensuring that the effect that we observe with the WT biosensor upon *ATG4B*
221 downregulation was not due to an intrinsic change in the lifetime properties of Aquamarine (Fig. S2E). To
222 make sure that the heterogeneity of Δ Lifetime pixels was correctly estimated in the different conditions, we
223 analyzed the data to visualize the Δ Lifetime distribution. We hypothesized that the presence of high Δ Lifetime
224 pixels with G120A biosensor-like Δ Lifetime values should change the overall Δ Lifetime distribution. To this
225 end, we superimposed the histograms of the cells expressing the WT biosensor with or without *ATG4B*
226 depletion, and we observed a shift in the histogram mode values of *ATG4B*-depleted cells towards higher

227 Δ Lifetime values (Fig. 2E). Since the mode value of a histogram corresponds to the value with the highest
228 frequency, a positive shift in the mode indicates that the Δ Lifetime distribution changes due to the presence
229 of FRET events in the biosensor.

230 Considering that, in addition to its priming activity, ATG4B also acts as a deconjugating enzyme that
231 governs the ATG8ylation levels [25,43], we checked if its depletion is causing an increase in the puncta-
232 shaped structures. In cells expressing the WT biosensor or donor, we observed a robust increase in the number
233 of LC3B puncta upon *ATG4B* downregulation compared to controls (Fig. 2F, S2F). This indicates that the
234 formation of puncta-shaped structures depends on the presence of ATG4B. As expected, no puncta were
235 observed in cells expressing the G120A biosensor or donor, regardless of the presence or absence of ATG4B
236 (Fig. 2F, S2F). Similarly, when we analyzed protein levels by western blotting, we detected a significant
237 increase in the lipidated levels of the biosensor (Aqua-LC3B-II) and of the endogenous LC3B-II upon *ATG4B*
238 downregulation, compared to the controls (Fig. S2C, D).

239 Taken together, these results show that the LC3B biosensor allows to visualize changes in the ATG4B-
240 dependent priming of proLC3B. We provide evidence that the biosensor can form LC3B puncta in an ATG4B-
241 dependent manner, demonstrating that our probe recapitulates the key features of endogenous LC3B. Last, we
242 demonstrate that analyzing the FRET response of the biosensor with different modalities allows to monitor
243 the cleavage of proLC3B both at the cellular and at the subcellular level. Our findings support the pertinence
244 of this tool to spatiotemporally characterize LC3B processing in cells.

245 ***The total depletion of ATG4B maximizes the FRET response of the LC3B biosensor***

246 To deepen our understanding of the mode of action of the LC3B biosensor in cells, we used *ATG4* knockout
247 (KO) HeLa cells generated by Agrotis *et al.* using CRISPR/Cas9-mediated approaches [24]. First, we
248 measured the FRET response of the WT or G120A biosensor expressed in control cells. Similarly to what
249 observed in U2OS cells (Fig. 2A, B), the WT biosensor displayed a Δ Lifetime close to zero, while the FLIM
250 readout of the cleavage-deficient G120A biosensor showed a \sim 400 psec Δ Lifetime (Fig. 3A, B). When looking
251

252 at the distribution of the two sensors, we observed that the WT biosensor was capable of forming puncta-like
253 structures while the G120A biosensor showed a cytosolic distribution as expected (Fig. 3A). Overall, the
254 FRET behavior and the distribution of the WT and G120A LC3B biosensors were consistent with our previous
255 observations in U2OS cells.

256 We then sought to explore the FRET/FLIM readout of the LC3B biosensor in cells completely devoid
257 of the ATG4 protease. We expressed the WT biosensor in *ATG4B* single knockout (SKO) HeLa cells and in
258 comparison to control cells, the WT biosensor displayed mean Δ Lifetime values of \sim 400 psec under these
259 conditions (Fig. 3A, B). These values were nearly identical to the mean Δ Lifetime of the G120A biosensor.
260 Similarly to the distribution of the G120A biosensor, the WT biosensor in SKO cells did not exhibit noticeable
261 puncta-like structures, and it remained cytosolic. Therefore, these findings support the loss of priming of the
262 WT biosensor in an *ATG4B* SKO background. The lack of priming of the LC3B biosensor was also evident
263 in western blotting analyses (Fig. S3). The WT biosensor expressed in control cells displayed two bands
264 corresponding to the primed and the lipidated forms of the probe, both in the \sim 43-45 kDa range. In contrast,
265 the WT biosensor expressed in *ATG4B* SKO cells exhibited a single band at \sim 95 kDa. This band is similar to
266 that observed in cells expressing G120A biosensor, therefore reinforcing the conclusion that the WT biosensor
267 remains unprimed in cells lacking the ATG4B protease. We observed that the complete knockout of *ATG4B*
268 also abolishes the priming of endogenous LC3B, which exhibits a single band at 15 kDa compatible with
269 unprimed proLC3B [44] (Fig. S3). These results indicate that ATG4B is indispensable for the priming and the
270 lipidation of the LC3B biosensor.

271 We then verified whether the A and C isoforms of ATG4 family could further contribute to the priming
272 of the LC3B biosensor. The mean Δ Lifetime values (Fig. 3A, B) and the western blotting profiles (Fig. S3) of
273 the WT biosensor expressed in *ATG4A/B* double knockout (DKO) or *ATG4A/B/C* triple knockout (TKO) HeLa
274 cells [24] showed no differences compared to the *ATG4B* SKO condition. This substantiates previous *in vitro*
275 reports showing that the catalytic activity of ATG4B is maximized towards LC3B [45]. To rule out every
276 possibility that the A or C isoforms could still contribute to the priming of LC3B to some extent, we increased

277 the sensitivity of our analyses by performing pixel-by-pixel FRET/FLIM calculations. We quantified the
278 number of pixels with Δ Lifetime values similar or higher than the Δ Lifetime of the G120A biosensor in
279 control, *ATG4B* SKO, *ATG4A/B* DKO or *ATG4A/B/C* TKO cells. With this, we aimed to explore subtle
280 changes possibly occurring between the KO cells that may remain undetected in mean Δ Lifetime analyses. As
281 expected, we observed a significant increase in the number of pixels with high Δ Lifetime in *ATG4B* SKO cells
282 expressing the LC3B biosensor when compared to control cells, further corroborating the results obtained with
283 mean Δ Lifetime analyses (Fig. 3C). However, these analyses did not highlight any significant increase in the
284 number of pixels with high Δ Lifetime upon further loss of *ATG4A* or *ATG4C* (Fig. 3C). Interestingly,
285 *ATG4A/B* DKO cells showed a slight shift towards higher Δ Lifetime values in their respective histogram mode
286 value compared to the mode value of *ATG4B* SKO cells (Fig. 3D). However, only a negligible histogram
287 mode value shift was observed in *ATG4A/B/C* TKO cells compared to *ATG4A/B* DKO cells. This suggests
288 that *ATG4A* could still mildly contribute to the priming of the LC3B biosensor, although *ATG4B* is the key
289 protease in this reaction.

290 Similarly to what observed for the endogenous LC3B protein, our results demonstrate that the priming
291 of the LC3B biosensor is highly dependent on the presence of *ATG4B*. When *ATG4B* is absent, the LC3B
292 biosensor displays a significant FRET response, it remains unprimed and cannot be lipidated to form puncta-
293 like structures, overall resembling the behavior of the cleavage- and lipidation-deficient G120A biosensor.

295 ***The ectopic expression of active ATG4B rescues the priming deficiency of the LC3B biosensor in ATG4B-*** 296 ***deficient cells***

297 After demonstrating that the priming of the LC3B biosensor is *ATG4B*-dependent, we then asked whether its
298 FRET response in *ATG4B*-deficient cells could be rescued by re-expressing *ATG4B*. To this end, we co-
299 expressed the LC3B biosensor together with an empty vector or with a vector coding for WT *ATG4B*. Then,
300 we evaluated the FRET/FLIM behavior of these conditions both in control and in *ATG4B* SKO cells.

301 Consistent with our previous findings (Fig. 3), the LC3B biosensor co-expressed with an empty vector in
302 *ATG4B* SKO cells showed a significant increase in its mean Δ Lifetime values compared to control cells (Fig.
303 4A, B). Conversely, the expression of WT ATG4B in *ATG4B* SKO cells caused a drastic decrease in the mean
304 Δ Lifetime values of the LC3B biosensor, which were close to zero. This suggests that the reintroduction of
305 WT ATG4B is sufficient to fully rescue the cleavage of the LC3 biosensor in a SKO background. Upon the
306 expression of exogenous ATG4B in control cells, we also observed that the distribution of the biosensor was
307 cytosolic and without significant puncta-like structures (Fig. 4A). On the contrary, control cells co-expressing
308 an empty vector were capable of forming puncta-like structures. This is in agreement with previous reports
309 showing that the overexpression of exogenous ATG4B blocks the lipidation of LC3B and by doing so, it leads
310 to the disappearance of LC3-positive puncta in cells [13,46,47].

311 Next, we assessed whether two mutant forms of ATG4B with different catalytic activities could rescue
312 the priming deficiency of the LC3B biosensor in *ATG4B* SKO cells. We first explored the consequences of
313 mutating the Cys74 residue of ATG4B into Ser (C74S). Cys74 belongs to a group of three aminoacids known
314 as the “catalytic triad”, and its mutation into Ala or Ser was shown to cause a complete loss of the catalytic
315 activity of ATG4B [13,35]. When ATG4B^{C74S} was co-expressed with the LC3B biosensor in *ATG4B* SKO
316 cells, we measured a mean Δ Lifetime comparable to *ATG4B* SKO cells transfected with an empty vector (Fig.
317 4A, B). This indicates that the catalytically-dead C74S mutant was unable to cleave and, by consequence
318 prime, the LC3B biosensor. We then tested a second mutant form of ATG4B where Trp142 was mutated into
319 Ala (W142A). Trp142 is one of the residues surrounding the catalytic triad, and its mutation into Ala was
320 reported to significantly reduce the catalytic activity of ATG4B *in vitro* [35]. Surprisingly, we observed that
321 ATG4B^{W142A} behaved similarly to WT ATG4B when expressed in SKO cells, and it resulted in a complete
322 cleavage of the LC3B biosensor in FRET/FLIM analyses (Fig. 4A, B). This supports the superior catalytic
323 efficiency of ATG4B to prime proLC3B in living cells, even in conditions where its catalytic activity is
324 severely compromised by the W142A mutation. To verify that these changes in mean Δ Lifetime were specific
325 to the LC3B biosensor, we analyzed the mean Δ Lifetime profiles of control or *ATG4B* SKO cells expressing

326 the donor-only Aquamarine-LC3B construct together with WT, C74S or W142A ATG4B (Fig. S4A). As
327 expected, we did not observe any difference among all the conditions tested, further confirming that the mean
328 Δ Lifetime FRET/FLIM readout is specific towards the ATG4B-mediated cleavage of the LC3B biosensor.

329 We then wanted to verify if our approach based on mean Δ Lifetime was sensitive enough to conclude
330 on the capacity of the W142A mutant to fully prime LC3B. Therefore, we further evaluated the readout of the
331 LC3B biosensor by performing pixel-by-pixel FRET/FLIM calculations, which we previously showed to be
332 more sensitive than mean Δ Lifetime analysis (Fig. 2). As expected, we observed a significant increase in the
333 number of pixels with high Δ Lifetime – indicating no LC3B priming – in *ATG4B* SKO cells co-expressing an
334 empty vector or *ATG4B*^{C74S} compared to control cells (Fig. 4C). Similarly to mean Δ Lifetime analyses (Fig.
335 4B), expressing WT *ATG4B* or *ATG4B*^{W142A} in *ATG4B* SKO cells revealed an absence of pixels with high
336 Δ Lifetime values, suggesting a complete rescue of the priming activity of the LC3B biosensor with both
337 constructs (Fig. 4C). Accordingly, the histogram analyses of the distribution of FRET pixels in all conditions
338 showed almost identical mode values in *ATG4B* SKO cells co-expressing WT or *ATG4B*^{W142A}, with their
339 respective mode values centered around zero (Fig. 4D). On the contrary, the mode values of *ATG4B* SKO
340 cells expressing an empty vector or *ATG4B*^{C74S} were drastically shifted towards 400 psec, which is again
341 indicative of significant FRET (Fig. 4D). As expected, the analysis of the high Δ Lifetime pixels in control or
342 SKO cells expressing the donor-only Aquamarine-LC3B and each of the *ATG4B* constructs did not reveal
343 any difference (Fig. S4B). Again, this substantiates the specificity of our different FRET/FLIM readouts for
344 the LC3B biosensor only. In addition to this, the WT biosensor expressed in control cells with each of the
345 *ATG4B* constructs exhibit similar histogram mode values (Fig. S4C). Nevertheless, we observed the presence
346 of a shoulder corresponding to Δ Lifetime values of ~200-300 psec in control cells co-expressing the WT
347 biosensor with *ATG4B*^{C74S} (Fig. S4C), which could reflect the previously reported dominant negative effects
348 of *ATG4B*^{C74S} on the soluble forms of LC3B [46].

349 Altogether, our results demonstrate that the proLC3B priming deficiency observed in *ATG4B* SKO
350 cells can be fully restored when co-expressing the WT or W142A forms of *ATG4B*, but not with the

351 catalytically-dead C74S. Although ATG4B^{W142A} was shown to display a reduced catalytic activity *in vitro*
352 [35], we demonstrate that this mutant is able to prime proLC3B in living cells similar to WT ATG4B. These
353 data were obtained with three independent methods to calculate the FRET behavior of the LC3B biosensor,
354 and they provide novel insights on the superior capacity of ATG4B to prime LC3B *in cellulo* even in
355 conditions where its catalytic activity is compromised. Importantly, they also support the notion that the
356 catalytic activity of ATG4B needs to be completely eliminated to abolish LC3B priming.

357

358 ***The LC3B biosensor reveals the mode of action of ATG4 inhibitors in cells***

359 Given that the biosensor reports on the priming of LC3B by ATG4B, we sought to investigate whether it is
360 also capable to respond to pharmacological compounds that inhibit the ATG4B-LC3B axis. We first explored
361 the effect of MG132, a peptide aldehyde that inhibits both the proteasome and cysteine proteases [48,49].
362 Considering that ATG4B is a cysteine protease [14,35], we reasoned that MG132 might be able to block its
363 catalytic activity towards LC3B. Therefore, we treated HeLa cells expressing the WT or G120A biosensor
364 with DMSO or MG132, and calculated their mean Δ Lifetime (Fig. S5A, B). FLIM analyses revealed a
365 significant increase in the mean Δ Lifetime values of the WT biosensor in the presence of MG132. We reasoned
366 that MG132 could promote FRET within the biosensor either by inhibiting the priming activity of ATG4B, or
367 by inhibiting LC3B degradation by the proteasome. To distinguish between these two possibilities, we relied
368 on the subcellular distribution of the biosensor. In this light, the biosensor should be retrieved in the cytosol
369 in case MG132 had mainly an ATG4B-specific inhibition on proLC3B priming. Alternatively, it should rather
370 be found in puncta-like structures if this drug acted as a proteasome inhibitor. We observed a significant
371 increase in the number of Aqua-LC3B-II puncta-like structures in cells expressing the WT biosensor and
372 treated with MG132, when compared to DMSO-treated cells (Fig. S5B). Therefore, this localization of the
373 sensor in puncta-like structures suggests that MG132 is more efficient as a proteasome inhibitor, rather than a
374 specific ATG4B inhibitor. Although the number of pixels with high Δ Lifetime values did not significantly
375 increase upon MG132 treatment (Fig. S5B), the histogram analysis of MG132-treated cells expressing the WT

376 biosensor revealed a mode value change when compared to DMSO-treated cells and to cells expressing the
377 G120A biosensor (Fig. S5C). Overall, this indicates that FRET events are quantitatively modest in the
378 presence of MG132, suggesting that MG132 preferentially acts as a proteasomal inhibitor rather than an
379 ATG4B-specific inhibitor. Although FRET events were limited under these conditions, we sought to explore
380 their spatial localization. Line analyses performed in cells expressing the WT biosensor and treated with
381 MG132 revealed that the Δ Lifetime variations of the biosensor were of \sim 200 psec in the cytosol, and reaching
382 Δ Lifetime values of the G120A biosensor (\sim 400 psec) on or near the LC3B puncta (Fig. S5B, D). In contrast,
383 no fluctuations were observed in the cytosol or near puncta in control cells. These two FRET values observed
384 after treating cells with MG132 could be recapitulative of the dual action of this compound: a modest ATG4B
385 inhibitor keeping the biosensor in the cytosol, and a more potent proteasomal inhibitor on LC3B-positive
386 puncta. Of note, since Aqua-LC3B can efficiently localize on puncta-like structures (Fig. S5B) which display
387 high FRET (Fig. S5B, D), our data raise the possibility that MG132 does not alter the cleavage of tdLanYFP
388 from the biosensor. It is possible that the inhibition of proteasomal activity impairs the degradation of the
389 FRET acceptor, thereby allowing for non-specific FRET events. Therefore, these results underline the
390 importance of performing spatially-resolved, pixel-by-pixel FRET calculations to understand where and to
391 what extent the biosensor is active. They also highlight the poor efficacy of MG132 as an ATG4B-specific
392 inhibitor.

393 Afterwards, we explored the readout of the LC3B biosensor on commercially-available inhibitors with
394 better specificity than MG132 towards ATG4. Tioconazole, LV-320, FMK-9a, NSC 185058 (NSC) and *Z-L*-
395 Phe chloromethyl ketone (ZPCK) were evaluated in their capacity to inhibit the priming and/or deconjugation
396 activities of ATG4B [50–55]. These inhibitors have either been synthesized or identified in screening studies,
397 and they were previously shown to inhibit ATG4B and/or other ATG4 isoforms. They were also reported to
398 have a significant therapeutic potential in chemotherapy-resistant cancer subtypes with elevated levels of
399 autophagy [29,30].

400 We first measured the mean Δ Lifetime values in HeLa cells expressing the WT or the G120A
401 biosensor, and treated or not with each of the five inhibitors. Based on our previous findings in *ATG4* KO
402 cells, we expected to observe a maximized FRET response when cells are treated with the inhibitors, along
403 with the cytosolic distribution of the WT biosensor. Within our selected set of inhibitors, two of them – NSC
404 and ZPCK – were found to significantly increase mean Δ Lifetime values compared to controls (Fig. 5A vs.
405 5E, F). On the contrary, Tioconazole, LV-320 and FMK-9a did not alter the mean Δ Lifetime values of the
406 biosensor (Fig. 5A-D). However, the mean Δ Lifetime values of cells treated with NSC or ZPCK remained
407 lower than those of cells expressing the G120A biosensor. This suggests that the inhibitory effect of these
408 drugs towards ATG4B remains partial. We then asked whether the main function of NSC and ZPCK is to
409 inhibit the ATG4B-dependent deconjugation of LC3B or its priming. We observed a significant increase in
410 the number of Aqua-LC3B-II puncta structures upon treatment with NSC or ZPCK, further supporting the
411 idea that autophagy can still be triggered in the presence of these compounds and that the inhibition of ATG4B
412 priming activity is not complete (Fig. 5E, F). However, increased levels of Aqua-LC3B-II puncta structures
413 were observed in cells treated with Tioconazole, LV-320 or FMK-9a as well (Fig. 5B-D), and we found no
414 correlation between puncta numbers and mean Δ Lifetime values with any of the inhibitors (Fig. S6). These
415 findings suggest that all the tested compounds preferentially hinder the deconjugation activity of ATG4B
416 towards LC3B, which was described to be more sensitive to ATG4B inhibition than the priming activity [56].
417 In addition to deconjugation, mean Δ Lifetime differences provide the first evidence that NSC and ZPCK also
418 inhibit the priming activity of ATG4B.

419 To dissect the efficacy of the five ATG4B inhibitors with methods allowing for greater sensitivity than
420 mean Δ Lifetime, we then performed high Δ Lifetime-pixel counting and histogram analyses. The high
421 Δ Lifetime-pixel counting analyses revealed that not only NSC and ZPCK, but also FMK-9a exhibited a
422 significantly increased number of pixels with high Δ Lifetime compared to control cells (Fig. 6A-D). When
423 we analyzed the distribution of Δ Lifetime pixels on histogram analyses, we observed that approximately 10-
424 20% of pixels in cells treated with NSC or ZPCK were exhibiting G120A biosensor-like Δ Lifetime values.

425 These values were lowered in the presence of Tioconazole, LV-320 and FMK-9a, further corroborating the
426 superiority of NSC and ZPCK in inhibiting ATG4B (Fig. S7). In line with these findings, histogram analyses
427 revealed that NSC (113 psec) and ZPCK (150 psec) have the largest histogram mode value shift from that of
428 control cells (Fig. 6C, D). Interestingly, these analyses showed that FMK-9a, Tioconazole and LV-320 also
429 display a mode value shift from that of control cells, respectively of 74, 65 and 47 psec (Fig. 6B, S7B-C).
430 Therefore, this sensitive analysis method indicates a mild inhibition of the priming activity of ATG4B by
431 FMK-9a, Tioconazole and LV-320 as well, which was undetectable with the other analysis methods.
432 Furthermore, this approach substantiates the superior capacity of NSC and ZPCK in inhibiting ATG4B.

433 Since we observed the presence of high Δ Lifetime pixels with all the inhibitors, we then sought to
434 investigate the subcellular location of these pixels using line analysis. Similarly to what observed on cells
435 silenced for *ATG4B* (Fig. 2) or treated with MG132 (Fig. S5), we noticed that high Δ Lifetime pixels were
436 located either on the puncta-shaped structures, or in the surrounding area (Fig. 6 and S7). Line analyses also
437 revealed that these pixels had Δ Lifetime values comparable to those of the G120A biosensor, regardless of
438 the compound used. Taken together, these findings show that ATG4B inhibition using commercially-available
439 drugs reduces the priming rates of proLC3B at discrete sites, where unprimed LC3B reservoirs can be found
440 within or in the proximity of puncta-shaped structures.

441 Overall, our data demonstrate that the LC3B FRET biosensor is a powerful tool to evaluate the mode
442 of inhibition of ATG4B-specific compounds. We also provide an innovative methodology where individual
443 sets of microscopy data can be analyzed using three independent approaches. Cumulating the information
444 obtained by the three approaches allows to spatially localize and quantify the ATG4B-dependent priming and
445 deconjugation of LC3B with unprecedented precision, and it is mandatory to characterize the mode of action
446 of present and future ATG4B-specific inhibitors.

447

448 **Discussion**

449 In this study, we demonstrated that the LC3B biosensor is a robust tool to monitor autophagy, as it responds
450 to the priming and deconjugation activities of ATG4B on LC3B. We showed that these functions of ATG4B
451 can be followed by using one single probe with a dual readout based on FRET, and on the accumulation of
452 the probe on autophagosomes.

453 Among the several approaches available to monitor autophagy, the most widely used assays rely on
454 the use of single fluorescent protein (FP)-tagged LC3B probes to quantify the number of autophagosomes
455 [57]. The LC3B biosensor retains this property, since it functions as a standard single FP-tagged probe after
456 LC3B is primed. We also show that the biosensor reports on autophagy induction and/or inhibition while
457 colocalizing with the lysosomal marker protein LAMP2 in an autophagy-dependent manner, similarly to other
458 LC3B-based fluorescent constructs. Since the LC3B biosensor is constituted of a pair of FPs resistant to acidic
459 pH, its readout can be followed throughout the entire autophagy pathway. Importantly, the LC3B biosensor
460 has the capacity to respond to proLC3B priming in living cells, thanks to these FPs behaving as a donor-
461 acceptor FRET pair. The proLC3B priming by ATG4s is among the earliest events occurring when autophagy
462 is triggered [13,36]. A FRET-based strategy relying on a CFP/YFP donor-acceptor pair has already been used
463 to measure the enzymatic activity of ATG4A and ATG4B towards the ATG8 family in a purely *in vitro* system
464 [58]. However, this strategy has never been implemented in living cells, most likely due to the lack of yellow
465 FPs retaining their acceptor properties in conditions of acidic pH. The recent development of tdLanYFP [39]
466 allowed us to create an LC3B biosensor suitable for living cells. By following the FRET behavior of the
467 biosensor, we showed that the probe responds to the ATG4B-dependent changes in proLC3B priming. It was
468 previously reported that proLC3B is primed nearly instantaneously after translation, due to the constitutive
469 proteolytic activity of ATG4B [36,59]. In line with this, we found that the LC3B biosensor was almost
470 completely primed under basal conditions, without any detectable accumulation of proLC3B in cells. In
471 contrast, we showed that the proLC3B priming activity is altered in cells silenced for *ATG4B*, and that the

472 unprimed biosensor is located on or in close vicinity of puncta-shaped structures. Since the priming activity
473 of ATG4B is more efficient than its deconjugation activity, alterations in ATG4B levels were shown to mostly
474 affect deconjugation rather than priming [56]. Our findings using the LC3B biosensor were complementary
475 to this notion, as we were able to observe a stark increase in the number of Aqua-LC3B-II puncta structures
476 when *ATG4B* was silenced. By using a combination of broad and sensitive approaches to quantify FRET, we
477 provided the first proof of concept that proLC3B priming events occur at discrete sites in cells. It is likely that
478 these sites are already present to a lower extent under basal conditions, and they are highlighted only when
479 ATG4B priming activity is altered. With microscopy approaches with higher resolution, it might be possible
480 to reveal the existence of these reservoirs under basal conditions as well. In this light, the LC3B FRET
481 biosensor has the unique capacity to identify these priming reservoirs in living cells and with subcellular
482 resolution, underlining the superior sensitivity of the LC3B biosensor to explore the functional relevance of
483 these structures and the proteins regulating their formation.

484 Furthermore, we confirmed that the isoform ATG4B is the major cysteine protease priming the LC3B
485 biosensor, and that its knockout results in a complete lack of priming. Additionally, we provided evidence that
486 ATG4A could mildly contribute to the priming of the LC3B biosensor in the absence of ATG4B, corroborating
487 previous findings concerning a functional redundancy among these isoforms [24,60]. Interestingly, our
488 biosensor provided novel information on the relevance of specific ATG4B residues for its priming activity. In
489 this light, we observed an unexpected ability of mutant ATG4B^{W142A} to fully prime proLC3B. Trp142 localizes
490 near the catalytic Cys74 residue, and it was suggested to be responsible for LC3 tail recognition [35]. In *in*
491 *vitro* cleavage assays, ATG4B with mutated Trp142 displayed a significantly reduced ability to cleave C-
492 terminally tagged LC3 [35]. Based on these findings, we were expecting to observe a reduced LC3B priming
493 with ATG4B^{W142A}, and no priming was expected with the catalytically-dead mutant ATG4B^{C74S}. While
494 ATG4B^{C74S} was incapable of priming proLC3B, we observed a full priming of the LC3B biosensor in the
495 presence of the ATG4B^{W142A} construct. Not only these results corroborate the high efficiency of ATG4B to

496 cleave proLC3B even in conditions where its catalytic activity is severely reduced, but they also highlight a
497 drastic difference between *in vitro* findings and data obtained in more complex paradigms.

498 Given the rising interest in developing inhibitors that block the early stages of autophagy by targeting
499 ATG4B, we challenged the LC3B biosensor with a selection of available inhibitors. Again, our biosensor
500 demonstrated to be a useful tool to investigate the mode of action and the efficacy of these compounds at the
501 concentrations and timepoints chosen for the analyses. First, we observed increased amounts of Aqua-LC3B-
502 II puncta after the incubation with all the inhibitors, indicating a reduction in the deconjugation activity of
503 ATG4B. These results were not surprising, as the deconjugation activity of ATG4B was reported to be less
504 efficient than the priming, and therefore more prone to get affected upon inhibition [56]. Furthermore, our
505 data also show that none of the inhibitors was able to completely abolish the priming activity of ATG4B
506 towards LC3B. Indeed, we did not observe a cytosolic distribution of the LC3B biosensor, nor Δ Lifetime
507 values similar to those measured with the priming-defective G120A biosensor. Despite an incomplete
508 inhibition on priming, we found that the cells treated with NSC or ZPCK exhibited a significant reduction in
509 LC3B priming compared to control cells. Cells treated with MG132 – a proteasome inhibitor with a capacity
510 to inhibit cysteine proteases [48,49] – exhibited a significant increase in the mean Δ Lifetime values, along
511 with a positive shift in the histogram mode value. In contrast, they did not display significant amounts of
512 pixels with high Δ Lifetime. It is possible that the incubation with MG132 does not prevent the complete
513 degradation of tdLanYFP once this moiety has been cleaved from the biosensor. In this case, the presence of
514 tdLanYFP in the close vicinity of Aqua-LC3B-II puncta would lead to unspecific FRET events, potentially
515 unrelated to the proLC3B priming readout of the biosensor. This is the reason why a multi-parameter FRET
516 quantification – mean Δ Lifetime, number of pixels with high Δ Lifetime, histogram distribution of the
517 Δ Lifetime values – is mandatory to characterize the specificity of ATG4B inhibitors. In this light, we propose
518 that an efficient ATG4B inhibitor should display a significant difference from controls in the three methods
519 of analysis. A compound that did not meet all the criteria but still displayed a significant increase in the number
520 of high- Δ Lifetime pixels with a positive histogram mode value shift was FMK-9a. Although FMK-based

521 compounds were shown to be very potent ATG4B inhibitors [30,52,61], a recent study showed that FMK-9a
522 induces autophagy independently of its inhibition on ATG4B activity [53]. Therefore, our findings support
523 these results since FMK-9a did not meet all the criteria to be considered as an efficient ATG4B inhibitor.
524 Finally, our results on Tioconazole and LV-320 indicate that these two compounds inhibit the priming of
525 proLC3B to a lesser extent than the other compounds. Since they only displayed a positive shift in the
526 histogram mode values and did not meet any other criteria, we propose that they should be considered as mild
527 ATG4B inhibitors. Overall, our results underline the lack of inhibitors that can fully inhibit the priming activity
528 of ATG4B. Future screenings using the LC3B biosensor will be useful to identify new inhibitory compounds,
529 as one would expect to observe a FRET behavior similar to that of the G120A biosensor or *ATG4* KO cells in
530 case of a full inhibition of proLC3B priming.

531 Since it is possible to calculate the number of pixels with high Δ Lifetime, additional information can
532 be provided by localizing these pixels at the subcellular level. We observed a consistent presence of pixels
533 with high Δ Lifetime around or on puncta-shaped structures, either upon ATG4B inhibition or *ATG4B*
534 silencing. In this light, we suggest that the local scarcity or the inhibition of ATG4B may cause alterations in
535 the proLC3B priming rates in discrete areas of the autophagosomes, which could be considered as priming
536 “hotspots”. As previously mentioned, these reservoirs or “hotspots” with reduced proLC3B priming rates may
537 be sites where proLC3B is temporarily stored while trying to re-establish the full priming capacity of ATG4B.

538 Overall, we present the LC3B biosensor as a second-generation FRET biosensor that can report on the
539 regulation of the soluble and the lipidated forms of LC3B by ATG4B. First, this tool can be used to infer on
540 the structural properties of ATG4B and on its enzymatic activity. Thanks to its dual FRET/localization
541 readout, it can also be used to follow LC3B priming and turnover with superior spatiotemporal resolution.
542 Finally, the LC3B biosensor has the potential to be used in high-content screenings to identify more potent
543 ATG4B inhibitors and reveal their mode of action in living cells, which is a unique feature of the biosensor
544 compared to *in vitro* screening methodologies. Thus, the LC3B biosensor paves the way to ATG4B-targeted
545 therapies in complex diseases.

546 **Materials and Methods**

547 ***Expression vectors and molecular cloning***

548 All the plasmids used in this study are listed in Supplementary Table 1. The cloning reactions were performed
549 using the Gibson Assembly Master Mix (New England Biolabs). Site-directed mutagenesis was performed
550 with the Quik-Change kit (Agilent). All the constructs from cloning and mutagenesis reactions were verified
551 using a 3130 XL sequencer (Applied Biosystems) and a BigDye Terminator V3.1 sequencing kit (Applied
552 Biosystems).

554 ***Cell culture and transfections***

555 U2OS cells (HTB-96) were purchased from American Type Culture Collection. Control and *ATG4* KO HeLa
556 cells were kind gifts of Dr. Robin Ketteler (UCL, LMCB, United Kingdom). Cells were cultured in DMEM
557 (Thermo Fisher Scientific) supplemented with 10% FBS (Eurobio Scientific) and penicillin-streptomycin (100
558 U/mL, Thermo Fisher Scientific) and maintained at 37°C with 5% CO₂. All cell lines were routinely checked
559 for the absence of mycoplasma. Before imaging, normal growth media was replaced with phenol red-free
560 Leibovitz's L-15 medium (Thermo Fisher Scientific) supplemented with 20% FBS and penicillin-
561 streptomycin (100 U/mL). Cells were seeded at 70% confluence in Nunc Lab-Tek II Chamber slides (Thermo
562 Fisher Scientific) or Cellview cell culture slides (Greiner bio-one, 543979) for live cell imaging, 24-well plates
563 for immunocytochemistry, or 6-well plates for total cell lysates. Plasmid DNA transfection, or plasmid DNA
564 and siRNA co-transfection experiments were performed using Lipofectamine 2000 (Invitrogen) according to
565 the manufacturer's instructions. Cells were analyzed 48h after transfection. AllStars negative control siRNA
566 (SI03650318) and the *ATG4B*-specific siRNA (SI03156314) were purchased from QIAGEN.

568 ***Chemical compounds***

569 The chemical compounds used in this study were as follows: Bafilomycin A1 (Sigma-Aldrich, B1793), FMK
570 9a (MedChemExpress, HY-100522), LV-320 (MedChemExpress, HY-112711), MG-132 (Selleckchem,
571 S2619), NSC 185058 (Selleckchem, S6716), Tioconazole (Sigma-Aldrich, 03907), Torin1 (Sigma-Aldrich,
572 475991), *Z-L-Phe* chloromethyl ketone (Sigma-Aldrich, 860794). All chemical compounds were dissolved in
573 dimethyl sulfoxide (Sigma-Aldrich, D2438) and stored at -80°C. For starvation assay, a home-made Hank's
574 Balanced Salt Solution (HBSS) containing 8 mg/ml NaCl, 0.4 mg/ml KCl, 0.06 mg/ml KH₂PO₄, 0.048 mg/ml
575 Na₂HPO₄ anhydrous, 1 mg/ml glucose, 0.348 mg/ml NaHCO₃ and penicillin-streptomycin (100 U/mL) was
576 used. Concentrations and durations of each treatment are indicated in the figure legends.

577

578 ***Western blotting***

579 To collect total cell lysates, cells were rinsed with ice-cold Phosphate Buffer Saline (PBS) (Euromedex,
580 ET330-A) and lysed on ice in a buffer containing 50 mM Tris-HCL (pH 7.4), 150 mM NaCl, 1% Triton X-
581 100 (Euromedex, 2000-A), 1.5 mM MgCl₂, supplemented with 0.2 mM Na₃VO₄, 0.5 mM DTT (Thermo
582 Fisher Scientific, R0861), 4 mg/ml NaF, 5.4 mg/ml β-glycerolphosphate and a protease inhibitor cocktail
583 (Roche, 11873580001) immediately prior to lysis. Lysates were centrifuged at 13000 g for 20 minutes at 4°C.
584 Protein levels were quantified by using the Bradford protein assay dye reagent (BioRad, 5000006). Lysates
585 were then heated in Laemmli sample buffer at 95°C for 5 minutes, resolved in home-made Acrylamide/Bis
586 37.5:1 SDS-PAGE mini gels and transferred onto nitrocellulose membrane (Amersham™ Protran®,
587 10600004). Membranes were blocked in a solution containing 5% skimmed milk in TBS-T (TBS [Euromedex,
588 ET220] containing 0.1% Tween [Euromedex, 2001-B]) and incubated overnight at 4°C with primary
589 antibodies diluted in the blocking solution. The next day, membrane was washed in TBS-T, incubated with
590 the secondary antibody diluted in the blocking solution for 1h at room temperature, and washed again in TBS-
591 T prior to detection. The primary antibodies and dilutions were as follows: rabbit anti-Actin (Sigma-Aldrich,
592 A5060; 1:1000), ATG4B (Cell Signaling, 5299; 1:1000), LC3B (Cell Signaling, 3868; 1:1000). The secondary
593 antibody used was a horseradish-peroxidase-conjugated goat anti-rabbit antibody (Jackson ImmunoResearch;

1:6000-1:10000). After incubating the membrane in an ECL western blotting substrate (Thermo Fisher Scientific, 32209), chemiluminescence signals were captured on a film (Thermo Fisher Scientific, 34091) and developed with a CURIX 60 developer (Agfa Healthcare). The density of the bands was quantified by using the *Gel Analyzer* function in Fiji (NIH) software. The relative abundance of each band was calculated by normalizing the density of the band to that of the respective loading control.

Immunocytochemistry, confocal and FLIM microscopy

For immunocytochemistry, cells were seeded on 15 mm round coverslips placed onto 24-well plates. Cells were washed with 1X PBS and fixed in 1X PBS containing a mixture of 4% paraformaldehyde (Electron Microscopy Sciences, 15710) and 0.2% Glutaraldehyde (Euromedex, EM-16221) at room temperature for 20 minutes. After washing in 1X PBS, cells were permeabilized with 0.2% Triton in PBS for 10 minutes, washed again in 1X PBS and blocked for 1h in 5% BSA (Euromedex, 04-100-812-C) in 1X PBS at room temperature. Cells were incubated overnight at 4°C with primary antibodies diluted in the blocking buffer, and then washed with 1X PBS. Cells were then incubated with the secondary antibody diluted in the blocking buffer for 45 minutes at room temperature. Primary monoclonal anti-LAMP2 (Abcam, ab25631; 1:200) was used as a primary antibody and a goat anti-mouse IgG (H+L) cross-adsorbed antibody Alexa Fluor™ 647 (Thermo Fisher Scientific, A-21235; 1:500) was used as a secondary antibody. After washing in 1X PBS, coverslips were mounted in ProLong Gold Antifade reagent (Invitrogen, P36930). Cells were imaged with a Leica SP8 inverted confocal microscope equipped with a 63x oil immersion objective (NA 1.4). Aquamarine fluorescence was acquired with a 440 nm excitation laser, and an emission wavelength of 467-499 nm. The fluorescence of tdLanYFP and of LAMP2/Alexa 647 were captured by using a 514 nm and a 633 nm argon laser, respectively. The emission wavelengths were 525-565 nm for tdLanYFP, and 650-720 nm for LAMP2/Alexa 647. For FLIM analyses, images were acquired with a time-gated custom-made setup based on a spinning disk microscope as described in [62]. Aquamarine was used as a FRET donor in all experiments, and excited at 440 ± 10 nm with a supercontinuum picosecond pulsed laser source. Emission was selected

619 using a band pass filter of 483/35 nm. The FLIM setup was controlled by the Inscoper Suite solution (Inscoper,
620 France), and Aquamarine lifetime was measured in real-time during acquisition with the Inscoper software.

621 622 ***Image analysis***

623 All the image analysis were performed in Fiji software. 3D puncta counting and fluorescence colocalization
624 analyses illustrated in Fig. 1B-D and Fig. S1 were performed by using the macro developed by Cordelières
625 and Zhang [63] in batch processing mode, and available in a GitHub repository at
626 <https://github.com/NEUBIAS/neubias-springer-book-2020>. The minimum size of the objects for Aquamarine-
627 LC3B and LAMP2/Alexa 647 was set to 10 voxels. The threshold to separate the objects from the background
628 was set manually for both channels. The total number of objects in Aquamarine-LC3B channel was used to
629 determine the number of Aqua-LC3B-II puncta-shaped structures. The objects in the Aquamarine-LC3B
630 channel superposing with the LAMP2/Alexa 647 objects were used for colocalization analyses, and only the
631 Aquamarine-LC3B objects superposing with the LAMP2/Alexa 647 objects with a ratio of 0.5 or more were
632 quantified for analyses. The colocalizing objects were then normalized to the total number of Aquamarine-
633 LC3B objects. For FLIM analysis, mean Δ Lifetime values were calculated as previously described [38]. In all
634 experiments, Aquamarine lifetime was calculated by the Inscoper software only when the pixel-by-pixel
635 fluorescence intensity in the first gate was above 1000 grey levels. The number of Aqua-LC3B-II puncta
636 structures in the accompanying fluorescence images (Fig. 2A, S2A, 5A-F, S5A-B) were quantified using the
637 *Find Maxima* function in the Fiji imaging software, and by setting the prominence value as 1500. To analyze
638 the high- Δ Lifetime pixels, the *Histogram* tool in Fiji was used to measure the number of pixels with a lifetime
639 between 2000 and 4000 psec. Each histogram was then converted to a Δ Lifetime format by using the mean
640 lifetime value of the donor-only construct as a normalizer. To determine the number of pixels with high
641 Δ Lifetime, the mean Δ Lifetime value of the G120A biosensor or the mean Δ Lifetime value of the WT
642 biosensor expressed in *ATG4B* SKO cells were used as a threshold. The number of pixels showing G120A
643 biosensor-like Δ Lifetime or higher were then quantified and normalized to the total number of pixels, and this

644 to determine the high- Δ Lifetime pixel ratio per cell. For line analysis, a 17.8 μm linear region of interest (ROI)
645 that contains both the high- and low- Δ Lifetime pixels was manually drawn near or on the puncta-like
646 structures. The *Plot profile* function in Fiji was then used to obtain Δ Lifetime values on the drawn line, which
647 were then plotted. For histogram analyses, the average number of pixels per Δ Lifetime was quantified for each
648 condition.

650 ***Statistical analysis***

651 All statistical tests were performed by using GraphPad Prism 9. Two-way ANOVA with Tukey method was
652 applied to make multiple comparisons in the following figures: 1C-D; 2B-C, F; 3B-C; 4B-C; 5B-F; 6B-D;
653 S2B, F; S4A-B; S5B; S7B-C. Two-way ANOVA with two-stage step-up method of Benjamini, Krieger and
654 Yekutieli was applied to make multiple comparisons in the following figures: 1F-G and S2D. Correlation
655 analysis between the Δ Lifetime values and the puncta numbers were performed to compute R^2 and P values
656 in Fig. S6.

658 ***Figure preparation***

659 The cartoon in Figure 1A was prepared by using the illustrations available at <https://smart.servier.com/> [64].
660 Graphs and figures were assembled in GraphPad Prism 9 and Inkscape, respectively.

662 ***Data and material availability***

663 Plasmids and macro used in this study and the source data that support the findings are available from the
664 corresponding authors (G.B. [giulia.bertolin@univ-rennes1.fr] and M.T. [marc.tramier@univ-rennes1.fr]) on
665 request.

667 **Acknowledgments**

668 We thank P. Govindin (MetaGenoPolis, INRAe, Jouy-en-Josas, France) for preliminary experiments with the
669 LC3B biosensor, S. Dutertre and X. Pinson at the Microscopy Rennes Imaging Center (MRic, *Biologie, Santé,*
670 *Innovation Technologique* - BIOSIT, Rennes, France) and G. Le Marchand (IGDR, Rennes, France) for help
671 and assistance. MRic is member of the national infrastructure France-BioImaging supported by the French
672 National Research Agency (ANR-10-INBS-04). We also thank R. Ketteler (UCL, LMCB, United Kingdom)
673 for sharing pGEX GST-ATG4B plasmid and *ATG4* KO HeLa cells. We are grateful to S. Ley-Ngardigal, R.
674 Smith, C. Chapuis and S. Zentout for technical assistance with the experiments, and Ç. Tuna for help with the
675 image analysis. This work was supported by the *Centre National de la Recherche Scientifique* (CNRS), the
676 University of Rennes 1, the *Ligue Contre le Cancer Comité d'Ille et Vilaine et du Finistère* and the *Association*
677 *pour la Recherche sur le Cancer* (ARC) to G.B., and by the *Institut National du Cancer* (INCa) and *ITMO*
678 *Cancer/Aviesan* to M.T. E.B.G. was supported by a fellowship from the *Ligue Contre le Cancer* and *Région*
679 *Bretagne* (Brittany region, France).

681 **Author Contributions**

682 E.B.G. designed, performed and analyzed the experiments and wrote the manuscript; A.C. performed the
683 experiments and revised the manuscript, M.T. co-supervised the work, revised the manuscript and provided
684 funding; G.B. co-supervised the work, designed the experiments, edited and revised the manuscript, and
685 provided funding.

687 **Conflict of interest**

688 The authors declare no conflict of interest.

690 **References**

- 691 1. Ohsumi, Y. Historical Landmarks of Autophagy Research. *Cell Research* **2014**, *24*, 9–23,
692 doi:10.1038/cr.2013.169.
- 693 2. Klionsky, D.J.; Emr, S.D. Autophagy as a Regulated Pathway of Cellular Degradation. *Science* **2000**,
694 *290*, 1717–1721, doi:10.1126/science.290.5497.1717.
- 695 3. Deretic, V.; Levine, B. Autophagy, Immunity, and Microbial Adaptations. *Cell Host & Microbe* **2009**,
696 *5*, 527–549, doi:10.1016/j.chom.2009.05.016.
- 697 4. Rodriguez-Rocha, H.; Garcia-Garcia, A.; Panayiotidis, M.I.; Franco, R. DNA Damage and Autophagy.
698 *Mutation Research/Fundamental and Molecular Mechanisms of Mutagenesis* **2011**, *711*, 158–166,
699 doi:10.1016/j.mrfmmm.2011.03.007.
- 700 5. Axe, E.L.; Walker, S.A.; Manifava, M.; Chandra, P.; Roderick, H.L.; Habermann, A.; Griffiths, G.;
701 Ktistakis, N.T. Autophagosome Formation from Membrane Compartments Enriched in
702 Phosphatidylinositol 3-Phosphate and Dynamically Connected to the Endoplasmic Reticulum. *J Cell*
703 *Biol* **2008**, *182*, 685–701, doi:10.1083/jcb.200803137.
- 704 6. Mizushima, N.; Yoshimori, T.; Ohsumi, Y. The Role of Atg Proteins in Autophagosome Formation.
705 *Annu Rev Cell Dev Biol* **2011**, *27*, 107–132, doi:10.1146/annurev-cellbio-092910-154005.
- 706 7. Ichimura, Y.; Kirisako, T.; Takao, T.; Satomi, Y.; Shimonishi, Y.; Ishihara, N.; Mizushima, N.; Tanida,
707 I.; Kominami, E.; Ohsumi, M.; et al. A Ubiquitin-like System Mediates Protein Lipidation. *Nature* **2000**,
708 *408*, 488–492, doi:10.1038/35044114.
- 709 8. Weidberg, H.; Shvets, E.; Shpilka, T.; Shimron, F.; Shinder, V.; Elazar, Z. LC3 and GATE-
710 16/GABARAP Subfamilies Are Both Essential yet Act Differently in Autophagosome Biogenesis. *The*
711 *EMBO Journal* **2010**, *29*, 1792–1802, doi:10.1038/emboj.2010.74.
- 712 9. Noda, N.N.; Ohsumi, Y.; Inagaki, F. Atg8-Family Interacting Motif Crucial for Selective Autophagy.
713 *FEBS Letters* **2010**, *584*, 1379–1385, doi:10.1016/j.febslet.2010.01.018.

- 714 10. Shpilka, T.; Weidberg, H.; Pietrokovski, S.; Elazar, Z. Atg8: An Autophagy-Related Ubiquitin-like
715 Protein Family. *Genome Biology* **2011**, *12*, 226, doi:10.1186/gb-2011-12-7-226.
- 716 11. Jatana, N.; Ascher, D.B.; Pires, D.E.V.; Gokhale, R.S.; Thukral, L. Human LC3 and GABARAP
717 Subfamily Members Achieve Functional Specificity via Specific Structural Modulations. *Autophagy*
718 **2020**, *16*, 239–255, doi:10.1080/15548627.2019.1606636.
- 719 12. Kirisako, T.; Ichimura, Y.; Okada, H.; Kabeya, Y.; Mizushima, N.; Yoshimori, T.; Ohsumi, M.; Takao,
720 T.; Noda, T.; Ohsumi, Y. The Reversible Modification Regulates the Membrane-Binding State of
721 Apg8/Aut7 Essential for Autophagy and the Cytoplasm to Vacuole Targeting Pathway. *J Cell Biol* **2000**,
722 *151*, 263–276, doi:10.1083/jcb.151.2.263.
- 723 13. Tanida, I.; Sou, Y.; Ezaki, J.; Minematsu-Ikeguchi, N.; Ueno, T.; Kominami, E.
724 HsAtg4B/HsApg4B/Autophagin-1 Cleaves the Carboxyl Termini of Three Human Atg8 Homologues
725 and Delipidates Microtubule-Associated Protein Light Chain 3- and GABAA Receptor-Associated
726 Protein-Phospholipid Conjugates. *J Biol Chem* **2004**, *279*, 36268–36276, doi:10.1074/jbc.M401461200.
- 727 14. Kabeya, Y.; Mizushima, N.; Yamamoto, A.; Oshitani-Okamoto, S.; Ohsumi, Y.; Yoshimori, T. LC3,
728 GABARAP and GATE16 Localize to Autophagosomal Membrane Depending on Form-II Formation.
729 *Journal of Cell Science* **2004**, *117*, 2805–2812, doi:10.1242/jcs.01131.
- 730 15. Hanada, T.; Noda, N.N.; Satomi, Y.; Ichimura, Y.; Fujioka, Y.; Takao, T.; Inagaki, F.; Ohsumi, Y. The
731 Atg12-Atg5 Conjugate Has a Novel E3-like Activity for Protein Lipidation in Autophagy. *J Biol Chem*
732 **2007**, *282*, 37298–37302, doi:10.1074/jbc.C700195200.
- 733 16. Martens, S.; Fracchiolla, D. Activation and Targeting of ATG8 Protein Lipidation. *Cell Discov* **2020**, *6*,
734 1–11, doi:10.1038/s41421-020-0155-1.
- 735 17. Nakatogawa, H.; Ichimura, Y.; Ohsumi, Y. Atg8, a Ubiquitin-like Protein Required for Autophagosome
736 Formation, Mediates Membrane Tethering and Hemifusion. *Cell* **2007**, *130*, 165–178,
737 doi:10.1016/j.cell.2007.05.021.

- 738 18. Xie, Z.; Nair, U.; Klionsky, D.J. Atg8 Controls Phagophore Expansion during Autophagosome
739 Formation. *Mol Biol Cell* **2008**, *19*, 3290–3298, doi:10.1091/mbc.E07-12-1292.
- 740 19. Pankiv, S.; Clausen, T.H.; Lamark, T.; Brech, A.; Bruun, J.-A.; Outzen, H.; Øvervatn, A.; Bjørkøy, G.;
741 Johansen, T. P62/SQSTM1 Binds Directly to Atg8/LC3 to Facilitate Degradation of Ubiquitinated
742 Protein Aggregates by Autophagy. *J Biol Chem* **2007**, *282*, 24131–24145, doi:10.1074/jbc.M702824200.
- 743 20. Mizushima, N. The ATG Conjugation Systems in Autophagy. *Current Opinion in Cell Biology* **2020**,
744 *63*, 1–10, doi:10.1016/j.ceb.2019.12.001.
- 745 21. Nair, U.; Yen, W.-L.; Mari, M.; Cao, Y.; Xie, Z.; Baba, M.; Reggiori, F.; Klionsky, D.J. A Role for
746 Atg8–PE Deconjugation in Autophagosome Biogenesis. *Autophagy* **2012**, *8*, 780–793,
747 doi:10.4161/auto.19385.
- 748 22. Nakatogawa, H.; Ishii, J.; Asai, E.; Ohsumi, Y. Atg4 Recycles Inappropriately Lipidated Atg8 to Promote
749 Autophagosome Biogenesis. *Autophagy* **2012**, *8*, 177–186, doi:10.4161/auto.8.2.18373.
- 750 23. Yu, Z.-Q.; Ni, T.; Hong, B.; Wang, H.-Y.; Jiang, F.-J.; Zou, S.; Chen, Y.; Zheng, X.-L.; Klionsky, D.J.;
751 Liang, Y.; et al. Dual Roles of Atg8–PE Deconjugation by Atg4 in Autophagy. *Autophagy* **2012**, *8*, 883–
752 892, doi:10.4161/auto.19652.
- 753 24. Agrotis, A.; Pengo, N.; Burden, J.J.; Ketteler, R. Redundancy of Human ATG4 Protease Isoforms in
754 Autophagy and LC3/GABARAP Processing Revealed in Cells. *Autophagy* **2019**, *15*, 976–997,
755 doi:10.1080/15548627.2019.1569925.
- 756 25. Nguyen, T.N.; Padman, B.S.; Zellner, S.; Khuu, G.; Uoselis, L.; Lam, W.K.; Skulsuppaisarn, M.;
757 Lindblom, R.S.J.; Watts, E.M.; Behrends, C.; et al. ATG4 Family Proteins Drive Phagophore Growth
758 Independently of the LC3/GABARAP Lipidation System. *Mol Cell* **2021**, *81*, 2013-2030.e9,
759 doi:10.1016/j.molcel.2021.03.001.
- 760 26. Betin, V.M.S.; Singleton, B.K.; Parsons, S.F.; Anstee, D.J.; Lane, J.D. Autophagy Facilitates Organelle
761 Clearance during Differentiation of Human Erythroblasts: Evidence for a Role for ATG4 Paralogs during
762 Autophagosome Maturation. *Autophagy* **2013**, *9*, 881–893, doi:10.4161/auto.24172.

- 763 27. Levine, B.; Kroemer, G. Biological Functions of Autophagy Genes: A Disease Perspective. *Cell* **2019**,
764 176, 11–42, doi:10.1016/j.cell.2018.09.048.
- 765 28. Galluzzi, L.; Bravo-San Pedro, J.M.; Levine, B.; Green, D.R.; Kroemer, G. Pharmacological Modulation
766 of Autophagy: Therapeutic Potential and Persisting Obstacles. *Nature Reviews Drug Discovery* **2017**,
767 16, 487–511, doi:10.1038/nrd.2017.22.
- 768 29. Ariosa, A.R.; Lahiri, V.; Lei, Y.; Yang, Y.; Yin, Z.; Zhang, Z.; Klionsky, D.J. A Perspective on the Role
769 of Autophagy in Cancer. *Biochimica et Biophysica Acta (BBA) - Molecular Basis of Disease* **2021**, 1867,
770 166262, doi:10.1016/j.bbadis.2021.166262.
- 771 30. Agrotis, A.; Ketteler, R. On ATG4B as Drug Target for Treatment of Solid Tumours-The Knowns and
772 the Unknowns. *Cells* **2019**, 9, E53, doi:10.3390/cells9010053.
- 773 31. *Principles of Fluorescence Spectroscopy*;
- 774 32. Truong, K.; Ikura, M. The Use of FRET Imaging Microscopy to Detect Protein–Protein Interactions and
775 Protein Conformational Changes in Vivo. *Current Opinion in Structural Biology* **2001**, 11, 573–578,
776 doi:10.1016/S0959-440X(00)00249-9.
- 777 33. Sizaire, F.; Tramier, M. FRET-Based Biosensors: Genetically Encoded Tools to Track Kinase Activity
778 in Living Cells. *Protein Phosphorylation* **2017**, doi:10.5772/intechopen.71005.
- 779 34. Padilla-Parra, S.; Tramier, M. FRET Microscopy in the Living Cell: Different Approaches, Strengths
780 and Weaknesses. *Truong & Ikura* **2012**, 34, 369–376, doi:10.1002/bies.201100086.
- 781 35. Sugawara, K.; Suzuki, N.N.; Fujioka, Y.; Mizushima, N.; Ohsumi, Y.; Inagaki, F. Structural Basis for
782 the Specificity and Catalysis of Human Atg4B Responsible for Mammalian Autophagy. *J Biol Chem*
783 **2005**, 280, 40058–40065, doi:10.1074/jbc.M509158200.
- 784 36. Kabeya, Y.; Mizushima, N.; Ueno, T.; Yamamoto, A.; Kirisako, T.; Noda, T.; Kominami, E.; Ohsumi,
785 Y.; Yoshimori, T. LC3, a Mammalian Homologue of Yeast Apg8p, Is Localized in Autophagosome
786 Membranes after Processing. *EMBO J* **2000**, 19, 5720–5728, doi:10.1093/emboj/19.21.5720.

- 787 37. Erard, M.; Fredj, A.; Pasquier, H.; Beltolngar, D.-B.; Bousmah, Y.; Derrien, V.; Vincent, P.; Merola, F.
788 Minimum Set of Mutations Needed to Optimize Cyan Fluorescent Proteins for Live Cell Imaging. *Mol.*
789 *BioSyst.* **2013**, *9*, 258–267, doi:10.1039/C2MB25303H.
- 790 38. Bertolin, G.; Sizaire, F.; Déméautis, C.; Chapuis, C.; Mérola, F.; Erard, M.; Tramier, M. Optimized
791 FRET Pairs and Quantification Approaches To Detect the Activation of Aurora Kinase A at Mitosis.
792 *ACS Sens* **2019**, *4*, 2018–2027, doi:10.1021/acssensors.9b00486.
- 793 39. Bousmah, Y.; Valenta, H.; Bertolin, G.; Singh, U.; Nicolas, V.; Pasquier, H.; Tramier, M.; Merola, F.;
794 Erard, M. TdLanYFP, a Yellow, Bright, Photostable, and PH-Insensitive Fluorescent Protein for Live-
795 Cell Imaging and Förster Resonance Energy Transfer-Based Sensing Strategies. *ACS Sens* **2021**, *6*,
796 3940–3947, doi:10.1021/acssensors.1c00874.
- 797 40. Tanida, I.; Minematsu-Ikeguchi, N.; Ueno, T.; Kominami, E. Lysosomal Turnover, but Not a Cellular
798 Level, of Endogenous LC3 Is a Marker for Autophagy. *Autophagy* **2005**, *1*, 84–91,
799 doi:10.4161/auto.1.2.1697.
- 800 41. Nash, Y.; Schmukler, E.; Trudler, D.; Pinkas-Kramarski, R.; Frenkel, D. DJ-1 Deficiency Impairs
801 Autophagy and Reduces Alpha-Synuclein Phagocytosis by Microglia. *J Neurochem* **2017**, *143*, 584–594,
802 doi:10.1111/jnc.14222.
- 803 42. Li, M.; Hou, Y.; Wang, J.; Chen, X.; Shao, Z.-M.; Yin, X.-M. Kinetics Comparisons of Mammalian Atg4
804 Homologues Indicate Selective Preferences toward Diverse Atg8 Substrates. *J Biol Chem* **2011**, *286*,
805 7327–7338, doi:10.1074/jbc.M110.199059.
- 806 43. Agrotis, A.; von Chamier, L.; Oliver, H.; Kiso, K.; Singh, T.; Ketteler, R. Human ATG4 Autophagy
807 Proteases Counteract Attachment of Ubiquitin-like LC3/GABARAP Proteins to Other Cellular Proteins.
808 *Journal of Biological Chemistry* **2019**, *294*, 12610–12621, doi:10.1074/jbc.AC119.009977.
- 809 44. Wang, W.; Chen, Z.; Billiar, T.R.; Stang, M.T.; Gao, W. The Carboxyl-Terminal Amino Acids Render
810 Pro-Human LC3B Migration Similar to Lipidated LC3B in SDS-PAGE. *PLOS ONE* **2013**, *8*, e74222,
811 doi:10.1371/journal.pone.0074222.

- 812 45. Li, M. Kinetics Comparisons of Mammalian Atg4 Homologues Indicate Selective Preferences toward
813 Diverse Atg8 Substrates*. **2011**, 286, 12.
- 814 46. Fujita, N.; Hayashi-Nishino, M.; Fukumoto, H.; Omori, H.; Yamamoto, A.; Noda, T.; Yoshimori, T. An
815 Atg4B Mutant Hampers the Lipidation of LC3 Paralogues and Causes Defects in Autophagosome
816 Closure. *Mol Biol Cell* **2008**, 19, 4651–4659, doi:10.1091/mbc.e08-03-0312.
- 817 47. Skytte Rasmussen, M.; Mouilleron, S.; Kumar Shrestha, B.; Wirth, M.; Lee, R.; Bowitz Larsen, K.;
818 Abudu Princely, Y.; O'Reilly, N.; Sjøttem, E.; Tooze, S.A.; et al. ATG4B Contains a C-Terminal LIR
819 Motif Important for Binding and Efficient Cleavage of Mammalian Orthologs of Yeast Atg8. *Autophagy*
820 **2017**, 13, 834–853, doi:10.1080/15548627.2017.1287651.
- 821 48. Steinhilb, M.L.; Turner, R.S.; Gaut, J.R. The Protease Inhibitor, MG132, Blocks Maturation of the
822 Amyloid Precursor Protein Swedish Mutant Preventing Cleavage by Beta-Secretase. *J Biol Chem* **2001**,
823 276, 4476–4484, doi:10.1074/jbc.M008793200.
- 824 49. Harer, S.L.; Bhatia, M.S.; Bhatia, N.M. Proteasome Inhibitors Mechanism; Source for Design of Newer
825 Therapeutic Agents. *J Antibiot* **2012**, 65, 279–288, doi:10.1038/ja.2011.84.
- 826 50. Liu, P.-F.; Tsai, K.-L.; Hsu, C.-J.; Tsai, W.-L.; Cheng, J.-S.; Chang, H.-W.; Shiao, C.-W.; Goan, Y.-G.;
827 Tseng, H.-H.; Wu, C.-H.; et al. Drug Repurposing Screening Identifies Tioconazole as an ATG4 Inhibitor
828 That Suppresses Autophagy and Sensitizes Cancer Cells to Chemotherapy. *Theranostics* **2018**, 8, 830–
829 845, doi:10.7150/thno.22012.
- 830 51. Bosc, D.; Vezenkov, L.; Bortnik, S.; An, J.; Xu, J.; Choutka, C.; Hannigan, A.M.; Kovacic, S.; Loo, S.;
831 Clark, P.G.K.; et al. A New Quinoline-Based Chemical Probe Inhibits the Autophagy-Related Cysteine
832 Protease ATG4B. *Sci Rep* **2018**, 8, 11653, doi:10.1038/s41598-018-29900-x.
- 833 52. Qiu, Z.; Kuhn, B.; Aebi, J.; Lin, X.; Ding, H.; Zhou, Z.; Xu, Z.; Xu, D.; Han, L.; Liu, C.; et al. Discovery
834 of Fluoromethylketone-Based Peptidomimetics as Covalent ATG4B (Autophagin-1) Inhibitors
835 Available online: <https://pubs.acs.org/doi/pdf/10.1021/acsmchemlett.6b00208> (accessed on 5 April
836 2022).

- 837 53. Chu, J.; Fu, Y.; Xu, J.; Zheng, X.; Gu, Q.; Luo, X.; Dai, Q.; Zhang, S.; Liu, P.; Hong, L.; et al. ATG4B
838 Inhibitor FMK-9a Induces Autophagy Independent on Its Enzyme Inhibition. *Arch Biochem Biophys*
839 **2018**, *644*, 29–36, doi:10.1016/j.abb.2018.03.001.
- 840 54. Akin, D.; Wang, S.K.; Habibzadegah-Tari, P.; Law, B.; Ostrov, D.; Li, M.; Yin, X.-M.; Kim, J.-S.;
841 Horenstein, N.; Dunn, W.A. A Novel ATG4B Antagonist Inhibits Autophagy and Has a Negative Impact
842 on Osteosarcoma Tumors. *Autophagy* **2014**, *10*, 2021–2035, doi:10.4161/auto.32229.
- 843 55. Nguyen, T.G.; Honson, N.S.; Arns, S.; Davis, T.L.; Dhe-Paganon, S.; Kovacic, S.; Kumar, N.S.; Pfeifer,
844 T.A.; Young, R.N. Development of Fluorescent Substrates and Assays for the Key Autophagy-Related
845 Cysteine Protease Enzyme, ATG4B. *Assay Drug Dev Technol* **2014**, *12*, 176–189,
846 doi:10.1089/adt.2013.561.
- 847 56. Kauffman, K.J.; Yu, S.; Jin, J.; Mugo, B.; Nguyen, N.; O'Brien, A.; Nag, S.; Lystad, A.H.; Melia, T.J.
848 Delipidation of Mammalian Atg8-Family Proteins by Each of the Four ATG4 Proteases. *Autophagy*
849 **2018**, *14*, 992–1010, doi:10.1080/15548627.2018.1437341.
- 850 57. Klionsky, D.J.; Abdel-Aziz, A.K.; Abdelfatah, S.; Abdellatif, M.; Abdoli, A.; Abel, S.; Abeliovich, H.;
851 Abildgaard, M.H.; Abudu, Y.P.; Acevedo-Arozena, A.; et al. Guidelines for the Use and Interpretation
852 of Assays for Monitoring Autophagy (4th Edition). *null* **2021**, 1–382,
853 doi:10.1080/15548627.2020.1797280.
- 854 58. Li, M.; Chen, X.; Ye, Q.-Z.; Vogt, A.; Yin, X.-M. A High-Throughput FRET-Based Assay for
855 Determination of Atg4 Activity. *Autophagy* **2012**, *8*, 401–412, doi:10.4161/auto.18777.
- 856 59. Scherz-Shouval, R.; Shvets, E.; Fass, E.; Shorer, H.; Gil, L.; Elazar, Z. Reactive Oxygen Species Are
857 Essential for Autophagy and Specifically Regulate the Activity of Atg4. *EMBO J* **2007**, *26*, 1749–1760,
858 doi:10.1038/sj.emboj.7601623.
- 859 60. Nguyen, N.; Olivas, T.J.; Mires, A.; Jin, J.; Yu, S.; Luan, L.; Nag, S.; Kauffman, K.J.; Melia, T.J. The
860 Insufficiency of ATG4A in Macroautophagy. *Journal of Biological Chemistry* **2020**, *295*, 13584–13600,
861 doi:10.1074/jbc.RA120.013897.

- 862 61. Xu, D.; Xu, Z.; Han, L.; Liu, C.; Zhou, Z.; Qiu, Z.; Lin, X.; Tang, G.; Shen, H.; Aebi, J.; et al.
863 Identification of New ATG4B Inhibitors Based on a Novel High-Throughput Screening Platform. *SLAS*
864 *Discov* **2017**, *22*, 338–347, doi:10.1177/1087057116639202.
- 865 62. Bertolin, G.; Sizaire, F.; Herbomel, G.; Rebutier, D.; Prigent, C.; Tramier, M. A FRET Biosensor
866 Reveals Spatiotemporal Activation and Functions of Aurora Kinase A in Living Cells. *Nat Commun*
867 **2016**, *7*, 12674, doi:10.1038/ncomms12674.
- 868 63. Cordelières, F.P.; Zhang, C. 3D Quantitative Colocalisation Analysis. In *Bioimage Data Analysis*
869 *Workflows*; Miura, K., Sladoje, N., Eds.; Learning Materials in Biosciences; Springer International
870 Publishing: Cham, 2020; pp. 33–66 ISBN 978-3-030-22386-1.
- 871 64. SMART Available online: <https://smart.servier.com/> (accessed on 3 May 2022).
- 872

The LC3B FRET biosensor monitors the modes of action of ATG4B during autophagy in living cells

Elif Begüm Gökerküçük et al.

Main figures

Figure 1

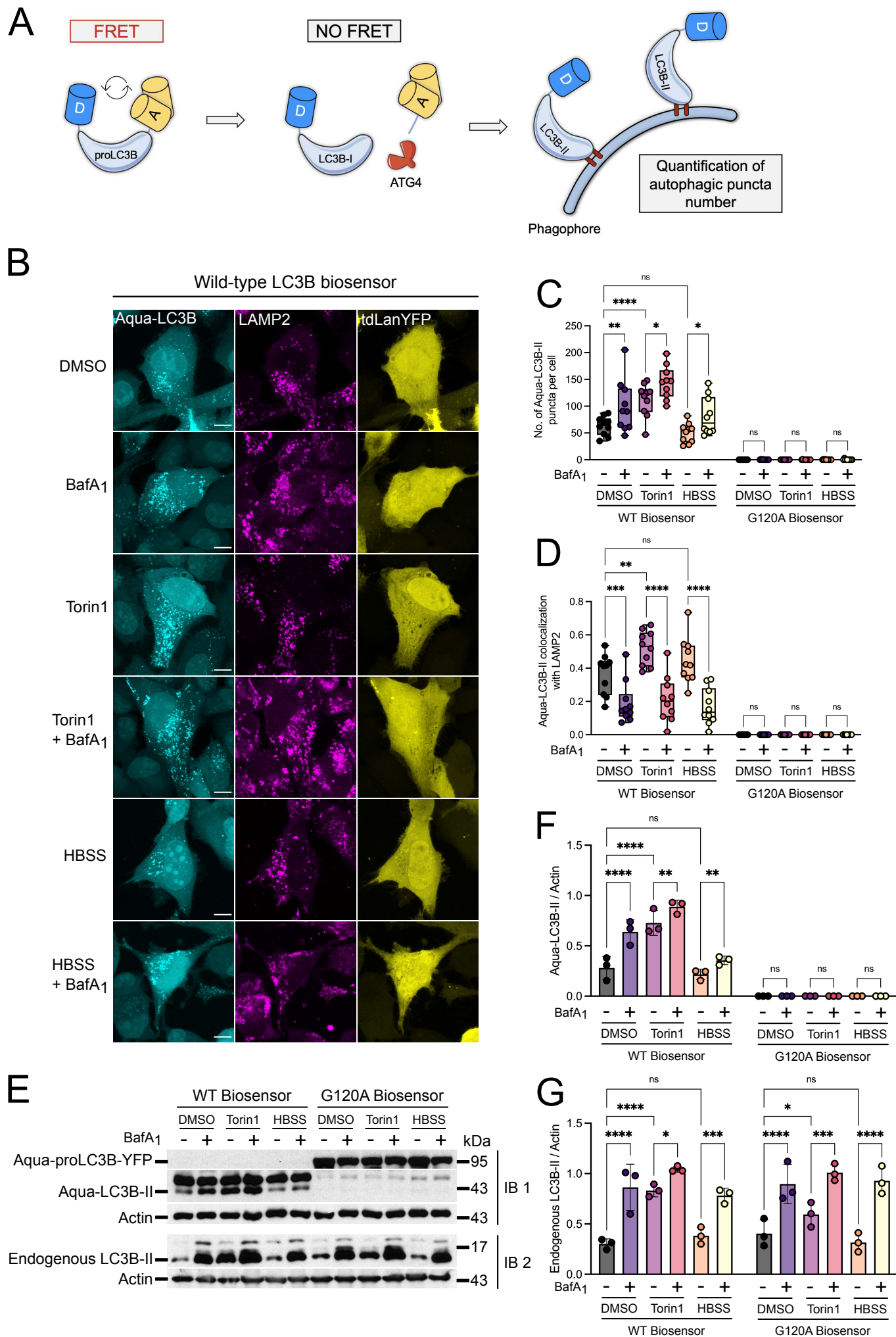


Figure 1. The LC3B biosensor reports on autophagy induction and/or lysosomal inhibition, and colocalizes with LAMP2 in an autophagy-dependent manner. (A) The cartoon illustrates the design and the mode of action of the LC3B biosensor. The biosensor was designed to flank the N- and C- termini of proLC3B with a donor (D, Aquamarine)-acceptor (A, tdLanYFP) FRET pair. When ATG4 is not active, the biosensor is expected to remain unprocessed in cells, allowing Aquamarine and tdLanYFP to perform FRET. Upon the proteolytic activity of ATG4, the biosensor is expected to be cleaved at its C-terminus, in turn losing its tdLanYFP moiety and the FRET effect with it. A successful priming of the biosensor is expected to yield Aquamarine-LC3B-I, which can then be integrated into the PE head groups of the phagophores and observed as puncta-shaped structures. The resulting Aquamarine-LC3B-II puncta-shaped structures can then be quantified to estimate the number of autophagosomes. (B) Representative fluorescence images of U2OS cells expressing the WT biosensor and stained for endogenous LAMP2. To investigate the changes in Aqua-LC3B puncta numbers and their colocalization with LAMP2, cells were treated with the following compounds: DMSO (6h), BafA₁ (6h, 100 nM), Torin1 (3h, 250 nM), Torin1 (3h, 250 nM) + BafA₁ (6h, 100 nM), HBSS (1h), HBSS (1h) + BafA₁ (6h, 100 nM). Scale bar: 9 μm. (C) Quantification of the number of Aqua-LC3B-II puncta in cells expressing the WT or G120A biosensor and treated as indicated. (D) Quantification of the ratio of Aqua-LC3B-II puncta structures colocalizing with LAMP2-positive objects in cells expressing the WT or G120A biosensor and treated as indicated. *n* = 10 cells per condition from one representative experiment (of three) in (C) and (D). (E) Representative western blotting images and corresponding quantifications (F, G) of total lysates from U2OS cells expressing the WT or G120A biosensor and treated as indicated. IB1 and IB2 correspond to the same lysates blotted for overexpressed (IB1) or endogenous (IB2) LC3B forms. Loading control: Actin. *n* = 3 independent experiments **P* < 0.05, ***P* < 0.01, ****P* < 0.001, *****P* < 0.0001, ns (not significant) as determined by two-way ANOVA with Tukey's multiple comparison test in (C) and (D), and with two-stage step-up method of Benjamini, Krieger and Yekutieli's multiple comparison test to control the false discovery rate in (F) and (G).

Figure 2

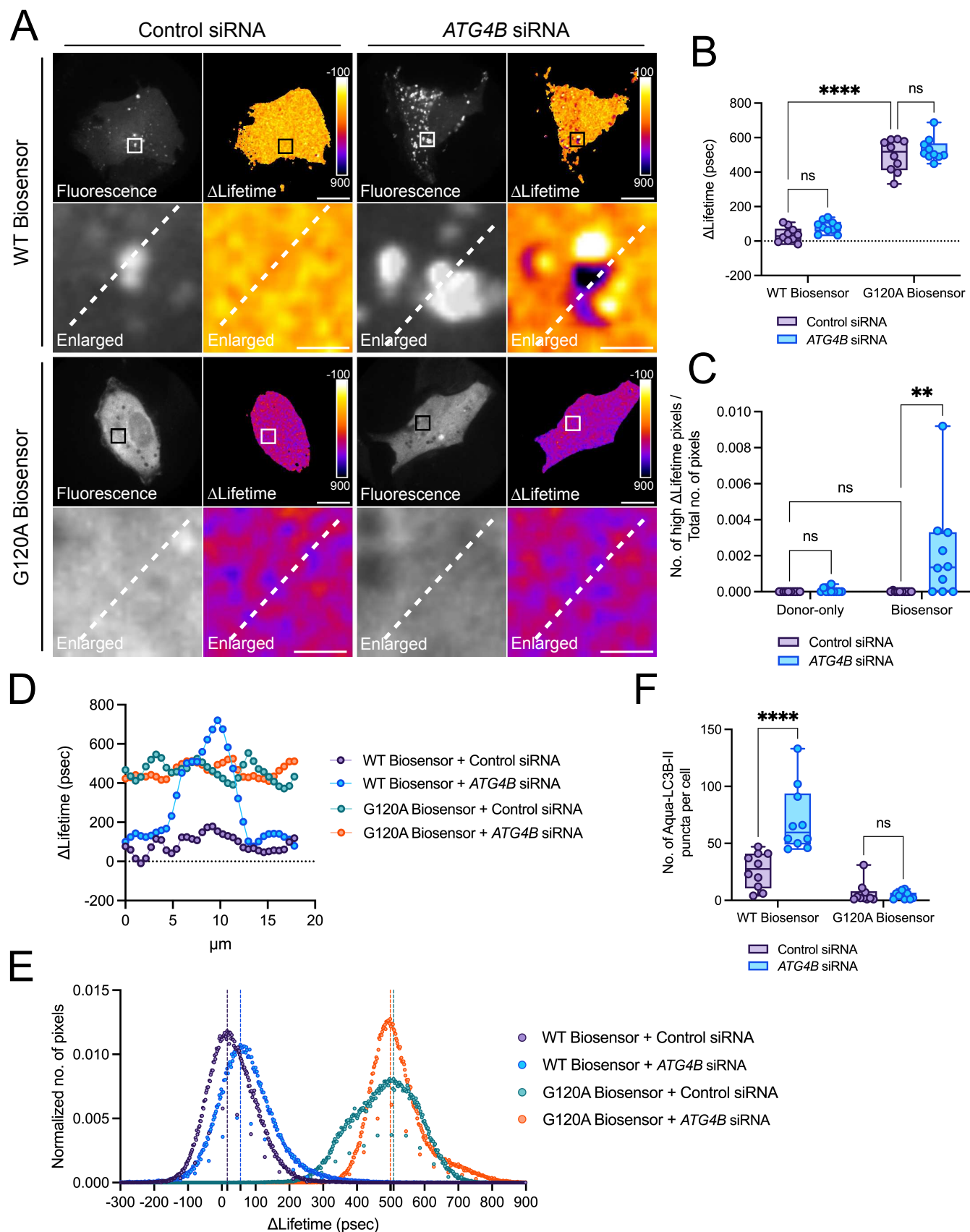
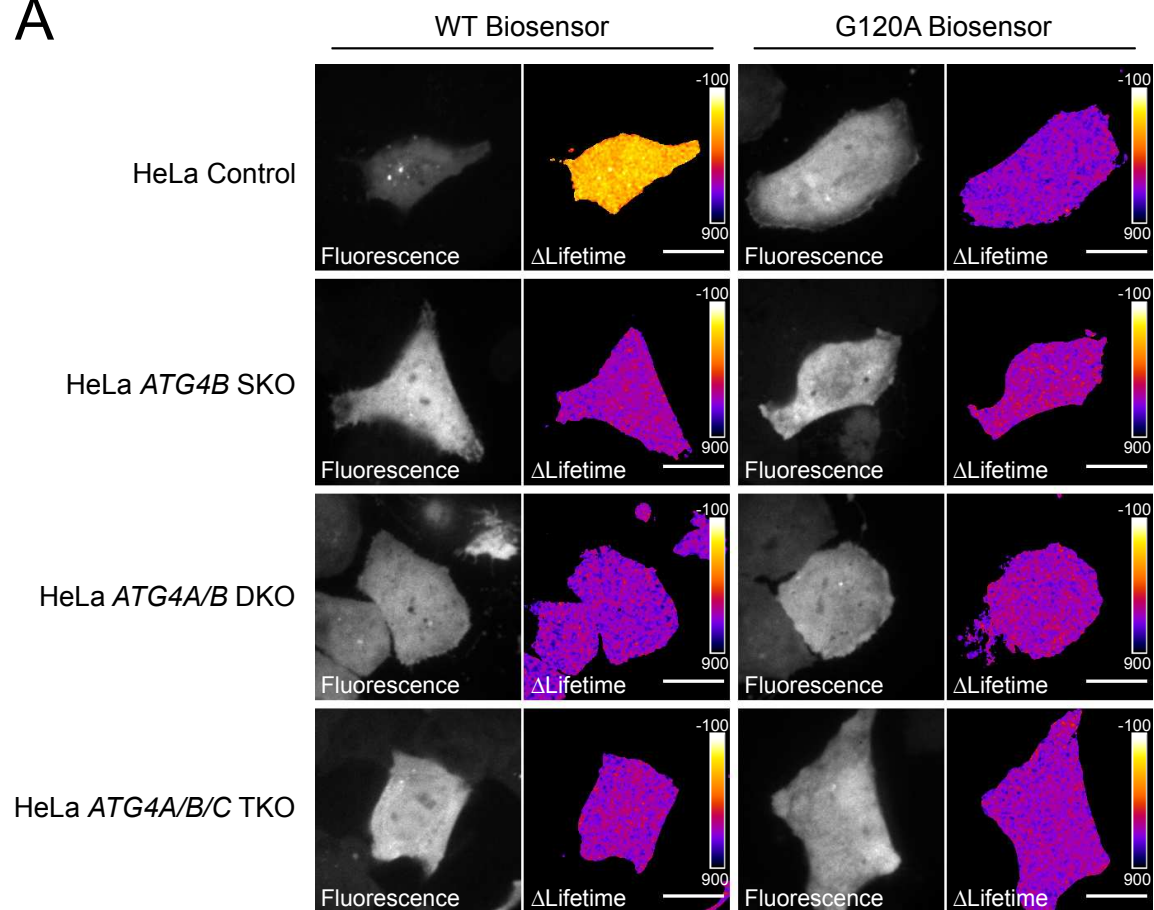


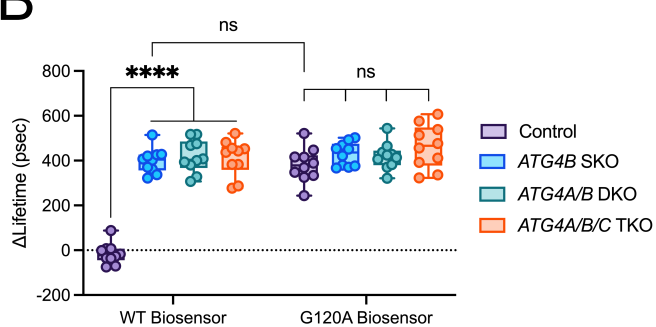
Figure 2. The knockdown of *ATG4B* lowers the priming of the LC3B biosensor. (A) Representative fluorescence and Δ Lifetime images of U2OS cells co-expressing the WT or G120A biosensor with control or *ATG4B*-specific siRNAs, and analyzed by FRET/FLIM. Squares on the top images of WT or G120A biosensor panels illustrate the location of the enlarged images. Dotted lines on the enlarged images illustrate where the line analysis was performed. Pseudocolor scale: pixel-by-pixel Δ Lifetime. Scale bars: overviews, 40 μ m; enlarged, 6 μ m. Mean Δ Lifetime (B), number of high Δ Lifetime pixels (C), line (D), histogram (E), and number of Aqua-LC3B-II puncta (F) analyses of U2OS cells co-expressing the WT or G120A biosensor with control or *ATG4B*-specific siRNAs in (B), (D), (E) and (F), and the WT donor or biosensor with control or *ATG4B* siRNA in (C). Vertical dotted lines on each histogram depicts the mode value in (E). $n = 10$ cells per condition from one representative experiment (of three) in (B), (C), (E) and (F). $**P < 0.01$, $****P < 0.0001$, ns (not significant) as determined by two-way ANOVA with Tukey's multiple comparison test in (B), (C) and (F).

Figure 3

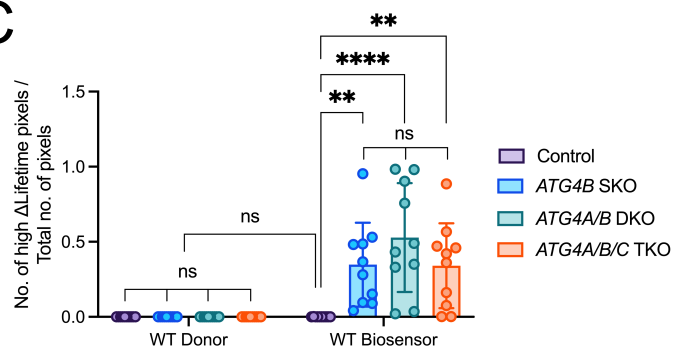
A



B



C



D

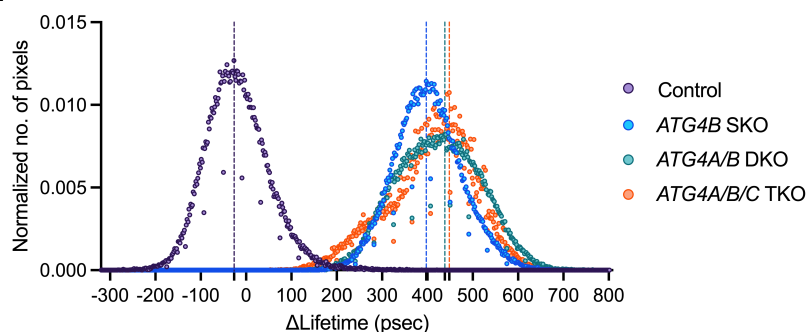


Figure 3. The absence of ATG4B maximizes the FRET response of the LC3B biosensor. (A) Representative fluorescence and Δ Lifetime images of HeLa control, *ATG4B* SKO, *ATG4A/B* DKO, *ATG4A/B/C* TKO cells expressing the WT or G120A biosensor and analyzed by FRET/FLIM. Pseudocolor scale: pixel-by-pixel Δ Lifetime. Scale bar: 40 μ m. Mean Δ Lifetime (B), number of high Δ Lifetime pixels (C) and histogram (D) analyses of HeLa control, *ATG4B* SKO, *ATG4A/B* DKO, *ATG4A/B/C* TKO cells expressing the WT or G120A biosensor. The vertical dotted lines on each histogram depict the mode value in (D). $n = 10$ cells per condition from one representative experiment (of three) in (B), (C) and (D). $**P < 0.01$, $****P < 0.0001$, ns (not significant) as determined by two-way ANOVA with Tukey's multiple comparison test in (B) and (C).

Figure 4

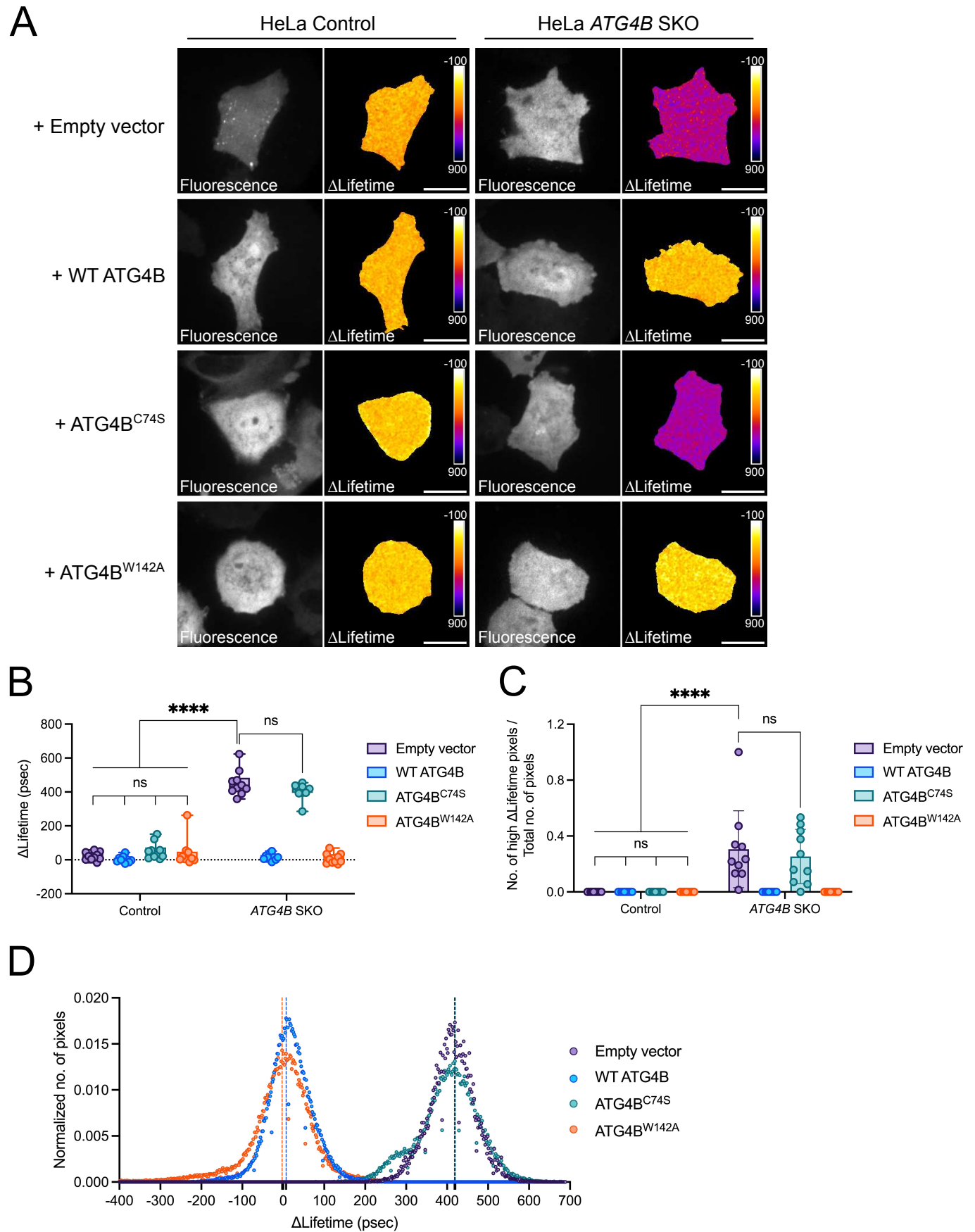


Figure 4. The priming deficiency of the LC3B biosensor is rescued when expressing WT or ATG4B^{W142A} in ATG4B SKO cells. (A) Representative fluorescence and Δ Lifetime images of control and ATG4B SKO HeLa cells co-expressing the WT biosensor with an empty vector, or with vectors expressing WT ATG4B, ATG4B^{C74S} or ATG4B^{W142A}, and analyzed by FRET/FLIM. Pseudocolor scale: pixel-by-pixel Δ Lifetime. Scale bar: 40 μ m. Mean Δ Lifetime (B) and number of high Δ Lifetime pixels (C) analyses of control and ATG4B SKO cells co-expressing the WT biosensor with an empty vector, or with vectors expressing WT ATG4B, ATG4B^{C74S} or ATG4B^{W142A}. (D) The histogram analysis of ATG4B SKO cells co-expressing the WT biosensor with an empty vector, or with vectors expressing WT ATG4B, ATG4B^{C74S} or ATG4B^{W142A}. Vertical dotted lines on each histogram depict the mode value in (D). $n = 10$ cells per condition from one representative experiment (of three) in (B), (C) and (D). **** $P < 0.0001$, ns (not significant) as determined by two-way ANOVA with Tukey's multiple comparison test in (B) and (C).

Figure 5

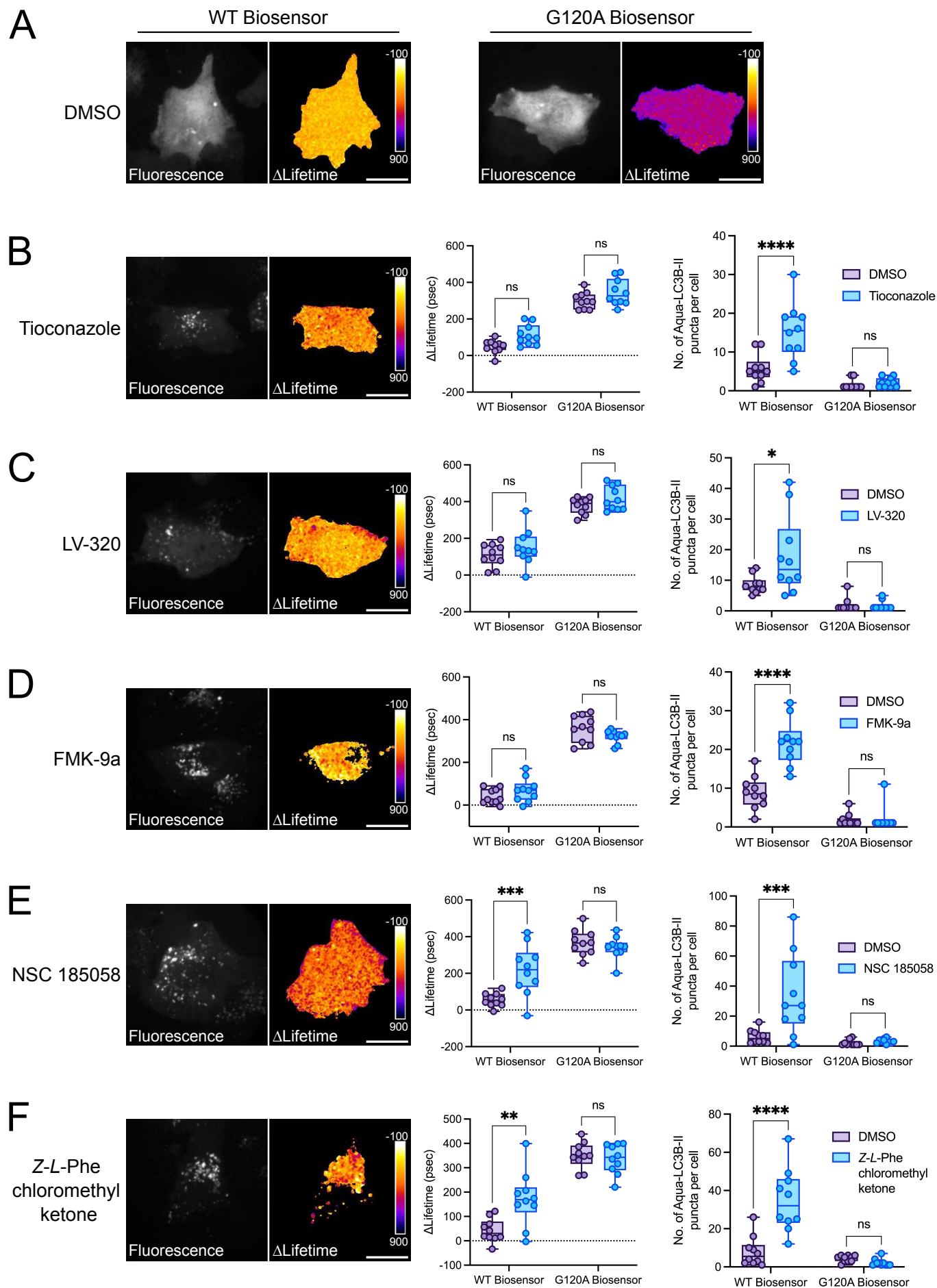


Figure 5. ATG4B inhibitors variably alter the Δ Lifetime behavior and LC3B puncta number in cells expressing the LC3B biosensor. (A) Representative fluorescence and Δ Lifetime images of HeLa cells expressing the WT or G120A biosensor, treated with DMSO (6h), and analyzed by FRET/FLIM. Representative fluorescence and Δ Lifetime images of HeLa cells expressing the WT biosensor and treated with Tioconazole (6h, 4 μ M) (B), LV-320 (6h, 120 μ M) (C), FMK-9a (6h, 10 μ M) (D), NSC 185058 (6h, 100 μ M) (E), or Z-L-Phe chloromethyl ketone (6h, 3 μ M) (F). Mean Δ Lifetime and number of Aqua-LC3B-II puncta analyses of HeLa cells expressing the WT or G120A biosensor and treated with Tioconazole (6h, 4 μ M) (B), LV-320 (6h, 120 μ M) (C), FMK-9a (6h, 10 μ M) (D), NSC 185058 (6h, 100 μ M) (E), or Z-L-Phe chloromethyl ketone (6h, 3 μ M) (F). Pseudocolor scale: pixel-by-pixel Δ Lifetime. Scale bars: 40 μ m. $n = 10$ cells per condition from one representative experiment (of three) in (B-F). * $P < 0.05$, ** $P < 0.01$, *** $P < 0.001$, **** $P < 0.0001$, ns (not significant) as determined by two-way ANOVA with Tukey's multiple comparison test in (B-F).

Figure 6

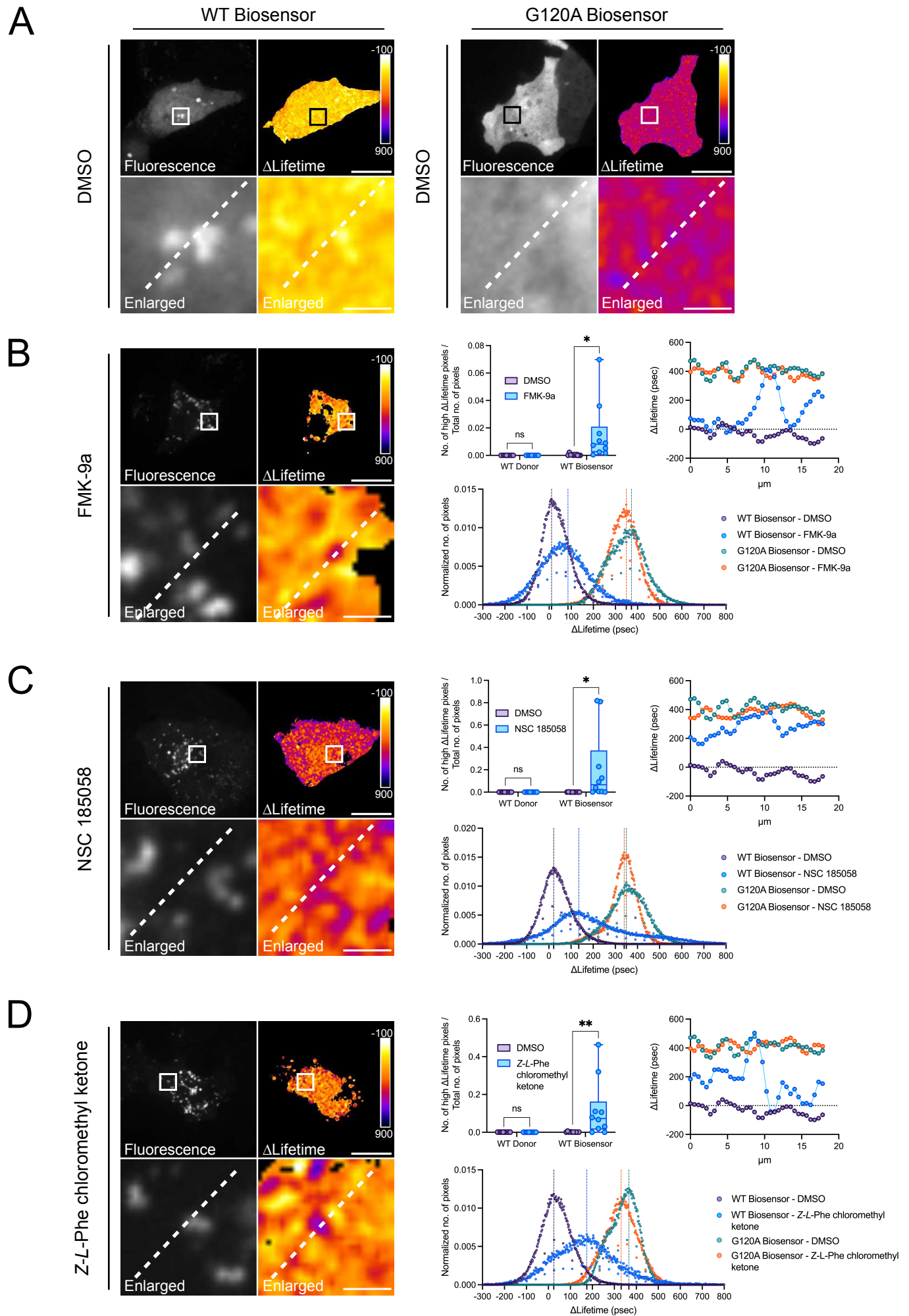


Figure 6. The LC3B biosensor reveals the mode of action of FMK-9a, NSC 185058 and Z-L-Phe chloromethyl ketone in cells. (A) Representative fluorescence and Δ Lifetime images of HeLa cells expressing the WT or G120A biosensor, treated with DMSO (6h), and analyzed by FRET/FLIM. Representative fluorescence and Δ Lifetime images of HeLa cells expressing the WT biosensor and treated with the following compounds: FMK-9a (6h, 10 μ M) (B), NSC 185058 (6h, 100 μ M) (C), or Z-L-Phe chloromethyl ketone (6h, 3 μ M) (D). Squares on the top images of WT or G120A biosensor panels illustrate the location of the enlarged images. Dotted lines on the enlarged images illustrate where the line analysis was performed. Pseudocolor scale: pixel-by-pixel Δ Lifetime. Scale bars: overviews, 40 μ m; enlarged, 6 μ m. Number of high Δ Lifetime pixels analysis of HeLa cells expressing the WT donor or biosensor and treated with FMK-9a (6h, 10 μ M) (B), NSC 185058 (6h, 100 μ M) (C), or Z-L-Phe chloromethyl ketone (6h, 3 μ M) (D). Line and histogram analyses of HeLa cells expressing the WT or G120A biosensor and treated with FMK-9a (6h, 10 μ M) (B), NSC 185058 (6h, 100 μ M) (C), or Z-L-Phe chloromethyl ketone (6h, 3 μ M) (D). $n = 10$ cells per condition from one representative experiment (of three) in (B-D). * $P < 0.05$, ** $P < 0.01$, ns (not significant) as determined by two-way ANOVA with Tukey's multiple comparison test in (B-D).

**The LC3B FRET biosensor monitors the modes of action of
ATG4B during autophagy in living cells**

Elif Begüm Gökerküçük et al.

Supplementary information

Figure S1

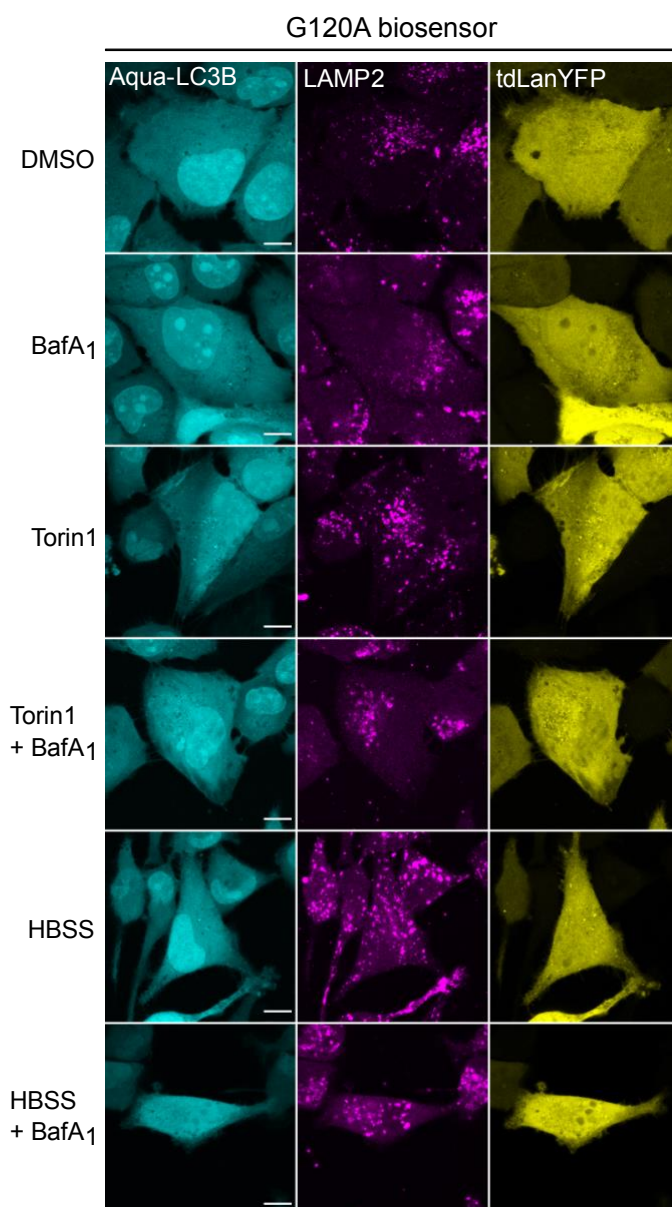


Figure S1. The G120A LC3B biosensor is not sensitive to autophagy induction and/or lysosomal inhibition, and it does not colocalize with LAMP2. Representative fluorescence images of U2OS expressing the G120A biosensor and stained for endogenous LAMP2. To investigate the changes in Aqua-LC3B puncta numbers and their colocalization with LAMP2, cells were treated with: DMSO (6h), BafA1 (6h, 100 nM), Torin1 (3h, 250 nM), Torin1 (3h, 250 nM) + BafA1 (6h, 100 nM), HBSS (1h), HBSS (1h) + BafA1 (6h, 100 nM). Scale bar: 9 μ m.

Figure S2

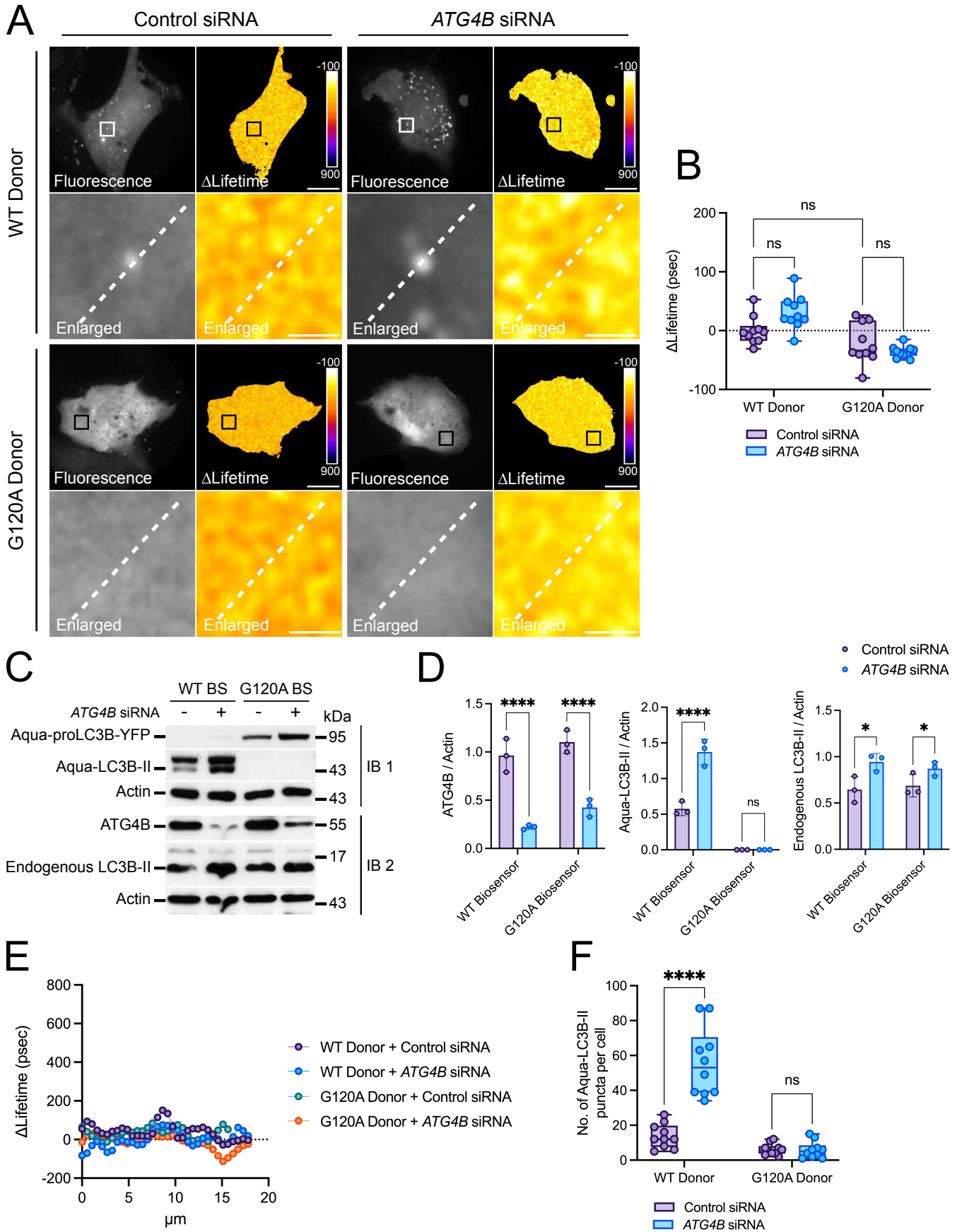


Figure S2. The WT or G120A donors do not respond to *ATG4B* silencing. (A) Representative fluorescence and Δ Lifetime images of U2OS cells co-expressing the WT or G120A donor with control or *ATG4B*-specific siRNAs, and analyzed by FRET/FLIM. Squares on the top images of WT or G120A donor panels illustrate the location of the enlarged images. Dotted lines on the enlarged images illustrate where the line analysis was performed. Pseudocolor scale: pixel-by-pixel Δ Lifetime. Scale bars: overviews, 40 μ m; enlarged, 6 μ m. (B) Mean Δ Lifetime analysis of U2OS cells co-expressing the WT or G120A donor with control or *ATG4B* siRNA. Representative western blotting images (C) and corresponding quantifications (D) of total lysates from U2OS cells co-expressing the WT or G120A biosensor with control or *ATG4B*-specific siRNAs. IB1 and IB2 correspond to the same lysates blotted for overexpressed (IB1) or endogenous (IB2) LC3B forms. Loading control: Actin. $n = 3$ independent experiments. (E) Line and (F) number of Aqua-LC3B-II puncta analyses of U2OS cells co-expressing the WT or G120A donor with control or *ATG4B* siRNA. $n = 10$ cells per condition from one representative experiment (of three) in (B) and (F). * $P < 0.05$, **** $P < 0.0001$, ns (not significant) as determined by two-way ANOVA with Tukey's multiple comparison test in (B) and (F), and with two-stage step-up method of Benjamini, Krieger and Yekutieli's multiple comparison test to control the false discovery rate in (D).

Figure S3

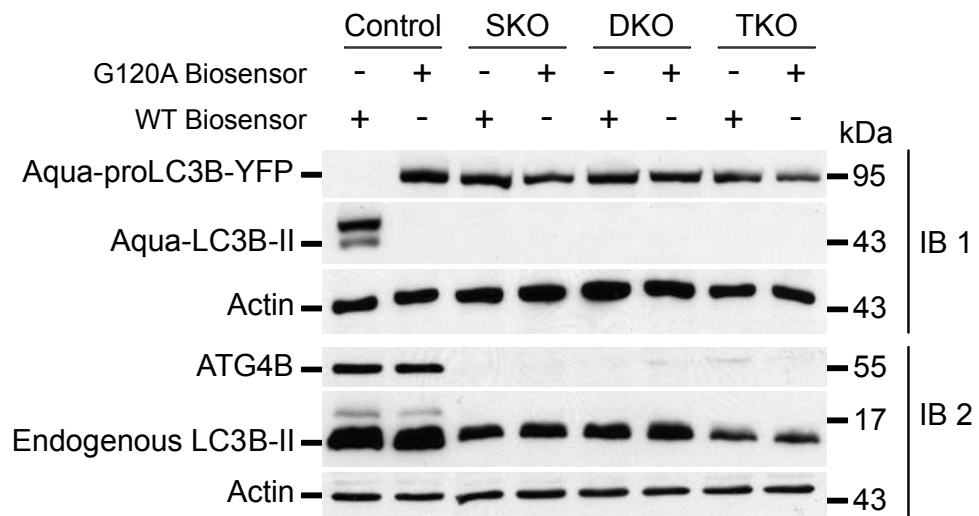
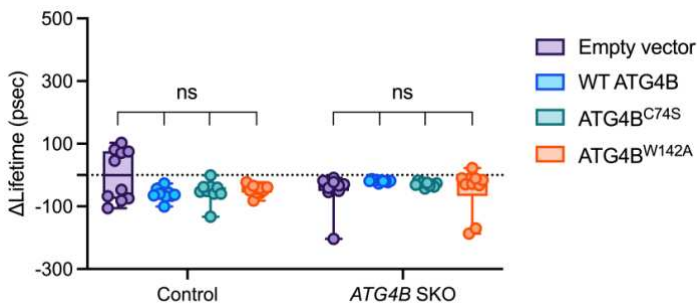


Figure S3. The LC3B biosensor and endogenous LC3B proteins cannot be primed in cells lacking ATG4B.

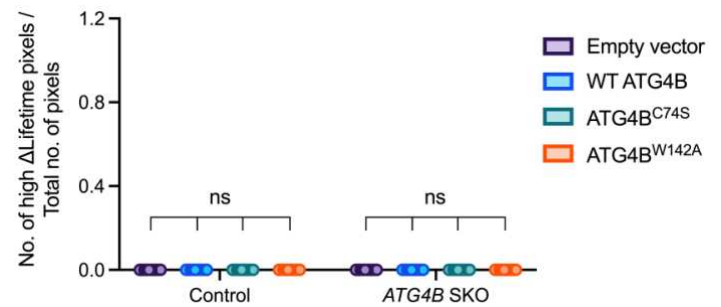
Representative western blotting images of total lysates from HeLa control, *ATG4B* SKO, *ATG4A/B* DKO, *ATG4A/B/C* TKO cells expressing the WT or G120A biosensor. IB1 and IB2 correspond to the same lysates blotted for overexpressed (IB1) or endogenous (IB2) LC3B forms. Loading control: Actin. $n = 3$ independent experiments.

Figure S4

A



B



C

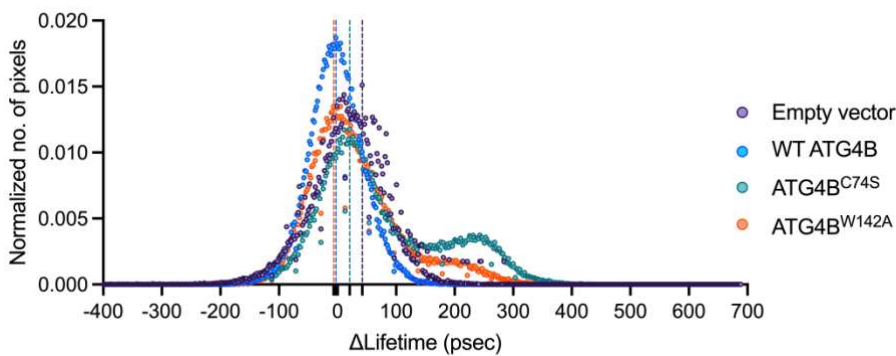
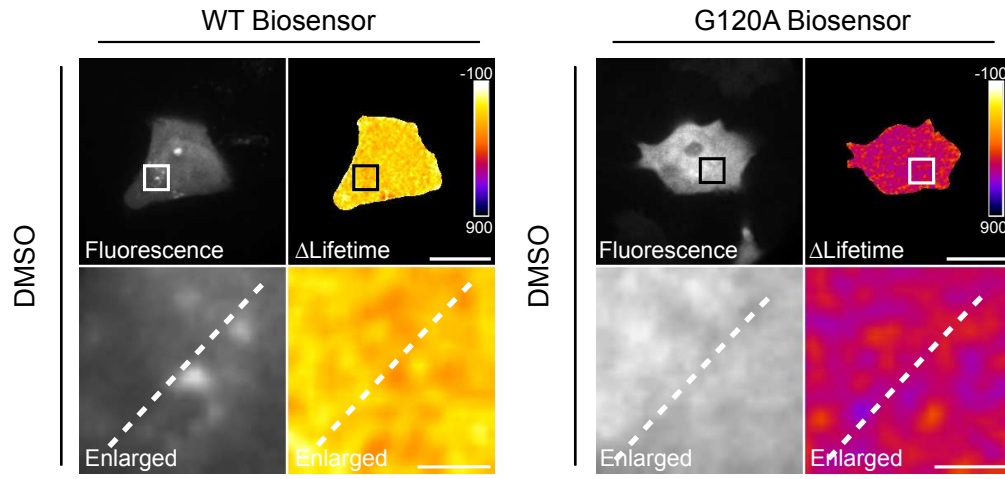


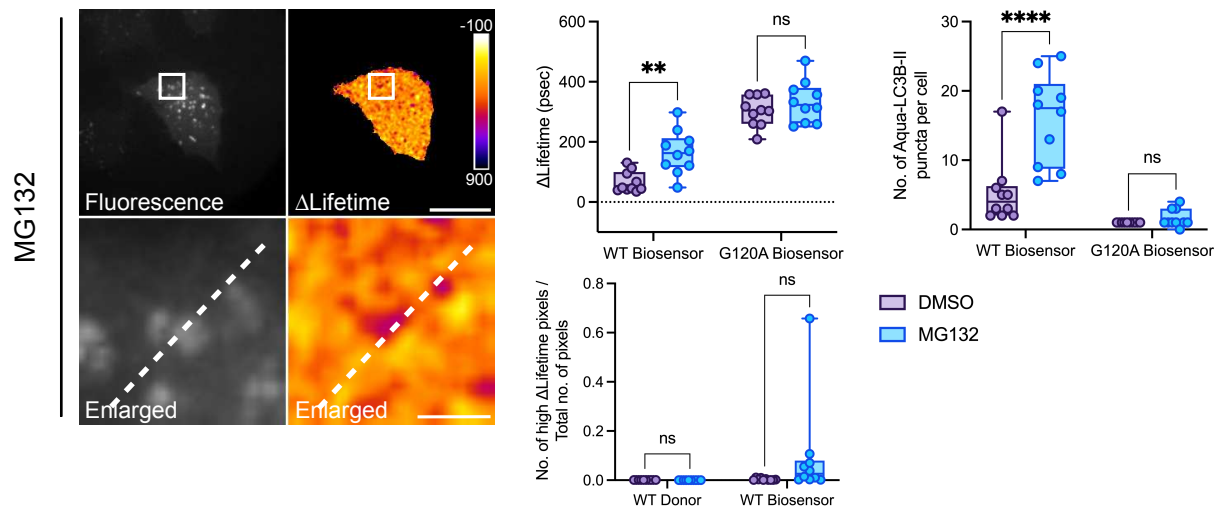
Figure S4. The ectopic expression of active *ATG4B* does not alter LC3B donor-only Δ lifetime variations in *ATG4B* SKO cells. Mean Δ Lifetime (**A**) and number of high Δ Lifetime pixels (**B**) analyses of control and *ATG4B* SKO HeLa cells co-expressing the WT donor with an empty vector, or with vectors expressing WT *ATG4B*, *ATG4B*^{C74S} or *ATG4B*^{W142A}. (**C**) Histogram analysis of HeLa control cells co-expressing the WT biosensor with an empty vector, or with vectors expressing WT *ATG4B*, *ATG4B*^{C74S} or *ATG4B*^{W142A}. Vertical dotted lines on each histogram depict the mode value. $n = 10$ cells per condition from one representative experiment (of three) in (**A**), (**B**) and (**C**). ns (not significant) as determined by two-way ANOVA with Tukey's multiple comparison test in (**A**) and (**B**).

Figure S5

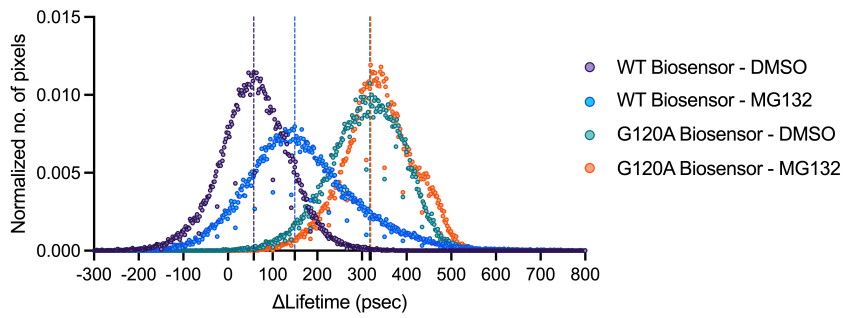
A



B



C



D

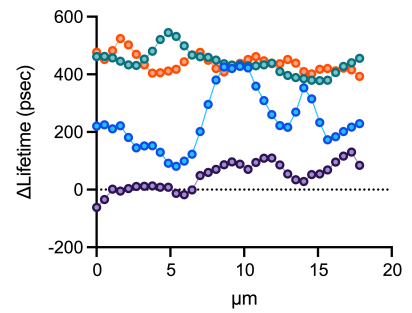


Figure S5. The LC3B biosensor reveals the mode of action of MG132 in cells. (A and B) Representative fluorescence and Δ Lifetime images of HeLa cells expressing the WT or G120A biosensor, treated with DMSO (6h) or MG132 (6h, 1 μ M), and analyzed by FRET/FLIM. Pseudocolor scale: pixel-by-pixel Δ Lifetime. Scale bars: overviews, 40 μ m; enlarged, 6 μ m. Mean Δ Lifetime (B), number of Aqua-LC3B-II puncta (B), histogram (C), and line (D) analyses of HeLa cells expressing the WT or G120A biosensor and treated with DMSO (6h) or MG132 (6h, 1 μ M). Number of high Δ Lifetime pixels analysis (B) of HeLa cells expressing the WT donor or biosensor and treated with DMSO (6h) or MG132 (6h, 1 μ M). Vertical dotted lines on each histogram depict the mode value in (C). $n = 10$ cells per condition from one representative experiment (of three) in (B) and (C). $**P < 0.01$, $****P < 0.0001$, ns (not significant) as determined by two-way ANOVA with Tukey's multiple comparison test in (B).

Figure S6

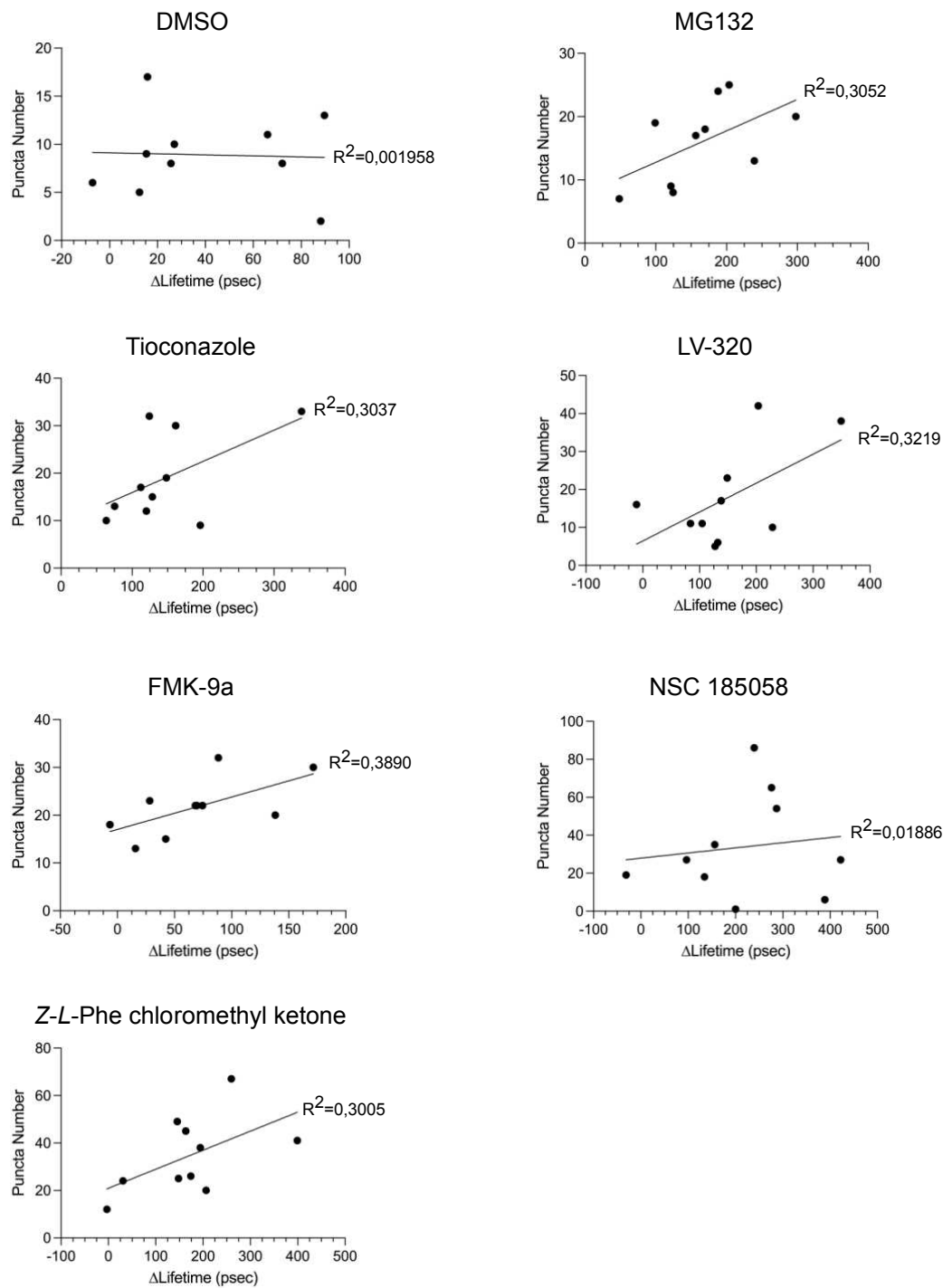
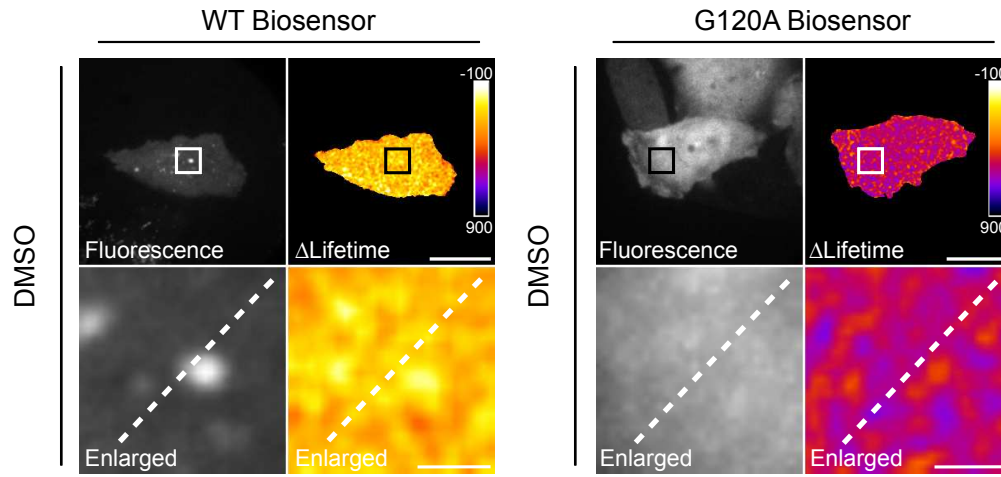


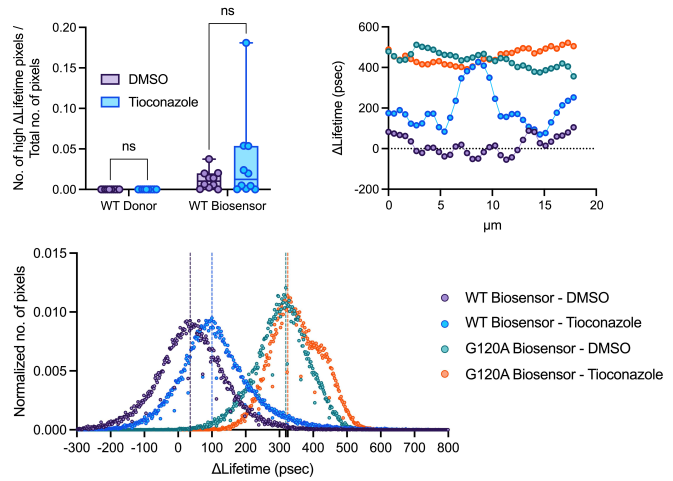
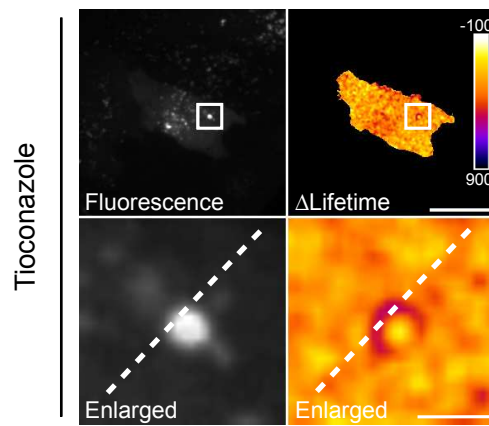
Figure S6. The number of Aqua-LC3B-II puncta and the mean Δ Lifetime values do not correlate. Correlation analyses of Aqua-LC3B-II puncta and the mean Δ Lifetime values of HeLa cells expressing the WT biosensor and treated with DMSO (6h), MG132 (6h, 1 μ M), Tioconazole (6h, 4 μ M), LV-320 (6h, 120 μ M), FMK-9a (6h, 10 μ M), NSC 185058 (6h, 100 μ M), or Z-L-Phe chloromethyl ketone (6h, 3 μ M). $n = 10$ cells per condition from one representative experiment (of three).

Figure S7

A



B



C

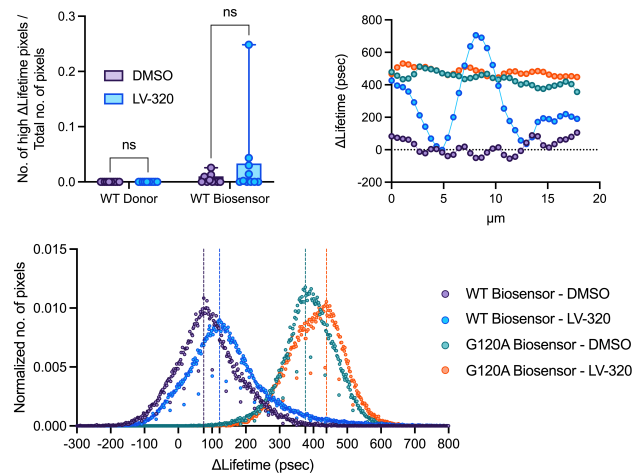
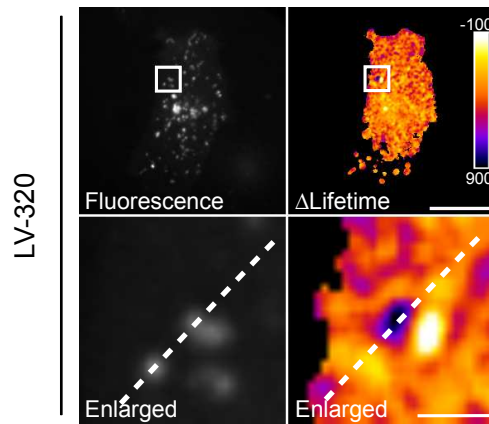


Figure S7. FRET/FLIM data analyzed by using sensitive methods reveal the mode of action of Tioconazole and LV-320 in cells. (A) Representative fluorescence and Δ Lifetime images of HeLa cells expressing the WT or G120A biosensor, treated with DMSO (6h), and analyzed by FRET/FLIM. Representative fluorescence and Δ Lifetime images of HeLa cells expressing the WT biosensor and treated with the following compounds: Tioconazole (6h, 4 μ M) (B), LV-320 (6h, 120 μ M) (C). Squares on the top images of WT or G120A biosensor panels illustrate the location of the enlarged images. Dotted lines on the enlarged images illustrate where the line analysis was performed. Pseudocolor scale: pixel-by-pixel Δ Lifetime. Scale bars: overviews, 40 μ m; enlarged, 6 μ m. Number of high Δ Lifetime pixels analysis of HeLa cells expressing the WT donor or biosensor and treated with Tioconazole (6h, 4 μ M) (B) or LV-320 (6h, 120 μ M) (C). Line, and histogram analyses of HeLa cells expressing the WT or G120A biosensor and treated with Tioconazole (6h, 4 μ M) (B) or LV-320 (6h, 120 μ M) (C). $n = 10$ cells per condition from one representative experiment (of three) in (B, C). ns (not significant) as determined by two-way ANOVA with Tukey's multiple comparison test in (B, C).

Table S1: List of plasmids used in this study. Table listing the source of each plasmid with the cloning sites and the primers for mutagenesis, if applicable.

Plasmid	Cloning sites	Remarks	Primers for mutagenesis (5' to 3'): sense	Primers for mutagenesis (5' to 3'): anti-sense
pcDNA 3.1		Purchased from Thermo Fisher Scientific.		
pCMV Aquamarine C1		Kind gift from F. Merola, Université Paris-Saclay, France		
pCMV Aquamarine-tdLanYFP tandem		Kind gift from F. Merola, Université Paris-Saclay, France		
pcDNA 3.1 mCherry-hLC3B		Addgene plasmid #40827.		
pCMV Aquamarine-proLC3B	BglIII/EcoRI	pCMV Aquamarine C1 was used as a backbone vector. Insert proLC3B was subcloned from pcDNA 3.1 mCherry-hLC3B.		
pCMV Aquamarine-proLC3B-tdLanYFP	BglIII/EcoRI	pCMV Aquamarine-tdLanYFP tandem was used as a backbone vector. proLC3B was inserted by subcloning it from pcDNA 3.1 mCherry-hLC3B.		
pCMV Aquamarine-proLC3B G120A		Obtained from pCMV Aquamarine-proLC3B	cactgacaatttcacggaacgtctcctggga	tcccaggagacgttcgcatgaaattgtcagtg
pCMV Aquamarine-proLC3B G120A-tdLanYFP		Obtained from pCMV Aquamarine-proLC3B-tdLanYFP	cactgacaatttcacggaacgtctcctggga	tcccaggagacgttcgcatgaaattgtcagtg
pGEX GST-ATG4B		Kind gift from R. Ketteler, LMCB, UCL, United Kingdom.		
pCMV WT ATG4B	NheI/EcoRI	pcDNA 3.1 was used as a backbone vector. Insert WT ATG4B was subcloned from pGEX GST-ATG4B.		
pCMV ATG4B C74S		Obtained from pCMV WT ATG4B	ccgcagcatgctgccccagcctg	caggctggggcagcatgctgcgg
pCMV ATG4B W142A		Obtained from pCMV WT ATG4B	gtgtggcccgtacgcctggcctatggactt	aagtccataggccaggcgtacgggccaacac

4.3 Mitochondrial changes in BRAFi sensitive and resistant melanoma cells

Over the course of my PhD studies, in addition to the development and characterization of the LC3B FRET biosensor, I also had the chance to investigate the mitochondrial changes in chemotherapy (BRAF inhibition) sensitive and resistant melanoma cells. Though it may seem diverse from my main PhD studies (therefore the related introduction presented in *section 4.3.1*), this study is part of a project that aims to use multiplexed FRET biosensors, including the LC3B biosensor, to monitor autophagy/mitophagy together with several other mitochondrial functions simultaneously in melanoma cells to decipher mechanisms leading to chemoresistance. To this end, the findings presented and discussed in this section represent the preliminary approaches that we took to investigate the changes in the mitochondrial signature of chemotherapy sensitive and resistant melanoma cells.

By being involved in this study, I also had the chance to supervise a talented Master's student, Khadidja Kacimi, who collected the data presented in this section. Thanks to this opportunity, I gained a valuable experience on people and project management which are important skills required for my future career. Along the process of this project, I also wrote a review article (*cf. Appendix A*), which was published in *Genes* in 2020 and describes the tools ranging from fluorescent dyes to genetically-encoded sensors to image and monitor mitochondrial functions.

4.3.1 Introduction

Melanoma is the most lethal form of skin cancer [277]. Although it only constitutes 4% of the skin cancer cases, it accounts for 75% of skin cancer deaths [277]. Worldwide incidence of melanoma has been reported to increase at a more rapid rate compared to any other type of cancer [278]. Racial skin phenotype, sun exposure and heritable mutations are the major determinants of melanoma incidences [279,280].

Melanoma is a malignant tumor arising from melanocytes which are the cells that lie at the basal level of epidermis and produce the UV absorbing pigment melanin [281]. Upon UV radiation, keratinocytes start to produce α -melanocyte stimulating hormone (α -

MSH), which binds to the melanocortin1 receptor (MC1R) of melanocytes to induce melanin signaling [282]. Melanin is then transferred from melanocytes to surrounding keratinocytes through finger-like projections and accumulates in sun-exposed keratinocytes to shield the nuclei from the mutagenic effects of UV radiation [283]. However, people with less functional variants of MC1R accumulate more mutations due to the susceptibility of skin cell nuclei to increased exposure of UV [277]. If mutations accumulate in critical regions of the genome, then skin cancers become inevitable.

4.3.1.1 BRAF-mutant melanomas

The molecular changes occurring in the progression of melanoma lead to overactivation of growth regulatory pathways such as the mitogen-activated protein kinase (MAPK) signaling pathway [284]. The MAPK pathway is essential in relaying extracellular signals to balance growth, proliferation, and apoptosis in the cell [285]. Driver mutations within MAPK pathway lead to uncontrollable growth which then develops into cancer [286]. BRAF mutation is the most commonly known driver mutation leading to the overactivation of MAPK pathway [284]. BRAF is one of the three isoforms represented in the Raf family of oncogenic serine-threonine protein kinases within the MAPK pathway and its mutations account for almost 50% of metastatic melanoma cases [286,287]. V600E mutation, which is the substitution of valine (V) at the amino acid position 600 for glutamic acid (E), represents 84.6% of BRAF mutations. BRAF mutant melanoma is characterized as a superficial spreading tumor or nodular tumor with a high chance of metastasizing into brain along with a shorter survival time in comparison to the non-BRAF mutant melanoma [280].

The currently available therapy options for BRAF mutant melanoma patients consist of a treatment with BRAF inhibitors such as vemurafenib or dabrafenib [280]. Although BRAF inhibition (BRAFi) therapy shows immediate tumor shrinkage lasting for 6 months, tumor relapse is observed along with the development of resistance to these inhibitors as the patient responses begin to drop [280,288].

4.3.1.2 Mechanisms of BRAFi resistance

Within the BRAFi resistant melanoma patient population, there are two general types of resistance – intrinsic resistance and acquired resistance [280]. Patients who do not respond to any type of BRAFi therapy are considered as the intrinsic resistance subtype. These individuals account for approximately 15% of the patient population. Acquired resistance, on the other hand, is the most common form of BRAFi resistance and observed within the individuals who show tumor regression as an initial response [289].

One of the mechanisms of acquired BRAFi resistance involve the dual activation of the MAPK and the PI3K-Act pathways to promote cell survival and proliferation. In this mechanism, upregulation of several receptor tyrosine kinases (RTKs) have been shown to directly activate MAPK pathway and RAS activation [290]. Several other upregulated RTKs such as the insulin like growth factor 1 receptor (IGFR1) and platelet derived growth factor receptor β (PDGFR β) have been demonstrated to activate PI3K-Act pathway in a non-ERK dependent manner [291,292]. Furthermore, epigenetic alterations of epidermal factor receptor (EGFR) have also been shown to induce PI3K-Act pathway in BRAFi resistant melanoma cells [292].

In addition to the genetic and epigenetic alterations in these pathways, metabolic rewiring through the changes in the mitochondrial signature have been suggested to contribute BRAFi resistance [293]. Indeed, in many different cancers including melanoma, altered energy metabolism is considered to be linked with cancer metastasis, drug resistance, and increased survival rates [294]. It has long been known that cancer cells favor glycolytic metabolism instead of ATP production through mitochondrial oxidative phosphorylation (OXPHOS) and therefore exhibit higher glucose uptake, a phenomenon known as Warburg effect [294]. However, increasing number of studies show that several types of cancers including melanoma still maintain high levels of mitochondrial energy metabolism as well [295–300].

In BRAF-mutant melanoma, BRAFi therapy decreases the glucose uptake and a subsequent glycolysis inhibition is observed in tumor cells in addition to the inhibition of MAPK cascade [301,302]. Based on *in vitro* studies, it is suggested that the degree of

glycolysis is positively correlated with the sensitivity to BRAFi [303,304]. Consistent with this finding, increased sensitivity to BRAFi has been reported in respiration-incompetent variant cell lines [305]. In addition to this, positron emission tomography-computed tomography with fluorine 18 (^{18}F) fluorodeoxyglucose (FDG PET/CT) imaging of BRAF-mutant melanoma patients has revealed inhibition in glucose uptake shortly after BRAFi therapy [306]. Altogether, these findings highlight the contribution of glycolysis inhibition in the anticancer effects of BRAF inhibition therapy [307].

Upon BRAF inhibition therapy, a high level of metabolic stress is observed in BRAF-mutant melanoma cells along with the glycolysis inhibition, which eventually results in cell death by apoptosis [304]. Based on the anticancer effect of glycolysis inhibition in BRAF-mutant melanoma cells, one plausible explanation of BRAFi-resistant melanoma cells survival is suggested to be related with the mitochondrial oxidative phenotype [307]. Based on this hypothesis, a sub-population of tumor cells are suggested to survive by entering cell cycle arrest, which in turn gives them the time to accumulate mutations and undergo metabolic rewiring to acquire drug-resistance [307]. To this end, high dependence on mitochondrial oxidative metabolism was suggested to maintain ATP levels and escape cell death pathway despite glycolysis inhibition [303,308–311]. However, the mitochondrial rewiring mechanisms that regulate this OXPHOS dependence in BRAFi resistant melanoma cells remain largely unknown and requires further investigation.

4.3.1.3 Altering mitochondrial dynamics: a way to become OXPHOS dependent?

As observed within many other functions of mitochondria, mitochondrial OXPHOS is intimately linked to mitochondrial morphology [312]. In this regard, mitochondrial dynamics, which are the opposing events of mitochondrial fusion and fission, are fundamental in regulating morphology through the changes in size, shape, number and distribution of mitochondria in cells (Fig. 27) [313]. Mitochondrial fusion is the interconnection of individual mitochondria by joining their respective outer and the inner membranes, along with the sharing of intramitochondrial content as mitochondrial DNA (mtDNA) molecules. Mitochondrial fission, on the other hand, is the division of a

mitochondrion into two or more mitochondrial units [314]. The balance between the opposing events of fusion and fission is not only required for proper mitochondrial functioning, but it is also necessary to adapt the mitochondrial network to the different metabolic states [315]. Mitochondrial fusion is required to regulate OXPHOS activity and maintains mtDNA integrity against the arousal of mutations or mitochondrial stress conditions [316,317]. In addition, pronounced fusion mechanisms during nutrient starvation were shown to protect the mitochondrial network from clearance through autophagy (mitophagy) [267]. Mitochondrial fission, however, is needed for the segregation and the consequent elimination of damaged mitochondrial parts during mitophagy, and for the inheritance of mtDNA to daughter cells during cell division [318,319].

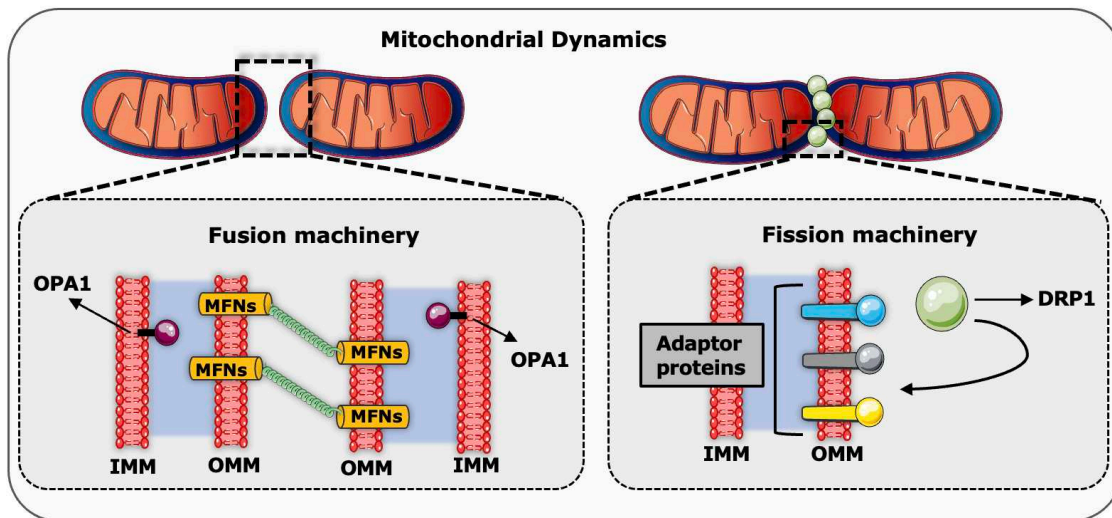


Figure 27: The opposing events of mitochondrial fusion and mission.

The key molecular players of the mitochondrial fusion and fission events are GTPase proteins, belonging to a highly conserved Dynamin family [320]. Mitochondrial fusion or fission is achieved by the ability of these proteins to oligomerize and change conformation to trigger membrane modeling [321]. Mitochondrial fusion starts with the fusion of the OMM and in mammals, this is ensured by mitofusin 1 (MFN1) and mitofusin 2 (MFN2) [320]. The fusion event starts with the tethering of two mitochondria by homo- and hetero-oligomerization of MFNs [322]. Then, the conformational change of MFNs induced by the hydrolysis of GTP leads to the docking of the two adjacent membranes, while gradually increasing the membrane contact sites, and finally fusing the two OMMs [323–325]. Following OMM fusion, the dynamin-like GTPase optic atrophy 1 (OPA1) and specific IMM lipid components such as cardiolipin mediate IMM fusion [326]. OPA1 has sites for proteolytic cleavage that can be processed by IMM-bound metalloproteases OMA1 and YME1L, to generate shorter forms of OPA1 (S-OPA1) [327–330]. While the longer forms of OPA1 (L-OPA1) has been shown to be sufficient to drive fusion [331], S-OPA1 were suggested to couple IMM fusion to metabolism [332]. Although there are different models describing IMM fusion, the interaction between L-OPA1 and cardiolipin was described to trigger the tethering of the two IMM,

which is then followed by the membrane fusion upon OPA1-dependent GTP hydrolysis [326].

Mitochondrial fission is mediated by the dynamin-related protein 1 (DRP1), which is a large cytosolic GTPase protein recruited to mitochondria upon fission initiation [333]. Mitochondrial sites where DRP1 will be recruited are initially marked by ER tubules to be constricted [334]. It has recently been discovered that the replicating mtDNA is also found in the mitochondrial fission sites, in order to be able to allow the distribution of mtDNA to fragmented mitochondria [335]. Initiation of mitochondrial fission and mtDNA synthesis on the ER-mitochondria contact site are followed by the oligomerization of DRP1 on the OMM. DRP1 constricts mitochondria by forming ring-like structures around the organelles while hydrolyzing GTP [336,337]. Actin polymerization is also required at this step to facilitate DRP1 accumulation [338]. Moreover, adaptor proteins such as MID49, MID51, and the mitochondrial fission factor (MFF), serve to recruit DRP1 by acting as receptors or recruitment factors for DRP1 [339–341]. Lastly, Dynamin 2 (DNM2) recruitment to the DRP1-mediated mitochondrial constriction sites finalizes the mitochondrial membrane scission [342]. As opposed to the well-described mechanisms of OMM constriction and scission, fission machinery, specifically dedicated to IMM, is still being investigated.

Although mitochondrial morphology can vary significantly across tissues and over a wide range of metabolic stimuli, in healthy cells hyperfused mitochondria are formed upon nutrient deprivation and in turn OXPHOS is favored for ATP production (Fig. 28) [315]. In contrary, under excess nutrient conditions, mitochondrial fragmentation may occur to facilitate mitophagy and OXPHOS is decreased due to the increased rates of glycolysis [315].

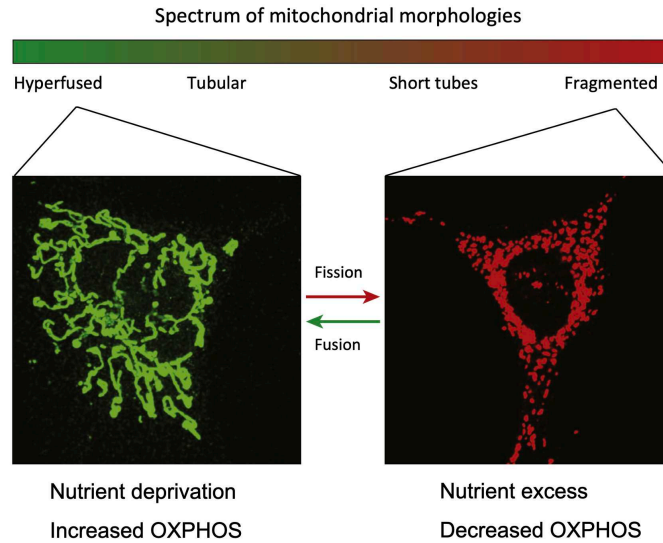


Figure 28: Spectrum of mitochondrial morphologies. Mitochondrial morphology changes in the cultured mouse embryonic fibroblasts as opposed to nutrient availability. Micrograph adapted from [315].

In contrast to normal cells, the link between mitochondrial morphology and OXPHOS dependency in pathologies such as cancer can be considerably heterogeneous as can be seen by the controversial reports in the literature. In some cancer cells, high levels of mitochondrial fission have been found to be associated with decreased levels of OXPHOS as evident by the altered levels of DRP1 and MFN2, which in turn support cancer cell survival and tumorigenicity [343–346]. On the other hand, in certain cancers, chemotherapy resistance was found to be associated with hyperfused mitochondrial network with increased levels of OXPHOS [347–349].

The biggest challenge here is likely to arise from the cancer cell heterogeneity which is determined by the tissue type and further induced by the status of nutrient availability and oxygen access. In this light, further studies are needed to decipher the link between mitochondrial morphology and OXPHOS dependency, and the evolution of this link in the process of acquiring chemotherapy resistance. To this end, we aimed to investigate changes in the mitochondrial dynamics and mitochondrial OXPHOS protein

levels of two different BRAFi-sensitive and -resistant pairs of melanoma cancer cells by using microscopy and biochemical approaches.

4.3.2 Changes in the mitochondrial dynamics of BRAFi sensitive and resistant melanoma cells

To investigate the changes in the mitochondrial dynamics of BRAFi sensitive and resistant melanoma cells, we used a fluorescent probe named mitoDendra2 (Fig. 29). Dendra2 is a photoconvertible fluorescent protein that irreversibly changes its fluorescence excitation and emission spectra upon excitation at a specific wavelength [350]. MitoDendra2 is a mitochondrial matrix-targeted version of Dendra2 and switches from green to red fluorescence (photoconversion) after excitation with a 405 nm laser [351]. To understand if the mitochondrial network of a cell expressing mitoDendra2 is interconnected, a subpopulation of mitochondria in a region of interest (ROI) is photoconverted to red and the fluorescence is observed from both green and red channels over time. If the mitochondrial network is interconnected, the red fluorescence signal diffuses out of the photoconverted ROI and mixes with the green mitochondria. This indicates the mitochondrial matrix fusion between the photoconverted and non-photoconverted mitochondrial subpopulations, and can be used as a readout to determine the status of the mitochondrial network.

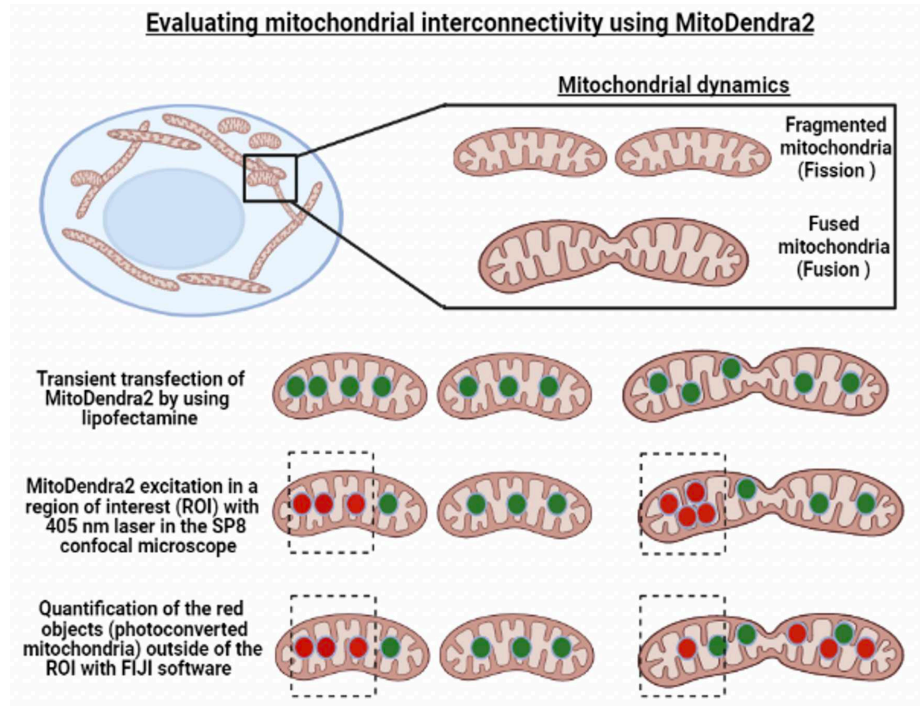


Figure 29: Scheme representing the principles of using mitoDendra2 to evaluate the mitochondrial interconnectivity. Diagram adapted from Khadija Kacimi's Master 1 report.

We performed our studies with mitoDendra2 in melanoma cell lines of 501Mel and SKMel28, which were kind gifts from the team of Marie-Dominique Galibert within our institute. Melanoma cell lines named 501Mel and SKMel28 are normally sensitive to BRAFi. The Galibert team generated the BRAFi resistant 501Mel and SKMel28 cells by treating sensitive cells with a BRAF inhibitor Vemurafenib for 3 months. These cells are pertinent tools to study molecular pathways leading to BRAFi resistance as they allow to perform comparative analysis between sensitive and resistant pairs with identical genetic background.

As a first attempt to investigate the alterations in the mitochondrial dynamics, we transiently expressed mitoDendra2 in BRAFi sensitive or resistant 501Mel and SKMel28 cells. Upon photoconverting a subpopulation of mitochondria in a ROI, we followed the diffusion of red signal while also acquiring the green signal for a duration of 80s. We

then determined the mitochondrial connectivity by normalizing the total number of red mitoDendra2 objects at 80s after photoconversion to the number of red mitoDendra2 objects in the ROI obtained in the first image taken right after the photoconversion (at 5s). Our analysis revealed no difference in the mitochondrial connectivity between the sensitive and resistant pairs of both cell lines (Fig. 30A-B). This suggests that the interconnectivity of the mitochondrial network in melanoma cells of 501Mel and SKMel28 is not altered due to BRAFi resistance. Interestingly, in all our experimental replicates, we observed highly fragmented mitochondrial network compared to any other cell line that we routinely worked with such as U2OS, HeLa or MCF-7. These fragmented mitochondrial units were appeared as spherical structures in both melanoma cell lines in contrast to the typical mitochondrial network appearance of tubular mitochondria mixed with spherical individual units. These fragmented mitochondria were also observed to be considerably motile when observed for a longer duration. We also observed a reduced mitochondrial mass in the BRAFi resistant sub-types of both cell lines, although this observation remained purely qualitative.

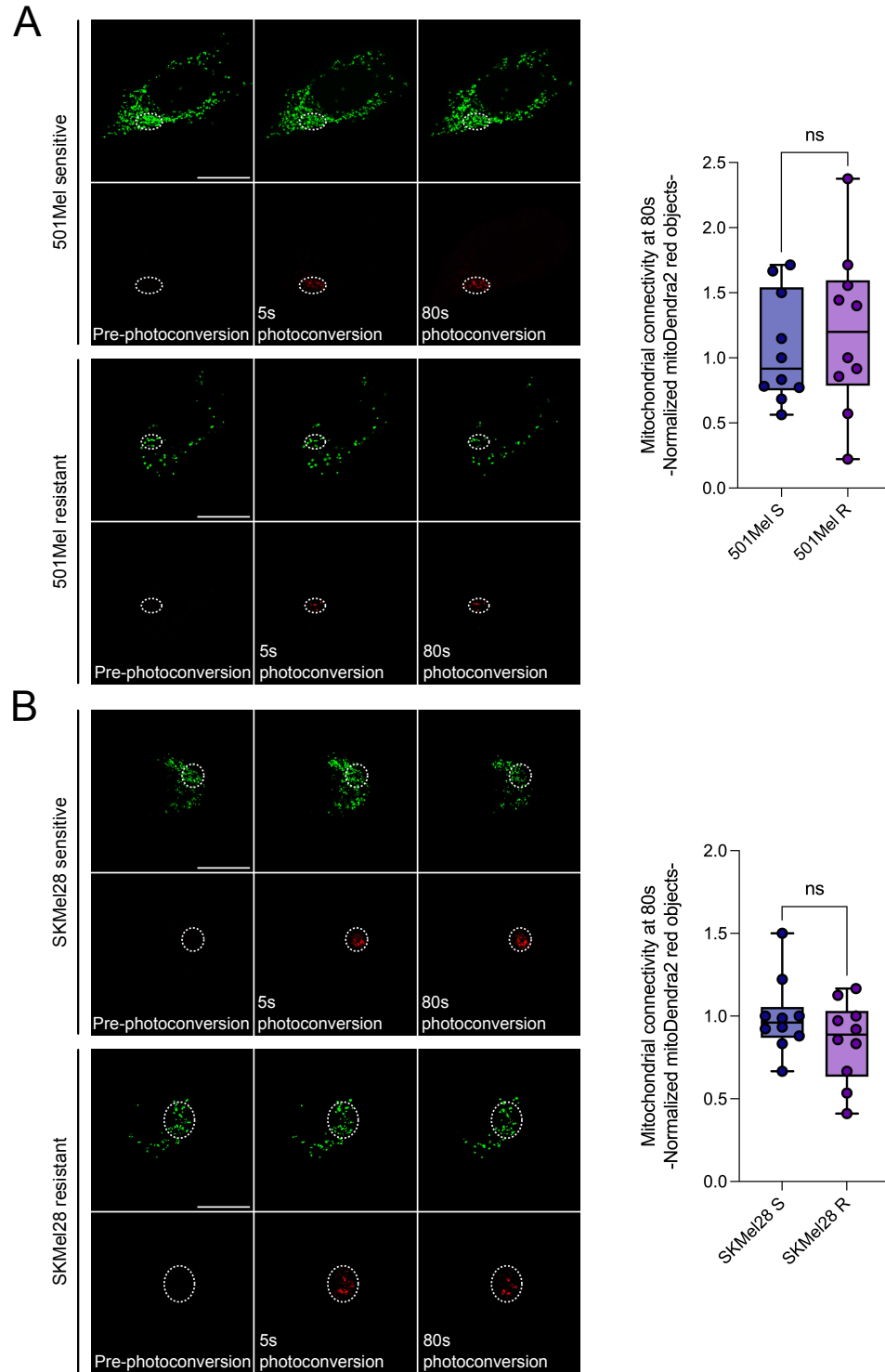


Figure 30: Mitochondrial network connectivity in melanoma cells of 501Mel and SKMel28 is not altered due to BRAFi resistance. (A) Representative fluorescence images and the quantification of mitoDendra2 photoconversion analysis for

Figure 30 continued on next page

Figure 30 continued

mitochondrial connectivity in 501Mel sensitive (501Mel S) and 501Mel resistant (501Mel R) cells. (B) Representative fluorescence images and the quantification of mitoDendra2 photoconversion analysis for mitochondrial connectivity in SKMel28 sensitive (SKMel28 S) and SKMel28 resistant (SKMel28 R) cells. Dotted line: photoconversion area. Scale bar: 20 μm . $n = 10$ cells per condition. ns (not significant) as determined by unpaired t test. The data presented in this figure collected by Khadidja Kacimi.

To conclude, our findings suggest a lack of mitochondrial interconnectivity in melanoma cells of 501Mel and SKMel28 regardless of their status on the BRAFi sensitivity/resistance. On the other hand, the mitochondrial alterations that may be induced upon BRAFi resistance could be restricted to the reduction in the overall mitochondrial mass.

4.3.3 Changes in the OXPHOS chain protein levels in BRAFi sensitive and resistant melanoma cells

Based on the anticancer effect of glycolysis inhibition in BRAF-mutant melanoma cells, one plausible explanation of BRAFi-resistant melanoma cells survival is suggested to be related with the mitochondrial oxidative phenotype [307]. Based on this hypothesis, a sub-population of tumor cells are suggested to survive by entering cell cycle arrest, which in turn gives them the time to accumulate mutations and undergo metabolic rewiring to acquire drug-resistance [307]. To this end, high dependence on mitochondrial oxidative metabolism was suggested to maintain ATP levels and escape cell death pathway despite glycolysis inhibition [303,308–311]. In the light of these findings, we performed western blotting assays to survey on the protein levels of the OXPHOS chain complexes in BRAFi sensitive and resistant melanoma cells. To this end, we used an antibody cocktail targeting proteins representing the five OXPHOS chain complexes (CI to V): CI-NDUFB8, CII-SDHB, CIII-UQCRC2, CIV-MTCO1 and CV-ATP5A. Despite our efforts, we were only able to blot CIII-UQCRC2 and CV-ATP5A but not the other OXPHOS complexes (Fig. 31). Among the blotted complexes, CIII-UQCRC2 was in fact

only observable in BRAFi resistant SKMel28 cells and became noticeable in BRAFi resistant SKMel28 or 501Mel sensitive and resistant cells upon longer exposure. CV-ATP5A, on the other hand, was observed to be drastically increased in BRAFi sensitive SKMel28 cells as compared to the resistant type. In BRAFi sensitive or resistant 501Mel cells, CV-ATP5A protein levels were observed to be rather similar.

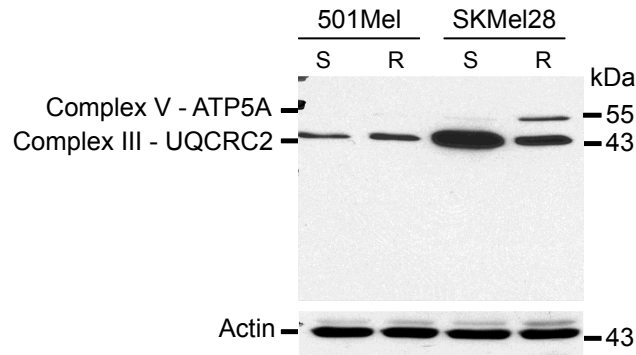


Figure 31: Abundance of OXPHOS chain proteins in BRAFi sensitive or resistant 501Mel and SKMel28 melanoma cells. Representative western blotting image of total lysates from BRAFi sensitive (S) or resistant (R) 501Mel and SKMel28 cells. Loading control: Actin. $n = 3$ independent experiments. The data presented in this figure collected by Khadidja Kacimi.

Based on these current findings, the technical difficulty causing the lack of bands regarding other complexes should be more thoroughly investigated. Nevertheless, it is still possible to grasp a preliminary understanding on the levels of the blotted proteins. For example, BRAFi resistance is observed to be causing an increase in CV-ATP5A levels and a decrease in CIII-UQCRC2 levels in SKMel28 cells but not in 501Mel cells. While this finding suggests that the abundance of these respiratory chain proteins may be altered by BRAFi resistance, it also highlights a possible variance between these two melanoma cell lines.

4.3.4 Discussion

In this preliminary study, we investigated the mitochondrial alterations upon developing BRAFi resistance in two different melanoma cell lines of 501Mel and SKMel28. To this end, we focused on two aspects of mitochondrial function: i) mitochondrial dynamics and ii) mitochondrial respiratory chain.

Among the mitochondrial alterations in which the cancer cells undergo, mitochondrial fusion over fission facilitate the metabolic shifts when acquiring resistance to treatments [347–349]. In this light, our initial assumption on the mitochondrial dynamics of 501Mel and SKMel28 cells was to observe a difference in the mitochondrial interconnectivity between BRAFi sensitive and resistant pairs. To our surprise, not only we detected any significant difference in the mitochondrial connectivity analyses of BRAFi sensitive and resistant pairs, but also, we observed highly fragmented and motile mitochondrial phenotype in all cells regardless of their BRAFi sensitivity/resistance. We also observed a reduced mitochondrial mass in the BRAFi resistant sub-types of both cell lines. Based on these preliminary findings and observations, we suggest that the elevated levels of fission events and increased mitochondrial motility could be the melanoma-related mitochondrial phenotypes observed in both 501Mel and SKMel28 cells. To unravel this, a comparative analysis between non-cancerous skin cells such as melanocytes and melanoma cells of 501Mel and SKMel28 can be performed to investigate the protein level changes on the mitochondrial fission and fusion proteins. In addition to this, it would be crucial to quantify mitochondrial mass to investigate the mitochondrial mass loss in BRAFi resistant melanoma cells by labelling both the plasma membrane and the mitochondria to quantify the mitochondrial mass per cellular area. Given that the elevated levels of mitochondrial fragmentation and mitochondrial mass loss are associated with increased mitochondrial degradation [352,353], it would also be interesting to investigate on the mitophagy rates of BRAFi sensitive and resistant melanoma cells. Any indication on the contribution of mitophagy in BRAFi resistance can further be investigated by inhibiting mitophagy with pharmacological compounds to possibly induce chemosensitivity.

In accordance with the role of mitochondrial fusion over fission in drug resistance, hyperfused mitochondrial network was found to favor OXPHOS to resist chemotherapy [349,354,355]. Based on this, one can easily assume to find elevated levels of OXPHOS chain proteins in BRAFi resistant melanoma cells. However, we saw the opposite effects in our models. Despite our efforts, we were only able to detect CIII-UQCRC2 and CV-ATP5A out of five OXPHOS chain complexes in western blotting. Though this could be due to a technical difficulty causing a lack of bands regarding other

complexes, this finding may also be related with the fragmented mitochondria phenotype. It is reported that the reduced levels of mitochondrial proteins including OXPHOS complexes are associated with the impairments in the mitochondrial fusion mechanisms [356,357]. If it is the case, the deficiency in OXPHOS proteins could be the hallmark of the defective mitochondrial fusion in melanoma cells of 501Mel and SKMel28 to possibly favor glycolysis over OXPHOS and by doing so, fragment and degrade the mitochondrial network.

Taken together, our preliminary findings and observations highlight an unexplored interplay between the mitochondrial dynamics and OXPHOS systems in 501Mel and SKMel28 melanoma cells. Further studies should be performed to decipher this interplay and whether it is altered upon BRAFi resistance.

5. CONCLUSIONS AND PERSPECTIVES

Over the course of my PhD studies, I worked on developing and characterizing microscopy-based approaches to monitor autophagy and mitochondrial functions in living cells. While my main work was dedicated to the LC3B FRET biosensor and different ways to quantify its response to monitor autophagy, I also studied ways to follow mitochondrial functions including mitophagy, mitochondrial dynamics and the abundance of mitochondrial respiration proteins.

Within the scope of my studies regarding the LC3B biosensor, we were able to revalidate the sensor in the research axis of LC3B-ATG4B and the regulation of this axis during autophagy. Based on our current understanding on the modes of action of ATG4B, this protease is responsible for the priming and deconjugation of LC3B and other ATG8 family of proteins. In living systems, the efficiency of priming is significantly higher than the deconjugation and almost instantaneously taking place after the translation of proLC3B. That is why, it is more challenging to follow this instantaneous and efficient priming activity as opposed to deconjugation where the effect of *ATG4B* downregulation or inhibition is immediately prominent. With the LC3B biosensor and different methods to analyze its response, we provided a tool and a framework of analyses to follow LC3B priming and deconjugation in living cells. We propose this tool to be useful not only to follow autophagy with a dual outcome, but also to study proLC3B priming in living systems as compared to the current methods that purely rely on *in vitro* systems [358]. With the advantage of being able to be used in living cells, the LC3B biosensor has the potential to answer questions regarding the physiological and pathophysiological relevance of proLC3B priming in various cellular processes. In processes where autophagy has been shown to be stalled such cell cycle [359], the LC3B biosensor can be used to investigate the relevance of proLC3B priming hotspots, thus can help to answer questions in regard to the molecular players of the link between the autophagy and the cell cycle.

Given the rising interest on targeting ATG4B to inhibit autophagy, there is an essential need for a robust tool to screen inhibitor libraries. To this end, we suggest that

the LC3B biosensor is a powerful tool to identify new ATG4B inhibitors. This is particularly important when we think about the desired effect of a potential ATG4B inhibitor. Here the aim should be identifying an inhibitor that can greatly – if not fully – abolish ATG4B priming activity on proLC3B. Otherwise, incomplete ATG4B inhibition results in the inhibition of deconjugation activity without having a strong impact on the priming as reported by us and others [360,361]. This is again due to the superior catalytic efficiency of ATG4B priming activity, which makes it more challenging to inhibit as compared to deconjugation. Thus, without a sensitive reporter, it is highly unlikely to detect proLC3B accumulation upon ATG4B inhibition in living cells. Thanks to its spatially-resolved, broad-to-sensitive analysis pipeline combining FRET and the quantification of autophagic puncta, the LC3B biosensor can detect the subtle changes in proLC3B priming rates while also reporting the puncta numbers. Especially by comparing the degree of changes in the histogram mode values and the number of high- Δ lifetime pixels, potential ATG4B inhibitors can be ranked on their efficiency to specifically inhibit the priming activity.

To increase the physiological relevance of the LC3B biosensor, it would be pertinent to generate cell lines or model organisms that can express the biosensor under the promoter of endogenous LC3B. Indeed, the current perspective on the LC3B biosensor in relation to the melanoma project (*cf. section 4.3*) is to be able to generate chemotherapy sensitive and resistant melanoma cell lines that express the LC3B biosensor to decipher potential link between reduced mitochondrial mass and the mitophagy. We believe these cells would serve as functional tools to study the LC3B-ATG4B axis and the involvement of autophagy/mitophagy in chemotherapy resistance. In the broader perspective and not only restricted to melanoma cells, it is also envisioned to multiplex the LC3B biosensor with our team's upcoming biosensors/fluorescent constructs to follow autophagy and multiple mitochondrial parameters simultaneously. If achieved, these multiplexed biosensor expressing cells would also allow to monitor mitophagy out of bulk autophagy by using the colocalization of the two sensors on mitochondrial network.

Taken together, my PhD studies on the LC3B FRET biosensor have led to the characterization of this tool to monitor autophagy in relation to the modes of action of ATG4B on LC3B. Furthermore, these studies combined with the preliminary findings in melanoma cells laid the foundation for multiplexing biosensors, therefore allowing the simultaneous monitoring of autophagy/mitophagy and other mitochondrial functions simultaneously.

6. REFERENCES

1. Ohsumi, Y. Historical Landmarks of Autophagy Research. *Cell Research* **2014**, *24*, 9–23, doi:10.1038/cr.2013.169.
2. Rothermel, B.A.; Diwan, A. Chapter 1 - Introduction. In *Autophagy in Health and Disease (Second Edition)*; Rothermel, B.A., Diwan, A., Eds.; Academic Press, 2022; pp. 3–8 ISBN 978-0-12-822003-0.
3. de Duve, C. The Lysosome Turns Fifty. *Nat Cell Biol* **2005**, *7*, 847–849, doi:10.1038/ncb0905-847.
4. Seglen, P.O.; Bohley, P. Autophagy and Other Vacuolar Protein Degradation Mechanisms. *Experientia* **1992**, *48*, 158–172, doi:10.1007/BF01923509.
5. Kim, J.; Klionsky, D.J. Autophagy, Cytoplasm-to-Vacuole Targeting Pathway, and Pexophagy in Yeast and Mammalian Cells. *Annu Rev Biochem* **2000**, *69*, 303–342, doi:10.1146/annurev.biochem.69.1.303.
6. Cuervo, A.M. Autophagy: Many Paths to the Same End. *Mol Cell Biochem* **2004**, *263*, 55–72.
7. Levine, B.; Klionsky, D.J. Development by Self-Digestion: Molecular Mechanisms and Biological Functions of Autophagy. *Developmental Cell* **2004**, *6*, 463–477, doi:10.1016/S1534-5807(04)00099-1.
8. Clark, S.L. Cellular Differentiation in the Kidneys of Newborn Mice Studies with the Electron Microscope. *J Biophys Biochem Cytol* **1957**, *3*, 349–362, doi:10.1083/jcb.3.3.349.
9. Ashford, T.P.; Porter, K.R. CYTOPLASMIC COMPONENTS IN HEPATIC CELL LYSOSOMES. *J Cell Biol* **1962**, *12*, 198–202.
10. Arstila, A.U.; Trump, B.F. Studies on Cellular Autophagocytosis. The Formation of Autophagic Vacuoles in the Liver after Glucagon Administration. *Am J Pathol* **1968**, *53*, 687–733.
11. Deter, R.L.; Baudhuin, P.; de Duve, C. PARTICIPATION OF LYSOSOMES IN CELLULAR AUTOPHAGY INDUCED IN RAT LIVER BY GLUCAGON. *J Cell Biol* **1967**, *35*, C11–C16.
12. Pfeifer, U.; Warmuth-Metz, M. Inhibition by Insulin of Cellular Autophagy in Proximal Tubular Cells of Rat Kidney. *Am J Physiol* **1983**, *244*, E109-114, doi:10.1152/ajpendo.1983.244.2.E109.
13. Mortimore, G.E.; Hutson, N.J.; Surmacz, C.A. Quantitative Correlation between Proteolysis and Macro- and Microautophagy in Mouse Hepatocytes during

- Starvation and Refeeding. *Proceedings of the National Academy of Sciences* **1983**, *80*, 2179–2183, doi:10.1073/pnas.80.8.2179.
14. Seglen, P.O.; Gordon, P.B.; Poli, A. Amino Acid Inhibition of the Autophagic/Lysosomal Pathway of Protein Degradation in Isolated Rat Hepatocytes. *Biochim Biophys Acta* **1980**, *630*, 103–118, doi:10.1016/0304-4165(80)90141-5.
 15. Wileman, T. Autophagy as a Defence against Intracellular Pathogens. *Essays Biochem* **2013**, *55*, 153–163, doi:10.1042/bse0550153.
 16. Eliopoulos, A.G.; Havaki, S.; Gorgoulis, V.G. DNA Damage Response and Autophagy: A Meaningful Partnership. *Frontiers in Genetics* **2016**, *7*.
 17. Levine, B. Autophagy and Cancer. *Nature* **2007**, *446*, 745–747, doi:10.1038/446745a.
 18. Vessoni, A.T.; Muotri, A.R.; Okamoto, O.K. Autophagy in Stem Cell Maintenance and Differentiation. *Stem Cells Dev* **2012**, *21*, 513–520, doi:10.1089/scd.2011.0526.
 19. Levine, B.; Mizushima, N.; Virgin, H.W. Autophagy in Immunity and Inflammation. *Nature* **2011**, *469*, 323–335, doi:10.1038/nature09782.
 20. Rubinsztein, D.C.; Mariño, G.; Kroemer, G. Autophagy and Aging. *Cell* **2011**, *146*, 682–695, doi:10.1016/j.cell.2011.07.030.
 21. Denton, D.; Kumar, S. Autophagy-Dependent Cell Death. *Cell Death Differ* **2019**, *26*, 605–616, doi:10.1038/s41418-018-0252-y.
 22. Parzych, K.R.; Klionsky, D.J. An Overview of Autophagy: Morphology, Mechanism, and Regulation. *Antioxid Redox Signal* **2014**, *20*, 460–473, doi:10.1089/ars.2013.5371.
 23. Marzella, L.; Ahlberg, J.; Glaumann, H. Autophagy, Heterophagy, Microautophagy and Crinophagy as the Means for Intracellular Degradation. *Virchows Arch B Cell Pathol Incl Mol Pathol* **1981**, *36*, 219–234, doi:10.1007/BF02912068.
 24. De Duve, C.; Wattiaux, R. Functions of Lysosomes. *Annu Rev Physiol* **1966**, *28*, 435–492, doi:10.1146/annurev.ph.28.030166.002251.
 25. Li, W.; Li, J.; Bao, J. Microautophagy: Lesser-Known Self-Eating. *Cell. Mol. Life Sci.* **2012**, *69*, 1125–1136, doi:10.1007/s00018-011-0865-5.
 26. Seki, T.; Katsuki, H. Chapter 26 - Mammalian Microautophagy: Mechanism and Roles in Disease. In *Autophagy in Health and Disease (Second Edition)*; Rothmel, B.A., Diwan, A., Eds.; Academic Press, 2022; pp. 385–397 ISBN 978-0-12-822003-0.

27. Sahu, R.; Kaushik, S.; Clement, C.C.; Cannizzo, E.S.; Scharf, B.; Follenzi, A.; Potalicchio, I.; Nieves, E.; Cuervo, A.M.; Santambrogio, L. Microautophagy of Cytosolic Proteins by Late Endosomes. *Developmental Cell* **2011**, *20*, 131–139, doi:10.1016/j.devcel.2010.12.003.
28. Tekirdag, K.; Cuervo, A.M. Chaperone-Mediated Autophagy and Endosomal Microautophagy: Jointed by a Chaperone. *Journal of Biological Chemistry* **2018**, *293*, 5414–5424, doi:10.1074/jbc.R117.818237.
29. Agarraberes, F.A.; Dice, J.F. A Molecular Chaperone Complex at the Lysosomal Membrane Is Required for Protein Translocation. *J Cell Sci* **2001**, *114*, 2491–2499, doi:10.1242/jcs.114.13.2491.
30. Cuervo, A.M.; Knecht, E.; Terlecky, S.R.; Dice, J.F. Activation of a Selective Pathway of Lysosomal Proteolysis in Rat Liver by Prolonged Starvation. *Am J Physiol* **1995**, *269*, C1200–1208, doi:10.1152/ajpcell.1995.269.5.C1200.
31. Cuervo, A.M.; Dice, J.F. A Receptor for the Selective Uptake and Degradation of Proteins by Lysosomes. *Science* **1996**, *273*, 501–503, doi:10.1126/science.273.5274.501.
32. Arias, E.; Cuervo, A.M. Chaperone-Mediated Autophagy in Protein Quality Control. *Curr Opin Cell Biol* **2011**, *23*, 184–189, doi:10.1016/j.ceb.2010.10.009.
33. Koga, H.; Martinez-Vicente, M.; Macian, F.; Verkhusha, V.V.; Cuervo, A.M. A Photoconvertible Fluorescent Reporter to Track Chaperone-Mediated Autophagy. *Nat Commun* **2011**, *2*, 386, doi:10.1038/ncomms1393.
34. Dong, S.; Aguirre-Hernandez, C.; Scrivo, A.; Eliscovich, C.; Arias, E.; Bravo-Cordero, J.J.; Cuervo, A.M. Monitoring Spatiotemporal Changes in Chaperone-Mediated Autophagy in Vivo. *Nat Commun* **2020**, *11*, 645, doi:10.1038/s41467-019-14164-4.
35. Dice, J.F. Peptide Sequences That Target Cytosolic Proteins for Lysosomal Proteolysis. *Trends Biochem Sci* **1990**, *15*, 305–309, doi:10.1016/0968-0004(90)90019-8.
36. Chiang, H.L.; Dice, J.F. Peptide Sequences That Target Proteins for Enhanced Degradation during Serum Withdrawal. *J Biol Chem* **1988**, *263*, 6797–6805.
37. Kiffin, R.; Christian, C.; Knecht, E.; Cuervo, A.M. Activation of Chaperone-Mediated Autophagy during Oxidative Stress. *Mol Biol Cell* **2004**, *15*, 4829–4840, doi:10.1091/mbc.E04-06-0477.
38. Zhang, L.; Sun, Y.; Fei, M.; Tan, C.; Wu, J.; Zheng, J.; Tang, J.; Sun, W.; Lv, Z.; Bao, J.; et al. Disruption of Chaperone-Mediated Autophagy-Dependent Degradation of MEF2A by Oxidative Stress-Induced Lysosome Destabilization. *Autophagy* **2014**, *10*, 1015–1035, doi:10.4161/auto.28477.

39. Park, C.; Suh, Y.; Cuervo, A.M. Regulated Degradation of Chk1 by Chaperone-Mediated Autophagy in Response to DNA Damage. *Nat Commun* **2015**, *6*, 6823, doi:10.1038/ncomms7823.
40. Wu, J.-H.; Guo, J.-P.; Shi, J.; Wang, H.; Li, L.-L.; Guo, B.; Liu, D.-X.; Cao, Q.; Yuan, Z.-Y. CMA Down-Regulates P53 Expression through Degradation of HMGB1 Protein to Inhibit Irradiation-Triggered Apoptosis in Hepatocellular Carcinoma. *World J Gastroenterol* **2017**, *23*, 2308–2317, doi:10.3748/wjg.v23.i13.2308.
41. Dohi, E.; Tanaka, S.; Seki, T.; Miyagi, T.; Hide, I.; Takahashi, T.; Matsumoto, M.; Sakai, N. Hypoxic Stress Activates Chaperone-Mediated Autophagy and Modulates Neuronal Cell Survival. *Neurochem Int* **2012**, *60*, 431–442, doi:10.1016/j.neuint.2012.01.020.
42. Hubbi, M.E.; Hu, H.; Kshitiz, null; Ahmed, I.; Levchenko, A.; Semenza, G.L. Chaperone-Mediated Autophagy Targets Hypoxia-Inducible Factor-1 α (HIF-1 α) for Lysosomal Degradation. *J Biol Chem* **2013**, *288*, 10703–10714, doi:10.1074/jbc.M112.414771.
43. Juste, Y.R.; Kaushik, S.; Bourdenx, M.; Aflakpui, R.; Bandyopadhyay, S.; Garcia, F.; Diaz, A.; Lindenau, K.; Tu, V.; Krause, G.J.; et al. Reciprocal Regulation of Chaperone-Mediated Autophagy and the Circadian Clock. *Nat Cell Biol* **2021**, *23*, 1255–1270, doi:10.1038/s41556-021-00800-z.
44. Kaushik, S.; Juste, Y.R.; Cuervo, A.M. Circadian Remodeling of the Proteome by Chaperone-Mediated Autophagy. *Autophagy* **2022**, *18*, 1205–1207, doi:10.1080/15548627.2022.2038503.
45. Seglen, P.O.; Gordon, P.B.; Holen, I. Non-Selective Autophagy. *Semin Cell Biol* **1990**, *1*, 441–448.
46. Yorimitsu, T.; Klionsky, D.J. Autophagy: Molecular Machinery for Self-Eating. *Cell Death Differ* **2005**, *12*, 1542–1552, doi:10.1038/sj.cdd.4401765.
47. Jézégou, A.; Llinares, E.; Anne, C.; Kieffer-Jaquinod, S.; O'Regan, S.; Aupetit, J.; Chabli, A.; Sagné, C.; Debacker, C.; Chadefaux-Vekemans, B.; et al. Heptahelical Protein PQLC2 Is a Lysosomal Cationic Amino Acid Exporter Underlying the Action of Cysteamine in Cystinosis Therapy. *Proc Natl Acad Sci U S A* **2012**, *109*, E3434–3443, doi:10.1073/pnas.1211198109.
48. Liu, B.; Du, H.; Rutkowski, R.; Gartner, A.; Wang, X. LAAT-1 Is the Lysosomal Lysine/Arginine Transporter That Maintains Amino Acid Homeostasis. *Science* **2012**, *337*, 351–354, doi:10.1126/science.1220281.
49. Sagné, C.; Agulhon, C.; Ravassard, P.; Darmon, M.; Hamon, M.; El Mestikawy, S.; Gasnier, B.; Giros, B. Identification and Characterization of a Lysosomal

- Transporter for Small Neutral Amino Acids. *Proc Natl Acad Sci U S A* **2001**, *98*, 7206–7211, doi:10.1073/pnas.121183498.
50. He, C.; Klionsky, D.J. Regulation Mechanisms and Signaling Pathways of Autophagy. *Annu. Rev. Genet.* **2009**, *43*, 67–93, doi:10.1146/annurev-genet-102808-114910.
 51. Biazik, J.; Ylä-Anttila, P.; Vihinen, H.; Jokitalo, E.; Eskelinen, E.-L. Ultrastructural Relationship of the Phagophore with Surrounding Organelles. *Autophagy* **2015**, *11*, 439–451, doi:10.1080/15548627.2015.1017178.
 52. Hayashi-Nishino, M.; Fujita, N.; Noda, T.; Yamaguchi, A.; Yoshimori, T.; Yamamoto, A. A Subdomain of the Endoplasmic Reticulum Forms a Cradle for Autophagosome Formation. *Nat Cell Biol* **2009**, *11*, 1433–1437, doi:10.1038/ncb1991.
 53. Ylä-Anttila, P.; Vihinen, H.; Jokitalo, E.; Eskelinen, E.-L. 3D Tomography Reveals Connections between the Phagophore and Endoplasmic Reticulum. *Autophagy* **2009**, *5*, 1180–1185, doi:10.4161/auto.5.8.10274.
 54. Nishimura, T.; Tamura, N.; Kono, N.; Shimanaka, Y.; Arai, H.; Yamamoto, H.; Mizushima, N. Autophagosome Formation Is Initiated at Phosphatidylinositol Synthase-Enriched ER Subdomains. *EMBO J* **2017**, *36*, 1719–1735, doi:10.15252/embj.201695189.
 55. He, C. Chapter 2 - Mechanisms of Autophagy: The Machinery of Macroautophagy and Points of Control. In *Autophagy in Health and Disease (Second Edition)*; Rothermel, B.A., Diwan, A., Eds.; Academic Press, 2022; pp. 9–19 ISBN 978-0-12-822003-0.
 56. Koyama-Honda, I.; Itakura, E.; Fujiwara, T.K.; Mizushima, N. Temporal Analysis of Recruitment of Mammalian ATG Proteins to the Autophagosome Formation Site. *Autophagy* **2013**, *9*, 1491–1499, doi:10.4161/auto.25529.
 57. Suzuki, K.; Kubota, Y.; Sekito, T.; Ohsumi, Y. Hierarchy of Atg Proteins in Pre-Autophagosomal Structure Organization. *Genes Cells* **2007**, *12*, 209–218, doi:10.1111/j.1365-2443.2007.01050.x.
 58. Karanasios, E.; Stapleton, E.; Manifava, M.; Kaizuka, T.; Mizushima, N.; Walker, S.A.; Ktistakis, N.T. Dynamic Association of the ULK1 Complex with Omegasomes during Autophagy Induction. *J Cell Sci* **2013**, *126*, 5224–5238, doi:10.1242/jcs.132415.
 59. Hosokawa, N.; Hara, T.; Kaizuka, T.; Kishi, C.; Takamura, A.; Miura, Y.; Iemura, S.; Natsume, T.; Takehana, K.; Yamada, N.; et al. Nutrient-Dependent MTORC1 Association with the ULK1-Atg13-FIP200 Complex Required for Autophagy. *Mol Biol Cell* **2009**, *20*, 1981–1991, doi:10.1091/mbc.e08-12-1248.

60. Jung, C.H.; Jun, C.B.; Ro, S.-H.; Kim, Y.-M.; Otto, N.M.; Cao, J.; Kundu, M.; Kim, D.-H. ULK-Atg13-FIP200 Complexes Mediate MTOR Signaling to the Autophagy Machinery. *Mol Biol Cell* **2009**, *20*, 1992–2003, doi:10.1091/mbc.e08-12-1249.
61. Itakura, E.; Mizushima, N. Characterization of Autophagosome Formation Site by a Hierarchical Analysis of Mammalian Atg Proteins. *Autophagy* **2010**, *6*, 764–776, doi:10.4161/auto.6.6.12709.
62. Burman, C.; Ktistakis, N.T. Regulation of Autophagy by Phosphatidylinositol 3-Phosphate. *FEBS Lett* **2010**, *584*, 1302–1312, doi:10.1016/j.febslet.2010.01.011.
63. He, C.; Levine, B. The Beclin 1 Interactome. *Curr Opin Cell Biol* **2010**, *22*, 140–149, doi:10.1016/j.ceb.2010.01.001.
64. Ohashi, Y.; Soler, N.; García Ortégón, M.; Zhang, L.; Kirsten, M.L.; Perisic, O.; Masson, G.R.; Burke, J.E.; Jakobi, A.J.; Apostolakis, A.A.; et al. Characterization of Atg38 and NRBF2, a Fifth Subunit of the Autophagic Vps34/PIK3C3 Complex. *Autophagy* **2016**, *12*, 2129–2144, doi:10.1080/15548627.2016.1226736.
65. Lu, J.; He, L.; Behrends, C.; Araki, M.; Araki, K.; Jun Wang, Q.; Catanzaro, J.M.; Friedman, S.L.; Zong, W.-X.; Fiel, M.I.; et al. NRBF2 Regulates Autophagy and Prevents Liver Injury by Modulating Atg14L-Linked Phosphatidylinositol-3 Kinase III Activity. *Nat Commun* **2014**, *5*, 3920, doi:10.1038/ncomms4920.
66. Takahashi, Y.; Coppola, D.; Matsushita, N.; Cialing, H.D.; Sun, M.; Sato, Y.; Liang, C.; Jung, J.U.; Cheng, J.Q.; Mulé, J.J.; et al. Bif-1 Interacts with Beclin 1 through UVRAG and Regulates Autophagy and Tumorigenesis. *Nat Cell Biol* **2007**, *9*, 1142–1151, doi:10.1038/ncb1634.
67. Liang, X.H.; Jackson, S.; Seaman, M.; Brown, K.; Kempkes, B.; Hibshoosh, H.; Levine, B. Induction of Autophagy and Inhibition of Tumorigenesis by Beclin 1. *Nature* **1999**, *402*, 672–676, doi:10.1038/45257.
68. Zeng, X.; Overmeyer, J.H.; Maltese, W.A. Functional Specificity of the Mammalian Beclin-Vps34 PI 3-Kinase Complex in Macroautophagy versus Endocytosis and Lysosomal Enzyme Trafficking. *J Cell Sci* **2006**, *119*, 259–270, doi:10.1242/jcs.02735.
69. Liang, X.H.; Kleeman, L.K.; Jiang, H.H.; Gordon, G.; Goldman, J.E.; Berry, G.; Herman, B.; Levine, B. Protection against Fatal Sindbis Virus Encephalitis by Beclin, a Novel Bcl-2-Interacting Protein. *J Virol* **1998**, *72*, 8586–8596, doi:10.1128/JVI.72.11.8586-8596.1998.
70. Furuya, N.; Yu, J.; Byfield, M.; Pattingre, S.; Levine, B. The Evolutionarily Conserved Domain of Beclin 1 Is Required for Vps34 Binding, Autophagy and Tumor Suppressor Function. *Autophagy* **2005**, *1*, 46–52, doi:10.4161/auto.1.1.1542.

71. Pattingre, S.; Tassa, A.; Qu, X.; Garuti, R.; Liang, X.H.; Mizushima, N.; Packer, M.; Schneider, M.D.; Levine, B. Bcl-2 Antiapoptotic Proteins Inhibit Beclin 1-Dependent Autophagy. *Cell* **2005**, *122*, 927–939, doi:10.1016/j.cell.2005.07.002.
72. Wei, Y.; Pattingre, S.; Sinha, S.; Bassik, M.; Levine, B. JNK1-Mediated Phosphorylation of Bcl-2 Regulates Starvation-Induced Autophagy. *Mol Cell* **2008**, *30*, 678–688, doi:10.1016/j.molcel.2008.06.001.
73. Cianfanelli, V.; Cecconi, F. AMBRA1: When Autophagy Meets Cell Proliferation. *Autophagy* **2015**, *11*, 1705–1707, doi:10.1080/15548627.2015.1053681.
74. Jeffries, T.R.; Dove, S.K.; Michell, R.H.; Parker, P.J. PtdIns-Specific MPR Pathway Association of a Novel WD40 Repeat Protein, WIPI49. *Mol Biol Cell* **2004**, *15*, 2652–2663, doi:10.1091/mbc.e03-10-0732.
75. Polson, H.E.J.; de Lartigue, J.; Rigden, D.J.; Reedijk, M.; Urbé, S.; Clague, M.J.; Tooze, S.A. Mammalian Atg18 (WIPI2) Localizes to Omegasome-Anchored Phagophores and Positively Regulates LC3 Lipidation. *Autophagy* **2010**, *6*, 506–522, doi:10.4161/auto.6.4.11863.
76. Proikas-Cezanne, T.; Waddell, S.; Gaugel, A.; Frickey, T.; Lupas, A.; Nordheim, A. WIPI-1alpha (WIPI49), a Member of the Novel 7-Bladed WIPI Protein Family, Is Aberrantly Expressed in Human Cancer and Is Linked to Starvation-Induced Autophagy. *Oncogene* **2004**, *23*, 9314–9325, doi:10.1038/sj.onc.1208331.
77. Bakula, D.; Müller, A.J.; Zuleger, T.; Takacs, Z.; Franz-Wachtel, M.; Thost, A.-K.; Brigger, D.; Tschan, M.P.; Frickey, T.; Robenek, H.; et al. WIPI3 and WIPI4 β -Propellers Are Scaffolds for LKB1-AMPK-TSC Signalling Circuits in the Control of Autophagy. *Nat Commun* **2017**, *8*, 15637, doi:10.1038/ncomms15637.
78. Krick, R.; Busse, R.A.; Scacioc, A.; Stephan, M.; Janshoff, A.; Thumm, M.; Kühnel, K. Structural and Functional Characterization of the Two Phosphoinositide Binding Sites of PROPPINs, a β -Propeller Protein Family. *Proc Natl Acad Sci U S A* **2012**, *109*, E2042-2049, doi:10.1073/pnas.1205128109.
79. Baskaran, S.; Ragusa, M.J.; Boura, E.; Hurley, J.H. Two-Site Recognition of Phosphatidylinositol 3-Phosphate by PROPPINs in Autophagy. *Mol Cell* **2012**, *47*, 339–348, doi:10.1016/j.molcel.2012.05.027.
80. Weidberg, H.; Shvets, E.; Elazar, Z. Biogenesis and Cargo Selectivity of Autophagosomes. *Annu Rev Biochem* **2011**, *80*, 125–156, doi:10.1146/annurev-biochem-052709-094552.
81. Kim, J.; Dalton, V.M.; Eggerton, K.P.; Scott, S.V.; Klionsky, D.J. Apg7p/Cvt2p Is Required for the Cytoplasm-to-Vacuole Targeting, Macroautophagy, and Peroxisome Degradation Pathways. *Mol Biol Cell* **1999**, *10*, 1337–1351, doi:10.1091/mbc.10.5.1337.

82. Ohsumi, Y. Molecular Dissection of Autophagy: Two Ubiquitin-like Systems. *Nat Rev Mol Cell Biol* **2001**, *2*, 211–216, doi:10.1038/35056522.
83. Shintani, T.; Mizushima, N.; Ogawa, Y.; Matsuura, A.; Noda, T.; Ohsumi, Y. Apg10p, a Novel Protein-Conjugating Enzyme Essential for Autophagy in Yeast. *EMBO J* **1999**, *18*, 5234–5241, doi:10.1093/emboj/18.19.5234.
84. Geng, J.; Klionsky, D.J. The Atg8 and Atg12 Ubiquitin-like Conjugation Systems in Macroautophagy. “Protein Modifications: Beyond the Usual Suspects” Review Series. *EMBO Rep* **2008**, *9*, 859–864, doi:10.1038/embo.2008.163.
85. Mizushima, N.; Kuma, A.; Kobayashi, Y.; Yamamoto, A.; Matsubae, M.; Takao, T.; Natsume, T.; Ohsumi, Y.; Yoshimori, T. Mouse Apg16L, a Novel WD-Repeat Protein, Targets to the Autophagic Isolation Membrane with the Apg12-Apg5 Conjugate. *J Cell Sci* **2003**, *116*, 1679–1688, doi:10.1242/jcs.00381.
86. Slobodkin, M.R.; Elazar, Z. The Atg8 Family: Multifunctional Ubiquitin-like Key Regulators of Autophagy. *Essays Biochem* **2013**, *55*, 51–64, doi:10.1042/bse0550051.
87. Jatana, N.; Ascher, D.B.; Pires, D.E.V.; Gokhale, R.S.; Thukral, L. Human LC3 and GABARAP Subfamily Members Achieve Functional Specificity via Specific Structural Modulations. *Autophagy* **2020**, *16*, 239–255, doi:10.1080/15548627.2019.1606636.
88. Shpilka, T.; Weidberg, H.; Pietrokovski, S.; Elazar, Z. Atg8: An Autophagy-Related Ubiquitin-like Protein Family. *Genome Biology* **2011**, *12*, 226, doi:10.1186/gb-2011-12-7-226.
89. Kabeya, Y.; Mizushima, N.; Yamamoto, A.; Oshitani-Okamoto, S.; Ohsumi, Y.; Yoshimori, T. LC3, GABARAP and GATE16 Localize to Autophagosomal Membrane Depending on Form-II Formation. *Journal of Cell Science* **2004**, *117*, 2805–2812, doi:10.1242/jcs.01131.
90. Klionsky, D.J.; Abdel-Aziz, A.K.; Abdelfatah, S.; Abdellatif, M.; Abdoli, A.; Abel, S.; Abeliovich, H.; Abildgaard, M.H.; Abudu, Y.P.; Acevedo-Arozena, A.; et al. Guidelines for the Use and Interpretation of Assays for Monitoring Autophagy (4th Edition). *null* **2021**, 1–382, doi:10.1080/15548627.2020.1797280.
91. Kirisako, T.; Ichimura, Y.; Okada, H.; Kabeya, Y.; Mizushima, N.; Yoshimori, T.; Ohsumi, M.; Takao, T.; Noda, T.; Ohsumi, Y. The Reversible Modification Regulates the Membrane-Binding State of Apg8/Aut7 Essential for Autophagy and the Cytoplasm to Vacuole Targeting Pathway. *J Cell Biol* **2000**, *151*, 263–276, doi:10.1083/jcb.151.2.263.
92. Tanida, I.; Sou, Y.; Ezaki, J.; Minematsu-Ikeguchi, N.; Ueno, T.; Kominami, E. HsAtg4B/HsApg4B/Autophagin-1 Cleaves the Carboxyl Termini of Three Human Atg8 Homologues and Delipidates Microtubule-Associated Protein Light Chain 3-

- and GABAA Receptor-Associated Protein-Phospholipid Conjugates. *J Biol Chem* **2004**, *279*, 36268–36276, doi:10.1074/jbc.M401461200.
93. Ichimura, Y.; Kirisako, T.; Takao, T.; Satomi, Y.; Shimonishi, Y.; Ishihara, N.; Mizushima, N.; Tanida, I.; Kominami, E.; Ohsumi, M.; et al. A Ubiquitin-like System Mediates Protein Lipidation. *Nature* **2000**, *408*, 488–492, doi:10.1038/35044114.
 94. Fujita, N.; Itoh, T.; Omori, H.; Fukuda, M.; Noda, T.; Yoshimori, T. The Atg16L Complex Specifies the Site of LC3 Lipidation for Membrane Biogenesis in Autophagy. *Mol Biol Cell* **2008**, *19*, 2092–2100, doi:10.1091/mbc.e07-12-1257.
 95. Hanada, T.; Noda, N.N.; Satomi, Y.; Ichimura, Y.; Fujioka, Y.; Takao, T.; Inagaki, F.; Ohsumi, Y. The Atg12-Atg5 Conjugate Has a Novel E3-like Activity for Protein Lipidation in Autophagy. *J Biol Chem* **2007**, *282*, 37298–37302, doi:10.1074/jbc.C700195200.
 96. Pengo, N.; Agrotis, A.; Prak, K.; Jones, J.; Ketteler, R. A Reversible Phospho-Switch Mediated by ULK1 Regulates the Activity of Autophagy Protease ATG4B. *Nat Commun* **2017**, *8*, 294, doi:10.1038/s41467-017-00303-2.
 97. Sánchez-Wandelmer, J.; Kriegenburg, F.; Rohringer, S.; Schuschnig, M.; Gómez-Sánchez, R.; Zens, B.; Abreu, S.; Hardenberg, R.; Hollenstein, D.; Gao, J.; et al. Atg4 Proteolytic Activity Can Be Inhibited by Atg1 Phosphorylation. *Nat Commun* **2017**, *8*, 295, doi:10.1038/s41467-017-00302-3.
 98. Nair, U.; Yen, W.-L.; Mari, M.; Cao, Y.; Xie, Z.; Baba, M.; Reggiori, F.; Klionsky, D.J. A Role for Atg8–PE Deconjugation in Autophagosome Biogenesis. *Autophagy* **2012**, *8*, 780–793, doi:10.4161/auto.19385.
 99. Nakatogawa, H.; Ishii, J.; Asai, E.; Ohsumi, Y. Atg4 Recycles Inappropriately Lipidated Atg8 to Promote Autophagosome Biogenesis. *Autophagy* **2012**, *8*, 177–186, doi:10.4161/auto.8.2.18373.
 100. Yu, Z.-Q.; Ni, T.; Hong, B.; Wang, H.-Y.; Jiang, F.-J.; Zou, S.; Chen, Y.; Zheng, X.-L.; Klionsky, D.J.; Liang, Y.; et al. Dual Roles of Atg8–PE Deconjugation by Atg4 in Autophagy. *Autophagy* **2012**, *8*, 883–892, doi:10.4161/auto.19652.
 101. Agrotis, A.; Pengo, N.; Burden, J.J.; Ketteler, R. Redundancy of Human ATG4 Protease Isoforms in Autophagy and LC3/GABARAP Processing Revealed in Cells. *Autophagy* **2019**, *15*, 976–997, doi:10.1080/15548627.2019.1569925.
 102. Nguyen, T.N.; Padman, B.S.; Zellner, S.; Khuu, G.; Uoselis, L.; Lam, W.K.; Skulsuppaisarn, M.; Lindblom, R.S.J.; Watts, E.M.; Behrends, C.; et al. ATG4 Family Proteins Drive Phagophore Growth Independently of the LC3/GABARAP Lipidation System. *Mol Cell* **2021**, *81*, 2013–2030.e9, doi:10.1016/j.molcel.2021.03.001.

103. Betin, V.M.S.; Singleton, B.K.; Parsons, S.F.; Anstee, D.J.; Lane, J.D. Autophagy Facilitates Organelle Clearance during Differentiation of Human Erythroblasts: Evidence for a Role for ATG4 Paralogs during Autophagosome Maturation. *Autophagy* **2013**, *9*, 881–893, doi:10.4161/auto.24172.
104. Mizushima, N.; Komatsu, M. Autophagy: Renovation of Cells and Tissues. *Cell* **2011**, *147*, 728–741, doi:10.1016/j.cell.2011.10.026.
105. Kuma, A.; Komatsu, M.; Mizushima, N. Autophagy-Monitoring and Autophagy-Deficient Mice. *Autophagy* **2017**, *13*, 1619–1628, doi:10.1080/15548627.2017.1343770.
106. Johansen, T.; Lamark, T. Selective Autophagy: ATG8 Family Proteins, LIR Motifs and Cargo Receptors. *J Mol Biol* **2020**, *432*, 80–103, doi:10.1016/j.jmb.2019.07.016.
107. Weidberg, H.; Shvets, E.; Shpilka, T.; Shimron, F.; Shinder, V.; Elazar, Z. LC3 and GATE-16/GABARAP Subfamilies Are Both Essential yet Act Differently in Autophagosome Biogenesis. *The EMBO Journal* **2010**, *29*, 1792–1802, doi:10.1038/emboj.2010.74.
108. Lystad, A.H.; Simonsen, A. Mechanisms and Pathophysiological Roles of the ATG8 Conjugation Machinery. *Cells* **2019**, *8*, E973, doi:10.3390/cells8090973.
109. He, C.; Song, H.; Yorimitsu, T.; Monastyrska, I.; Yen, W.-L.; Legakis, J.E.; Klionsky, D.J. Recruitment of Atg9 to the Preautophagosomal Structure by Atg11 Is Essential for Selective Autophagy in Budding Yeast. *J Cell Biol* **2006**, *175*, 925–935, doi:10.1083/jcb.200606084.
110. Yamamoto, H.; Kakuta, S.; Watanabe, T.M.; Kitamura, A.; Sekito, T.; Kondo-Kakuta, C.; Ichikawa, R.; Kinjo, M.; Ohsumi, Y. Atg9 Vesicles Are an Important Membrane Source during Early Steps of Autophagosome Formation. *J Cell Biol* **2012**, *198*, 219–233, doi:10.1083/jcb.201202061.
111. Young, A.R.J.; Chan, E.Y.W.; Hu, X.W.; Köchl, R.; Crawshaw, S.G.; High, S.; Hailey, D.W.; Lippincott-Schwartz, J.; Tooze, S.A. Starvation and ULK1-Dependent Cycling of Mammalian Atg9 between the TGN and Endosomes. *J Cell Sci* **2006**, *119*, 3888–3900, doi:10.1242/jcs.03172.
112. Mizushima, N.; Klionsky, D.J. Protein Turnover via Autophagy: Implications for Metabolism. *Annu Rev Nutr* **2007**, *27*, 19–40, doi:10.1146/annurev.nutr.27.061406.093749.
113. Pfeifer, U. Inhibition by Insulin of the Formation of Autophagic Vacuoles in Rat Liver. A Morphometric Approach to the Kinetics of Intracellular Degradation by Autophagy. *J Cell Biol* **1978**, *78*, 152–167, doi:10.1083/jcb.78.1.152.

114. Schworer, C.M.; Shiffer, K.A.; Mortimore, G.E. Quantitative Relationship between Autophagy and Proteolysis during Graded Amino Acid Deprivation in Perfused Rat Liver. *J Biol Chem* **1981**, *256*, 7652–7658.
115. Monastyrska, I.; Rieter, E.; Klionsky, D.J.; Reggiori, F. Multiple Roles of the Cytoskeleton in Autophagy. *Biol Rev Camb Philos Soc* **2009**, *84*, 431–448, doi:10.1111/j.1469-185X.2009.00082.x.
116. Yang, Z.; Klionsky, D.J. An Overview of the Molecular Mechanism of Autophagy. *Curr Top Microbiol Immunol* **2009**, *335*, 1–32, doi:10.1007/978-3-642-00302-8_1.
117. Berg, T.O.; Fengsrud, M.; Strømhaug, P.E.; Berg, T.; Seglen, P.O. Isolation and Characterization of Rat Liver Amphisomes. Evidence for Fusion of Autophagosomes with Both Early and Late Endosomes. *J Biol Chem* **1998**, *273*, 21883–21892, doi:10.1074/jbc.273.34.21883.
118. Tooze, J.; Hollinshead, M.; Ludwig, T.; Howell, K.; Hoflack, B.; Kern, H. In Exocrine Pancreas, the Basolateral Endocytic Pathway Converges with the Autophagic Pathway Immediately after the Early Endosome. *J Cell Biol* **1990**, *111*, 329–345, doi:10.1083/jcb.111.2.329.
119. Itakura, E.; Kishi-Itakura, C.; Mizushima, N. The Hairpin-Type Tail-Anchored SNARE Syntaxin 17 Targets to Autophagosomes for Fusion with Endosomes/Lysosomes. *Cell* **2012**, *151*, 1256–1269, doi:10.1016/j.cell.2012.11.001.
120. Diao, J.; Liu, R.; Rong, Y.; Zhao, M.; Zhang, J.; Lai, Y.; Zhou, Q.; Wilz, L.M.; Li, J.; Vivona, S.; et al. ATG14 Promotes Membrane Tethering and Fusion of Autophagosomes to Endolysosomes. *Nature* **2015**, *520*, 563–566, doi:10.1038/nature14147.
121. Sugawara, K.; Suzuki, N.N.; Fujioka, Y.; Mizushima, N.; Ohsumi, Y.; Inagaki, F. The Crystal Structure of Microtubule-Associated Protein Light Chain 3, a Mammalian Homologue of *Saccharomyces Cerevisiae* Atg8. *Genes to Cells* **2004**, *9*, 611–618, doi:10.1111/j.1356-9597.2004.00750.x.
122. Paz, Y.; Elazar, Z.; Fass, D. Structure of GATE-16, Membrane Transport Modulator and Mammalian Ortholog of Autophagocytosis Factor Aut7p. *J Biol Chem* **2000**, *275*, 25445–25450, doi:10.1074/jbc.C000307200.
123. Bavro, V.N.; Sola, M.; Bracher, A.; Kneussel, M.; Betz, H.; Weissenhorn, W. Crystal Structure of the GABAA-Receptor-Associated Protein, GABARAP. *EMBO Rep* **2002**, *3*, 183–189, doi:10.1093/embo-reports/kvf026.
124. Coyle, J.E.; Qamar, S.; Rajashankar, K.R.; Nikolov, D.B. Structure of GABARAP in Two Conformations: Implications for GABAA Receptor Localization and Tubulin Binding. *Neuron* **2002**, *33*, 63–74, doi:10.1016/S0896-6273(01)00558-X.

125. Knight, D.; Harris, R.; McAlister, M.S.B.; Phelan, J.P.; Geddes, S.; Moss, S.J.; Driscoll, P.C.; Keep, N.H. The X-Ray Crystal Structure and Putative Ligand-Derived Peptide Binding Properties of Gamma-Aminobutyric Acid Receptor Type A Receptor-Associated Protein. *J Biol Chem* **2002**, *277*, 5556–5561, doi:10.1074/jbc.M109753200.
126. Stangler, T.; Mayr, L.M.; Willbold, D. Solution Structure of Human GABA(A) Receptor-Associated Protein GABARAP: Implications for Biological Function and Its Regulation. *J Biol Chem* **2002**, *277*, 13363–13366, doi:10.1074/jbc.C200050200.
127. Kumeta, H.; Watanabe, M.; Nakatogawa, H.; Yamaguchi, M.; Ogura, K.; Adachi, W.; Fujioka, Y.; Noda, N.N.; Ohsumi, Y.; Inagaki, F. The NMR Structure of the Autophagy-Related Protein Atg8. *J Biomol NMR* **2010**, *47*, 237–241, doi:10.1007/s10858-010-9420-1.
128. Schwarten, M.; Stoldt, M.; Mohrlüder, J.; Willbold, D. Solution Structure of Atg8 Reveals Conformational Polymorphism of the N-Terminal Domain. *Biochemical and Biophysical Research Communications* **2010**, *395*, 426–431, doi:10.1016/j.bbrc.2010.04.043.
129. Wu, F.; Watanabe, Y.; Guo, X.-Y.; Qi, X.; Wang, P.; Zhao, H.-Y.; Wang, Z.; Fujioka, Y.; Zhang, H.; Ren, J.-Q.; et al. Structural Basis of the Differential Function of the Two C. Elegans Atg8 Homologs, LGG-1 and LGG-2, in Autophagy. *Mol. Cell* **2015**, *60*, 914–929, doi:10.1016/j.molcel.2015.11.019.
130. Kopitz, J.; Kisen, G.O.; Gordon, P.B.; Bohley, P.; Seglen, P.O. Nonselective Autophagy of Cytosolic Enzymes by Isolated Rat Hepatocytes. *J Cell Biol* **1990**, *111*, 941–953, doi:10.1083/jcb.111.3.941.
131. Kuma, A.; Hatano, M.; Matsui, M.; Yamamoto, A.; Nakaya, H.; Yoshimori, T.; Ohsumi, Y.; Tokuhisa, T.; Mizushima, N. The Role of Autophagy during the Early Neonatal Starvation Period. *Nature* **2004**, *432*, 1032–1036, doi:10.1038/nature03029.
132. Kraft, C.; Reggiori, F.; Peter, M. Selective Types of Autophagy in Yeast. *Biochim Biophys Acta* **2009**, *1793*, 1404–1412, doi:10.1016/j.bbamcr.2009.02.006.
133. Khaminets, A.; Behl, C.; Dikic, I. Ubiquitin-Dependent And Independent Signals In Selective Autophagy. *Trends Cell Biol.* **2016**, *26*, 6–16, doi:10.1016/j.tcb.2015.08.010.
134. Rogov, V.; Dötsch, V.; Johansen, T.; Kirkin, V. Interactions between Autophagy Receptors and Ubiquitin-like Proteins Form the Molecular Basis for Selective Autophagy. *Mol Cell* **2014**, *53*, 167–178, doi:10.1016/j.molcel.2013.12.014.
135. Galluzzi, L.; Baehrecke, E.H.; Ballabio, A.; Boya, P.; Bravo-San Pedro, J.M.; Cecconi, F.; Choi, A.M.; Chu, C.T.; Codogno, P.; Colombo, M.I.; et al. Molecular

- Definitions of Autophagy and Related Processes. *EMBO J* **2017**, *36*, 1811–1836, doi:10.15252/embj.201796697.
136. Ahsan, N.; Jena, K.K.; Mehto, S.; Chauhan, S. Chapter 4 - Selectivity and Trafficking of Autophagic Cargoes. In *Autophagy in Health and Disease (Second Edition)*; Rothermel, B.A., Diwan, A., Eds.; Academic Press, 2022; pp. 39–56 ISBN 978-0-12-822003-0.
 137. Morimoto, D.; Shirakawa, M. The Evolving World of Ubiquitin: Transformed Polyubiquitin Chains. *Biomol Concepts* **2016**, *7*, 157–167, doi:10.1515/bmc-2016-0009.
 138. Husnjak, K.; Dikic, I. Ubiquitin-Binding Proteins: Decoders of Ubiquitin-Mediated Cellular Functions. *Annu Rev Biochem* **2012**, *81*, 291–322, doi:10.1146/annurev-biochem-051810-094654.
 139. Bjørkøy, G.; Lamark, T.; Brech, A.; Outzen, H.; Perander, M.; Overvatn, A.; Stenmark, H.; Johansen, T. P62/SQSTM1 Forms Protein Aggregates Degraded by Autophagy and Has a Protective Effect on Huntingtin-Induced Cell Death. *J. Cell Biol.* **2005**, *171*, 603–614, doi:10.1083/jcb.200507002.
 140. Øverbye, A.; Fengsrud, M.; Seglen, P.O. Proteomic Analysis of Membrane-Associated Proteins from Rat Liver Autophagosomes. *Autophagy* **2007**, *3*, 300–322, doi:10.4161/auto.3910.
 141. Vadlamudi, R.K.; Joung, I.; Strominger, J.L.; Shin, J. P62, a Phosphotyrosine-Independent Ligand of the SH2 Domain of P56lck, Belongs to a New Class of Ubiquitin-Binding Proteins. *J Biol Chem* **1996**, *271*, 20235–20237, doi:10.1074/jbc.271.34.20235.
 142. Tal, R.; Winter, G.; Ecker, N.; Klionsky, D.J.; Abeliovich, H. Aup1p, a Yeast Mitochondrial Protein Phosphatase Homolog, Is Required for Efficient Stationary Phase Mitophagy and Cell Survival. *J Biol Chem* **2007**, *282*, 5617–5624, doi:10.1074/jbc.M605940200.
 143. Kim, I.; Rodriguez-Enriquez, S.; Lemasters, J.J. Selective Degradation of Mitochondria by Mitophagy. *Archives of Biochemistry and Biophysics* **2007**, *462*, 245–253, doi:10.1016/j.abb.2007.03.034.
 144. Wallace, D.C.; Fan, W.; Procaccio, V. Mitochondrial Energetics and Therapeutics. *Annu Rev Pathol* **2010**, *5*, 297–348, doi:10.1146/annurev.pathol.4.110807.092314.
 145. Mammucari, C.; Patron, M.; Granatiero, V.; Rizzuto, R. Molecules and Roles of Mitochondrial Calcium Signaling. *Biofactors* **2011**, *37*, 219–227, doi:10.1002/biof.160.
 146. Wang, C.; Youle, R.J. The Role of Mitochondria in Apoptosis. *Annu Rev Genet* **2009**, *43*, 95–118, doi:10.1146/annurev-genet-102108-134850.

147. Wong, H.-S.; Dighe, P.A.; Mezera, V.; Monternier, P.-A.; Brand, M.D. Production of Superoxide and Hydrogen Peroxide from Specific Mitochondrial Sites under Different Bioenergetic Conditions. *J Biol Chem* **2017**, *292*, 16804–16809, doi:10.1074/jbc.R117.789271.
148. Ross, W.N. Understanding Calcium Waves and Sparks in Central Neurons. *Nat Rev Neurosci* **2012**, *13*, 157–168, doi:10.1038/nrn3168.
149. James, A.M.; Murphy, M.P. How Mitochondrial Damage Affects Cell Function. *J. Biomed. Sci.* **2002**, *9*, 475–487, doi:10.1159/000064721.
150. Martin, S.J.; Henry, C.M.; Cullen, S.P. A Perspective on Mammalian Caspases as Positive and Negative Regulators of Inflammation. *Molecular Cell* **2012**, *46*, 387–397, doi:10.1016/j.molcel.2012.04.026.
151. Hu, L.; Wang, H.; Huang, L.; Zhao, Y.; Wang, J. The Protective Roles of ROS-Mediated Mitophagy on 125I Seeds Radiation Induced Cell Death in HCT116 Cells. *Oxid Med Cell Longev* **2016**, *2016*, doi:10.1155/2016/9460462.
152. Lemasters, J.J. Selective Mitochondrial Autophagy, or Mitophagy, as a Targeted Defense Against Oxidative Stress, Mitochondrial Dysfunction, and Aging. *Rejuvenation Research* **2005**, *8*, 3–5, doi:10.1089/rej.2005.8.3.
153. Narendra, D.; Tanaka, A.; Suen, D.-F.; Youle, R.J. Parkin Is Recruited Selectively to Impaired Mitochondria and Promotes Their Autophagy. *The Journal of Cell Biology* **2008**, *183*, 795–803, doi:10.1083/jcb.200809125.
154. Pickrell, A.M.; Youle, R.J. The Roles of PINK1, Parkin, and Mitochondrial Fidelity in Parkinson's Disease. *Neuron* **2015**, *85*, 257–273, doi:10.1016/j.neuron.2014.12.007.
155. Jin, S.M.; Lazarou, M.; Wang, C.; Kane, L.A.; Narendra, D.P.; Youle, R.J. Mitochondrial Membrane Potential Regulates PINK1 Import and Proteolytic Destabilization by PARL. *J. Cell Biol.* **2010**, *191*, 933–942, doi:10.1083/jcb.201008084.
156. Deas, E.; Plun-Favreau, H.; Gandhi, S.; Desmond, H.; Kjaer, S.; Loh, S.H.Y.; Renton, A.E.M.; Harvey, R.J.; Whitworth, A.J.; Martins, L.M.; et al. PINK1 Cleavage at Position A103 by the Mitochondrial Protease PARL. *Hum. Mol. Genet.* **2011**, *20*, 867–879, doi:10.1093/hmg/ddq526.
157. Meissner, C.; Lorenz, H.; Weihofen, A.; Selkoe, D.J.; Lemberg, M.K. The Mitochondrial Intramembrane Protease PARL Cleaves Human Pink1 to Regulate Pink1 Trafficking. *J. Neurochem.* **2011**, *117*, 856–867, doi:10.1111/j.1471-4159.2011.07253.x.
158. Greene, A.W.; Grenier, K.; Aguilera, M.A.; Muise, S.; Farazifard, R.; Haque, M.E.; McBride, H.M.; Park, D.S.; Fon, E.A. Mitochondrial Processing Peptidase

- Regulates PINK1 Processing, Import and Parkin Recruitment. *EMBO Rep* **2012**, *13*, 378–385, doi:10.1038/embor.2012.14.
159. Harper, J.W.; Ordureau, A.; Heo, J.-M. Building and Decoding Ubiquitin Chains for Mitophagy. *Nat. Rev. Mol. Cell Biol.* **2018**, *19*, 93–108, doi:10.1038/nrm.2017.129.
160. Sekine, S.; Youle, R.J. PINK1 Import Regulation; a Fine System to Convey Mitochondrial Stress to the Cytosol. *BMC Biol.* **2018**, *16*, 2, doi:10.1186/s12915-017-0470-7.
161. Lazarou, M.; Jin, S.M.; Kane, L.A.; Youle, R.J. Role of PINK1 Binding to the TOM Complex and Alternate Intracellular Membranes in Recruitment and Activation of the E3 Ligase Parkin. *Dev. Cell* **2012**, *22*, 320–333, doi:10.1016/j.devcel.2011.12.014.
162. Okatsu, K.; Uno, M.; Koyano, F.; Go, E.; Kimura, M.; Oka, T.; Tanaka, K.; Matsuda, N. A Dimeric PINK1-Containing Complex on Depolarized Mitochondria Stimulates Parkin Recruitment. *J. Biol. Chem.* **2013**, *288*, 36372–36384, doi:10.1074/jbc.M113.509653.
163. Hasson, S.A.; Kane, L.A.; Yamano, K.; Huang, C.-H.; Sliter, D.A.; Buehler, E.; Wang, C.; Heman-Ackah, S.M.; Hessa, T.; Guha, R.; et al. High-Content Genome-Wide RNAi Screens Identify Regulators of Parkin Upstream of Mitophagy. *Nature* **2013**, *504*, 291–295, doi:10.1038/nature12748.
164. Koyano, F.; Okatsu, K.; Kosako, H.; Tamura, Y.; Go, E.; Kimura, M.; Kimura, Y.; Tsuchiya, H.; Yoshihara, H.; Hirokawa, T.; et al. Ubiquitin Is Phosphorylated by PINK1 to Activate Parkin. *Nature* **2014**, *510*, 162–166, doi:10.1038/nature13392.
165. Chan, N.C.; Salazar, A.M.; Pham, A.H.; Sweredoski, M.J.; Kolawa, N.J.; Graham, R.L.J.; Hess, S.; Chan, D.C. Broad Activation of the Ubiquitin-Proteasome System by Parkin Is Critical for Mitophagy. *Hum. Mol. Genet.* **2011**, *20*, 1726–1737, doi:10.1093/hmg/ddr048.
166. Yoshii, S.R.; Kishi, C.; Ishihara, N.; Mizushima, N. Parkin Mediates Proteasome-Dependent Protein Degradation and Rupture of the Outer Mitochondrial Membrane. *J. Biol. Chem.* **2011**, *286*, 19630–19640, doi:10.1074/jbc.M110.209338.
167. Gong, G.; Song, M.; Csordas, G.; Kelly, D.P.; Matkovich, S.J.; Dorn, G.W. Parkin-Mediated Mitophagy Directs Perinatal Cardiac Metabolic Maturation in Mice. *Science* **2015**, *350*, aad2459–aad2459, doi:10.1126/science.aad2459.
168. Ordureau, A.; Paulo, J.A.; Zhang, W.; Ahfeldt, T.; Zhang, J.; Cohn, E.F.; Hou, Z.; Heo, J.-M.; Rubin, L.L.; Sidhu, S.S.; et al. Dynamics of PARKIN-Dependent Mitochondrial Ubiquitylation in Induced Neurons and Model Systems Revealed by Digital Snapshot Proteomics. *Mol. Cell* **2018**, *70*, 211–227.e8, doi:10.1016/j.molcel.2018.03.012.

169. Rose, C.M.; Isasa, M.; Ordureau, A.; Prado, M.A.; Beausoleil, S.A.; Jedrychowski, M.P.; Finley, D.J.; Harper, J.W.; Gygi, S.P. Highly Multiplexed Quantitative Mass Spectrometry Analysis of Ubiquitylomes. *Cell Systems* **2016**, *3*, 395-403.e4, doi:10.1016/j.cels.2016.08.009.
170. Sarraf, S.A.; Raman, M.; Guarani-Pereira, V.; Sowa, M.E.; Huttlin, E.L.; Gygi, S.P.; Harper, J.W. Landscape of the PARKIN-Dependent Ubiquitylome in Response to Mitochondrial Depolarization. *Nature* **2013**, *496*, 372–376, doi:10.1038/nature12043.
171. Geisler, S.; Holmström, K.M.; Skujat, D.; Fiesel, F.C.; Rothfuss, O.C.; Kahle, P.J.; Springer, W. PINK1/Parkin-Mediated Mitophagy Is Dependent on VDAC1 and P62/SQSTM1. *Nat. Cell Biol.* **2010**, *12*, 119–131, doi:10.1038/ncb2012.
172. Narendra, D.P.; Youle, R.J. Targeting Mitochondrial Dysfunction: Role for PINK1 and Parkin in Mitochondrial Quality Control. *Antioxidants & Redox Signaling* **2011**, *14*, 1929–1938, doi:10.1089/ars.2010.3799.
173. Palikaras, K.; Lionaki, E.; Tavernarakis, N. Mechanisms of Mitophagy in Cellular Homeostasis, Physiology and Pathology. *Nat Cell Biol* **2018**, *20*, 1013–1022, doi:10.1038/s41556-018-0176-2.
174. Gao, F.; Chen, D.; Si, J.; Hu, Q.; Qin, Z.; Fang, M.; Wang, G. The Mitochondrial Protein BNIP3L Is the Substrate of PARK2 and Mediates Mitophagy in PINK1/PARK2 Pathway. *Hum Mol Genet* **2015**, *24*, 2528–2538, doi:10.1093/hmg/ddv017.
175. Zhang, T.; Xue, L.; Li, L.; Tang, C.; Wan, Z.; Wang, R.; Tan, J.; Tan, Y.; Han, H.; Tian, R.; et al. BNIP3 Protein Suppresses PINK1 Kinase Proteolytic Cleavage to Promote Mitophagy. *J Biol Chem* **2016**, *291*, 21616–21629, doi:10.1074/jbc.M116.733410.
176. Wei, Y.; Chiang, W.-C.; Sumpter, R.; Mishra, P.; Levine, B. Prohibitin 2 Is an Inner Mitochondrial Membrane Mitophagy Receptor. *Cell* **2017**, *168*, 224-238.e10, doi:10.1016/j.cell.2016.11.042.
177. Yan, C.; Gong, L.; Chen, L.; Xu, M.; Abou-Hamdan, H.; Tang, M.; Désaubry, L.; Song, Z. PHB2 (Prohibitin 2) Promotes PINK1-PRKN/Parkin-Dependent Mitophagy by the PARL-PGAM5-PINK1 Axis. *Autophagy* **2020**, *16*, 419–434, doi:10.1080/15548627.2019.1628520.
178. Levine, B.; Kroemer, G. Biological Functions of Autophagy Genes: A Disease Perspective. *Cell* **2019**, *176*, 11–42, doi:10.1016/j.cell.2018.09.048.
179. Mizushima, N.; Yoshimori, T.; Levine, B. Methods in Mammalian Autophagy Research. *Cell* **2010**, *140*, 313–326, doi:10.1016/j.cell.2010.01.028.

180. Mizushima, N.; Yoshimori, T. How to Interpret LC3 Immunoblotting. *Autophagy* **2007**, *3*, 542–545, doi:10.4161/auto.4600.
181. Andres, A. Chapter 6 - Methods for Measuring Autophagy. In *Autophagy in Health and Disease (Second Edition)*; Rothermel, B.A., Diwan, A., Eds.; Academic Press, 2022; pp. 71–79 ISBN 978-0-12-822003-0.
182. Kabeya, Y.; Mizushima, N.; Ueno, T.; Yamamoto, A.; Kirisako, T.; Noda, T.; Kominami, E.; Ohsumi, Y.; Yoshimori, T. LC3, a Mammalian Homologue of Yeast Apg8p, Is Localized in Autophagosomal Membranes after Processing. *EMBO J* **2000**, *19*, 5720–5728, doi:10.1093/emboj/19.21.5720.
183. Runwal, G.; Stamatakou, E.; Siddiqi, F.H.; Puri, C.; Zhu, Y.; Rubinsztein, D.C. LC3-Positive Structures Are Prominent in Autophagy-Deficient Cells. *Scientific Reports* **2019**, *9*, 10147, doi:10.1038/s41598-019-46657-z.
184. Eskelinen, E.-L.; Reggiori, F.; Baba, M.; Kovács, A.L.; Seglen, P.O. Seeing Is Believing: The Impact of Electron Microscopy on Autophagy Research. *Autophagy* **2011**, *7*, 935–956, doi:10.4161/auto.7.9.15760.
185. Lichtman, J.W.; Conchello, J.-A. Fluorescence Microscopy. *Nat Methods* **2005**, *2*, 910–919, doi:10.1038/nmeth817.
186. Shimomura, O.; Johnson, F.H.; Saiga, Y. Extraction, Purification and Properties of Aequorin, a Bioluminescent Protein from the Luminous Hydromedusan, Aequorea. *J Cell Comp Physiol* **1962**, *59*, 223–239, doi:10.1002/jcp.1030590302.
187. Eason, M.G.; Damry, A.M.; Chica, R.A. Structure-Guided Rational Design of Red Fluorescent Proteins: Towards Designer Genetically-Encoded Fluorophores. *Curr Opin Struct Biol* **2017**, *45*, 91–99, doi:10.1016/j.sbi.2016.12.001.
188. Goedhart, J.; von Stetten, D.; Noirclerc-Savoye, M.; Lelimousin, M.; Joosen, L.; Hink, M.A.; van Weeren, L.; Gadella, T.W.J.; Royant, A. Structure-Guided Evolution of Cyan Fluorescent Proteins towards a Quantum Yield of 93%. *Nat Commun* **2012**, *3*, 751, doi:10.1038/ncomms1738.
189. Kamiyama, D.; Sekine, S.; Barsi-Rhyne, B.; Hu, J.; Chen, B.; Gilbert, L.A.; Ishikawa, H.; Leonetti, M.D.; Marshall, W.F.; Weissman, J.S.; et al. Versatile Protein Tagging in Cells with Split Fluorescent Protein. *Nat Commun* **2016**, *7*, 11046, doi:10.1038/ncomms11046.
190. Li, Y.; Tsien, R.W. PHTomato, a Red, Genetically Encoded Indicator That Enables Multiplex Interrogation of Synaptic Activity. *Nat Neurosci* **2012**, *15*, 1047–1053, doi:10.1038/nn.3126.
191. Sankaranarayanan, S.; De Angelis, D.; Rothman, J.E.; Ryan, T.A. The Use of Phluorins for Optical Measurements of Presynaptic Activity. *Biophys J* **2000**, *79*, 2199–2208, doi:10.1016/S0006-3495(00)76468-X.

192. Shen, Y.; Rosendale, M.; Campbell, R.E.; Perrais, D. PHuji, a PH-Sensitive Red Fluorescent Protein for Imaging of Exo- and Endocytosis. *J Cell Biol* **2014**, *207*, 419–432, doi:10.1083/jcb.201404107.
193. Heim, R.; Prasher, D.C.; Tsien, R.Y. Wavelength Mutations and Posttranslational Autoxidation of Green Fluorescent Protein. *Proc Natl Acad Sci U S A* **1994**, *91*, 12501–12504, doi:10.1073/pnas.91.26.12501.
194. Pakhomov, A.A.; Martynov, V.I. GFP Family: Structural Insights into Spectral Tuning. *Chem Biol* **2008**, *15*, 755–764, doi:10.1016/j.chembiol.2008.07.009.
195. Remington, S.J. Fluorescent Proteins: Maturation, Photochemistry and Photophysics. *Curr Opin Struct Biol* **2006**, *16*, 714–721, doi:10.1016/j.sbi.2006.10.001.
196. Stepanenko, O.V.; Stepanenko, O.V.; Shcherbakova, D.M.; Kuznetsova, I.M.; Turoverov, K.K.; Verkhusha, V.V. Modern Fluorescent Proteins: From Chromophore Formation to Novel Intracellular Applications. *Biotechniques* **2011**, *51*, 313–314, 316, 318 passim, doi:10.2144/000113765.
197. Kim, H.; Seong, J. Fluorescent Protein-Based Autophagy Biosensors. *Materials (Basel)* **2021**, *14*, 3019, doi:10.3390/ma14113019.
198. Bains, M.; Heidenreich, K.A. Live-Cell Imaging of Autophagy Induction and Autophagosome-Lysosome Fusion in Primary Cultured Neurons. *Methods Enzymol* **2009**, *453*, 145–158, doi:10.1016/S0076-6879(08)04007-X.
199. Demarchi, F.; Bertoli, C.; Copetti, T.; Tanida, I.; Brancolini, C.; Eskelinen, E.-L.; Schneider, C. Calpain Is Required for Macroautophagy in Mammalian Cells. *J Cell Biol* **2006**, *175*, 595–605, doi:10.1083/jcb.200601024.
200. Flavin, W.P.; Bousset, L.; Green, Z.C.; Chu, Y.; Skarpathiotis, S.; Chaney, M.J.; Kordower, J.H.; Melki, R.; Campbell, E.M. Endocytic Vesicle Rupture Is a Conserved Mechanism of Cellular Invasion by Amyloid Proteins. *Acta Neuropathol* **2017**, *134*, 629–653, doi:10.1007/s00401-017-1722-x.
201. Jahreiss, L.; Menzies, F.M.; Rubinsztein, D.C. The Itinerary of Autophagosomes: From Peripheral Formation to Kiss-and-Run Fusion with Lysosomes. *Traffic* **2008**, *9*, 574–587, doi:10.1111/j.1600-0854.2008.00701.x.
202. Mizushima, N.; Yamamoto, A.; Hatano, M.; Kobayashi, Y.; Kabeya, Y.; Suzuki, K.; Tokuhiya, T.; Ohsumi, Y.; Yoshimori, T. Dissection of Autophagosome Formation Using Apg5-Deficient Mouse Embryonic Stem Cells. *J Cell Biol* **2001**, *152*, 657–668, doi:10.1083/jcb.152.4.657.
203. Tanida, I.; Yamaji, T.; Ueno, T.; Ishiura, S.; Kominami, E.; Hanada, K. Consideration about Negative Controls for LC3 and Expression Vectors for Four

- Colored Fluorescent Protein-LC3 Negative Controls. *Autophagy* **2008**, *4*, 131–134, doi:10.4161/auto.5233.
204. Kuma, A.; Matsui, M.; Mizushima, N. LC3, an Autophagosome Marker, Can Be Incorporated into Protein Aggregates Independent of Autophagy: Caution in the Interpretation of LC3 Localization. *Autophagy* **2007**, *3*, 323–328, doi:10.4161/auto.4012.
205. Tsien, R.Y. The Green Fluorescent Protein. *Annu Rev Biochem* **1998**, *67*, 509–544, doi:10.1146/annurev.biochem.67.1.509.
206. Chen, R.; Jäättelä, M.; Liu, B. Lysosome as a Central Hub for Rewiring PH Homeostasis in Tumors. *Cancers (Basel)* **2020**, *12*, 2437, doi:10.3390/cancers12092437.
207. Buckingham, E.M.; Carpenter, J.E.; Jackson, W.; Grose, C. Nuclear LC3-Positive Puncta in Stressed Cells Do Not Represent Autophagosomes. *Biotechniques* **2014**, *57*, 241–244, doi:10.2144/000114226.
208. Lee, Y.-K.; Jun, Y.-W.; Choi, H.-E.; Huh, Y.H.; Kaang, B.-K.; Jang, D.-J.; Lee, J.-A. Development of LC3/GABARAP Sensors Containing a LIR and a Hydrophobic Domain to Monitor Autophagy. *EMBO J* **2017**, *36*, 1100–1116, doi:10.15252/embj.201696315.
209. Kimura, S.; Noda, T.; Yoshimori, T. Dissection of the Autophagosome Maturation Process by a Novel Reporter Protein, Tandem Fluorescent-Tagged LC3. *Autophagy* **2007**, *3*, 452–460, doi:10.4161/auto.4451.
210. Kim, H.; Kim, H.; Choi, J.; Inn, K.-S.; Seong, J. Visualization of Autophagy Progression by a Red–Green–Blue Autophagy Sensor. *ACS Sens.* **2020**, *5*, 3850–3861, doi:10.1021/acssensors.0c00809.
211. Kaizuka, T.; Morishita, H.; Hama, Y.; Tsukamoto, S.; Matsui, T.; Toyota, Y.; Kodama, A.; Ishihara, T.; Mizushima, T.; Mizushima, N. An Autophagic Flux Probe That Releases an Internal Control. *Mol Cell* **2016**, *64*, 835–849, doi:10.1016/j.molcel.2016.09.037.
212. Allen, G.F.G.; Toth, R.; James, J.; Ganley, I.G. Loss of Iron Triggers PINK1/Parkin-Independent Mitophagy. *EMBO Rep.* **2013**, *14*, 1127–1135, doi:10.1038/embor.2013.168.
213. Kim, S.-J.; Khan, M.; Quan, J.; Till, A.; Subramani, S.; Siddiqui, A. Hepatitis B Virus Disrupts Mitochondrial Dynamics: Induces Fission and Mitophagy to Attenuate Apoptosis. *PLoS Pathog.* **2013**, *9*, e1003722, doi:10.1371/journal.ppat.1003722.
214. McWilliams, T.G.; Prescott, A.R.; Allen, G.F.G.; Tamjar, J.; Munson, M.J.; Thomson, C.; Muqit, M.M.K.; Ganley, I.G. Mito-QC Illuminates Mitophagy and

- Mitochondrial Architecture in Vivo. *J. Cell Biol.* **2016**, *214*, 333–345, doi:10.1083/jcb.201603039.
215. Sun, N.; Yun, J.; Liu, J.; Malide, D.; Liu, C.; Rovira, I.I.; Holmström, K.M.; Fergussan, M.M.; Yoo, Y.H.; Combs, C.A.; et al. Measuring In Vivo Mitophagy. *Molecular Cell* **2015**, *60*, 685–696, doi:10.1016/j.molcel.2015.10.009.
216. Katayama, H.; Kogure, T.; Mizushima, N.; Yoshimori, T.; Miyawaki, A. A Sensitive and Quantitative Technique for Detecting Autophagic Events Based on Lysosomal Delivery. *Chem. Biol.* **2011**, *18*, 1042–1052, doi:10.1016/j.chembiol.2011.05.013.
217. Bingol, B.; Tea, J.S.; Phu, L.; Reichelt, M.; Bakalarski, C.E.; Song, Q.; Foreman, O.; Kirkpatrick, D.S.; Sheng, M. The Mitochondrial Deubiquitinase USP30 Opposes Parkin-Mediated Mitophagy. *Nature* **2014**, *510*, 370–375, doi:10.1038/nature13418.
218. Algar, W.R.; Hildebrandt, N.; Vogel, S.S.; Medintz, I.L. FRET as a Biomolecular Research Tool - Understanding Its Potential While Avoiding Pitfalls. *Nat Methods* **2019**, *16*, 815–829, doi:10.1038/s41592-019-0530-8.
219. Medintz, I.L.; Hildebrandt, N. *FRET - FRET Resonance Energy Transfer: From Theory to Applications*; Wiley-VCH Verlag GmbH: Weinheim, Germany, 2014; ISBN 978-3-527-65602-8.
220. Forster, Th. Energiewanderung und Fluoreszenz. *Naturwissenschaften* **1946**, *33*, 166–175, doi:10.1007/BF00585226.
221. Ma, L.; Yang, F.; Zheng, J. Application of Fluorescence Resonance Energy Transfer in Protein Studies. *J Mol Struct* **2014**, *1077*, 87–100, doi:10.1016/j.molstruc.2013.12.071.
222. Vogel, S.S.; Thaler, C.; Koushik, S.V. Fanciful FRET. *Sci STKE* **2006**, *2006*, re2, doi:10.1126/stke.3312006re2.
223. Cottet, M.; Faklaris, O.; Zwier, J.M.; Trinquet, E.; Pin, J.-P.; Durroux, T. Original Fluorescent Ligand-Based Assays Open New Perspectives in G-Protein Coupled Receptor Drug Screening. *Pharmaceuticals (Basel)* **2011**, *4*, 202–214, doi:10.3390/ph4010202.
224. Schlessinger, J. Novel Fluorescent Approaches for Studying Cell Signaling in Single Cells. *Nat Biotechnol* **2000**, *18*, 262–263, doi:10.1038/73687.
225. Szöllosi, J.; Damjanovich, S.; Mátyus, L. Application of Fluorescence Resonance Energy Transfer in the Clinical Laboratory: Routine and Research. *Cytometry* **1998**, *34*, 159–179.

226. Albrecht, C. Joseph R. Lakowicz: Principles of Fluorescence Spectroscopy, 3rd Edition. *Anal Bioanal Chem* **2008**, *390*, 1223–1224, doi:10.1007/s00216-007-1822-x.
227. Stryer, L.; Haugland, R.P. Energy Transfer: A Spectroscopic Ruler. *Proc Natl Acad Sci U S A* **1967**, *58*, 719–726.
228. Truong, K.; Ikura, M. The Use of FRET Imaging Microscopy to Detect Protein-Protein Interactions and Protein Conformational Changes in Vivo. *Curr Opin Struct Biol* **2001**, *11*, 573–578, doi:10.1016/s0959-440x(00)00249-9.
229. Sizaire, F.; Tramier, M. FRET-Based Biosensors: Genetically Encoded Tools to Track Kinase Activity in Living Cells. *Protein Phosphorylation* **2017**, doi:10.5772/intechopen.71005.
230. Skruzny, M.; Pohl, E.; Abella, M. FRET Microscopy in Yeast. *Biosensors* **2019**, *9*, 122, doi:10.3390/bios9040122.
231. Padilla-Parra, S.; Auduge, N.; Coppey-Moisan, M.; Tramier, M. Non Fitting Based FRET-FLIM Analysis Approaches Applied to Quantify Protein-Protein Interactions in Live Cells. *Biophys Rev* **2011**, *3*, 63–70, doi:10.1007/s12551-011-0047-6.
232. Lakowicz, J.R.; Szymanski, H.; Nowaczyk, K.; Berndt, K.W.; Johnson, M. Fluorescence Lifetime Imaging. *Analytical Biochemistry* **1992**, *202*, 316–330, doi:10.1016/0003-2697(92)90112-K.
233. Chen, Y.; Periasamy, A. Characterization of Two-Photon Excitation Fluorescence Lifetime Imaging Microscopy for Protein Localization. *Microsc Res Tech* **2004**, *63*, 72–80, doi:10.1002/jemt.10430.
234. Berezin, M.Y.; Achilefu, S. Fluorescence Lifetime Measurements and Biological Imaging. *Chem Rev* **2010**, *110*, 2641–2684, doi:10.1021/cr900343z.
235. Bastiaens, P.I.H.; Squire, A. Fluorescence Lifetime Imaging Microscopy: Spatial Resolution of Biochemical Processes in the Cell. *Trends in Cell Biology* **1999**, *9*, 48–52, doi:10.1016/S0962-8924(98)01410-X.
236. Becker, W. Fluorescence Lifetime Imaging by Multi-Dimensional Time Correlated Single Photon Counting. *Medical Photonics* **2015**, *27*, 41–61, doi:10.1016/j.medpho.2015.02.001.
237. Hirvonen, L.M.; Suhling, K. Fast Timing Techniques in FLIM Applications. *Frontiers in Physics* **2020**, *8*.
238. *Advanced Time-Correlated Single Photon Counting Techniques*;
239. *Advanced Time-Correlated Single Photon Counting Applications*;

240. Kalisz, J. Review of Methods for Time Interval Measurements with Picosecond Resolution. **2004**, doi:10.1088/0026-1394/41/1/004.
241. Fast Fluorescence Lifetime Imaging Techniques: A Review on Challenge and Development | Journal of Innovative Optical Health Sciences Available online: <https://www.worldscientific.com/doi/10.1142/S1793545819300039> (accessed on 17 July 2022).
242. Cole, M.J.; Siegel, J.; Webb, S.E.; Jones, R.; Dowling, K.; Dayel, M.J.; Parsons-Karavassilis, D.; French, P.M.; Lever, M.J.; Sucharov, L.O.; et al. Time-Domain Whole-Field Fluorescence Lifetime Imaging with Optical Sectioning. *J Microsc* **2001**, *203*, 246–257, doi:10.1046/j.1365-2818.2001.00894.x.
243. Owen, D.M.; Auksoorius, E.; Manning, H.B.; Talbot, C.B.; Beule, P.A.A. de; Dunsby, C.; Neil, M.A.A.; French, P.M.W. Excitation-Resolved Hyperspectral Fluorescence Lifetime Imaging Using a UV-Extended Supercontinuum Source. *Opt. Lett., OL* **2007**, *32*, 3408–3410, doi:10.1364/OL.32.003408.
244. Padilla-Parra, S.; Audugé, N.; Lalucque, H.; Mevel, J.-C.; Coppey-Moisan, M.; Tramier, M. Quantitative Comparison of Different Fluorescent Protein Couples for Fast FRET-FLIM Acquisition. *Biophys J* **2009**, *97*, 2368–2376, doi:10.1016/j.bpj.2009.07.044.
245. Grant, D.M.; Zhang, W.; McGhee, E.J.; Bunney, T.D.; Talbot, C.B.; Kumar, S.; Munro, I.; Dunsby, C.; Neil, M.A.A.; Katan, M.; et al. Multiplexed FRET to Image Multiple Signaling Events in Live Cells. *Biophysical Journal* **2008**, *95*, L69–L71, doi:10.1529/biophysj.108.139204.
246. Padilla-Parra, S.; Audugé, N.; Coppey-Moisan, M.; Tramier, M. Quantitative FRET Analysis by Fast Acquisition Time Domain FLIM at High Spatial Resolution in Living Cells. *Biophysical Journal* **2008**, *95*, 2976–2988, doi:10.1529/biophysj.108.131276.
247. Leray, A.; Padilla-Parra, S.; Roul, J.; Héliot, L.; Tramier, M. Spatio-Temporal Quantification of FRET in Living Cells by Fast Time-Domain FLIM: A Comparative Study of Non-Fitting Methods [Corrected]. *PLoS One* **2013**, *8*, e69335, doi:10.1371/journal.pone.0069335.
248. Demeautis, C.; Sipieter, F.; Roul, J.; Chapuis, C.; Padilla-Parra, S.; Riquet, F.B.; Tramier, M. Multiplexing PKA and ERK1&2 Kinases FRET Biosensors in Living Cells Using Single Excitation Wavelength Dual Colour FLIM. *Sci Rep* **2017**, *7*, doi:10.1038/srep41026.
249. Bertolin, G.; Sizaire, F.; Herbomel, G.; Rebutier, D.; Prigent, C.; Tramier, M. A FRET Biosensor Reveals Spatiotemporal Activation and Functions of Aurora Kinase A in Living Cells. *Nat Commun* **2016**, *7*, 12674, doi:10.1038/ncomms12674.

250. Bertolin, G.; Alves-Guerra, M.-C.; Cheron, A.; Burel, A.; Prigent, C.; Le Borgne, R.; Tramier, M. Mitochondrial Aurora Kinase A Induces Mitophagy by Interacting with MAP1LC3 and Prohibitin 2. *Life Sci Alliance* **2021**, *4*, e202000806, doi:10.26508/lsa.202000806.
251. Sizaïre, F.; Le Marchand, G.; Pécréaux, J.; Bouchareb, O.; Tramier, M. Automated Screening of AURKA Activity Based on a Genetically Encoded FRET Biosensor Using Fluorescence Lifetime Imaging Microscopy. *Methods Appl Fluoresc* **2020**, *8*, 024006, doi:10.1088/2050-6120/ab73f5.
252. Esposito, A.; Gralle, M.; Dani, M.A.C.; Lange, D.; Wouters, F.S. PHlameleons: A Family of FRET-Based Protein Sensors for Quantitative PH Imaging. *Biochemistry* **2008**, *47*, 13115–13126, doi:10.1021/bi8009482.
253. Kremers, G.-J.; Goedhart, J.; van Munster, E.B.; Gadella, T.W.J. Cyan and Yellow Super Fluorescent Proteins with Improved Brightness, Protein Folding, and FRET Förster Radius. *Biochemistry* **2006**, *45*, 6570–6580, doi:10.1021/bi0516273.
254. Elsliger, M.A.; Wachter, R.M.; Hanson, G.T.; Kallio, K.; Remington, S.J. Structural and Spectral Response of Green Fluorescent Protein Variants to Changes in PH. *Biochemistry* **1999**, *38*, 5296–5301, doi:10.1021/bi9902182.
255. Nagai, T.; Ibata, K.; Park, E.S.; Kubota, M.; Mikoshiba, K.; Miyawaki, A. A Variant of Yellow Fluorescent Protein with Fast and Efficient Maturation for Cell-Biological Applications. *Nat Biotechnol* **2002**, *20*, 87–90, doi:10.1038/nbt0102-87.
256. Shimozono, S.; Hosoi, H.; Mizuno, H.; Fukano, T.; Tahara, T.; Miyawaki, A. Concatenation of Cyan and Yellow Fluorescent Proteins for Efficient Resonance Energy Transfer. *Biochemistry* **2006**, *45*, 6267–6271, doi:10.1021/bi060093i.
257. Burgstaller, S.; Bischof, H.; Gensch, T.; Stryeck, S.; Gottschalk, B.; Ramadani-Muja, J.; Eroglu, E.; Rost, R.; Balfanz, S.; Baumann, A.; et al. PH-Lemon, a Fluorescent Protein-Based PH Reporter for Acidic Compartments. *ACS Sens.* **2019**, *4*, 883–891, doi:10.1021/acssensors.8b01599.
258. Katayama, H.; Hama, H.; Nagasawa, K.; Kurokawa, H.; Sugiyama, M.; Ando, R.; Funata, M.; Yoshida, N.; Homma, M.; Nishimura, T.; et al. Visualizing and Modulating Mitophagy for Therapeutic Studies of Neurodegeneration. *Cell* **2020**, *181*, 1176–1187.e16, doi:10.1016/j.cell.2020.04.025.
259. Wang, L.; Shen, H.-M. Seeing Is Believing: A Novel Tool for Quantitating Mitophagy. *Cell Res* **2020**, *30*, 715–716, doi:10.1038/s41422-020-0360-3.
260. Cordelières, F.P.; Zhang, C. 3D Quantitative Colocalisation Analysis. In *Bioimage Data Analysis Workflows*; Miura, K., Sladoje, N., Eds.; Learning Materials in Biosciences; Springer International Publishing: Cham, 2020; pp. 33–66 ISBN 978-3-030-22386-1.

261. Bolte, S.; Cordelières, F.P. A Guided Tour into Subcellular Colocalization Analysis in Light Microscopy. *Journal of Microscopy* **2006**, *224*, 213–232, doi:10.1111/j.1365-2818.2006.01706.x.
262. Erard, M.; Fredj, A.; Pasquier, H.; Beltolngar, D.-B.; Bousmah, Y.; Derrien, V.; Vincent, P.; Merola, F. Minimum Set of Mutations Needed to Optimize Cyan Fluorescent Proteins for Live Cell Imaging. *Mol. BioSyst.* **2013**, *9*, 258–267, doi:10.1039/C2MB25303H.
263. Bousmah, Y.; Valenta, H.; Bertolin, G.; Singh, U.; Nicolas, V.; Pasquier, H.; Tramier, M.; Merola, F.; Erard, M. TdLanYFP, a Yellow, Bright, Photostable, and PH-Insensitive Fluorescent Protein for Live-Cell Imaging and Förster Resonance Energy Transfer-Based Sensing Strategies. *ACS Sens* **2021**, *6*, 3940–3947, doi:10.1021/acssensors.1c00874.
264. Yamamoto, A.; Tagawa, Y.; Yoshimori, T.; Moriyama, Y.; Masaki, R.; Tashiro, Y. Bafilomycin A1 Prevents Maturation of Autophagic Vacuoles by Inhibiting Fusion between Autophagosomes and Lysosomes in Rat Hepatoma Cell Line, H-4-II-E Cells. *Cell Struct Funct* **1998**, *23*, 33–42, doi:10.1247/csf.23.33.
265. Seglen, P.O.; Gordon, P.B. 3-Methyladenine: Specific Inhibitor of Autophagic/Lysosomal Protein Degradation in Isolated Rat Hepatocytes. *Proc Natl Acad Sci U S A* **1982**, *79*, 1889–1892, doi:10.1073/pnas.79.6.1889.
266. During Autophagy Mitochondria Elongate, Are Spared from Degradation and Sustain Cell Viability - PubMed Available online: <https://pubmed.ncbi.nlm.nih.gov/21478857/> (accessed on 28 August 2020).
267. Rambold, A.S.; Kostecky, B.; Elia, N.; Lippincott-Schwartz, J. Tubular Network Formation Protects Mitochondria from Autophagosomal Degradation during Nutrient Starvation. *Proc. Natl. Acad. Sci. U.S.A.* **2011**, *108*, 10190–10195, doi:10.1073/pnas.1107402108.
268. Tanida, I.; Ueno, T.; Kominami, E. Human Light Chain 3/MAP1LC3B Is Cleaved at Its Carboxyl-Terminal Met121 to Expose Gly120 for Lipidation and Targeting to Autophagosomal Membranes. *J. Biol. Chem.* **2004**, *279*, 47704–47710, doi:10.1074/jbc.M407016200.
269. Shvets, E.; Fass, E.; Scherz-Shouval, R.; Elazar, Z. The N-Terminus and Phe52 Residue of LC3 Recruit P62/SQSTM1 into Autophagosomes. *Journal of Cell Science* **2008**, *121*, 2685–2695, doi:10.1242/jcs.026005.
270. Maruyama, T.; Noda, N.N. Autophagy-Regulating Protease Atg4: Structure, Function, Regulation and Inhibition. *The Journal of Antibiotics* **2018**, *71*, 72–78, doi:10.1038/ja.2017.104.

271. Ciechomska, I.A.; Tolkovsky, A.M. Non-Autophagic GFP-LC3 Puncta Induced by Saponin and Other Detergents. *Autophagy* **2007**, *3*, 586–590, doi:10.4161/auto.4843.
272. Szeto, J.; Kaniuk, N.A.; Canadien, V.; Nisman, R.; Mizushima, N.; Yoshimori, T.; Bazett-Jones, D.P.; Brumell, J.H. ALIS Are Stress-Induced Protein Storage Compartments for Substrates of the Proteasome and Autophagy. *Autophagy* **2006**, *2*, 189–199, doi:10.4161/auto.2731.
273. Weidberg, H.; Shpilka, T.; Shvets, E.; Abada, A.; Shimron, F.; Elazar, Z. LC3 and GATE-16 N Termini Mediate Membrane Fusion Processes Required for Autophagosome Biogenesis. *Dev Cell* **2011**, *20*, 444–454, doi:10.1016/j.devcel.2011.02.006.
274. Yu, S.; Melia, T.J. The Coordination of Membrane Fission and Fusion at the End of Autophagosome Maturation. *Curr. Opin. Cell Biol.* **2017**, *47*, 92–98, doi:10.1016/j.ceb.2017.03.010.
275. Scherz-Shouval, R.; Sagiv, Y.; Shorer, H.; Elazar, Z. The COOH Terminus of GATE-16, an Intra-Golgi Transport Modulator, Is Cleaved by the Human Cysteine Protease HsApg4A*. *Journal of Biological Chemistry* **2003**, *278*, 14053–14058, doi:10.1074/jbc.M212108200.
276. Scherz-Shouval, R.; Shvets, E.; Fass, E.; Shorer, H.; Gil, L.; Elazar, Z. Reactive Oxygen Species Are Essential for Autophagy and Specifically Regulate the Activity of Atg4. *EMBO J* **2007**, *26*, 1749–1760, doi:10.1038/sj.emboj.7601623.
277. Davis, L.E.; Shalin, S.C.; Tackett, A.J. Current State of Melanoma Diagnosis and Treatment. *Cancer Biol Ther* **2019**, *20*, 1366–1379, doi:10.1080/15384047.2019.1640032.
278. Ali, Z.; Yousaf, N.; Larkin, J. Melanoma Epidemiology, Biology and Prognosis. *EJC Suppl* **2013**, *11*, 81–91, doi:10.1016/j.ejcsup.2013.07.012.
279. Leonardi, G.C.; Falzone, L.; Salemi, R.; Zanghi, A.; Spandidos, D.A.; Mccubrey, J.A.; Candido, S.; Libra, M. Cutaneous Melanoma: From Pathogenesis to Therapy (Review). *International Journal of Oncology* **2018**, *52*, 1071–1080, doi:10.3892/ijo.2018.4287.
280. Patel, H.; Yacoub, N.; Mishra, R.; White, A.; Long, Y.; Alanazi, S.; Garrett, J.T. Current Advances in the Treatment of BRAF-Mutant Melanoma. *Cancers (Basel)* **2020**, *12*, E482, doi:10.3390/cancers12020482.
281. Lin, J.Y.; Fisher, D.E. Melanocyte Biology and Skin Pigmentation. *Nature* **2007**, *445*, 843–850, doi:10.1038/nature05660.
282. Williams, P.F.; Olsen, C.M.; Hayward, N.K.; Whiteman, D.C. Melanocortin 1 Receptor and Risk of Cutaneous Melanoma: A Meta-Analysis and Estimates of

- Population Burden. *International Journal of Cancer* **2011**, *129*, 1730–1740, doi:10.1002/ijc.25804.
283. Seiberg, M. Keratinocyte–Melanocyte Interactions During Melanosome Transfer. *Pigment Cell Research* **2001**, *14*, 236–242, doi:10.1034/j.1600-0749.2001.140402.x.
284. Street, W. Cancer Facts & Figures 2019. **1930**, 76.
285. Fecher, L.A.; Amaravadi, R.K.; Flaherty, K.T. The MAPK Pathway in Melanoma. *Curr Opin Oncol* **2008**, *20*, 183–189, doi:10.1097/CCO.0b013e3282f5271c.
286. Dhillon, A.S.; Hagan, S.; Rath, O.; Kolch, W. MAP Kinase Signalling Pathways in Cancer. *Oncogene* **2007**, *26*, 3279–3290, doi:10.1038/sj.onc.1210421.
287. Millet, A.; Martin, A.R.; Ronco, C.; Rocchi, S.; Benhida, R. Metastatic Melanoma: Insights Into the Evolution of the Treatments and Future Challenges. *Med Res Rev* **2017**, *37*, 98–148, doi:10.1002/med.21404.
288. Sosman, J.A.; Kim, K.B.; Schuchter, L.; Gonzalez, R.; Pavlick, A.C.; Weber, J.S.; McArthur, G.A.; Hutson, T.E.; Moschos, S.J.; Flaherty, K.T.; et al. Survival in BRAF V600-Mutant Advanced Melanoma Treated with Vemurafenib. *N Engl J Med* **2012**, *366*, 707–714, doi:10.1056/NEJMoa1112302.
289. Manzano, J.L.; Layos, L.; Bugés, C.; de los Llanos Gil, M.; Vila, L.; Martínez-Balibrea, E.; Martínez-Cardús, A. Resistant Mechanisms to BRAF Inhibitors in Melanoma. *Ann Transl Med* **2016**, *4*, 237, doi:10.21037/atm.2016.06.07.
290. Sullivan, R.J.; Flaherty, K.T. Resistance to BRAF-Targeted Therapy in Melanoma. *Eur J Cancer* **2013**, *49*, 1297–1304, doi:10.1016/j.ejca.2012.11.019.
291. Nazarian, R.; Shi, H.; Wang, Q.; Kong, X.; Koya, R.C.; Lee, H.; Chen, Z.; Lee, M.-K.; Attar, N.; Sazegar, H.; et al. Melanomas Acquire Resistance to B-RAF(V600E) Inhibition by RTK or N-RAS Upregulation. *Nature* **2010**, *468*, 973–977, doi:10.1038/nature09626.
292. Villanueva, J.; Vultur, A.; Lee, J.T.; Somasundaram, R.; Fukunaga-Kalabis, M.; Cipolla, A.K.; Wubbenhorst, B.; Xu, X.; Gimotty, P.A.; Kee, D.; et al. Acquired Resistance to BRAF Inhibitors Mediated by a RAF Kinase Switch in Melanoma Can Be Overcome by Cotargeting MEK and IGF-1R/PI3K. *Cancer Cell* **2010**, *18*, 683–695, doi:10.1016/j.ccr.2010.11.023.
293. Huang, C.; Radi, R.H.; Arbiser, J.L. Mitochondrial Metabolism in Melanoma. *Cells* **2021**, *10*, 3197, doi:10.3390/cells10113197.
294. Läsche, M.; Emons, G.; Gründker, C. Shedding New Light on Cancer Metabolism: A Metabolic Tightrope Between Life and Death. *Front Oncol* **2020**, *10*, 409, doi:10.3389/fonc.2020.00409.

295. Vasan, K.; Werner, M.; Chandel, N.S. Mitochondrial Metabolism as a Target for Cancer Therapy. *Cell Metab* **2020**, *32*, 341–352, doi:10.1016/j.cmet.2020.06.019.
296. Grasso, D.; Zampieri, L.X.; Capelôa, T.; Velde, J.A.V. de; Sonveaux, P. Mitochondria in Cancer. *Cell Stress* **2020**, *4*, 114–146, doi:10.15698/cst2020.06.221.
297. Barbi de Moura, M.; Vincent, G.; Fayewicz, S.L.; Bateman, N.W.; Hood, B.L.; Sun, M.; Suhan, J.; Duensing, S.; Yin, Y.; Sander, C.; et al. Mitochondrial Respiration--an Important Therapeutic Target in Melanoma. *PLoS One* **2012**, *7*, e40690, doi:10.1371/journal.pone.0040690.
298. Feichtinger, R.G.; Lang, R.; Geilberger, R.; Rathje, F.; Mayr, J.A.; Sperl, W.; Bauer, J.W.; Hauser-Kronberger, C.; Kofler, B.; Emberger, M. Melanoma Tumors Exhibit a Variable but Distinct Metabolic Signature. *Exp Dermatol* **2018**, *27*, 204–207, doi:10.1111/exd.13465.
299. Fischer, G.M.; Vashisht Gopal, Y.N.; McQuade, J.L.; Peng, W.; DeBerardinis, R.J.; Davies, M.A. Metabolic Strategies of Melanoma Cells: Mechanisms, Interactions with the Tumor Microenvironment, and Therapeutic Implications. *Pigment Cell Melanoma Res* **2018**, *31*, 11–30, doi:10.1111/pcmr.12661.
300. Ho, J.; de Moura, M.B.; Lin, Y.; Vincent, G.; Thorne, S.; Duncan, L.M.; Hui-Min, L.; Kirkwood, J.M.; Becker, D.; Van Houten, B.; et al. Importance of Glycolysis and Oxidative Phosphorylation in Advanced Melanoma. *Mol Cancer* **2012**, *11*, 76, doi:10.1186/1476-4598-11-76.
301. Marchetti, P.; Guerreschi, P.; Kluza, J.; Mortier, L. Metabolic Features of Melanoma: A Gold Mine of New Therapeutic Targets? *Curr Cancer Drug Targets* **2014**, *14*, 357–370, doi:10.2174/1568009614666140407113124.
302. Theodosakis, N.; Held, M.A.; Marzuka-Alcala, A.; Meeth, K.M.; Micevic, G.; Long, G.V.; Scolyer, R.A.; Stern, D.F.; Bosenberg, M.W. BRAF Inhibition Decreases Cellular Glucose Uptake in Melanoma in Association with Reduction in Cell Volume. *Mol Cancer Ther* **2015**, *14*, 1680–1692, doi:10.1158/1535-7163.MCT-15-0080.
303. Corazao-Rozas, P.; Guerreschi, P.; André, F.; Gabert, P.-E.; Lancel, S.; Dekioux, S.; Fontaine, D.; Tardivel, M.; Savina, A.; Quesnel, B.; et al. Mitochondrial Oxidative Phosphorylation Controls Cancer Cell's Life and Death Decisions upon Exposure to MAPK Inhibitors. *Oncotarget* **2016**, *7*, 39473–39485, doi:10.18632/oncotarget.7790.
304. Hardeman, K.N.; Peng, C.; Paudel, B.B.; Meyer, C.T.; Luong, T.; Tyson, D.R.; Young, J.D.; Quaranta, V.; Fessel, J.P. Dependence On Glycolysis Sensitizes BRAF-Mutated Melanomas For Increased Response To Targeted BRAF Inhibition. *Sci Rep* **2017**, *7*, 42604, doi:10.1038/srep42604.

305. Marchetti, P.; Susin, S.A.; Decaudin, D.; Gamen, S.; Castedo, M.; Hirsch, T.; Zamzami, N.; Naval, J.; Senik, A.; Kroemer, G. Apoptosis-Associated Derangement of Mitochondrial Function in Cells Lacking Mitochondrial DNA. *Cancer Res* **1996**, *56*, 2033–2038.
306. Schmitt, R.J.; Kreidler, S.M.; Glueck, D.H.; Amaria, R.N.; Gonzalez, R.; Lewis, K.; Bagrosky, B.M.; Kwak, J.J.; Koo, P.J. Correlation between Early 18F-FDG PET/CT Response to BRAF and MEK Inhibition and Survival in Patients with BRAF-Mutant Metastatic Melanoma. *Nucl Med Commun* **2016**, *37*, 122–128, doi:10.1097/MNM.0000000000000406.
307. Marchetti, P.; Trinh, A.; Khamari, R.; Kluza, J. Melanoma Metabolism Contributes to the Cellular Responses to MAPK/ERK Pathway Inhibitors. *Biochim Biophys Acta Gen Subj* **2018**, *1862*, 999–1005, doi:10.1016/j.bbagen.2018.01.018.
308. Hall, A.; Meyle, K.D.; Lange, M.K.; Klima, M.; Sanderhoff, M.; Dahl, C.; Abildgaard, C.; Thorup, K.; Moghimi, S.M.; Jensen, P.B.; et al. Dysfunctional Oxidative Phosphorylation Makes Malignant Melanoma Cells Addicted to Glycolysis Driven by the (V600E)BRAF Oncogene. *Oncotarget* **2013**, *4*, 584–599, doi:10.18632/oncotarget.965.
309. Haq, R.; Shoag, J.; Andreu-Perez, P.; Yokoyama, S.; Edelman, H.; Rowe, G.C.; Frederick, D.T.; Hurley, A.D.; Nellore, A.; Kung, A.L.; et al. Oncogenic BRAF Regulates Oxidative Metabolism via PGC1 α and MITF. *Cancer Cell* **2013**, *23*, 302–315, doi:10.1016/j.ccr.2013.02.003.
310. Corazao-Rozas, P.; Guerreschi, P.; Jendoubi, M.; André, F.; Jonneaux, A.; Scalbert, C.; Garçon, G.; Malet-Martino, M.; Balayssac, S.; Rocchi, S.; et al. Mitochondrial Oxidative Stress Is the Achille's Heel of Melanoma Cells Resistant to Braf-Mutant Inhibitor. *Oncotarget* **2013**, *4*, 1986–1998, doi:10.18632/oncotarget.1420.
311. Trotta, A.P.; Gelles, J.D.; Serasinghe, M.N.; Loi, P.; Arbiser, J.L.; Chipuk, J.E. Disruption of Mitochondrial Electron Transport Chain Function Potentiates the Pro-Apoptotic Effects of MAPK Inhibition. *J Biol Chem* **2017**, *292*, 11727–11739, doi:10.1074/jbc.M117.786442.
312. Maycotte, P.; Marín-Hernández, A.; Goyri-Aguirre, M.; Anaya-Ruiz, M.; Reyes-Leyva, J.; Cortés-Hernández, P. Mitochondrial Dynamics and Cancer. *Tumour Biol.* **2017**, *39*, 1010428317698391, doi:10.1177/1010428317698391.
313. Liesa, M.; Palacín, M.; Zorzano, A. Mitochondrial Dynamics in Mammalian Health and Disease. *Physiol. Rev.* **2009**, *89*, 799–845, doi:10.1152/physrev.00030.2008.
314. Detmer, S.A.; Chan, D.C. Functions and Dysfunctions of Mitochondrial Dynamics. *Nat. Rev. Mol. Cell Biol.* **2007**, *8*, 870–879, doi:10.1038/nrm2275.
315. Wai, T.; Langer, T. Mitochondrial Dynamics and Metabolic Regulation. *Trends Endocrinol. Metab.* **2016**, *27*, 105–117, doi:10.1016/j.tem.2015.12.001.

316. Chen, H.; Chomyn, A.; Chan, D.C. Disruption of Fusion Results in Mitochondrial Heterogeneity and Dysfunction. *J. Biol. Chem.* **2005**, *280*, 26185–26192, doi:10.1074/jbc.M503062200.
317. Chen, H.; Vermulst, M.; Wang, Y.E.; Chomyn, A.; Prolla, T.A.; McCaffery, J.M.; Chan, D.C. Mitochondrial Fusion Is Required for MtDNA Stability in Skeletal Muscle and Tolerance of MtDNA Mutations. *Cell* **2010**, *141*, 280–289, doi:10.1016/j.cell.2010.02.026.
318. Otera, H.; Ishihara, N.; Mihara, K. New Insights into the Function and Regulation of Mitochondrial Fission. *Biochim. Biophys. Acta* **2013**, *1833*, 1256–1268, doi:10.1016/j.bbamcr.2013.02.002.
319. Pickles, S.; Vigié, P.; Youle, R.J. Mitophagy and Quality Control Mechanisms in Mitochondrial Maintenance. *Current Biology* **2018**, *28*, R170–R185, doi:10.1016/j.cub.2018.01.004.
320. Youle, R.J.; van der Bliek, A.M. Mitochondrial Fission, Fusion, and Stress. *Science* **2012**, *337*, 1062–1065, doi:10.1126/science.1219855.
321. Ferguson, S.M.; De Camilli, P. Dynamin, a Membrane-Remodelling GTPase. *Nat. Rev. Mol. Cell Biol.* **2012**, *13*, 75–88, doi:10.1038/nrm3266.
322. Koshiba, T.; Detmer, S.A.; Kaiser, J.T.; Chen, H.; McCaffery, J.M.; Chan, D.C. Structural Basis of Mitochondrial Tethering by Mitofusin Complexes. *Science* **2004**, *305*, 858–862, doi:10.1126/science.1099793.
323. Brandt, T.; Cavellini, L.; Kühlbrandt, W.; Cohen, M.M. A Mitofusin-Dependent Docking Ring Complex Triggers Mitochondrial Fusion in Vitro. *Elife* **2016**, *5*, doi:10.7554/eLife.14618.
324. Ishihara, N.; Eura, Y.; Mihara, K. Mitofusin 1 and 2 Play Distinct Roles in Mitochondrial Fusion Reactions via GTPase Activity. *J. Cell. Sci.* **2004**, *117*, 6535–6546, doi:10.1242/jcs.01565.
325. Legros, F.; Lombès, A.; Frachon, P.; Rojo, M. Mitochondrial Fusion in Human Cells Is Efficient, Requires the Inner Membrane Potential, and Is Mediated by Mitofusins. *Mol. Biol. Cell* **2002**, *13*, 4343–4354, doi:10.1091/mbc.e02-06-0330.
326. Ban, T.; Ishihara, T.; Kohno, H.; Saita, S.; Ichimura, A.; Maenaka, K.; Oka, T.; Mihara, K.; Ishihara, N. Molecular Basis of Selective Mitochondrial Fusion by Heterotypic Action between OPA1 and Cardiolipin. *Nat. Cell Biol.* **2017**, *19*, 856–863, doi:10.1038/ncb3560.
327. Head, B.; Griparic, L.; Amiri, M.; Gandre-Babbe, S.; van der Bliek, A.M. Inducible Proteolytic Inactivation of OPA1 Mediated by the OMA1 Protease in Mammalian Cells. *J. Cell Biol.* **2009**, *187*, 959–966, doi:10.1083/jcb.200906083.

328. Ehses, S.; Raschke, I.; Mancuso, G.; Bernacchia, A.; Geimer, S.; Tondera, D.; Martinou, J.-C.; Westermann, B.; Rugarli, E.I.; Langer, T. Regulation of OPA1 Processing and Mitochondrial Fusion by M-AAA Protease Isoenzymes and OMA1 Control of OPA1 by m-AAA Protease and OMA1. *J Cell Biol* **2009**, *187*, 1023–1036, doi:10.1083/jcb.200906084.
329. Griparic, L.; Kanazawa, T.; van der Bliek, A.M. Regulation of the Mitochondrial Dynamin-like Protein Opal by Proteolytic Cleavage. *J Cell Biol* **2007**, *178*, 757–764, doi:10.1083/jcb.200704112.
330. Song, Z.; Chen, H.; Fiket, M.; Alexander, C.; Chan, D.C. OPA1 Processing Controls Mitochondrial Fusion and Is Regulated by MRNA Splicing, Membrane Potential, and Yme1L. *J. Cell Biol.* **2007**, *178*, 749–755, doi:10.1083/jcb.200704110.
331. MacVicar, T.; Langer, T. OPA1 Processing in Cell Death and Disease - the Long and Short of It. *J. Cell. Sci.* **2016**, *129*, 2297–2306, doi:10.1242/jcs.159186.
332. Mishra, P.; Carelli, V.; Manfredi, G.; Chan, D.C. Proteolytic Cleavage of Opal Stimulates Mitochondrial Inner Membrane Fusion and Couples Fusion to Oxidative Phosphorylation. *Cell Metabolism* **2014**, *19*, 630–641, doi:10.1016/j.cmet.2014.03.011.
333. Smirnova, E.; Griparic, L.; Shurland, D.L.; van der Bliek, A.M. Dynamin-Related Protein Drp1 Is Required for Mitochondrial Division in Mammalian Cells. *Mol. Biol. Cell* **2001**, *12*, 2245–2256, doi:10.1091/mbc.12.8.2245.
334. Friedman, J.R.; Lackner, L.L.; West, M.; DiBenedetto, J.R.; Nunnari, J.; Voeltz, G.K. ER Tubules Mark Sites of Mitochondrial Division. *Science* **2011**, *334*, 358–362, doi:10.1126/science.1207385.
335. Lewis, S.C.; Uchiyama, L.F.; Nunnari, J. ER-Mitochondria Contacts Couple MtDNA Synthesis with Mitochondrial Division in Human Cells. *Science* **2016**, *353*, doi:10.1126/science.aaf5549.
336. Fröhlich, C.; Grabiger, S.; Schwefel, D.; Faelber, K.; Rosenbaum, E.; Mears, J.; Rocks, O.; Daumke, O. Structural Insights into Oligomerization and Mitochondrial Remodelling of Dynamin 1-like Protein. *EMBO J.* **2013**, *32*, 1280–1292, doi:10.1038/emboj.2013.74.
337. Mears, J.A.; Lackner, L.L.; Fang, S.; Ingerman, E.; Nunnari, J.; Hinshaw, J.E. Conformational Changes in Dnm1 Support a Contractile Mechanism for Mitochondrial Fission. *Nat. Struct. Mol. Biol.* **2011**, *18*, 20–26, doi:10.1038/nsmb.1949.
338. Hatch, A.L.; Ji, W.-K.; Merrill, R.A.; Strack, S.; Higgs, H.N. Actin Filaments as Dynamic Reservoirs for Drp1 Recruitment. *Mol. Biol. Cell* **2016**, *27*, 3109–3121, doi:10.1091/mbc.E16-03-0193.

339. Palmer, C.S.; Osellame, L.D.; Laine, D.; Koutsopoulos, O.S.; Frazier, A.E.; Ryan, M.T. MiD49 and MiD51, New Components of the Mitochondrial Fission Machinery. *EMBO Rep.* **2011**, *12*, 565–573, doi:10.1038/embor.2011.54.
340. Losón, O.C.; Song, Z.; Chen, H.; Chan, D.C. Fis1, Mff, MiD49, and MiD51 Mediate Drp1 Recruitment in Mitochondrial Fission. *Mol. Biol. Cell* **2013**, *24*, 659–667, doi:10.1091/mbc.E12-10-0721.
341. Gandre-Babbe, S.; van der Blik, A.M. The Novel Tail-Anchored Membrane Protein Mff Controls Mitochondrial and Peroxisomal Fission in Mammalian Cells. *Mol. Biol. Cell* **2008**, *19*, 2402–2412, doi:10.1091/mbc.e07-12-1287.
342. Lee, J.E.; Westrate, L.M.; Wu, H.; Page, C.; Voeltz, G.K. Multiple Dynamin Family Members Collaborate to Drive Mitochondrial Division. *Nature* **2016**, *540*, 139–143, doi:10.1038/nature20555.
343. Chen, H.; Chan, D.C. Mitochondrial Dynamics in Regulating the Unique Phenotypes of Cancer and Stem Cells. *Cell Metab* **2017**, *26*, 39–48, doi:10.1016/j.cmet.2017.05.016.
344. Rehman, J.; Zhang, H.J.; Toth, P.T.; Zhang, Y.; Marsboom, G.; Hong, Z.; Salgia, R.; Husain, A.N.; Wietholt, C.; Archer, S.L. Inhibition of Mitochondrial Fission Prevents Cell Cycle Progression in Lung Cancer. *FASEB J* **2012**, *26*, 2175–2186, doi:10.1096/fj.11-196543.
345. Serasinghe, M.N.; Wieder, S.Y.; Renault, T.T.; Elkholi, R.; Ascioia, J.J.; Yao, J.L.; Jadoo, O.; Hoehn, K.; Kageyama, Y.; Sesaki, H.; et al. Mitochondrial Division Is Requisite to RAS-Induced Transformation and Targeted by Oncogenic MAPK Pathway Inhibitors. *Mol Cell* **2015**, *57*, 521–536, doi:10.1016/j.molcel.2015.01.003.
346. Xie, Q.; Wu, Q.; Horbinski, C.M.; Flavahan, W.A.; Yang, K.; Zhou, W.; Dombrowski, S.M.; Huang, Z.; Fang, X.; Shi, Y.; et al. Mitochondrial Control by DRP1 in Brain Tumor Initiating Cells. *Nat Neurosci* **2015**, *18*, 501–510, doi:10.1038/nn.3960.
347. Avagliano, A.; Fiume, G.; Pelagalli, A.; Sanità, G.; Ruocco, M.R.; Montagnani, S.; Arcucci, A. Metabolic Plasticity of Melanoma Cells and Their Crosstalk With Tumor Microenvironment. *Front Oncol* **2020**, *10*, 722, doi:10.3389/fonc.2020.00722.
348. Vyas, S.; Zaganjor, E.; Haigis, M.C. Mitochondria and Cancer. *Cell* **2016**, *166*, 555–566, doi:10.1016/j.cell.2016.07.002.
349. Decker, C.W.; Garcia, J.; Gatchalian, K.; Arceneaux, D.; Choi, C.; Han, D.; Hernandez, J.B. Mitofusin-2 Mediates Doxorubicin Sensitivity and Acute Resistance in Jurkat Leukemia Cells. *Biochem Biophys Res Commun* **2020**, *24*, 100824, doi:10.1016/j.bbrep.2020.100824.



350. Chudakov, D.M.; Lukyanov, S.; Lukyanov, K.A. Using Photoactivatable Fluorescent Protein Dendra2 to Track Protein Movement. *BioTechniques* **2007**, *42*, 553, 555, 557 passim, doi:10.2144/000112470.
351. Pham, A.H.; McCaffery, J.M.; Chan, D.C. Mouse Lines with Photo-Activatable Mitochondria to Study Mitochondrial Dynamics. *genesis* **2012**, *50*, 833–843, doi:10.1002/dvg.22050.
352. Twig, G.; Shirihai, O.S. The Interplay Between Mitochondrial Dynamics and Mitophagy. *Antioxidants & Redox Signaling* **2011**, *14*, 1939–1951, doi:10.1089/ars.2010.3779.
353. Ma, K.; Chen, G.; Li, W.; Kepp, O.; Zhu, Y.; Chen, Q. Mitophagy, Mitochondrial Homeostasis, and Cell Fate. *Front Cell Dev Biol* **2020**, *8*, 467, doi:10.3389/fcell.2020.00467.
354. Sancho, P.; Barneda, D.; Heeschen, C. Hallmarks of Cancer Stem Cell Metabolism. *Br J Cancer* **2016**, *114*, 1305–1312, doi:10.1038/bjc.2016.152.
355. Pastò, A.; Bellio, C.; Pilotto, G.; Ciminale, V.; Silic-Benussi, M.; Guzzo, G.; Rasola, A.; Frasson, C.; Nardo, G.; Zulato, E.; et al. Cancer Stem Cells from Epithelial Ovarian Cancer Patients Privilege Oxidative Phosphorylation, and Resist Glucose Deprivation. *Oncotarget* **2014**, *5*, 4305–4319, doi:10.18632/oncotarget.2010.
356. Yao, C.-H.; Wang, R.; Wang, Y.; Kung, C.-P.; Weber, J.D.; Patti, G.J. Mitochondrial Fusion Supports Increased Oxidative Phosphorylation during Cell Proliferation. *eLife* **2019**, *8*, e41351, doi:10.7554/eLife.41351.
357. Zeng, Y.; Pan, Q.; Wang, X.; Li, D.; Lin, Y.; Man, F.; Xiao, F.; Guo, L. Impaired Mitochondrial Fusion and Oxidative Phosphorylation Triggered by High Glucose Is Mediated by Tom22 in Endothelial Cells. *Oxidative Medicine and Cellular Longevity* **2019**, *2019*, e4508762, doi:10.1155/2019/4508762.
358. Li, M.; Chen, X.; Ye, Q.-Z.; Vogt, A.; Yin, X.-M. A High-Throughput FRET-Based Assay for Determination of Atg4 Activity. *Autophagy* **2012**, *8*, 401–412, doi:10.4161/auto.18777.
359. Mathiassen, S.G.; De Zio, D.; Cecconi, F. Autophagy and the Cell Cycle: A Complex Landscape. *Front Oncol* **2017**, *7*, 51, doi:10.3389/fonc.2017.00051.
360. Yoshimura, K.; Shibata, M.; Koike, M.; Gotoh, K.; Fukaya, M.; Watanabe, M.; Uchiyama, Y. Effects of RNA Interference of Atg4B on the Limited Proteolysis of LC3 in PC12 Cells and Expression of Atg4B in Various Rat Tissues. *Autophagy* **2006**, *2*, 200–208, doi:10.4161/auto.2744.
361. Kauffman, K.J.; Yu, S.; Jin, J.; Mugo, B.; Nguyen, N.; O'Brien, A.; Nag, S.; Lystad, A.H.; Melia, T.J. Delipidation of Mammalian Atg8-Family Proteins by Each of the

Four ATG4 Proteases. *Autophagy* **2018**, *14*, 992–1010,
doi:10.1080/15548627.2018.1437341.

APPENDIX A

Review

Imaging Mitochondrial Functions: From Fluorescent Dyes to Genetically-Encoded Sensors

Elif Begüm Gökerküçük , Marc Tramier and Giulia Bertolin * Univ Rennes, CNRS, IGDR [Institut de génétique et développement de Rennes] UMR 6290,
F-35000 Rennes, France

* Correspondence: giulia.bertolin@univ-rennes1.fr; Tel.: +33-(0)223237516

Received: 29 December 2019; Accepted: 21 January 2020; Published: 23 January 2020



Abstract: Mitochondria are multifunctional organelles that are crucial to cell homeostasis. They constitute the major site of energy production for the cell, they are key players in signalling pathways using secondary messengers such as calcium, and they are involved in cell death and redox balance paradigms. Mitochondria quickly adapt their dynamics and biogenesis rates to meet the varying energy demands of the cells, both in normal and in pathological conditions. Therefore, understanding simultaneous changes in mitochondrial functions is crucial in developing mitochondria-based therapy options for complex pathological conditions such as cancer, neurological disorders, and metabolic syndromes. To this end, fluorescence microscopy coupled to live imaging represents a promising strategy to track these changes in real time. In this review, we will first describe the commonly available tools to follow three key mitochondrial functions using fluorescence microscopy: Calcium signalling, mitochondrial dynamics, and mitophagy. Then, we will focus on how the development of genetically-encoded fluorescent sensors became a milestone for the understanding of these mitochondrial functions. In particular, we will show how these tools allowed researchers to address several biochemical activities in living cells, and with high spatiotemporal resolution. With the ultimate goal of tracking multiple mitochondrial functions simultaneously, we will conclude by presenting future perspectives for the development of novel genetically-encoded fluorescent biosensors.

Keywords: mitochondria; Ca²⁺ signalling; mitochondrial dynamics; mitophagy; fluorescence microscopy; chemical dyes; genetically-encoded sensors; super-resolution microscopy

1. Introduction

Mitochondria are essentially known for their role in adenosine triphosphate (ATP) synthesis and contribution to cellular metabolism, yet these organelles regulate a multitude of cellular functions. These functions include Ca²⁺ buffering, cellular signalling, reactive oxygen species (ROS) production, and apoptotic cell death [1–4]. Mitochondria are also the major sites where the key steps of heme biosynthesis, ketone bodies generation, and hormone synthesis are performed [5–7]. In response to different physiological or pathological cues, mitochondria form highly dynamic networks to meet the metabolic demands of the cellular sub-domains [8]. Similarly, at the tissue level, mitochondria within a group of specialized cells can show a trend towards a certain mitochondrial network architecture. This parameter was shown to be of importance with respect to the bioenergetic efficiency of the tissue [9]. Furthermore, mitochondria have their own genome containing 37 genes, and 13 of them encode the core protein subunits of the oxidative phosphorylation system [10].

This functional and morphological diversity of mitochondria is important for the maintenance of cellular homeostasis. Therefore, it is not surprising that mitochondrial defects play a major role in many pathologies, including neurodegeneration, aging, cancer, diabetes, obesity, and cardiomyopathies [11].

In order to better understand not only the fundamental mitochondrial biology, but also the mitochondrial pathophysiology, imaging techniques with chemical dyes and genetically-encoded sensors provide the opportunity of gathering detailed insights of complex mitochondrial functions. In this review, we will be addressing three key mitochondrial functions: Calcium signalling, mitochondrial dynamics, and mitophagy. After a brief description of the molecular mechanisms underlying these functions, we will discuss the selection of probes that are available to study these complex mitochondrial functions.

2. Mitochondria and Ca^{2+}

Understanding the role of Ca^{2+} in physiology dates back to the observations by Sydney Ringer in 1883, where he showed that the addition of Ca^{2+} to the perfusion buffer of isolated hearts triggered their contraction [12]. Almost 80 years after this finding, isolated mitochondria have been shown to accumulate high amounts of Ca^{2+} using respiratory energy (under the form of ATP) [13,14]. With the continuous development of probes and methods for Ca^{2+} imaging over the years, mitochondria are now known to be important regulators of cellular Ca^{2+} levels and Ca^{2+} signalling. This coordination was shown to be required for cellular metabolism, survival, and cell-type specific functions. In terms of Ca^{2+} buffering and signalling, mitochondrial activity depends on their close communication with endoplasmic reticulum (ER) (sarcoplasmic reticulum in muscle cells) [15].

2.1. Mitochondrial Ca^{2+} Transport

Upon stimulation with agents, increasing Ca^{2+} concentration ($[\text{Ca}^{2+}]$), mitochondria have the potential to accumulate from 10 to 20-fold more Ca^{2+} than what is stored in the cytosol [16]. The driving force behind the accumulation of positively charged Ca^{2+} ions in the mitochondrial matrix is the membrane potential difference ($\Delta\Psi$) generated by the respiratory chain. To be able to reach the mitochondrial matrix, Ca^{2+} ions have to cross both the outer mitochondrial membrane (OMM) and the inner mitochondrial membrane (IMM) (Figure 1). Voltage-dependent anion-selective channel proteins (VDACs), located on the OMM, are the first barriers regulating Ca^{2+} uptake, and their high expression in cultured cells was shown to ensure permeability [17]. Once the Ca^{2+} ions are in the intermembrane space (IMS), they reach the matrix via the mitochondrial Ca^{2+} uniporter (MCU) complex [18,19]. The MCU is a macromolecular complex containing pore-forming subunits located on the IMM, and several regulatory proteins protruding into the IMS [20–22]. While MCU-dependent Ca^{2+} uptake is highly selective, this complex has a low dissociation constant (K_D) for Ca^{2+} [23]. The tight control of MCU opening is controlled by the Ca^{2+} -sensing regulatory proteins mitochondrial Ca^{2+} uptake 1 (MICU1) and mitochondrial Ca^{2+} uptake 2 (MICU2), which contain EF-hand motifs directly binding to Ca^{2+} ions [24,25]. MICU 1/2 serve as gatekeepers of the MCU complex by reacting with the cytoplasmic Ca^{2+} concentration ($[\text{Ca}^{2+}]_c$). When the $[\text{Ca}^{2+}]_c$ is low, MICU 1/2 interact with the central MCU unit to keep the gate closed and prevent mitochondrial Ca^{2+} uptake [26–28]. Conversely, the release of Ca^{2+} from ER results in an increase of local $[\text{Ca}^{2+}]_c$ at the ER-mitochondria interface. Since Ca^{2+} binds the EF hand domains of MICU 1/2 when the $[\text{Ca}^{2+}]_c$ is high, this binding triggers a conformational change of MICU 1/2 that results in the opening of the MCU [28].

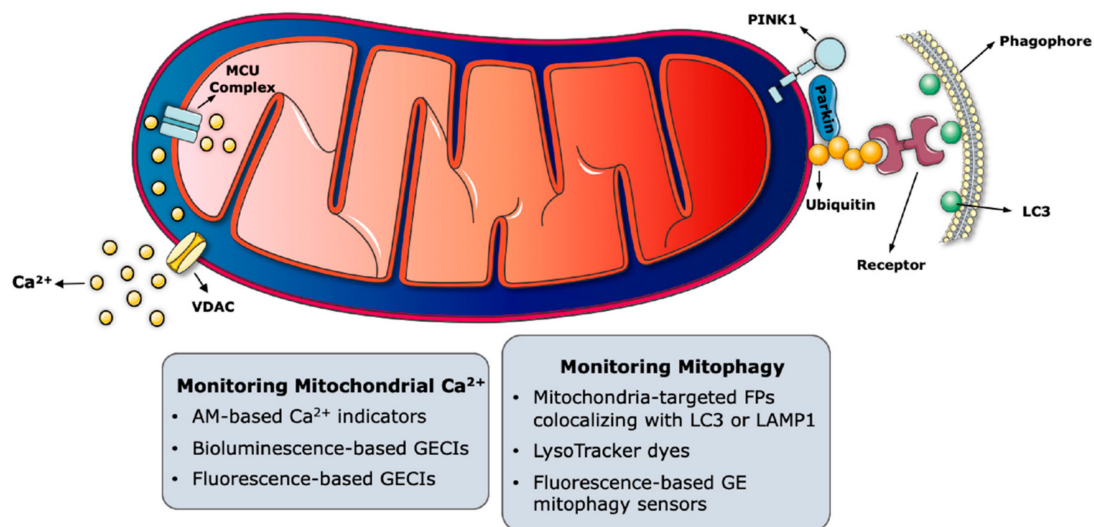


Figure 1. Probes to monitor mitochondrial Ca^{2+} signalling and mitophagy. The major molecular players regulating these functions are symbolized within mitochondria. Key imaging-based approaches are listed in the grey boxes in proximity to the corresponding mitochondrial function. MCU complex, mitochondrial Ca^{2+} uniporter complex; VDAC, voltage-dependent anion-selective channel proteins; PINK1, phosphatase and tension homologue (PTEN)-induced putative kinase 1; Parkin, E3 ligase PARK2; LC3, microtubule-associated protein 1 light chain 3; LAMP1, the lysosomal-associated membrane protein 1; AM, acetoxymethyl ester; GECIs, genetically-encoded Ca^{2+} indicators; FPs, fluorescent proteins; GE, genetically-encoded. The figure was generated with elements provided in the Servier Medical Art depository (<https://smart.servier.com/>) and are licensed under a Creative Commons Attribution 3.0 Unported License (CC BY 3.0).

While the MCU complex regulates Ca^{2+} influx into the mitochondrial matrix, efflux of Ca^{2+} is regulated by the mitochondrial $\text{Na}^+/\text{Ca}^{2+}$ exchanger (mNCX) and the mitochondrial $\text{H}^+/\text{Ca}^{2+}$ exchanger (mHCE) [29–31]. Since the action of mNCX might trigger excess Na^+ accumulation in the matrix, this is then calibrated by the Na^+/H^+ exchanger, which extrudes Na^+ in the IMS [32]. The mitochondrial permeability transient pore (mPTP) has also been shown to have a role in Ca^{2+} efflux in cardiac cells to regulate the cellular metabolism according to the myocardial workload [33]. Interestingly, transient mPTP opening in myocytes were also proposed to act as “reset mechanisms” for mitochondria, counteracting a Ca^{2+} overload or dissipating high ROS damage [34]. Last, the leucine zipper-EF-hand-containing transmembrane protein 1 (LETM1) has been proposed as a mitochondrial $\text{Ca}^{2+}/\text{H}^+$ antiporter in a genome-wide RNAi screen study [35]. However, these findings are still debated, and a clear role of mPTP and LETM1 in Ca^{2+} efflux has not been established yet [36–38].

2.2. Role of Mitochondria in Ca^{2+} Homeostasis

Changes in mitochondrial Ca^{2+} concentration ($[\text{Ca}^{2+}]_{\text{mito}}$) have been shown to regulate many cellular processes such as ATP production by oxidative phosphorylation [39–41], apoptosis [42–44], autophagy [45,46], and organelle crosstalk between the mitochondria, and ER [47]. The ability of mitochondria to capture Ca^{2+} molecules released at the Ca^{2+} -signalling microdomains—formed between mitochondria and plasma membrane or at the ER-mitochondria junctions—can modulate the activity of Ca^{2+} channels by modifying the local $[\text{Ca}^{2+}]_{\text{c}}$ in these microdomains [48,49]. Mitochondria can also contribute to the accumulation of Ca^{2+} ions by forming a “mitochondrial belt”. This structure, described in specific cellular types such as neuronal cells [50–54] or in pancreatic acinar cells [55–58], acts as a physical barrier, preventing Ca^{2+} diffusion away from defined subcellular domains.

Cellular metabolism and survival can also be affected by mitochondrial Ca^{2+} uptake. On the one hand, the localization of mitochondria to the sites of high $[\text{Ca}^{2+}]_{\text{c}}$, followed by the MCU-mediated $[\text{Ca}^{2+}]_{\text{mito}}$ increase, activates the Ca^{2+} -sensitive dehydrogenases of the Krebs cycle and the ATP

synthase, ultimately leading to ATP production [59,60]. On the other hand, excessive Ca^{2+} overload in the mitochondrial matrix is known to be associated with apoptosis, due to the sustained activation of mPTP and the release of apoptosome components such as cytochrome *c* into the cytosol [61].

Overall, the interplay between cellular Ca^{2+} and mitochondrial Ca^{2+} plays an important role in energy production and in a variety of signalling processes.

2.3. Probes to Measure Mitochondrial Ca^{2+}

Of all the probes generated to monitor mitochondrial functions, the ones dedicated to track Ca^{2+} ions and to measure their concentration are the most abundant (Figure 1). Probes monitoring intracellular Ca^{2+} or sensors measuring changes in Ca^{2+} levels within mitochondria and other organelles have thoroughly helped researchers to elucidate the broad spectrum of functions that are regulated by Ca^{2+} ions.

The choice of the most suitable tool(s) from the palette of Ca^{2+} probes currently available depends on the type of assay and the desired readout. To this end, several elements must be taken into account. First, the type of probe to be used is a crucial parameter, as the choice must be made between chemical vs. genetically-encoded Ca^{2+} indicators. Second, probe(s) to monitor Ca^{2+} in living cells must be selected according to the cell type of interest and on the overall duration of the experiment to perform. This parameter is of key importance, as it should be carefully chosen to optimize the sensitivity and spatiotemporal accuracy of the Ca^{2+} probe. Last, the Ca^{2+} affinity and spectral properties of the probe should also be taken into account [62,63]. These elements are discussed in the sections below.

2.3.1. Chemically-Engineered Ca^{2+} Indicators

Initial attempts to measure cytosolic Ca^{2+} have been performed with chemically-engineered fluorophores that change their fluorescence properties upon Ca^{2+} binding. These Ca^{2+} indicators have varying affinities for Ca^{2+} , along with different spectral properties. However, most of them are acetoxymethyl ester (AM)-based compounds [64]. AM-based Ca^{2+} indicators are hydrophobic and primarily diffuse into the cytoplasm, where they are hydrolyzed by the cellular esterases and become trapped inside the cells [64,65]. While this strategy overcomes the problem of the complexity of microinjections, it cannot be used to specifically target organelles as mitochondria.

The spectral changes that can be observed in Ca^{2+} indicators upon Ca^{2+} binding are: (i) Change in fluorescence intensity without shifts in the excitation/emission wavelengths, as in single wavelength indicators, or (ii) shift in excitation and/or emission spectra, as in ratiometric indicators. Classical examples of Ca^{2+} indicators can be Fura-2 and Indo-1, which were originally developed by Tsien et al. in the 1980s [66]. Here, Ca^{2+} binding can either cause a shift in the excitation or emission wavelength of Fura-2 and Indo-1, respectively. In the case of other indicators such as Fluo-3 and Calcium-Green, Ca^{2+} binding increases the emitted fluorescence. While these indicators are mainly used to monitor intracellular Ca^{2+} , Rhod-2 of the rhodamine-based family of indicators represents an exception in terms of mitochondrial Ca^{2+} monitoring. The advantage of Rhod-2 is its net positive charge (both the AM and the hydrolysed forms), which promotes the accumulation of Rhod-2 into the mitochondrial matrix and a fluorescence increase upon Ca^{2+} binding [64]. However, Rhod-2 diffuses out of mitochondria soon after its entry into these organelles, causing inaccuracy during long time-course experiments.

Today, a broad spectrum of chemically-engineered Ca^{2+} indicators offers solutions for many biological questions related to Ca^{2+} . Some of these indicators, like Rhod-2 and Fura-2, are not only used to report qualitative Ca^{2+} level changes, but they are also useful to measure the exact $[\text{Ca}^{2+}]_{\text{mito}}$ [67–69]. However, and in addition to accurate targeting problems, the toxicity caused by the de-esterification reaction during a prolonged excitation is an important disadvantage related to the use of these probes [65,70,71].

2.3.2. Genetically-Encoded Ca^{2+} Indicators

Our knowledge of Ca^{2+} signalling has been accelerated with the creation of genetically-encoded Ca^{2+} indicators (GECIs). These probes offer convenient solutions for the problems associated with chemical Ca^{2+} indicators. GECIs possess either bioluminescent (based on aequorin) or fluorescent (based on green fluorescent protein (GFP) and its derivatives) proteins to report changes in Ca^{2+} signalling [72–76]. One of the biggest advantages that GECIs offer is that they can be targeted to desired organelles or cytoplasmic domains when they are fused with specific targeting signal peptides. Their expression can also be spatiotemporally controlled via tissue-specific or inducible promoters. Moreover, as GECIs are genetically-encoded, they offer a better substrate specificity and less variance in probe uptake, as compared to chemical Ca^{2+} indicators [77]. However, special attention must be given when choosing a specific GECI to use. GECIs are larger in size, as compared to chemical Ca^{2+} indicators, and their expression might potentially alter mitochondrial morphology or functions [65]. Similar to chemical Ca^{2+} indicators, several GECIs can be employed to measure the exact $[\text{Ca}^{2+}]_{\text{mito}}$ [78–80].

Bioluminescence-based GECIs are derived from the Ca^{2+} -sensitive photoprotein Aequorin (Aeq) isolated from the *Aequorea victoria* jellyfish [81]. Aeq has EF-hand motifs for Ca^{2+} binding and a hydrophobic core that can bind to an external cofactor like coelenterazine. Upon Ca^{2+} binding, Aeq undergoes an irreversible reaction in the presence of coelenterazine, and produces a photon of light [82]. The speed of emitted light can then be used to determine $[\text{Ca}^{2+}]$ [83]. A bioluminescence-based GECI named mtAEQ, which was composed of the mitochondrial targeting sequence of the cytochrome *c* oxidase polypeptide VIII (COX8) and fused with HA1-tagged native Aeq, was the first organelle-targeted GECI developed [84]. In fact, the first, direct evidence of mitochondrial Ca^{2+} accumulation in living cells upon stimulation has been made possible with the use of the mtAEQ probe. While bioluminescence-based GECIs have led the way to organelle-specific targeting, they have the disadvantage of being dim, as compared to fluorescence-based GECIs [85]. In addition, long-term imaging with these GECIs is not possible, due to the consumption of Aeq during the course of the reaction [86].

Fluorescent GECIs are comprised of a Ca^{2+} -sensing polypeptide and can trigger a change in the fluorescence properties of the fused fluorescence protein. Fluorescent GECIs can be grouped into two classes: single-fluorophore and Förster resonance energy transfer (FRET)-based GECIs. While single fluorophore GECIs exhibit changes in the fluorescence intensity or wavelength, FRET-based GECIs benefit from the energy transfer potential of the two fluorophores with partially overlapping excitation/emission spectra.

One of the first examples of single fluorophore GECIs is the Camgaroo family indicator. These indicators have a calmodulin- Ca^{2+} binding domain, and they undergo a shift in the absorbance peak of the fluorescence protein upon Ca^{2+} binding [87]. Another example of single-fluorophore GECIs is the GCaMP. GCaMPs rely on the circular permutation of GFP: The N- and C-termini are fused, thereby creating two new N- and C-termini. These termini are then fused to the M13 domain of a myosin light chain kinase, and calmodulin-binding domain, respectively [88]. Ca^{2+} binding to the calmodulin moiety of GCaMP leads to changes in the chromophore environment, which results in an increased fluorescence intensity. Ever since their discovery, GCaMP GECIs have been extensively improved in terms of their spectral properties, Ca^{2+} affinity, brightness, and kinetics [89].

The very first examples of the FRET-based GECIs are cameleons, consisting of blue and green fluorescent proteins, acting as donor and acceptor FRET pairs. These fluorophores are connected with a calmodulin domain fused to a myosin light chain kinase M13 [90]. The principle behind the Ca^{2+} -sensing function of the cameleons rely on the FRET phenomenon, which is a non-radiative energy transfer between a donor and an acceptor fluorophore. FRET can only occur when the donor-acceptor pair is in close proximity (<10 nm) and when the emission spectrum of the donor fluorophore overlaps with the excitation spectrum of the acceptor [91,92]. In the case of FRET-based GECIs, Ca^{2+} binding to the calmodulin domain changes the conformation of the probe, bringing the donor and acceptor pair into close proximity. This interaction allows the FRET reaction to occur, thus the changes in FRET

efficiency can be directly used to estimate changes in $[Ca^{2+}]$ [93]. Similarly to GCaMPs, cameleons have been extensively improved since their first discovery. New versions of cameleons now show a decreased sensitivity to acidic pH, along with higher fluorescence intensities and decreased propensity to photobleaching [94].

In addition to bioluminescence and FRET-based GECIs, a new GECI family named GECO indicators, have been recently developed. They were engineered by performing directed evolution on GCaMP3 [95]. GECOs were shown to measure $[Ca^{2+}]$ in two different organelles or in different mitochondrial compartments simultaneously. Compared to FRET-based GECIs, GECO indicators have better signal-to-noise ratios, and they allow for multicolour imaging of Ca^{2+} ions in different organelles, or in different compartments of an organelle [96]. They are currently available with red, blue, and green intensimetric emissions [95].

As described in this section, the generous palette of chemically and genetically engineered Ca^{2+} indicators portrays the complexity of Ca^{2+} homeostasis within the cell. Thus far, being among the most fruitful sub-fields in mitochondrial research, elucidating the interplay between mitochondria and Ca^{2+} signalling will not only deepen our fundamental knowledge about the physiology of the cell, but it will also encourage the development of more sophisticated microscopy-based tools.

3. Mitochondrial Dynamics

The dynamic properties of mitochondria have been initially reported in the early 1900s, owing to the advancements in the field of bright-field microscopy [97]. Later, in the 1990s, the use of fluorescent dyes and proteins coupled to time-lapse microscopy revealed the first detailed insights about the changes in the mitochondrial morphology in living cells [98–102]. Mitochondria are very dynamic organelles, constantly undergoing fusion and fission events. These events are the interconnection of the organelles or the fragmentation of them into smaller units, respectively [103]. A wide series of reports over the last two decades demonstrated that changes in mitochondrial morphology have impacts on cellular metabolism, apoptosis, immunity, cell cycle, and mitochondrial quality control [104–106]. Furthermore, pathogenic mutations in genes coding for mitochondrial fusion and fission proteins have been associated with severe developmental defects and neuromuscular and central nervous system syndromes in mice and humans [107,108].

3.1. Molecular Players of the Mitochondrial Dynamics

Mitochondrial dynamics refers to the balance between mitochondrial fusion and fission events to regulate the size, shape, number, and distribution of mitochondria in cells, and this balance is constantly adjusted in response to physiological cues (Figure 2) [107]. On the one hand, mitochondrial fusion is the interconnection of individual mitochondria by joining their respective outer and the inner membranes, along with the sharing of intramitochondrial content as mitochondrial DNA (mtDNA) molecules. Mitochondrial fission, on the other hand, is the division of a mitochondrion into two or more mitochondrial units [109].

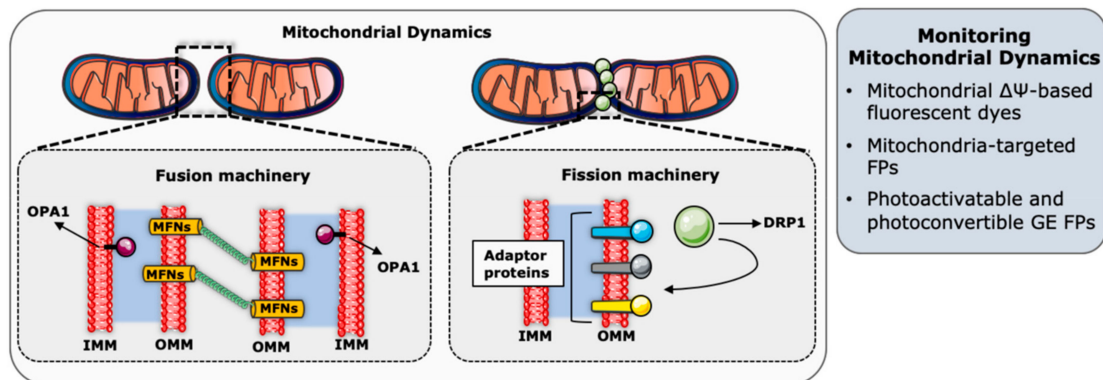


Figure 2. Probes to monitor mitochondrial dynamics. The major molecular players regulating these functions are symbolized within mitochondria. Key imaging-based approaches are listed in the grey box. OPA1, dynamin-like GTPase optic atrophy 1; MFNs, mitofusin 1 and mitofusin 2; DRP1, dynamamin-related protein 1; IMM, inner mitochondrial membrane; OMM, outer mitochondrial membrane; $\Delta\Psi$, membrane potential difference; FPs, fluorescent proteins; and GE, genetically-encoded. The figure was generated with elements provided in the Servier Medical Art depository (<https://smart.servier.com/>) and are licensed under a Creative Commons Attribution 3.0 Unported License (CC BY 3.0).

The balance between the opposing events of fusion and fission is not only required for proper mitochondrial functioning, but it is also necessary to adapt the mitochondrial network to the different metabolic states [105]. Mitochondrial fusion is required to regulate the respiratory chain activity, and maintains mtDNA integrity against the arousal of mutations or mitochondrial stress conditions [110,111]. In addition, pronounced fusion mechanisms during nutrient starvation were shown to protect the mitochondrial network from clearance through autophagy (mitophagy) [112]. Mitochondrial fission, however, is needed for the segregation and the consequent elimination of damaged mitochondrial parts during mitophagy, and for the inheritance of mtDNA to daughter cells during cell division [113,114].

The key molecular players of the mitochondrial fusion and fission events are GTPase proteins, belonging to a highly conserved Dynamin family [115]. Mitochondrial fusion or fission is achieved by the ability of these proteins to oligomerize and change conformation to trigger membrane modeling [116]. Mitochondrial fusion starts with the fusion of the OMM and in mammals, this is ensured by mitofusin 1 (MFN1) and mitofusin 2 (MFN2) [115]. The fusion event starts with the tethering of two mitochondria by homo- and hetero-oligomerization of MFNs [117]. Then, the conformational change of MFNs induced by the hydrolysis of GTP leads to the docking of the two adjacent membranes, while gradually increasing the membrane contact sites, and finally fusing the two OMMs [118–120]. Following OMM fusion, the dynamin-like GTPase optic atrophy 1 (OPA1) and specific IMM lipid components such as cardiolipin mediate IMM fusion [121]. OPA1 has sites for proteolytic cleavage that can be processed by IMM-bound metalloproteases OMA1 and YME1L, to generate shorter forms of OPA1 (S-OPA1) [122–125]. While the longer forms of OPA1 (L-OPA1) has been shown to be sufficient to drive fusion [126], S-OPA1 were suggested to couple IMM fusion to metabolism [127]. While there are different models describing IMM fusion, the interaction between L-OPA1 and cardiolipin was described to trigger the tethering of the two IMM, which is then followed by the membrane fusion upon OPA1-dependent GTP hydrolysis [121].

Mitochondrial fission is mediated by the dynamin-related protein 1 (DRP1), which is a large cytosolic GTPase protein recruited to mitochondria upon fission initiation [128]. Mitochondrial sites where DRP1 will be recruited are initially marked by ER tubules to be constricted [129]. It has recently been discovered that the replicating mtDNA is also found in the mitochondrial fission sites, in order to be able to allow the distribution of mtDNA to fragmented mitochondria [130]. Initiation of mitochondrial fission and mtDNA synthesis on the ER-mitochondria contact site are followed by the oligomerization of DRP1 on the OMM. DRP1 constricts mitochondria by forming ring-like structures around the organelles while hydrolyzing GTP [131,132]. Actin polymerization is also required at this

step to facilitate DRP1 accumulation [133]. Moreover, adaptor proteins such as MID49, MID51, and the mitochondrial fission factor (MFF), serve to recruit DRP1 by acting as receptors or recruitment factors for DRP1 [134–136]. Lastly, Dynamin 2 (DNM2) recruitment to the DRP1-mediated mitochondrial constriction sites finalizes the mitochondrial membrane scission [137]. As opposed to the well-described mechanisms of OMM constriction and scission, fission machinery, specifically dedicated to IMM, is still being investigated. Some studies claimed that IMM division is Ca^{2+} -dependent as this is supported by the observation of MCU loss leading to mitochondrial elongation [138–140]. The IMM protein MTP18 was also proposed to have a role in IMM fission, since its depletion results in mitochondrial hyperfusion and its overexpression causes mitochondrial fragmentation [141].

3.2. Probes and Methods to Study Mitochondrial Dynamics

Early studies focusing on mitochondria and their structural features generally rely on electron microscopy data. These approaches were the first ones to reveal that mitochondria have two membranes: A smooth outer membrane, and a convoluted inner membrane organized in cristae and projected into the mitochondrial matrix [142]. While electron microscopy techniques paved the way to our understanding of the mitochondrial ultrastructure, they cannot be employed to monitor fast changes in mitochondrial dynamics in living cells. To this end, advances in fluorescent microscopy techniques and tools were needed to study mitochondrial dynamics in real time and in living cells (Figure 2).

3.2.1. Mitochondria-Specific Fluorescent Dyes and Proteins

Mitochondria can be labeled in living cells by using several fluorescent dyes that are mainly based on mitochondrial $\Delta\Psi$ [143]. Examples of such cationic, $\Delta\Psi$ -sensitive fluorescent probes are Rhodamine 123 (R123), tetramethylrhodamine ethyl ester (TMRE), tetramethylrhodamine methyl ester (TMRM), and 5,5,6,6'-tetrachloro-1,1',3,3' tetraethylbenzimidazolylcarbocyanine iodide (JC-1). In order to label mitochondria with these fluorophores, mitochondria should be functional to generate membrane potential. While these dyes have been used to monitor $\Delta\Psi$ in several cell types, they are not the ideal probes to study dynamic changes in mitochondrial morphology since they leak from mitochondria upon a loss in mitochondrial $\Delta\Psi$ [144]. The exception among them is the MitoTracker Green, due to its ability to bind to the free thiol groups in the mitochondria. This allows the dye to maintain its intramitochondrial localization even after a loss in mitochondrial $\Delta\Psi$ [145,146]. The other available MitoTracker dyes are MitoTracker Red, Orange, and Deep Red. However, their sensitivity to mitochondrial $\Delta\Psi$ is debated and may differ depending on the experimental setup [145,147–149]. Recently, alternative fluorescent probes for mitochondria based on naphthalimide (NPA-TPP) [150] or boron-dipyrromethene (BODIPY) [151] show better photostability, higher brightness, and lower cytotoxicity, thus enabling researchers to monitor changes in mitochondrial morphology in long time-course experiments [150,151].

Another approach to label mitochondria is to use fluorescent proteins targeted specifically to these organelles. Here, the idea is to fuse a fluorescent protein gene with a mitochondrial targeting sequence (MTS). Depending on the desired readout, different types of MTSs can be used to target fluorescence proteins to different mitochondrial sub-compartments. Moreover, two or more of the same MTS can be put in a series to facilitate the targeting of the fluorescent protein [152]. Once the construct is ready, it is essential to verify that the genetically-encoded fusion product is targeted properly to the desired mitochondrial sub-compartment. To do so, mitochondria can be imaged in the presence of dyes (such as MitoTrackers) to verify that the genetically-encoded fluorescent protein is not causing any change in the mitochondrial morphology. The validated construct can then be used to acquire time-lapse fluorescence videos to monitor changes in mitochondrial morphology. Acquired data can then be analyzed with conventional software programs designed to calculate size, shape, number, and the interconnectivity rate of mitochondrial objects.

3.2.2. Imaging Methodologies with Genetically-Encoded Fluorescent Proteins

Due to the complex nature of mitochondrial dynamics, analyzing mitochondrial morphological changes alone is not sufficient to quantify fusion and fission events [153]. To this end, the use of mitochondria-targeted photoactivable and photoconvertible forms of fluorescent proteins has enabled researchers to differentiate between these events. Moreover, fluorescence recovery after photobleaching (FRAP) or fluorescence loss in photobleaching (FLIP) methods with regular mitochondrially-targeted fluorescence proteins provided the means to study diffusion properties within mitochondria.

A photoactivable GFP, named PAGFP, increases its fluorescence intensity 100-times after photoactivation [154]. By analyzing green-only pixels upon photoactivation, mitochondrial dynamics can be monitored in living cells expressing mitochondria-targeted photoactivable GFP (PAGFPmt) [154,155]. If the photoconverted PAGFPmt molecules are transferred to unlabeled mitochondrial units, this is indicative of fusion events, whereas a fission event can be followed if the PAGFPmt signal continuity is lost [153]. Photoactivable probes can also be used in combination with regular mitochondrial fluorescent proteins to distinguish non-fusing mitochondria. In order to do so, mitochondria that are co-expressing PAGFPmt and a mitochondrially-targeted DsRed fluorescent protein (mtDsRed) can be photoactivated for PAGFPmt, while bleaching mtDsRed in a region of interest by using 2-photon laser stimulation. In the resulting mitochondrial population, non-fusing units can only be identified with PAGFPmt signal in the region of interest. Fusing units, however, would show overlapping signals of photoactivated PAGFPmt and mtDsRed, if they interconnect with the surrounding non-photobleached and non-photoconverted mitochondria residing outside the region of interest [153].

Similar to photoactivation approaches, the photoconversion of genetically-encoded fluorescent proteins can be used to evaluate the interconnectivity of mitochondria. Photoconvertible fluorescent proteins employ an irreversible change in the fluorescence excitation and emission spectra upon an excitation at a specific wavelength [156]. A commonly employed example of this type of probe is Dendra2, which is a fluorescent protein switching from green to red when excited with a 405 nm laser [157]. In this context, mitochondrially-targeted Dendra2 (mitoDendra2) can be photoconverted to follow the diffusion of red molecules over green ones, thereby monitoring the continuity of the mitochondrial network [158]. Thus far, mitoDendra2 has been used to analyze mitochondrial interconnectivity in cultured cells and in several model organisms, including *C. elegans* [159], *Drosophila* [160,161], and mice [158].

Apart from photoactivable and photoconvertible fluorescent proteins, FRAP or FLIP methods can be utilized with regular mitochondrially-targeted fluorescent proteins to study mitochondrial dynamics. In FRAP experiments, a region of interest is photobleached and the fluorescence recovery in the bleached area over time is followed during time-lapse acquisitions [162]. As the recovery is due to the diffusion of fluorescent proteins adjacent to the bleached areas, this can be used as an indication of the interconnectivity of mitochondria [163]. In FLIP experiments, repeated photobleaching of a region of interest is performed while imaging the rest of the cell. This allows for the monitoring of the gradual loss in the fluorescence signal due to the movement of fluorescent proteins [162]. If the mitochondrial network is interconnected with the mitochondrial units in the bleached area, a decrease in the fluorescence signal in the rest of the cell is observed [162].

3.2.3. Super-Resolution Microscopy for Mitochondrial Ultrastructure

Considering the size of a typical mitochondrion being close to the resolution limit of a conventional fluorescence microscope, super resolution microscopy techniques offer the opportunity to investigate the mitochondrial ultrastructure with their superior resolution. Some of the commonly available super resolution microscopes devised so far are structured illumination microscopy (SIM) [164], stimulated emission depletion microscopy (STED) [165], photo-activated localization microscopy (PALM) [166], and stochastic optical reconstruction microscopy (STORM) [167]. Utilization of these methods in the field of mitochondrial research significantly expanded over the last decade. On the one hand,

three-dimensional SIM (3D SIM) imaging of mitochondria, labeled with MitoTracker Green, has resolved cristae structures, which were previously visible only in electron microscopy images [168]. On the other hand, STORM allowed for the visualization of the mitochondrial inner membrane dynamics by using MitoTracker probes in living cells [169]. Moreover, STED microscopy revealed an array of Mitochondrial INner membrane Organizing System (MINOS) clusters in human mitochondria, by showing the distribution of three individual MINOS subunits in mammalian cells [170]. STED has also been employed to demonstrate distinct mitochondrial ribosome clusters that interact with proteins involved in mRNA metabolism and respiratory chain assembly [171]. When it comes to the structural arrangement of mtDNA in nucleoids, 2D and 3D applications of PALM have enabled the visualization of ellipsoidal nucleoids containing extremely condensed mtDNA. The properties of the photoconvertible protein mEOS2 fused to the mitochondrial transcription factor TFAM allowed individual nucleoids to be resolved, to calculate their dimensions, and their distribution in the matrix [172].

Despite the clear gain in resolution reached with these techniques, it must be kept in mind that super-resolution microscopy is heavily time-consuming, and the available image analysis solutions are still not user-friendly. Moreover, the biggest challenge nowadays is to optimize these systems to perform dynamic live cell imaging while achieving super resolution. To this end, a recently developed imaging technique called MINFLUX combines STED and PALM/STORM approaches. Therefore, MINFLUX offers an increased resolution—by a factor of 100—at the nanometer scale, while imaging in living cells [173]. Another exciting alternative that can also allow for live cell imaging on a molecular scale is the lattice light sheet microscopy [174]. This technique has recently been used to demonstrate mitochondrial positioning according to the ATP:ADP gradient in mouse embryonic fibroblasts [175]. Technological and methodological upgrades, both in super-resolution approaches and lattice light sheet microscopy techniques, will certainly become the next frontier for the analysis of mitochondrial dynamics with an unprecedented spatial resolution in living cells.

4. Mitophagy

During stress conditions, mitochondria were shown to produce excessive amounts of ROS that can disrupt the organelle function in terms of ATP synthesis [176,177]. Increased levels of mitochondrial ROS can promote excessive Ca^{2+} uptake, leading to a loss in membrane potential and subsequently causing the release of apoptotic factors that can initiate cell death signalling [178–180]. In this context, mitochondrial quality control, and thus the maintenance of a healthy and functional mitochondrial population, is an important determinant of cell fate [181]. To this end, a selective form of autophagy—termed mitophagy—serves as a protective mechanism to selectively sequester and degrade damaged mitochondrial units before they activate cell death pathways [182,183].

Ever since the first observation of mitochondria inside an autophagosome in 1957, a considerable amount of work has been done to delineate the molecular pathways leading to mitophagy [184]. However, the field is still in need of robust live imaging tools to monitor and quantify mitophagy events in real time.

4.1. Molecular Pathways of Mitophagy

The most well studied molecular pathway of mitophagy is mediated by the phosphatase and tension homologue (PTEN)-induced putative kinase 1 (PINK1) and the E3 ligase PARK2 (Parkin) (Figure 1) [185]. Under basal conditions, PINK1 is imported into the IMM and cleaved by several intramitochondrial proteases [186–189]. Truncated PINK1 is then released into the cytoplasm and degraded by the ubiquitin-proteasome system [190,191]. Upon membrane potential loss, PINK1 can no longer be imported into the IMM, but it is rather stabilized on the OMM [192–194] where it recruits Parkin [192]. The E3 ligase activity of Parkin is activated when PINK1 phosphorylates ubiquitin at Ser 65 [195]. Parkin then ubiquitinates OMM proteins for their recognition and engulfment by the autophagosomes or degradation by proteasomal machinery [196–201]. In the case of autophagosomal engulfment, autophagy receptor proteins such as sequestosome 1 (SQSTM1)/p62 bind

to the ubiquitinated mitochondrial units to link them with autophagosomes via microtubule-associated protein 1 light chain 3 (MAP1LC3, mostly known as LC3) [202]. Subsequent fusion of the autophagosomes with the lysosomes results in the complete degradation of mitochondrial remnants. This mechanism was shown to be impaired in inherited forms of Parkinson disease, in which the accumulation of dysfunctional mitochondria contributes to the death of dopaminergic neurons [203].

Aside from PINK1/Parkin-dependent mitophagy, mitochondrial clearance pathways regulated by other ubiquitin E3 ligases, such as Gp78, SMURF1, SIAH1, MUL1, and ARIH1, have been reported [204]. Similar to Parkin, these proteins can generate ubiquitin chains and modulate the recruitment of autophagy adaptor proteins [204]. A common trait between PINK1/Parkin-dependent and independent pathways is that several mitochondrial proteins appear to serve as mitophagy receptors. Due to their direct binding to LC3, they target dysfunctional mitochondria to autophagosomes for degradation [205]. A recent example of such a receptor is Prohibitin 2 (PHB2), which is an IMM protein shown to directly interact with LC3 after OMM rupture and to be indispensable for Parkin-dependent and independent mitophagy [206].

4.2. Roles of Mitophagy in Cellular Homeostasis

Under physiological conditions, mitophagy can occur at a basal rate to guarantee the normal turnover of metabolically inefficient organelles, or damaged parts of the mitochondrial network [207,208]. This rate is regulated in a tissue-specific manner to meet the varying metabolic needs of different tissues [209,210]. Additionally, basal mitophagy rates can be upregulated upon environmental stress factors such as starvation, hypoxia, and the administration of mitochondrial uncouplers to facilitate mitochondrial quality control [211–213]. Moreover, cells may perform programmed mitophagy events to enforce mitochondrial clearance during development [214,215], the degradation of paternal mitochondria upon fertilization [216], or when a metabolic switch from glycolysis to oxidative phosphorylation occurs [217,218]. A growing body of evidence shows that the complex interplay between these different mitophagy paradigms requires the utilization of different molecular players, and the crosstalk with mitochondrial dynamics and endosomal pathways [219–221].

4.3. Probes to Monitor Mitophagy

The first image-based strategy to observe mitophagy was performed with electron microscopy, where the mitochondria were engulfed by lysosomes and appeared to be in stages of “breakdown” or “hydrolysis” [222]. These early studies provided the first ultrastructure of mitophagy events, and although showing an unprecedented spatial resolution of this process, electron microscopy approaches have little temporal resolution. In light of this, strategies to image mitophagy have evolved to employ confocal or widefield fluorescence microscopy, as these image capabilities have a convenient spatiotemporal resolution and can be used in a quantitative mode. It should be noted that these strategies are often coupled with biochemical approaches such as Western blotting, to follow the degradation of specific mitochondrial markers.

In the following section, we will focus on some of the commonly used probes that can be used to monitor mitophagy by fluorescence microscopy (Figure 1).

4.3.1. Colocalization of Mitochondrial Probes with Autophagic or Lysosomal Markers

Colocalization analyses of mitochondrial fluorescent probes with markers of autophagosomes or lysosomes were one of the initial approaches to quantify mitochondrial units undergoing mitophagy. In these studies, LC3 was often used as a marker protein of autophagosomes, as it is tethered into the autophagic membranes upon the induction of autophagy [223]. LC3 can be monitored by fusing it with a fluorescent protein such as GFP. Mitochondria, however, can be labeled with a mitochondria-targeted red fluorescent protein (RFP) [112], or with MitoTracker dyes spectrally-compatible with GFP-LC3 [224]. Visualization and quantification of GFP-LC3 punctate structures colocalizing with mitochondrial markers can then be indicative of mitochondria undergoing mitophagy [225]. While this method

has been used in many studies, it has two main limitations. First, LC3 was shown to accumulate into intracellular protein aggregates, which are independent of autophagy, thus making it difficult to separate random aggregation events from true mitophagy [223]. Second, the GFP fluorophore is quenched in environments with an acidic pH. Such drops in pH occur in the late stages of the mitophagy pathway, when the autophagosome fuses with the lysosome [225]. Therefore, this strategy cannot be used as a direct read-out of mitochondrial degradation, since the hydrolysis of mitochondria cannot be observed [226].

In order to monitor the degradation of mitochondria into lysosomes, lysosomal marker proteins such as the lysosomal-associated membrane protein 1 (LAMP1) can be fused with fluorescent proteins resistant to acidic pH (i.e. mCherry, DsRed2, and their derivatives). Fluorescent LAMP1 can then be used in combination with mitochondrial probes to follow the later events of mitophagy [227]. Alternatively, LysoTracker dyes can also be used to follow the colocalization of mitochondria with lysosomes [224,228,229]. These dyes have acidotropic properties, and therefore, they are recruited to the acidic compartments in the cell [230]. However, they have been reported to photobleach rapidly, thus posing a potential threat for long time-course experiments [231].

4.3.2. Genetically-Encoded Mitophagy Sensors

Recently, several genetically-encoded mitophagy sensors have been developed to provide spatio-temporal information while monitoring mitophagy events in live cells. Considering the mitophagy flow as a dynamic course of events, these sensors have the potential to give detailed insights about the mitophagy pathway by sensing certain elements of this flux.

A tandem RFP-GFP fusion protein targeted to mitochondria is an example of genetically-encoded mitophagy sensor. It is designed to distinguish key steps in the mitophagy flux as the events of autophagosome formation and their fusion with lysosomes [232]. The idea behind this probe relies on the differences in the pK_a of GFP and RFP (c.f. previous chapter). When the autophagosomes are formed but not yet fused with the lysosomes, they have colocalized red and green signals of the punctate structures, which would indicate that the mitochondria are engulfed by the autophagosomes. Conversely, the red-only punctate structures can be used to identify autophagosomes fused with lysosomes. This is due to the acidic environment of lysosomes, which would cause the quenching of GFP, but not of RFP [232]. For instance, an OMM-targeted RFP-GFP tandem has been used to identify iron-chelators as PINK1/Parkin-independent mitophagy inducers [233], whereas an IMM-targeted RFP-GFP tandem was used to show mitophagy activation upon hepatitis B virus infection [234].

By following a similar experimental strategy, a transgenic mouse model with a pH-sensitive mitochondrial fluorescent probe was developed [207]. This construct was named mito-Quality Control (mito-QC), and it is constituted of a mCherry-GFP tandem protein targeted to the OMM via the MTS of the mitochondrial fission protein FIS1 [207]. By following the mCherry-only punctate structures, McWilliams et al. used mito-QC to monitor mitochondria targeted at lysosomes upon mitophagy activation.

Mt-Keima is another genetically-encoded fluorescent reporter used to follow mitophagy events in cells and in vivo [208,235]. Mt-Keima is a probe targeted to the mitochondrial matrix that can change its spectral properties depending on the surrounding pH [235]. When mt-Keima is in an environment with elevated or physiological pH, as in mitochondria (pH ~8.0), it has a green fluorescence. On the contrary, when pH drops as in lysosomes (pH ~4.5), mt-Keima becomes ionized and it shows a red fluorescence [235]. Mt-Keima has been used to follow the delivery of mitochondria to lysosomes upon mitophagy activation, and it was reported to be stable in lysosomes [235,236]. It should also be acknowledged that mt-Keima was shown to have limitations in terms of spectral separation between the green and the red forms [207], which therefore questions whether its use is pertinent for mitophagy.

In addition to mitophagy, mitochondrial biogenesis and turnover can also be monitored to assess mitochondrial “aging” in cells. For this purpose, a probe named MitoTimer was developed by targeting the Timer fluorescent protein to the mitochondrial matrix [237,238]. Along the process of

maturation, the Timer protein undergoes an oxidation, which induces an irreversible fluorescence shift from green to red over time [238]. Given that it works as a molecular clock, this probe was used to obtain spatiotemporal information on mitochondrial biogenesis (green organelles) and turnover (red mitochondria).

5. Conclusions

As described in this review, mitochondria are organelles with diverse functions and morphological features. While the complex nature of these organelles is important to regulate cellular homeostasis and metabolism, it also makes it challenging to follow and image them. However, the majority of studies have benefited from imaging probes targeted at mitochondria. In this context, our chance to deepen our knowledge about mitochondria and their function in health and disease relies on the availability of the microscopy-based tools, and recent advances in live imaging techniques.

Benefiting from a variety of chemically and genetically-engineered reporters, mitochondrial Ca^{2+} buffering and signalling is the most extensively-studied mitochondrial function. However, the available probes for monitoring mitochondrial dynamics and mitophagy pathways are limited in terms of their ability to follow the complete flow of events. This is especially noteworthy for monitoring mitophagy events, as the majority of studies focus on the colocalization of LC3 with a mitochondria-targeted fluorescent probe. As discussed above, this can be misleading due to the lack of knowledge about the early and late time-points of the mitophagy pathway. In light of this, the investigation of alternate and specialized marker proteins recruited to autophagosomes will certainly pave the way to the design of new probes.

Genetically-encoded sensors are advantageous compared to chemical reporters, as they are engineered to be substrate-specific, therefore allowing for the following of a detailed series of events over a long period of time [77,239]. An exciting challenge in this field would be the use of two— or potentially more—genetically-encoded sensors at the same time in order to be able to follow different mitochondrial functions simultaneously. This strategy could be further extended by using these biosensors in combination with chemical reporters, and also in screening modes. This would allow for the performing of high-content analyses of mitochondria in response to pharmaceutical compounds, or to discover new mitochondria-based therapeutic agents.

Ongoing research to improve the spectral properties of the fluorescent proteins, and the advances in imaging methodologies, will certainly allow researchers to develop mitochondria-based diagnostic and drug-screening technologies in the near future. These technologies will eventually lay the groundwork for personalized medicine for people suffering from a mitochondrial disease, or from multifaceted pathologies where mitochondria play a key role.

Author Contributions: E.B.G. participated in the conceptualization of this review and wrote the original draft; M.T. provided support; G.B. co-conceptualized the manuscript, supervised, provided funding, and reviewed the manuscript. All authors have read and agreed to the published version of the manuscript.

Funding: This research was funded by the CNRS (*Centre National de la Recherche Scientifique*), the University of Rennes 1, the Ligue Contre Le Cancer Grand-Ouest—*Comité d'Ille et Vilaine, Comité des Côtes d'Armor et Comité du Finistère*—to GB. EBG was funded by the Ligue Contre Le Cancer and the Brittany Region (*Région Bretagne*).

Acknowledgments: We thank Seyta Ley-Ngardigal for helpful discussions and support.

Conflicts of Interest: The authors declare no conflict of interest. The funders had no role in the design of the study; in the collection, analyses, or interpretation of data; in the writing of the manuscript, or in the decision to publish the results.

References

1. Wallace, D.C.; Fan, W.; Procaccio, V. Mitochondrial energetics and therapeutics. *Annu. Rev. Pathol.* **2010**, *5*, 297–348. [[CrossRef](#)] [[PubMed](#)]
2. Mammucari, C.; Patron, M.; Granatiero, V.; Rizzuto, R. Molecules and roles of mitochondrial calcium signaling. *Biofactors* **2011**, *37*, 219–227. [[CrossRef](#)] [[PubMed](#)]

3. Murphy, M.P. How mitochondria produce reactive oxygen species. *Biochem. J.* **2009**, *417*, 1–13. [[CrossRef](#)] [[PubMed](#)]
4. Wang, C.; Youle, R.J. The Role of Mitochondria in Apoptosis. *Annu. Rev. Genet.* **2009**, *43*, 95–118. [[CrossRef](#)] [[PubMed](#)]
5. Nilsson, R.; Schultz, I.J.; Pierce, E.L.; Soltis, K.A.; Naranuntarat, A.; Ward, D.M.; Baughman, J.M.; Paradkar, P.N.; Kingsley, P.D.; Culotta, V.C.; et al. Discovery of Genes Essential for Heme Biosynthesis through Large-Scale Gene Expression Analysis. *Cell Metab.* **2009**, *10*, 119–130. [[CrossRef](#)] [[PubMed](#)]
6. Laffel, L. Ketone bodies: A review of physiology, pathophysiology and application of monitoring to diabetes. *Diabetes/Metab. Res. Rev.* **1999**, *15*, 412–426. [[CrossRef](#)]
7. Miller, W.L. Steroid hormone synthesis in mitochondria. *Mol. Cell. Endocrinol.* **2013**, *379*, 62–73. [[CrossRef](#)]
8. Chan, D.C. Mitochondria: Dynamic organelles in disease, aging, and development. *Cell* **2006**, *125*, 1241–1252. [[CrossRef](#)]
9. Liesa, M.; Shirihai, O.S. Mitochondrial Dynamics in the Regulation of Nutrient Utilization and Energy Expenditure. *Cell Metab.* **2013**, *17*, 491–506. [[CrossRef](#)]
10. Anderson, S.; Bankier, A.T.; Barrell, B.G.; de Bruijn, M.H.L.; Coulson, A.R.; Drouin, J.; Eperon, I.C.; Nierlich, D.P.; Roe, B.A.; Sanger, F.; et al. Sequence and organization of the human mitochondrial genome. *Nature* **1981**, *290*, 457–465. [[CrossRef](#)]
11. Wallace, D.C. Mitochondrial Diseases in Man and Mouse. *Science* **1999**, *283*, 1482–1488. [[CrossRef](#)] [[PubMed](#)]
12. Ringer, S. A third contribution regarding the Influence of the Inorganic Constituents of the Blood on the Ventricular Contraction. *J. Physiol. (Lond.)* **1883**, *4*, 222–225. [[CrossRef](#)] [[PubMed](#)]
13. Vasington, F.D.; Murphy, J.V. Ca ion uptake by rat kidney mitochondria and its dependence on respiration and phosphorylation. *J. Biol. Chem.* **1962**, *237*, 2670–2677. [[PubMed](#)]
14. Deluca, H.F.; Engstrom, G.W. Calcium uptake by rat kidney mitochondria. *Proc. Natl. Acad. Sci. USA* **1961**, *47*, 1744–1750. [[CrossRef](#)] [[PubMed](#)]
15. Marchi, S.; Bittremieux, M.; Missiroli, S.; Morganti, C.; Patergnani, S.; Sbrano, L.; Rimessi, A.; Kerkhofs, M.; Parys, J.B.; Bultynck, G.; et al. Endoplasmic Reticulum-Mitochondria Communication Through Ca²⁺ Signaling: The Importance of Mitochondria-Associated Membranes (MAMs). *Adv. Exp. Med. Biol.* **2017**, *997*, 49–67.
16. Hoek, J.B.; Walajtys-Rode, E.; Wang, X. Hormonal stimulation, mitochondrial Ca²⁺ accumulation, and the control of the mitochondrial permeability transition in intact hepatocytes. *Mol. Cell. Biochem.* **1997**, *174*, 173–179. [[CrossRef](#)]
17. Rapizzi, E.; Pinton, P.; Szabadkai, G.; Wieckowski, M.R.; Vandecasteele, G.; Baird, G.; Tuft, R.A.; Fogarty, K.E.; Rizzuto, R. Recombinant expression of the voltage-dependent anion channel enhances the transfer of Ca²⁺ microdomains to mitochondria. *J. Cell Biol.* **2002**, *159*, 613–624. [[CrossRef](#)]
18. Baughman, J.M.; Perocchi, F.; Girgis, H.S.; Plovanich, M.; Belcher-Timme, C.A.; Sancak, Y.; Bao, X.R.; Strittmatter, L.; Goldberger, O.; Bogorad, R.L.; et al. Integrative genomics identifies MCU as an essential component of the mitochondrial calcium uniporter. *Nature* **2011**, *476*, 341–345. [[CrossRef](#)]
19. De Stefani, D.; Raffaello, A.; Teardo, E.; Szabò, I.; Rizzuto, R. A forty-kilodalton protein of the inner membrane is the mitochondrial calcium uniporter. *Nature* **2011**, *476*, 336–340. [[CrossRef](#)]
20. Kamer, K.J.; Mootha, V.K. The molecular era of the mitochondrial calcium uniporter. *Nat. Rev. Mol. Cell Biol.* **2015**, *16*, 545–553. [[CrossRef](#)]
21. Marchi, S.; Pinton, P. The mitochondrial calcium uniporter complex: Molecular components, structure and physiopathological implications. *J. Physiol. (Lond.)* **2014**, *592*, 829–839. [[CrossRef](#)] [[PubMed](#)]
22. Foskett, J.K.; Philipson, B. The mitochondrial Ca²⁺ uniporter complex. *J. Mol. Cell. Cardiol.* **2015**, *78*, 3–8. [[CrossRef](#)] [[PubMed](#)]
23. Bragadin, M.; Pozzan, T.; Azzone, G.F. Kinetics of Ca²⁺ carrier in rat liver mitochondria. *Biochemistry* **1979**, *18*, 5972–5978. [[CrossRef](#)] [[PubMed](#)]
24. Perocchi, F.; Gohil, V.M.; Girgis, H.S.; Bao, X.R.; McCombs, J.E.; Palmer, A.E.; Mootha, V.K. MICU1 encodes a mitochondrial EF hand protein required for Ca²⁺ uptake. *Nature* **2010**, *467*, 291–296. [[CrossRef](#)]
25. Plovanich, M.; Bogorad, R.L.; Sancak, Y.; Kamer, K.J.; Strittmatter, L.; Li, A.A.; Girgis, H.S.; Kuchimanchi, S.; Groot, J.D.; Speciner, L.; et al. MICU2, a Paralog of MICU1, Resides within the Mitochondrial Uniporter Complex to Regulate Calcium Handling. *PLoS ONE* **2013**, *8*, e55785. [[CrossRef](#)]

26. Csordás, G.; Golenár, T.; Seifert, E.L.; Kamer, K.J.; Sancak, Y.; Perocchi, F.; Moffat, C.; Weaver, D.; de la Fuente Perez, S.; Bogorad, R.; et al. MICU1 controls both the threshold and cooperative activation of the mitochondrial Ca^{2+} uniporter. *Cell Metab.* **2013**, *17*, 976–987. [[CrossRef](#)]
27. Mallilankaraman, K.; Doonan, P.; Cárdenas, C.; Chandramoorthy, H.C.; Müller, M.; Miller, R.; Hoffman, N.E.; Gandhirajan, R.K.; Molgó, J.; Birnbaum, M.J.; et al. MICU1 is an essential gatekeeper for MCU-mediated mitochondrial Ca^{2+} uptake that regulates cell survival. *Cell* **2012**, *151*, 630–644. [[CrossRef](#)]
28. Patron, M.; Checchetto, V.; Raffaello, A.; Teardo, E.; Vecellio Reane, D.; Mantoan, M.; Granatiero, V.; Szabò, I.; De Stefani, D.; Rizzuto, R. MICU1 and MICU2 finely tune the mitochondrial Ca^{2+} uniporter by exerting opposite effects on MCU activity. *Mol. Cell* **2014**, *53*, 726–737. [[CrossRef](#)]
29. Jung, D.W.; Baysal, K.; Brierley, G.P. The sodium-calcium antiport of heart mitochondria is not electroneutral. *J. Biol. Chem.* **1995**, *270*, 672–678. [[CrossRef](#)]
30. Dash, R.K.; Beard, D.A. Analysis of cardiac mitochondrial Na^+ - Ca^{2+} exchanger kinetics with a biophysical model of mitochondrial Ca^{2+} handling suggests a 3:1 stoichiometry. *J. Physiol. (Lond.)* **2008**, *586*, 3267–3285. [[CrossRef](#)]
31. Gunter, K.K.; Zuscik, M.J.; Gunter, T.E. The Na^+ -independent Ca^{2+} efflux mechanism of liver mitochondria is not a passive $\text{Ca}^{2+}/2\text{H}^+$ exchanger. *J. Biol. Chem.* **1991**, *266*, 21640–21648. [[PubMed](#)]
32. Numata, M.; Petrecca, K.; Lake, N.; Orłowski, J. Identification of a mitochondrial Na^+/H^+ exchanger. *J. Biol. Chem.* **1998**, *273*, 6951–6959. [[CrossRef](#)] [[PubMed](#)]
33. Elrod, J.W.; Wong, R.; Mishra, S.; Vagnozzi, R.J.; Sakthivel, B.; Goonasekera, S.A.; Karch, J.; Gabel, S.; Farber, J.; Force, T.; et al. Cyclophilin D controls mitochondrial pore-dependent Ca^{2+} exchange, metabolic flexibility, and propensity for heart failure in mice. *J. Clin. Investig.* **2010**, *120*, 3680–3687. [[CrossRef](#)] [[PubMed](#)]
34. Lu, X.; Kwong, J.Q.; Molkentin, J.D.; Bers, D.M. Individual Cardiac Mitochondria Undergo Rare Transient Permeability Transition Pore Openings. *Circ. Res.* **2016**, *118*, 834–841. [[CrossRef](#)]
35. Jiang, D.; Zhao, L.; Clapham, D.E. Genome-wide RNAi screen identifies Letm1 as a mitochondrial $\text{Ca}^{2+}/\text{H}^+$ antiporter. *Science* **2009**, *326*, 144–147. [[CrossRef](#)]
36. De Marchi, E.; Bonora, M.; Giorgi, C.; Pinton, P. The mitochondrial permeability transition pore is a dispensable element for mitochondrial calcium efflux. *Cell Calcium* **2014**, *56*, 1–13. [[CrossRef](#)]
37. Austin, S.; Tavakoli, M.; Pfeiffer, C.; Seifert, J.; Mattarei, A.; De Stefani, D.; Zoratti, M.; Nowikovsky, K. LETM1-Mediated K^+ and Na^+ Homeostasis Regulates Mitochondrial Ca^{2+} Efflux. *Front. Physiol.* **2017**, *8*, 839. [[CrossRef](#)]
38. De Marchi, U.; Santo-Domingo, J.; Castelbou, C.; Sekler, I.; Wiederkehr, A.; Demaurex, N. NCLX protein, but not LETM1, mediates mitochondrial Ca^{2+} extrusion, thereby limiting Ca^{2+} -induced NAD(P)H production and modulating matrix redox state. *J. Biol. Chem.* **2014**, *289*, 20377–20385. [[CrossRef](#)]
39. McCormack, J.G.; Halestrap, A.P.; Denton, R.M. Role of calcium ions in regulation of mammalian intramitochondrial metabolism. *Physiol. Rev.* **1990**, *70*, 391–425. [[CrossRef](#)]
40. Hansford, R.G. Physiological role of mitochondrial Ca^{2+} transport. *J. Bioenerg. Biomembr.* **1994**, *26*, 495–508. [[CrossRef](#)]
41. McCormack, J.G.; Denton, R.M. The effects of calcium ions and adenine nucleotides on the activity of pig heart 2-oxoglutarate dehydrogenase complex. *Biochem. J.* **1979**, *180*, 533–544. [[CrossRef](#)] [[PubMed](#)]
42. Szalai, G.; Krishnamurthy, R.; Hajnóczky, G. Apoptosis driven by IP (3)-linked mitochondrial calcium signals. *EMBO J.* **1999**, *18*, 6349–6361. [[CrossRef](#)] [[PubMed](#)]
43. Jacobson, J.; Duchen, M.R. Mitochondrial oxidative stress and cell death in astrocytes—Requirement for stored Ca^{2+} and sustained opening of the permeability transition pore. *J. Cell Sci.* **2002**, *115*, 1175–1188. [[PubMed](#)]
44. Davidson, S.M.; Yellon, D.M.; Murphy, M.P.; Duchen, M.R. Slow calcium waves and redox changes precede mitochondrial permeability transition pore opening in the intact heart during hypoxia and reoxygenation. *Cardiovasc. Res.* **2012**, *93*, 445–453. [[CrossRef](#)] [[PubMed](#)]
45. Høyer-Hansen, M.; Bastholm, L.; Szyniarowski, P.; Campanella, M.; Szabadkai, G.; Farkas, T.; Bianchi, K.; Fehrenbacher, N.; Elling, F.; Rizzuto, R.; et al. Control of Macroautophagy by Calcium, Calmodulin-Dependent Kinase Kinase- β , and Bcl-2. *Mol. Cell* **2007**, *25*, 193–205. [[CrossRef](#)]
46. Gastaldello, A.; Callaghan, H.; Gami, P.; Campanella, M. Ca^{2+} -dependent autophagy is enhanced by the pharmacological agent PK11195. *Autophagy* **2010**, *6*, 607–613. [[CrossRef](#)]

47. Filadi, R.; Theurey, P.; Pizzo, P. The endoplasmic reticulum-mitochondria coupling in health and disease: Molecules, functions and significance. *Cell Calcium* **2017**, *62*, 1–15. [[CrossRef](#)]
48. Bezprozvanny, I.; Watras, J.; Ehrlich, B.E. Bell-shaped calcium-response curves of Ins (1,4,5)P₃- and calcium-gated channels from endoplasmic reticulum of cerebellum. *Nature* **1991**, *351*, 751–754. [[CrossRef](#)]
49. Moshkforoush, A.; Ashenagar, B.; Tsoukias, N.M.; Alevriadou, B.R. Modeling the role of endoplasmic reticulum-mitochondria microdomains in calcium dynamics. *Sci. Rep.* **2019**, *9*, 1–16. [[CrossRef](#)]
50. Tang, Y.; Zucker, R.S. Mitochondrial involvement in post-tetanic potentiation of synaptic transmission. *Neuron* **1997**, *18*, 483–491. [[CrossRef](#)]
51. Billups, B.; Forsythe, I.D. Presynaptic mitochondrial calcium sequestration influences transmission at mammalian central synapses. *J. Neurosci.* **2002**, *22*, 5840–5847. [[CrossRef](#)] [[PubMed](#)]
52. Medler, K.; Gleason, E.L. Mitochondrial Ca²⁺ buffering regulates synaptic transmission between retinal amacrine cells. *J. Neurophysiol.* **2002**, *87*, 1426–1439. [[CrossRef](#)] [[PubMed](#)]
53. Talbot, J.D.; David, G.; Barrett, E.F. Inhibition of mitochondrial Ca²⁺ uptake affects phasic release from motor terminals differently depending on external [Ca²⁺]. *J. Neurophysiol.* **2003**, *90*, 491–502. [[CrossRef](#)] [[PubMed](#)]
54. David, G.; Barrett, E.F. Mitochondrial Ca²⁺ uptake prevents desynchronization of quantal release and minimizes depletion during repetitive stimulation of mouse motor nerve terminals. *J. Physiol.* **2003**, *548*, 425–438. [[CrossRef](#)]
55. Voronina, S.; Sukhomlin, T.; Johnson, P.R.; Erdemli, G.; Petersen, O.H.; Tepikin, A. Correlation of NADH and Ca²⁺ signals in mouse pancreatic acinar cells. *J. Physiol. (Lond.)* **2002**, *539*, 41–52. [[CrossRef](#)]
56. Cancela, J.M.; Van Coppenolle, F.; Galione, A.; Tepikin, A.V.; Petersen, O.H. Transformation of local Ca²⁺ spikes to global Ca²⁺ transients: The combinatorial roles of multiple Ca²⁺ releasing messengers. *EMBO J.* **2002**, *21*, 909–919. [[CrossRef](#)]
57. Sutton, R.; Criddle, D.; Raraty, M.G.T.; Tepikin, A.; Neoptolemos, J.P.; Petersen, O.H. Signal transduction, calcium and acute pancreatitis. *Pancreatology* **2003**, *3*, 497–505. [[CrossRef](#)]
58. Murphy, J.A.; Criddle, D.N.; Sherwood, M.; Chvanov, M.; Mukherjee, R.; McLaughlin, E.; Booth, D.; Gerasimenko, J.V.; Raraty, M.G.T.; Ghaneh, P.; et al. Direct activation of cytosolic Ca²⁺ signaling and enzyme secretion by cholecystokinin in human pancreatic acinar cells. *Gastroenterology* **2008**, *135*, 632–641. [[CrossRef](#)]
59. Jouaville, L.S.; Pinton, P.; Bastianutto, C.; Rutter, G.A.; Rizzuto, R. Regulation of mitochondrial ATP synthesis by calcium: Evidence for a long-term metabolic priming. *Proc. Natl. Acad. Sci. USA* **1999**, *96*, 13807–13812. [[CrossRef](#)]
60. Tarasov, A.I.; Griffiths, E.J.; Rutter, G.A. Regulation of ATP production by mitochondrial Ca²⁺. *Cell Calcium* **2012**, *52*, 28–35. [[CrossRef](#)]
61. Rasola, A.; Bernardi, P. Mitochondrial permeability transition in Ca²⁺-dependent apoptosis and necrosis. *Cell Calcium* **2011**, *50*, 222–233. [[CrossRef](#)] [[PubMed](#)]
62. Paredes, R.M.; Etzler, J.C.; Watts, L.T.; Zheng, W.; Lechleiter, J.D. Chemical calcium indicators. *Methods* **2008**, *46*, 143–151. [[CrossRef](#)] [[PubMed](#)]
63. Bassett, J.J.; Monteith, G.R. Genetically Encoded Calcium Indicators as Probes to Assess the Role of Calcium Channels in Disease and for High-Throughput Drug Discovery. *Adv. Pharmacol.* **2017**, *79*, 141–171. [[PubMed](#)]
64. Minta, A.; Kao, J.P.; Tsien, R.Y. Fluorescent indicators for cytosolic calcium based on rhodamine and fluorescein chromophores. *J. Biol. Chem.* **1989**, *264*, 8171–8178.
65. Rudolf, R.; Mongillo, M.; Rizzuto, R.; Pozzan, T. Looking forward to seeing calcium. *Nat. Rev. Mol. Cell Biol.* **2003**, *4*, 579–586. [[CrossRef](#)]
66. Grynkiewicz, G.; Poenie, M.; Tsien, R.Y. A new generation of Ca²⁺ indicators with greatly improved fluorescence properties. *J. Biol. Chem.* **1985**, *260*, 3440–3450.
67. Collins, T.J.; Lipp, P.; Berridge, M.J.; Bootman, M.D. Mitochondrial Ca²⁺ uptake depends on the spatial and temporal profile of cytosolic Ca²⁺ signals. *J. Biol. Chem.* **2001**, *276*, 26411–26420. [[CrossRef](#)]
68. Pitter, J.G.; Maechler, P.; Wollheim, C.B.; Spät, A. Mitochondria respond to Ca²⁺ already in the submicromolar range: Correlation with redox state. *Cell Calcium* **2002**, *31*, 97–104. [[CrossRef](#)]
69. Andrienko, T.N.; Picht, E.; Bers, D.M. Mitochondrial free calcium regulation during sarcoplasmic reticulum calcium release in rat cardiac myocytes. *J. Mol. Cell. Cardiol.* **2009**, *46*, 1027–1036. [[CrossRef](#)]
70. Pozzan, T.; Rudolf, R. Measurements of mitochondrial calcium in vivo. *Biochim. Biophys. Acta* **2009**, *1787*, 1317–1323. [[CrossRef](#)]

71. Thomas, D.; Tovey, S.C.; Collins, T.J.; Bootman, M.D.; Berridge, M.J.; Lipp, P. A comparison of fluorescent Ca^{2+} indicator properties and their use in measuring elementary and global Ca^{2+} signals. *Cell Calcium* **2000**, *28*, 213–223. [[CrossRef](#)] [[PubMed](#)]
72. De Giorgi, F.; Ahmed, Z.; Bastianutto, C.; Brini, M.; Jouaville, L.S.; Marsault, R.; Murgia, M.; Pinton, P.; Pozzan, T.; Rizzuto, R. Targeting GFP to organelles. *Methods Cell Biol.* **1999**, *58*, 75–85. [[PubMed](#)]
73. Rizzuto, R.; Brini, M.; Pozzan, T. Intracellular targeting of the photoprotein aequorin: A new approach for measuring, in living cells, Ca^{2+} concentrations in defined cellular compartments. *Cytotechnology* **1993**, *11* (Suppl. 1), S44–S46. [[CrossRef](#)]
74. Rizzuto, R.; Brini, M.; Pozzan, T. Targeting recombinant aequorin to specific intracellular organelles. *Methods Cell Biol.* **1994**, *40*, 339–358. [[PubMed](#)]
75. Filippin, L.; Abad, M.C.; Gastaldello, S.; Magalhães, P.J.; Sandonà, D.; Pozzan, T. Improved strategies for the delivery of GFP-based Ca^{2+} sensors into the mitochondrial matrix. *Cell Calcium* **2005**, *37*, 129–136. [[CrossRef](#)] [[PubMed](#)]
76. Palmer, A.E.; Tsien, R.Y. Measuring calcium signaling using genetically targetable fluorescent indicators. *Nat. Protoc.* **2006**, *1*, 1057. [[CrossRef](#)] [[PubMed](#)]
77. De Michele, R.; Carimi, F.; Frommer, W.B. Mitochondrial biosensors. *Int. J. Biochem. Cell Biol.* **2014**, *48*, 39–44. [[CrossRef](#)]
78. Arnaudeau, S.; Kelley, W.L.; Walsh, J.V.; Demaurex, N. Mitochondria recycle Ca^{2+} to the endoplasmic reticulum and prevent the depletion of neighboring endoplasmic reticulum regions. *J. Biol. Chem.* **2001**, *276*, 29430–29439. [[CrossRef](#)]
79. Lu, X.; Ginsburg, K.S.; Kettlewell, S.; Bossuyt, J.; Smith, G.L.; Bers, D.M. Measuring local gradients of intramitochondrial $[\text{Ca}^{2+}]$ in cardiac myocytes during sarcoplasmic reticulum Ca^{2+} release. *Circ. Res.* **2013**, *112*, 424–431. [[CrossRef](#)]
80. Wüst, R.C.I.; Helmes, M.; Martin, J.L.; van der Wardt, T.J.T.; Musters, R.J.P.; van der Velden, J.; Stienen, G.J.M. Rapid frequency-dependent changes in free mitochondrial calcium concentration in rat cardiac myocytes. *J. Physiol. (Lond.)* **2017**, *595*, 2001–2019. [[CrossRef](#)]
81. Shimomura, O.; Johnson, F.H.; Saiga, Y. Extraction, purification and properties of aequorin, a bioluminescent protein from the luminous hydromedusa, *Aequorea*. *J. Cell Comp. Physiol.* **1962**, *59*, 223–239. [[CrossRef](#)] [[PubMed](#)]
82. Brini, M.; Pinton, P.; Pozzan, T.; Rizzuto, R. Targeted recombinant aequorins: Tools for monitoring $[\text{Ca}^{2+}]$ in the various compartments of a living cell. *Microsc. Res. Tech.* **1999**, *46*, 380–389. [[CrossRef](#)]
83. Brini, M.; Marsault, R.; Bastianutto, C.; Alvarez, J.; Pozzan, T.; Rizzuto, R. Transfected aequorin in the measurement of cytosolic Ca^{2+} concentration ($[\text{Ca}^{2+}]_c$). A critical evaluation. *J. Biol. Chem.* **1995**, *270*, 9896–9903. [[CrossRef](#)] [[PubMed](#)]
84. Rizzuto, R.; Simpson, A.W.; Brini, M.; Pozzan, T. Rapid changes of mitochondrial Ca^{2+} revealed by specifically targeted recombinant aequorin. *Nature* **1992**, *358*, 325–327. [[CrossRef](#)] [[PubMed](#)]
85. Ottolini, D.; Cali, T.; Brini, M. Methods to measure intracellular Ca^{2+} fluxes with organelle-targeted aequorin-based probes. *Methods Enzymol.* **2014**, *543*, 21–45. [[PubMed](#)]
86. Bonora, M.; Giorgi, C.; Bononi, A.; Marchi, S.; Patergnani, S.; Rimessi, A.; Rizzuto, R.; Pinton, P. Subcellular calcium measurements in mammalian cells using jellyfish photoprotein aequorin-based probes. *Nat. Protoc.* **2013**, *8*, 2105–2118. [[CrossRef](#)]
87. Baird, G.S.; Zacharias, D.A.; Tsien, R.Y. Circular permutation and receptor insertion within green fluorescent proteins. *Proc. Natl. Acad. Sci. USA* **1999**, *96*, 11241–11246. [[CrossRef](#)]
88. Nakai, J.; Ohkura, M.; Imoto, K. A high signal-to-noise Ca^{2+} probe composed of a single green fluorescent protein. *Nat. Biotechnol.* **2001**, *19*, 137–141. [[CrossRef](#)]
89. Chen, T.-W.; Wardill, T.J.; Sun, Y.; Pulver, S.R.; Renninger, S.L.; Baohan, A.; Schreiter, E.R.; Kerr, R.A.; Orger, M.B.; Jayaraman, V.; et al. Ultrasensitive fluorescent proteins for imaging neuronal activity. *Nature* **2013**, *499*, 295–300. [[CrossRef](#)]
90. Miyawaki, A.; Llopis, J.; Heim, R.; McCaffery, J.M.; Adams, J.A.; Ikura, M.; Tsien, R.Y. Fluorescent indicators for Ca^{2+} based on green fluorescent proteins and calmodulin. *Nature* **1997**, *388*, 882–887. [[CrossRef](#)]
91. Selvin, P.R. The renaissance of fluorescence resonance energy transfer. *Nat. Struct. Biol.* **2000**, *7*, 730–734. [[CrossRef](#)] [[PubMed](#)]

92. Padilla-Parra, S.; Tramier, M. FRET microscopy in the living cell: Different approaches, strengths and weaknesses. *Bioessays* **2012**, *34*, 369–376. [[CrossRef](#)] [[PubMed](#)]
93. Romoser, V.A.; Hinkle, P.M.; Persechini, A. Detection in living cells of Ca²⁺-dependent changes in the fluorescence emission of an indicator composed of two green fluorescent protein variants linked by a calmodulin-binding sequence. A new class of fluorescent indicators. *J. Biol. Chem.* **1997**, *272*, 13270–13274. [[CrossRef](#)] [[PubMed](#)]
94. Palmer, A.E.; Qin, Y.; Park, J.G.; McCombs, J.E. Design and application of genetically encoded biosensors. *Trends Biotechnol.* **2011**, *29*, 144–152. [[CrossRef](#)] [[PubMed](#)]
95. Zhao, Y.; Araki, S.; Wu, J.; Teramoto, T.; Chang, Y.-F.; Nakano, M.; Abdelfattah, A.S.; Fujiwara, M.; Ishihara, T.; Nagai, T.; et al. An expanded palette of genetically encoded Ca²⁺ indicators. *Science* **2011**, *333*, 1888–1891. [[CrossRef](#)] [[PubMed](#)]
96. Deng, H.; Yan, S.; Huang, Y.; Lei, C.; Nie, Z. Design strategies for fluorescent proteins/mimics and their applications in biosensing and bioimaging. *TrAC Trends in Anal. Chem.* **2020**, *122*, 115757. [[CrossRef](#)]
97. Lewis, M.R.; Lewis, W.H. Mitochondria in Tissue Culture. *Science* **1914**, *39*, 330–333. [[CrossRef](#)]
98. Bereiter-Hahn, J.; Vöth, M. Dynamics of mitochondria in living cells: Shape changes, dislocations, fusion, and fission of mitochondria. *Microsc. Res. Tech.* **1994**, *27*, 198–219. [[CrossRef](#)]
99. Cortese, J.D. Stimulation of rat liver mitochondrial fusion by an outer membrane-derived aluminum fluoride-sensitive protein fraction. *Exp. Cell Res.* **1998**, *240*, 122–133. [[CrossRef](#)]
100. Cortese, J.D.; Voglino, L.A.; Hackenbrock, C.R. Novel fluorescence membrane fusion assays reveal GTP-dependent fusogenic properties of outer mitochondrial membrane-derived proteins. *Biochimica et Biophysica Acta (BBA) Biomembranes* **1998**, *1371*, 185–198. [[CrossRef](#)]
101. Nunnari, J.; Marshall, W.F.; Straight, A.; Murray, A.; Sedat, J.W.; Walter, P. Mitochondrial transmission during mating in *Saccharomyces cerevisiae* is determined by mitochondrial fusion and fission and the intramitochondrial segregation of mitochondrial DNA. *Mol. Biol. Cell* **1997**, *8*, 1233–1242. [[CrossRef](#)] [[PubMed](#)]
102. Rizzuto, R.; Pinton, P.; Carrington, W.; Fay, F.S.; Fogarty, K.E.; Lifshitz, L.M.; Tuft, R.A.; Pozzan, T. Close Contacts with the Endoplasmic Reticulum as Determinants of Mitochondrial Ca²⁺ Responses. *Science* **1998**, *280*, 1763–1766. [[CrossRef](#)] [[PubMed](#)]
103. Westermann, B. Mitochondrial fusion and fission in cell life and death. *Nat. Rev. Mol. Cell Biol.* **2010**, *11*, 872–884. [[CrossRef](#)] [[PubMed](#)]
104. Chan, D.C. Mitochondrial fusion and fission in mammals. *Annu. Rev. Cell Dev. Biol.* **2006**, *22*, 79–99. [[CrossRef](#)] [[PubMed](#)]
105. Wai, T.; Langer, T. Mitochondrial Dynamics and Metabolic Regulation. *Trends Endocrinol. Metab.* **2016**, *27*, 105–117. [[CrossRef](#)] [[PubMed](#)]
106. Tilokani, L.; Nagashima, S.; Paupe, V.; Prudent, J. Mitochondrial dynamics: Overview of molecular mechanisms. *Essays Biochem.* **2018**, *62*, 341–360.
107. Liesa, M.; Palacín, M.; Zorzano, A. Mitochondrial dynamics in mammalian health and disease. *Physiol. Rev.* **2009**, *89*, 799–845. [[CrossRef](#)]
108. Burté, F.; Carelli, V.; Chinnery, P.F.; Yu-Wai-Man, P. Disturbed mitochondrial dynamics and neurodegenerative disorders. *Nat. Rev. Neurol.* **2015**, *11*, 11–24. [[CrossRef](#)]
109. Detmer, S.A.; Chan, D.C. Functions and dysfunctions of mitochondrial dynamics. *Nat. Rev. Mol. Cell Biol.* **2007**, *8*, 870–879. [[CrossRef](#)]
110. Chen, H.; Chomyn, A.; Chan, D.C. Disruption of fusion results in mitochondrial heterogeneity and dysfunction. *J. Biol. Chem.* **2005**, *280*, 26185–26192. [[CrossRef](#)]
111. Chen, H.; Vermulst, M.; Wang, Y.E.; Chomyn, A.; Prolla, T.A.; McCaffery, J.M.; Chan, D.C. Mitochondrial fusion is required for mtDNA stability in skeletal muscle and tolerance of mtDNA mutations. *Cell* **2010**, *141*, 280–289. [[CrossRef](#)] [[PubMed](#)]
112. Rambold, A.S.; Kostelecky, B.; Elia, N.; Lippincott-Schwartz, J. Tubular network formation protects mitochondria from autophagosomal degradation during nutrient starvation. *Proc. Natl. Acad. Sci. USA* **2011**, *108*, 10190–10195. [[CrossRef](#)] [[PubMed](#)]
113. Otera, H.; Ishihara, N.; Mihara, K. New insights into the function and regulation of mitochondrial fission. *Biochim. Biophys. Acta* **2013**, *1833*, 1256–1268. [[CrossRef](#)] [[PubMed](#)]

114. Pickles, S.; Vigié, P.; Youle, R.J. Mitophagy and Quality Control Mechanisms in Mitochondrial Maintenance. *Curr. Biol.* **2018**, *28*, R170–R185. [[CrossRef](#)] [[PubMed](#)]
115. Youle, R.J.; van der Bliek, A.M. Mitochondrial fission, fusion, and stress. *Science* **2012**, *337*, 1062–1065. [[CrossRef](#)] [[PubMed](#)]
116. Ferguson, S.M.; De Camilli, P. Dynamin, a membrane-remodelling GTPase. *Nat. Rev. Mol. Cell Biol.* **2012**, *13*, 75–88. [[CrossRef](#)]
117. Koshiba, T.; Detmer, S.A.; Kaiser, J.T.; Chen, H.; McCaffery, J.M.; Chan, D.C. Structural basis of mitochondrial tethering by mitofusin complexes. *Science* **2004**, *305*, 858–862. [[CrossRef](#)]
118. Brandt, T.; Cavellini, L.; Kühlbrandt, W.; Cohen, M.M. A mitofusin-dependent docking ring complex triggers mitochondrial fusion in vitro. *Elife* **2016**, *5*, e14618. [[CrossRef](#)]
119. Ishihara, N.; Eura, Y.; Mihara, K. Mitofusin 1 and 2 play distinct roles in mitochondrial fusion reactions via GTPase activity. *J. Cell. Sci.* **2004**, *117*, 6535–6546. [[CrossRef](#)]
120. Legros, F.; Lombès, A.; Frachon, P.; Rojo, M. Mitochondrial fusion in human cells is efficient, requires the inner membrane potential, and is mediated by mitofusins. *Mol. Biol. Cell* **2002**, *13*, 4343–4354. [[CrossRef](#)]
121. Ban, T.; Ishihara, T.; Kohno, H.; Saita, S.; Ichimura, A.; Maenaka, K.; Oka, T.; Mihara, K.; Ishihara, N. Molecular basis of selective mitochondrial fusion by heterotypic action between OPA1 and cardiolipin. *Nat. Cell Biol.* **2017**, *19*, 856–863. [[CrossRef](#)] [[PubMed](#)]
122. Head, B.; Griparic, L.; Amiri, M.; Gandre-Babbe, S.; van der Bliek, A.M. Inducible proteolytic inactivation of OPA1 mediated by the OMA1 protease in mammalian cells. *J. Cell Biol.* **2009**, *187*, 959–966. [[CrossRef](#)] [[PubMed](#)]
123. Ehses, S.; Raschke, I.; Mancuso, G.; Bernacchia, A.; Geimer, S.; Tondera, D.; Martinou, J.-C.; Westermann, B.; Rugarli, E.I.; Langer, T. Regulation of OPA1 processing and mitochondrial fusion by m-AAA protease isoenzymes and OMA1 Control of OPA1 by m-AAA protease and OMA1. *J. Cell Biol.* **2009**, *187*, 1023–1036. [[CrossRef](#)] [[PubMed](#)]
124. Griparic, L.; Kanazawa, T.; van der Bliek, A.M. Regulation of the mitochondrial dynamin-like protein Opa1 by proteolytic cleavage. *J. Cell Biol.* **2007**, *178*, 757–764. [[CrossRef](#)] [[PubMed](#)]
125. Song, Z.; Chen, H.; Fiket, M.; Alexander, C.; Chan, D.C. OPA1 processing controls mitochondrial fusion and is regulated by mRNA splicing, membrane potential, and Yme1L. *J. Cell Biol.* **2007**, *178*, 749–755. [[CrossRef](#)] [[PubMed](#)]
126. MacVicar, T.; Langer, T. OPA1 processing in cell death and disease—the long and short of it. *J. Cell. Sci.* **2016**, *129*, 2297–2306. [[CrossRef](#)]
127. Mishra, P.; Carelli, V.; Manfredi, G.; Chan, D.C. Proteolytic Cleavage of Opa1 Stimulates Mitochondrial Inner Membrane Fusion and Couples Fusion to Oxidative Phosphorylation. *Cell Metab.* **2014**, *19*, 630–641. [[CrossRef](#)]
128. Smirnova, E.; Griparic, L.; Shurland, D.L.; van der Bliek, A.M. Dynamin-related protein Drp1 is required for mitochondrial division in mammalian cells. *Mol. Biol. Cell* **2001**, *12*, 2245–2256. [[CrossRef](#)]
129. Friedman, J.R.; Lackner, L.L.; West, M.; DiBenedetto, J.R.; Nunnari, J.; Voeltz, G.K. ER Tubules Mark Sites of Mitochondrial Division. *Science* **2011**, *334*, 358–362. [[CrossRef](#)]
130. Lewis, S.C.; Uchiyama, L.F.; Nunnari, J. ER-mitochondria contacts couple mtDNA synthesis with mitochondrial division in human cells. *Science* **2016**, *353*, aaf5549. [[CrossRef](#)]
131. Fröhlich, C.; Grabiger, S.; Schwefel, D.; Faelber, K.; Rosenbaum, E.; Mears, J.; Rocks, O.; Daumke, O. Structural insights into oligomerization and mitochondrial remodelling of dynamin 1-like protein. *EMBO J.* **2013**, *32*, 1280–1292. [[CrossRef](#)] [[PubMed](#)]
132. Mears, J.A.; Lackner, L.L.; Fang, S.; Ingerman, E.; Nunnari, J.; Hinshaw, J.E. Conformational changes in Dnm1 support a contractile mechanism for mitochondrial fission. *Nat. Struct. Mol. Biol.* **2011**, *18*, 20–26. [[CrossRef](#)] [[PubMed](#)]
133. Hatch, A.L.; Ji, W.-K.; Merrill, R.A.; Strack, S.; Higgs, H.N. Actin filaments as dynamic reservoirs for Drp1 recruitment. *Mol. Biol. Cell* **2016**, *27*, 3109–3121. [[CrossRef](#)] [[PubMed](#)]
134. Palmer, C.S.; Osellame, L.D.; Laine, D.; Koutsopoulos, O.S.; Frazier, A.E.; Ryan, M.T. MiD49 and MiD51, new components of the mitochondrial fission machinery. *EMBO Rep.* **2011**, *12*, 565–573. [[CrossRef](#)] [[PubMed](#)]
135. Losón, O.C.; Song, Z.; Chen, H.; Chan, D.C. Fis1, Mff, MiD49, and MiD51 mediate Drp1 recruitment in mitochondrial fission. *Mol. Biol. Cell* **2013**, *24*, 659–667. [[CrossRef](#)]

136. Gandre-Babbe, S.; van der Blik, A.M. The novel tail-anchored membrane protein Mff controls mitochondrial and peroxisomal fission in mammalian cells. *Mol. Biol. Cell* **2008**, *19*, 2402–2412. [[CrossRef](#)]
137. Lee, J.E.; Westrate, L.M.; Wu, H.; Page, C.; Voeltz, G.K. Multiple dynamin family members collaborate to drive mitochondrial division. *Nature* **2016**, *540*, 139–143. [[CrossRef](#)]
138. Chakrabarti, R.; Ji, W.-K.; Stan, R.V.; de Juan Sanz, J.; Ryan, T.A.; Higgs, H.N. INF2-mediated actin polymerization at the ER stimulates mitochondrial calcium uptake, inner membrane constriction, and division. *J. Cell Biol.* **2018**, *217*, 251–268. [[CrossRef](#)]
139. Cho, B.; Cho, H.M.; Jo, Y.; Kim, H.D.; Song, M.; Moon, C.; Kim, H.; Kim, K.; Sesaki, H.; Rhyu, I.J.; et al. Constriction of the mitochondrial inner compartment is a priming event for mitochondrial division. *Nat. Commun.* **2017**, *8*, 15754. [[CrossRef](#)]
140. Hom, J.R.; Gewandter, J.S.; Michael, L.; Sheu, S.-S.; Yoon, Y. Thapsigargin induces biphasic fragmentation of mitochondria through calcium-mediated mitochondrial fission and apoptosis. *J. Cell. Physiol.* **2007**, *212*, 498–508. [[CrossRef](#)]
141. Tondera, D.; Czauderna, F.; Paulick, K.; Schwarzer, R.; Kaufmann, J.; Santel, A. The mitochondrial protein MTP18 contributes to mitochondrial fission in mammalian cells. *J. Cell. Sci.* **2005**, *118*, 3049–3059. [[CrossRef](#)] [[PubMed](#)]
142. Palade, G.E. The fine structure of mitochondria. *Anat. Rec.* **1952**, *114*, 427–451. [[CrossRef](#)] [[PubMed](#)]
143. Joshi, D.C.; Bakowska, J.C. Determination of Mitochondrial Membrane Potential and Reactive Oxygen Species in Live Rat Cortical Neurons. *J. Vis. Exp.* **2011**, *51*, e2704. [[CrossRef](#)] [[PubMed](#)]
144. Chazotte, B. Labeling Mitochondria with Fluorescent Dyes for Imaging. *Cold Spring Harb. Protoc.* **2009**, *2009*, pdb-prot4948. [[CrossRef](#)] [[PubMed](#)]
145. Buckman, J.F.; Hernández, H.; Kress, G.J.; Votyakova, T.V.; Pal, S.; Reynolds, I.J. MitoTracker labeling in primary neuronal and astrocytic cultures: Influence of mitochondrial membrane potential and oxidants. *J. Neurosci. Methods* **2001**, *104*, 165–176. [[CrossRef](#)]
146. Chazotte, B. Labeling Mitochondria with MitoTracker Dyes. *Cold Spring Harb. Protoc.* **2011**, *2011*, pdb-prot5648. [[CrossRef](#)]
147. Poot, M.; Gibson, L.L.; Singer, V.L. Detection of apoptosis in live cells by MitoTracker red CMXRos and SYTO dye flow cytometry. *Cytometry* **1997**, *27*, 358–364. [[CrossRef](#)]
148. Hallap, T.; Nagy, S.; Jaakma, U.; Johannisson, A.; Rodriguez-Martinez, H. Mitochondrial activity of frozen-thawed spermatozoa assessed by MitoTracker Deep Red 633. *Theriogenology* **2005**, *63*, 2311–2322. [[CrossRef](#)]
149. Cottet-Rousselle, C.; Ronot, X.; Leverve, X.; Mayol, J.-F. Cytometric assessment of mitochondria using fluorescent probes. *Cytom. Part A* **2011**, *79A*, 405–425. [[CrossRef](#)]
150. Huang, S.; Han, R.; Zhuang, Q.; Du, L.; Jia, H.; Liu, Y.; Liu, Y. New photostable naphthalimide-based fluorescent probe for mitochondrial imaging and tracking. *Biosens. Bioelectron.* **2015**, *71*, 313–321. [[CrossRef](#)]
151. Gao, T.; He, H.; Huang, R.; Zheng, M.; Wang, F.-F.; Hu, Y.-J.; Jiang, F.-L.; Liu, Y. BODIPY-based fluorescent probes for mitochondria-targeted cell imaging with superior brightness, low cytotoxicity and high photostability. *Dyes Pigment.* **2017**, *141*, 530–535. [[CrossRef](#)]
152. Galanis, M.; Devenish, R.J.; Nagley, P. Duplication of leader sequence for protein targeting to mitochondria leads to increased import efficiency. *FEBS Lett.* **1991**, *282*, 425–430. [[CrossRef](#)]
153. Molina, A.J.A.; Shirihai, O.S. Monitoring mitochondrial dynamics with photoactivatable [corrected] green fluorescent protein. *Methods Enzymol.* **2009**, *457*, 289–304. [[PubMed](#)]
154. Patterson, G.H.; Lippincott-Schwartz, J. A Photoactivatable GFP for Selective Photolabeling of Proteins and Cells. *Science* **2002**, *297*, 1873–1877. [[CrossRef](#)]
155. Jakobs, S.; Schauss, A.C.; Hell, S.W. Photoconversion of matrix targeted GFP enables analysis of continuity and intermixing of the mitochondrial lumen. *FEBS Lett.* **2003**, *554*, 194–200. [[CrossRef](#)]
156. Mellott, A.J.; Shinogle, H.E.; Moore, D.S.; Detamore, M.S. Fluorescent Photo-conversion: A second chance to label unique cells. *Cell. Mol. Bioeng.* **2015**, *8*, 187–196. [[CrossRef](#)]
157. Chudakov, D.M.; Lukyanov, S.; Lukyanov, K.A. Using photoactivatable fluorescent protein Dendra2 to track protein movement. *BioTechniques* **2007**, *42*, 553–556. [[CrossRef](#)]
158. Pham, A.H.; McCaffery, J.M.; Chan, D.C. Mouse lines with photo-activatable mitochondria to study mitochondrial dynamics. *Genesis* **2012**, *50*, 833–843. [[CrossRef](#)]

159. Han, S.M.; Baig, H.S.; Hammarlund, M. Mitochondria Localize to Injured Axons to Support Regeneration. *Neuron* **2016**, *92*, 1308–1323. [[CrossRef](#)]
160. Bertolin, G.; Bulteau, A.-L.; Alves-Guerra, M.-C.; Burel, A.; Lavault, M.-T.; Gavard, O.; Le Bras, S.; Gagné, J.-P.; Poirier, G.G.; Le Borgne, R.; et al. Aurora kinase A localises to mitochondria to control organelle dynamics and energy production. *Elife* **2018**, *7*, e38111. [[CrossRef](#)]
161. Fissi, N.E.; Rojo, M.; Aouane, A.; Karatas, E.; Poliacikova, G.; David, C.; Royet, J.; Rival, T. Mitofusin gain and loss of function drive pathogenesis in Drosophila models of CMT2A neuropathy. *EMBO Rep.* **2018**, *19*, e45241. [[CrossRef](#)]
162. Jakobs, S. High resolution imaging of live mitochondria. *Biochim. Biophys. Acta* **2006**, *1763*, 561–575. [[CrossRef](#)]
163. Simula, L.; Campello, S. Monitoring the Mitochondrial Dynamics in Mammalian Cells. *Methods Mol. Biol.* **2018**, *1782*, 267–285. [[PubMed](#)]
164. Gustafsson, M.G.L. Nonlinear structured-illumination microscopy: Wide-field fluorescence imaging with theoretically unlimited resolution. *Proc. Natl. Acad. Sci. USA* **2005**, *102*, 13081–13086. [[CrossRef](#)] [[PubMed](#)]
165. Hell, S.W.; Wichmann, J. Breaking the diffraction resolution limit by stimulated emission: Stimulated-emission-depletion fluorescence microscopy. *Opt. Lett.* **1994**, *19*, 780–782. [[CrossRef](#)] [[PubMed](#)]
166. Betzig, E.; Patterson, G.H.; Sougrat, R.; Lindwasser, O.W.; Olenych, S.; Bonifacino, J.S.; Davidson, M.W.; Lippincott-Schwartz, J.; Hess, H.F. Imaging intracellular fluorescent proteins at nanometer resolution. *Science* **2006**, *313*, 1642–1645. [[CrossRef](#)]
167. Rust, M.J.; Bates, M.; Zhuang, X. Stochastic optical reconstruction microscopy (STORM) provides sub-diffraction-limit image resolution. *Nat. Methods* **2006**, *3*, 793–795. [[CrossRef](#)]
168. Fiolka, R.; Shao, L.; Rego, E.H.; Davidson, M.W.; Gustafsson, M.G.L. Time-lapse two-color 3D imaging of live cells with doubled resolution using structured illumination. *Proc. Natl. Acad. Sci. USA* **2012**, *109*, 5311–5315. [[CrossRef](#)]
169. Shim, S.-H.; Xia, C.; Zhong, G.; Babcock, H.P.; Vaughan, J.C.; Huang, B.; Wang, X.; Xu, C.; Bi, G.-Q.; Zhuang, X. Super-resolution fluorescence imaging of organelles in live cells with photoswitchable membrane probes. *Proc. Natl. Acad. Sci. USA* **2012**, *109*, 13978–13983. [[CrossRef](#)]
170. Jans, D.C.; Wurm, C.A.; Riedel, D.; Wenzel, D.; Stage, F.; Deckers, M.; Rehling, P.; Jakobs, S. STED super-resolution microscopy reveals an array of MINOS clusters along human mitochondria. *Proc. Natl. Acad. Sci. USA* **2013**, *110*, 8936–8941. [[CrossRef](#)]
171. Kehrein, K.; Schilling, R.; Möller-Hergt, B.V.; Wurm, C.A.; Jakobs, S.; Lamkemeyer, T.; Langer, T.; Ott, M. Organization of Mitochondrial Gene Expression in Two Distinct Ribosome-Containing Assemblies. *Cell Rep.* **2015**, *10*, 843–853. [[CrossRef](#)] [[PubMed](#)]
172. Brown, T.A.; Tkachuk, A.N.; Shtengel, G.; Kopek, B.G.; Bogenhagen, D.F.; Hess, H.F.; Clayton, D.A. Superresolution Fluorescence Imaging of Mitochondrial Nucleoids Reveals Their Spatial Range, Limits, and Membrane Interaction. *Mol. Cell. Biol.* **2011**, *31*, 4994–5010. [[CrossRef](#)] [[PubMed](#)]
173. Balzarotti, F.; Eilers, Y.; Gwosch, K.C.; Gynnå, A.H.; Westphal, V.; Stefani, F.D.; Elf, J.; Hell, S.W. Nanometer resolution imaging and tracking of fluorescent molecules with minimal photon fluxes. *Science* **2017**, *355*, 606–612. [[CrossRef](#)] [[PubMed](#)]
174. Chen, B.-C.; Legant, W.R.; Wang, K.; Shao, L.; Milkie, D.E.; Davidson, M.W.; Janetopoulos, C.; Wu, X.S.; Hammer, J.A.; Liu, Z.; et al. Lattice light-sheet microscopy: Imaging molecules to embryos at high spatiotemporal resolution. *Science* **2014**, *346*, 1257998. [[CrossRef](#)]
175. Schuler, M.-H.; Lewandowska, A.; Caprio, G.D.; Skillern, W.; Upadhyayula, S.; Kirchhausen, T.; Shaw, J.M.; Cunniff, B. Miro1-mediated mitochondrial positioning shapes intracellular energy gradients required for cell migration. *Mol. Biol. Cell* **2017**, *28*, 2159–2169. [[CrossRef](#)]
176. Sinha, K.; Das, J.; Pal, P.B.; Sil, P.C. Oxidative stress: The mitochondria-dependent and mitochondria-independent pathways of apoptosis. *Arch. Toxicol.* **2013**, *87*, 1157–1180. [[CrossRef](#)]
177. Guo, C.; Sun, L.; Chen, X.; Zhang, D. Oxidative stress, mitochondrial damage and neurodegenerative diseases. *Neural Regen. Res.* **2013**, *8*, 2003–2014.
178. Ross, W.N. Understanding calcium waves and sparks in central neurons. *Nat. Rev. Neurosci.* **2012**, *13*, 157–168. [[CrossRef](#)]
179. James, A.M.; Murphy, M.P. How mitochondrial damage affects cell function. *J. Biomed. Sci.* **2002**, *9*, 475–487. [[CrossRef](#)]

180. Martin, S.J.; Henry, C.M.; Cullen, S.P. A Perspective on Mammalian Caspases as Positive and Negative Regulators of Inflammation. *Mol. Cell* **2012**, *46*, 387–397. [[CrossRef](#)]
181. Hu, L.; Wang, H.; Huang, L.; Zhao, Y.; Wang, J. The Protective Roles of ROS-Mediated Mitophagy on 125I Seeds Radiation Induced Cell Death in HCT116 Cells. *Oxidative Med. Cell. Longev.* **2016**, *2016*, 18. [[CrossRef](#)] [[PubMed](#)]
182. Lemasters, J.J. Selective Mitochondrial Autophagy, or Mitophagy, as a Targeted Defense against Oxidative Stress, Mitochondrial Dysfunction, and Aging. *Rejuvenation Res.* **2005**, *8*, 3–5. [[CrossRef](#)] [[PubMed](#)]
183. Narendra, D.; Tanaka, A.; Suen, D.-F.; Youle, R.J. Parkin is recruited selectively to impaired mitochondria and promotes their autophagy. *J. Cell Biol.* **2008**, *183*, 795–803. [[CrossRef](#)] [[PubMed](#)]
184. Clark, S.L. Cellular differentiation in the kidneys of newborn mice studied with the electron microscope. *J. Biophys. Biochem. Cytol.* **1957**, *3*, 349–362. [[CrossRef](#)] [[PubMed](#)]
185. Pickrell, A.M.; Youle, R.J. The Roles of PINK1, Parkin, and Mitochondrial Fidelity in Parkinson's disease. *Neuron* **2015**, *85*, 257–273. [[CrossRef](#)] [[PubMed](#)]
186. Jin, S.M.; Lazarou, M.; Wang, C.; Kane, L.A.; Narendra, D.P.; Youle, R.J. Mitochondrial membrane potential regulates PINK1 import and proteolytic destabilization by PARL. *J. Cell Biol.* **2010**, *191*, 933–942. [[CrossRef](#)]
187. Deas, E.; Plun-Favreau, H.; Gandhi, S.; Desmond, H.; Kjaer, S.; Loh, S.H.Y.; Renton, A.E.M.; Harvey, R.J.; Whitworth, A.J.; Martins, L.M.; et al. PINK1 cleavage at position A103 by the mitochondrial protease PARL. *Hum. Mol. Genet.* **2011**, *20*, 867–879. [[CrossRef](#)]
188. Meissner, C.; Lorenz, H.; Weihofen, A.; Selkoe, D.J.; Lemberg, M.K. The mitochondrial intramembrane protease PARL cleaves human Pink1 to regulate Pink1 trafficking. *J. Neurochem.* **2011**, *117*, 856–867. [[CrossRef](#)]
189. Greene, A.W.; Grenier, K.; Aguilera, M.A.; Muise, S.; Farazifard, R.; Haque, M.E.; McBride, H.M.; Park, D.S.; Fon, E.A. Mitochondrial processing peptidase regulates PINK1 processing, import and Parkin recruitment. *EMBO Rep.* **2012**, *13*, 378–385. [[CrossRef](#)]
190. Harper, J.W.; Ordureau, A.; Heo, J.-M. Building and decoding ubiquitin chains for mitophagy. *Nat. Rev. Mol. Cell Biol.* **2018**, *19*, 93–108. [[CrossRef](#)]
191. Sekine, S.; Youle, R.J. PINK1 import regulation; a fine system to convey mitochondrial stress to the cytosol. *BMC Biol.* **2018**, *16*, 2. [[CrossRef](#)]
192. Lazarou, M.; Jin, S.M.; Kane, L.A.; Youle, R.J. Role of PINK1 binding to the TOM complex and alternate intracellular membranes in recruitment and activation of the E3 ligase Parkin. *Dev. Cell* **2012**, *22*, 320–333. [[CrossRef](#)]
193. Okatsu, K.; Uno, M.; Koyano, F.; Go, E.; Kimura, M.; Oka, T.; Tanaka, K.; Matsuda, N. A dimeric PINK1-containing complex on depolarized mitochondria stimulates Parkin recruitment. *J. Biol. Chem.* **2013**, *288*, 36372–36384. [[CrossRef](#)]
194. Hasson, S.A.; Kane, L.A.; Yamano, K.; Huang, C.-H.; Sliter, D.A.; Buehler, E.; Wang, C.; Heman-Ackah, S.M.; Hessa, T.; Guha, R.; et al. High-content genome-wide RNAi screens identify regulators of parkin upstream of mitophagy. *Nature* **2013**, *504*, 291–295. [[CrossRef](#)]
195. Koyano, F.; Okatsu, K.; Kosako, H.; Tamura, Y.; Go, E.; Kimura, M.; Kimura, Y.; Tsuchiya, H.; Yoshihara, H.; Hirokawa, T.; et al. Ubiquitin is phosphorylated by PINK1 to activate parkin. *Nature* **2014**, *510*, 162–166. [[CrossRef](#)]
196. Chan, N.C.; Salazar, A.M.; Pham, A.H.; Sweredoski, M.J.; Kolawa, N.J.; Graham, R.L.J.; Hess, S.; Chan, D.C. Broad activation of the ubiquitin-proteasome system by Parkin is critical for mitophagy. *Hum. Mol. Genet.* **2011**, *20*, 1726–1737. [[CrossRef](#)] [[PubMed](#)]
197. Yoshii, S.R.; Kishi, C.; Ishihara, N.; Mizushima, N. Parkin Mediates Proteasome-dependent Protein Degradation and Rupture of the Outer Mitochondrial Membrane. *J. Biol. Chem.* **2011**, *286*, 19630–19640. [[CrossRef](#)] [[PubMed](#)]
198. Gong, G.; Song, M.; Csordas, G.; Kelly, D.P.; Matkovich, S.J.; Dorn, G.W. Parkin-mediated mitophagy directs perinatal cardiac metabolic maturation in mice. *Science* **2015**, *350*, aad2459. [[CrossRef](#)] [[PubMed](#)]
199. Ordureau, A.; Paulo, J.A.; Zhang, W.; Ahfeldt, T.; Zhang, J.; Cohn, E.F.; Hou, Z.; Heo, J.-M.; Rubin, L.L.; Sidhu, S.S.; et al. Dynamics of PARKIN-Dependent Mitochondrial Ubiquitylation in Induced Neurons and Model Systems Revealed by Digital Snapshot Proteomics. *Mol. Cell* **2018**, *70*, 211–227. [[CrossRef](#)] [[PubMed](#)]
200. Rose, C.M.; Isasa, M.; Ordureau, A.; Prado, M.A.; Beausoleil, S.A.; Jedrychowski, M.P.; Finley, D.J.; Harper, J.W.; Gygi, S.P. Highly Multiplexed Quantitative Mass Spectrometry Analysis of Ubiquitylomes. *Cell Syst.* **2016**, *3*, 395–403. [[CrossRef](#)]

201. Sarraf, S.A.; Raman, M.; Guarani-Pereira, V.; Sowa, M.E.; Huttlin, E.L.; Gygi, S.P.; Harper, J.W. Landscape of the PARKIN-dependent ubiquitylome in response to mitochondrial depolarization. *Nature* **2013**, *496*, 372–376. [[CrossRef](#)] [[PubMed](#)]
202. Geisler, S.; Holmström, K.M.; Skujat, D.; Fiesel, F.C.; Rothfuss, O.C.; Kahle, P.J.; Springer, W. PINK1/Parkin-mediated mitophagy is dependent on VDAC1 and p62/SQSTM1. *Nat. Cell Biol.* **2010**, *12*, 119–131. [[CrossRef](#)] [[PubMed](#)]
203. Narendra, D.P.; Youle, R.J. Targeting Mitochondrial Dysfunction: Role for PINK1 and Parkin in Mitochondrial Quality Control. *Antioxid. Redox Signal.* **2011**, *14*, 1929–1938. [[CrossRef](#)] [[PubMed](#)]
204. Palikaras, K.; Lionaki, E.; Tavernarakis, N. Mechanisms of mitophagy in cellular homeostasis, physiology and pathology. *Nat. Cell Biol.* **2018**, *20*, 1013–1022. [[CrossRef](#)]
205. Khaminets, A.; Behl, C.; Dikic, I. Ubiquitin-Dependent and Independent Signals In Selective Autophagy. *Trends Cell Biol.* **2016**, *26*, 6–16. [[CrossRef](#)]
206. Wei, Y.; Chiang, W.-C.; Sumpter, R.; Mishra, P.; Levine, B. Prohibitin 2 Is an Inner Mitochondrial Membrane Mitophagy Receptor. *Cell* **2017**, *168*, 224–238. [[CrossRef](#)]
207. McWilliams, T.G.; Prescott, A.R.; Allen, G.F.G.; Tamjar, J.; Munson, M.J.; Thomson, C.; Muqit, M.M.K.; Ganley, I.G. mito-QC illuminates mitophagy and mitochondrial architecture in vivo. *J. Cell Biol.* **2016**, *214*, 333–345. [[CrossRef](#)]
208. Sun, N.; Yun, J.; Liu, J.; Malide, D.; Liu, C.; Rovira, I.I.; Holmström, K.M.; Fergusson, M.M.; Yoo, Y.H.; Combs, C.A.; et al. Measuring In Vivo Mitophagy. *Mol. Cell* **2015**, *60*, 685–696. [[CrossRef](#)]
209. Glick, D.; Zhang, W.; Beaton, M.; Marsboom, G.; Gruber, M.; Simon, M.C.; Hart, J.; Dorn, G.W.; Brady, M.J.; Macleod, K.F. BNIP3 Regulates Mitochondrial Function and Lipid Metabolism in the Liver. *Mol. Cell. Biol.* **2012**, *32*, 2570–2584. [[CrossRef](#)]
210. Yasuda, M.; Han, J.W.; Dionne, C.A.; Boyd, J.M.; Chinnadurai, G. BNIP3alpha: A human homolog of mitochondrial proapoptotic protein BNIP3. *Cancer Res.* **1999**, *59*, 533–537.
211. Liu, L.; Feng, D.; Chen, G.; Chen, M.; Zheng, Q.; Song, P.; Ma, Q.; Zhu, C.; Wang, R.; Qi, W.; et al. Mitochondrial outer-membrane protein FUNDC1 mediates hypoxia-induced mitophagy in mammalian cells. *Nat. Cell Biol.* **2012**, *14*, 177–185. [[CrossRef](#)] [[PubMed](#)]
212. Kanki, T.; Wang, K.; Cao, Y.; Baba, M.; Klionsky, D.J. Atg32 is a mitochondrial protein that confers selectivity during mitophagy. *Dev. Cell* **2009**, *17*, 98–109. [[CrossRef](#)] [[PubMed](#)]
213. Whitworth, A.J.; Pallanck, L.J. PINK1/Parkin mitophagy and neurodegeneration—what do we really know in vivo? *Curr. Opin. Genet. Dev.* **2017**, *44*, 47–53. [[CrossRef](#)] [[PubMed](#)]
214. Sandoval, H.; Thiagarajan, P.; Dasgupta, S.K.; Schumacher, A.; Prchal, J.T.; Chen, M.; Wang, J. Essential role for Nix in autophagic maturation of erythroid cells. *Nature* **2008**, *454*, 232–235. [[CrossRef](#)]
215. Schweers, R.L.; Zhang, J.; Randall, M.S.; Loyd, M.R.; Li, W.; Dorsey, F.C.; Kundu, M.; Opferman, J.T.; Cleveland, J.L.; Miller, J.L.; et al. NIX is required for programmed mitochondrial clearance during reticulocyte maturation. *Proc. Natl. Acad. Sci. USA* **2007**, *104*, 19500–19505. [[CrossRef](#)]
216. Al Rawi, S.; Louvet-Vallée, S.; Djeddi, A.; Sachse, M.; Culetto, E.; Hajjar, C.; Boyd, L.; Legouis, R.; Galy, V. Postfertilization autophagy of sperm organelles prevents paternal mitochondrial DNA transmission. *Science* **2011**, *334*, 1144–1147. [[CrossRef](#)]
217. Melser, S.; Chatelain, E.H.; Lavie, J.; Mahfouf, W.; Jose, C.; Obre, E.; Goorden, S.; Priault, M.; Elgersma, Y.; Rezvani, H.R.; et al. Rheb Regulates Mitophagy Induced by Mitochondrial Energetic Status. *Cell Metab.* **2013**, *17*, 719–730. [[CrossRef](#)]
218. Gottlieb, R.A.; Bernstein, D. Mitochondria shape cardiac metabolism. *Science* **2015**, *350*, 1162–1163. [[CrossRef](#)]
219. Pryde, K.R.; Smith, H.L.; Chau, K.-Y.; Schapira, A.H.V. PINK1 disables the anti-fission machinery to segregate damaged mitochondria for mitophagy. *J. Cell Biol.* **2016**, *213*, 163–171. [[CrossRef](#)]
220. Twig, G.; Shirihai, O.S. The Interplay between Mitochondrial Dynamics and Mitophagy. *Antioxid. Redox Signal.* **2011**, *14*, 1939–1951. [[CrossRef](#)]
221. Yamano, K.; Fogel, A.I.; Wang, C.; van der Bliek, A.M.; Youle, R.J. Mitochondrial Rab GAPs govern autophagosome biogenesis during mitophagy. *Elife* **2014**, *3*, e01612. [[CrossRef](#)] [[PubMed](#)]
222. Ashford, T.P.; Porter, K.R. Cytoplasmic components in hepatic cell lysosomes. *J. Cell Biol.* **1962**, *12*, 198–202. [[CrossRef](#)] [[PubMed](#)]

223. Kuma, A.; Matsui, M.; Mizushima, N. LC3, an Autophagosome Marker, Can be incorporated into Protein Aggregates Independent of Autophagy: Caution in the Interpretation of LC3 Localization. *Autophagy* **2007**, *3*, 323–328. [[CrossRef](#)] [[PubMed](#)]
224. Dagda, R.K.; Cherra, S.J.; Kulich, S.M.; Tandon, A.; Park, D.; Chu, C.T. Loss of PINK1 function promotes mitophagy through effects on oxidative stress and mitochondrial fission. *J. Biol. Chem.* **2009**, *284*, 13843–13855. [[CrossRef](#)] [[PubMed](#)]
225. Mizushima, N.; Yoshimori, T.; Levine, B. Methods in mammalian autophagy research. *Cell* **2010**, *140*, 313–326. [[CrossRef](#)] [[PubMed](#)]
226. Williams, J.A.; Zhao, K.; Jin, S.; Ding, W.-X. New methods for monitoring mitochondrial biogenesis and mitophagy in vitro and in vivo. *Exp. Biol. Med. (Maywood)* **2017**, *242*, 781–787. [[CrossRef](#)]
227. Dolman, N.J.; Chambers, K.M.; Mandavilli, B.; Batchelor, R.H.; Janes, M.S. Tools and techniques to measure mitophagy using fluorescence microscopy. *Autophagy* **2013**, *9*, 1653–1662. [[CrossRef](#)]
228. Kim, I.; Lemasters, J.J. Mitophagy selectively degrades individual damaged mitochondria after photoirradiation. *Antioxid. Redox Signal.* **2011**, *14*, 1919–1928. [[CrossRef](#)]
229. Elmore, S.P.; Qian, T.; Grissom, S.F.; Lemasters, J.J. The mitochondrial permeability transition initiates autophagy in rat hepatocytes. *FASEB J.* **2001**, *15*, 2286–2287. [[CrossRef](#)]
230. DeVorkin, L.; Gorski, S.M. LysoTracker Staining to Aid in Monitoring Autophagy in Drosophila. *Cold Spring Harb. Protoc.* **2014**, *2014*, pdb-prot080325. [[CrossRef](#)]
231. Pierzyńska-Mach, A.; Janowski, P.A.; Dobrucki, J.W. Evaluation of acridine orange, LysoTracker Red, and quinacrine as fluorescent probes for long-term tracking of acidic vesicles. *Cytom. Part A* **2014**, *85*, 729–737. [[CrossRef](#)] [[PubMed](#)]
232. Kimura, S.; Noda, T.; Yoshimori, T. Dissection of the autophagosome maturation process by a novel reporter protein, tandem fluorescent-tagged LC3. *Autophagy* **2007**, *3*, 452–460. [[CrossRef](#)] [[PubMed](#)]
233. Allen, G.F.G.; Toth, R.; James, J.; Ganley, I.G. Loss of iron triggers PINK1/Parkin-independent mitophagy. *EMBO Rep.* **2013**, *14*, 1127–1135. [[CrossRef](#)] [[PubMed](#)]
234. Kim, S.-J.; Khan, M.; Quan, J.; Till, A.; Subramani, S.; Siddiqui, A. Hepatitis B virus disrupts mitochondrial dynamics: Induces fission and mitophagy to attenuate apoptosis. *PLoS Pathog.* **2013**, *9*, e1003722. [[CrossRef](#)] [[PubMed](#)]
235. Katayama, H.; Kogure, T.; Mizushima, N.; Yoshimori, T.; Miyawaki, A. A sensitive and quantitative technique for detecting autophagic events based on lysosomal delivery. *Chem. Biol.* **2011**, *18*, 1042–1052. [[CrossRef](#)]
236. Bingol, B.; Tea, J.S.; Phu, L.; Reichelt, M.; Bakalarski, C.E.; Song, Q.; Foreman, O.; Kirkpatrick, D.S.; Sheng, M. The mitochondrial deubiquitinase USP30 opposes parkin-mediated mitophagy. *Nature* **2014**, *510*, 370–375. [[CrossRef](#)]
237. Ferree, A.W.; Trudeau, K.; Zik, E.; Benador, I.Y.; Twig, G.; Gottlieb, R.A.; Shirihai, O.S. MitoTimer probe reveals the impact of autophagy, fusion, and motility on subcellular distribution of young and old mitochondrial protein and on relative mitochondrial protein age. *Autophagy* **2013**, *9*, 1887–1896. [[CrossRef](#)]
238. Hernandez, G.; Thornton, C.; Stotland, A.; Lui, D.; Sin, J.; Ramil, J.; Magee, N.; Andres, A.; Quarato, G.; Carreira, R.S.; et al. MitoTimer: A novel tool for monitoring mitochondrial turnover. *Autophagy* **2013**, *9*, 1852–1861. [[CrossRef](#)]
239. Jones, A.M.; Grossmann, G.; Danielson, J.Å.; Sosso, D.; Chen, L.-Q.; Ho, C.-H.; Frommer, W.B. In vivo biochemistry: Applications for small molecule biosensors in plant biology. *Curr. Opin. Plant Biol.* **2013**, *16*, 389–395. [[CrossRef](#)]



Titre : Développement et caractérisation d'approches basées sur la microscopie pour surveiller le processus d'autophagie et les fonctions mitochondriales au sein des cellules vivantes

Mots clés : autophagie, LC3, ATG4, mitochondrie, FRET-FLIM, biocapteur

Résumé : Bien que plusieurs mécanismes de l'autophagie aient été caractérisés au cours de la dernière décennie, suivre cette voie en temps réel est un véritable défi. Parmi les événements précoces conduisant à l'activation de l'autophagie, la protéase ATG4B amorce le protagoniste clé de l'autophagie, LC3B. En regard du manque de reporters pour suivre cet événement dans les cellules vivantes, nous avons développé un biocapteur basé sur la technologie Förster's Resonance Energy Transfer (FRET), répondant à l'amorçage de LC3B par ATG4B. Le biocapteur a été généré en encadrant LC3B dans une paire de fluorophores FRET donneur-accepteur résistant au pH que sont Aquamarine et tdLanYFP. La majeure partie de mon travail de thèse fut consacrée à caractériser ce biocapteur en utilisant un microscope développé dans notre équipe appelé fastFLIM (fast Fluorescence Lifetime Imaging Microscopy). Nous avons montré ici que le biocapteur a une double application. Premièrement, le phénomène de FRET indique l'amorçage de LC3B par ATG4B et la résolution de l'image FRET permet de caractériser la répartition spatiale de l'activité d'amorçage. Secondairement, la quantification du nombre de foyers Aquamarine-LC3B détermine le degré d'activation de l'autophagie au sein des cellules vivantes. Nous avons ensuite montré grâce à la régulation négative d'ATG4B (par technologie siRNA), qu'il existe de légers pools de LC3B non amorcés, et que

l'amorçage du biocapteur est complètement aboli dans les cellules dont la présence d'ATG4B est totalement abrogée (par technologie CRISPR). Enfin, nous avons criblé les inhibiteurs d'ATG4B disponibles dans le commerce et nous avons illustré leur différent mode d'action en mettant en œuvre une méthode d'analyse à résolution spatiale et haute sensibilité, en combinant la technologie de FRET et la quantification des foyers autophagiques. Ainsi, le biocapteur LC3B FRET ouvre la voie à un suivi hautement quantitatif de l'activité ATG4B dans les cellules vivantes et en temps réel, avec une résolution spatio-temporelle sans précédent. Parallèlement à cette partie de mes études de thèse, j'ai étudié certaines des altérations mitochondriales retrouvées dans les cellules cancéreuses de mélanome sensibles et résistantes à la chimiothérapie. En effet, j'ai analysé la dynamique mitochondriale ainsi que les niveaux de protéines mitochondriales dites OXPHOS dans les cellules de mélanome résistantes ou non en utilisant un test de microscopie de photoconversion et des tests biochimiques. Les découvertes et observations préliminaires résultant de cette étude ont jeté les bases du projet plus vaste de notre équipe consistant à utiliser des biocapteurs multiplex, y compris le biocapteur LC3B, pour suivre l'autophagie/mitophagie et diverses fonctions mitochondriales simultanément dans les cellules cancéreuses du mélanome.

Title : Development and characterization of microscopy-based approaches to monitor autophagy and mitochondrial functions in living cells

Keywords : autophagy, LC3, ATG4, mitochondria, FRET-FLIM, biosensor

Abstract : Although several mechanisms of autophagy have been dissected in the last decade, following this pathway in real time remains challenging. Among the early events leading to autophagy activation, the ATG4B protease primes the key autophagy player LC3B. Given the lack of reporters to follow this event in living cells, we developed a Förster's Resonance Energy Transfer (FRET) biosensor responding to the priming of LC3B by ATG4B. The biosensor was generated by flanking LC3B within a pH-resistant donor-acceptor FRET pair, Aquamarine/tdLanYFP. My main thesis work was dedicated to characterize this biosensor by using a microscope developed in our team called fastFLIM (fast Fluorescence Lifetime Imaging Microscopy). We here showed that the biosensor has a dual readout. First, FRET indicates the priming of LC3B by ATG4B and the resolution of the FRET image allows to characterize the spatial heterogeneity of the priming activity. Second, quantifying the number of Aquamarine-LC3B puncta determines the degree of autophagy activation. We then showed that there are small pools of unprimed LC3B upon

ATG4B downregulation, and that the priming of the biosensor is completely abolished in *ATG4B* knockout cells. Last we screened for commercially-available *ATG4B* inhibitors, and we illustrated their differential mode of action by implementing a spatially-resolved, broad-to-sensitive analysis pipeline combining FRET and the quantification of autophagic puncta. Therefore, the LC3B FRET biosensor paves the way for a highly-quantitative monitoring of the *ATG4B* activity in living cells and in real time, with unprecedented spatiotemporal resolution. In the second part of my thesis studies, I investigated the alterations in the mitochondrial dynamics and mitochondrial OXPHOS protein levels in chemotherapy sensitive and resistant melanoma cancer cells by using a microscopy assay of photoconversion and biochemical assays. Preliminary findings and observations resulting from this study have laid the groundwork of our team's greater project of using multiplex biosensors including the LC3B biosensor to follow autophagy/mitophagy and several mitochondrial functions simultaneously in melanoma cancer cells.